

MESOPOROUS ONE-DIMENSIONAL NANOMATERIALS FOR ELECTROCHEMICAL SUPERCAPACITORS

Ph.D. Thesis

By

KITCHAMSETTI NARASIMHARAO



**DEPARTMENT OF METALLURGY ENGINEERING AND
MATERIALS SCIENCE
INDIAN INSTITUTE OF TECHNOLOGY INDORE
JUNE, 2021**

MESOPOROUS ONE-DIMENSIONAL NANOMATERIALS FOR ELECTROCHEMICAL SUPERCAPACITORS

A THESIS

*Submitted in partial fulfillment of the requirements for the
Award of the degree of*

DOCTOR OF PHILOSOPHY

By

**KITCHAMSETTI NARASIMHARAO
(PHD1701105003)**



**DEPARTMENT OF METALLURGY ENGINEERING AND
MATERIALS SCIENCE
INDIAN INSTITUTE OF TECHNOLOGY INDORE
JUNE, 2021**



INDIAN INSTITUTE OF TECHNOLOGY INDORE

CANDIDATE'S DECLARATION

I hereby certify that the work which is being presented in the thesis entitled “**MESOPOROUS ONE-DIMENSIONAL NANOMATERIALS FOR ELECTROCHEMICAL SUPERCAPACITORS**” in the partial fulfillment of the requirements for the award of the degree of **DOCTOR OF PHILOSOPHY** and submitted in the **DEPARTMENT OF METALLURGY ENGINEERING AND MATERIALS SCIENCE, INDIAN INSTITUTE OF TECHNOLOGY INDORE**, is an authentic record of my own work carried out during the time period from July, 2017 to June, 2021 under the supervision of Dr. Rupesh S. Devan, Associate Professor, Department of Metallurgy Engineering and Materials Science.

The matter presented in this thesis has not been submitted by me for the award of any other degree of this or any other institute.

K. Narasimharao
29/01/2021
Signature of the student with date

(KITCHAMSETTI NARASIMHARAO)

This is to certify that the above statement made by the candidate is correct to the best of my/our knowledge.

Rupesh
29/01/2021
Signature of Thesis Supervisor with date

(Dr. RUPESH S. DEVAN)

KITCHAMSETTI NARASIMHARAO has successfully given his/her Ph.D. Oral Examination held on **04/06/2021**.

Rupesh
09/06/2021
Signature of Thesis Supervisor with date

(Dr. RUPESH S. DEVAN)

ACKNOWLEDGEMENTS

I express my sincere thanks to the PSPC (Ph.D. Student Progress Committee) members, Dr. Parasharam M. Shirage (Associate Professor, Department of Metallurgy Engineering and Materials Science) and Dr. Kiran Bala (Associate Professor, Department of Biosciences and Biomedical Engineering) for their continuous observation and valuable suggestions to improve the quality of my Ph.D. work. I am grateful to Dr. Shirage for access to the Electrochemical workstation. I also thank Dr. Santosh S. Hosmani (Associate Professor, Department of Metallurgy Engineering and Materials Science) and Dr. Sunil Kumar (Assistant Professor, Department of Metallurgy Engineering and Materials Science) for their valuable suggestions and also direct access to their laboratory during my experimental work. I extend my gratitude to Prof. Yuan-Ron Ma, Department of Physics, National Dong Hwa University, Taiwan, for providing the necessary research facilities during my doctoral work.

I acknowledge the IIT Indore for providing me the financial support under the teaching assistantship (TA) category during the entire course of my doctoral work. I wish to thank the Department of Metallurgy Engineering and Materials Science and Sophisticated Instruments Center (SIC) IIT Indore for providing access to various experimental and characterization facilities to complete this research work. I am thankful to Mr. Mayur Dhake for providing me helping hand in many technical and non-technical works. Further, I would like to thank all individuals from the support staff of IIT Indore who directly or indirectly contributed to my Ph.D. work.

I am thankful to my colleagues from Nano-architectures Research Group, Dr. Parameshwar R. Chikate, Mr. Vishesh Manjunath, Mr. Santosh Bimli, and Ms. Sameena Mulani, for their company during my Ph.D. work. I am also thankful to all past colleagues from the Nano-architectures Research Group for their company during my Ph.D. work. I would also like to thank my seniors and friends from IIT Indore, Dr. Alfa Sharma, Mr. Digvijay Singh, Mr. Aditya Kumar Litoria, Dr. Yogendra Kumar, and Dr. Prateek Bhojane for their valuable time, constant encouragement, and contribution to accomplish my Ph.D. work.

I would like to express my sincere gratitude to my respectable thesis supervisor Dr. Rupesh S. Devan, for his intellectual guidance and encouragement during my Ph.D. I benefitted a lot from his valuable suggestions, patience, and comments while performing experiments, writing the papers, preparing the answers for the reviewers questions, and the thesis preparation. I am very much thankful to him for his kind support to improve my thesis quality. His support and trust mean a lot to me.

Most importantly, the credit of this all goes to my lovely parents Shri Kitchamsetti Pakeeraiah and Smt. Kitchamsetti Subbayamma. I express my deepest gratitude to them for making me what I am today. They have been my biggest strength throughout this journey of Ph.D. I would not have come up to here without them. Further, I would like to thank my family members and friends (Dr. Ashok Kumar, Dr. M. Venkateswarulu, Dr. Rambabu, Mr. M. Yogesh, Mr. Ashish Kumar, Mr. T. Parameshwararao, Mr. G. Nagamalleswararao, Mr. A. Ramanji Reddy, Mr. M. Pullarao, and Mr. P. Samuel) for always being supportive and encouraging.

Date:04/06/2021

(Kitchamsetti Narasimharao)

Dedicated

To my parents

Kitchamsetti Subbayamma and

Kitchamsetti Pakeeraiah

LIST OF PUBLICATIONS

PAPER-1

N. Kitchamsetti, P. R. Chikate, R. A. Patil, Y. R. Ma, P. M. Shirage, and R. S. Devan, “Perforated mesoporous NiO nanostructures for enhanced pseudocapacitive performance with ultra-high rate capability and high energy density,” *CrystEngComm*, **21** (2019) 7130-7140.

PAPER-2

N. Kitchamsetti, Y. R. Ma, P. M. Shirage, and R. S. Devan, “Mesoporous perovskite of interlocked nickel titanate nanoparticles for efficient electrochemical supercapacitor electrode,” *J. Alloys. Compd.*, **833** (2020) 155134.

PAPER-3

N. Kitchamsetti, R.J. Choudhary, D. M. Phase, and R. S. Devan, “Structural correlation of a nanoparticle-embedded mesoporous CoTiO₃ perovskite for an efficient electrochemical supercapacitor,” *RSC Adv.*, **10** (2020) 23446-23456.

PAPER-4

N. Kitchamsetti, Y. R. Ma, P. M. Shirage, and R. S. Devan, “Hybrid core-shell heteroarchitecture of two-dimensional MnO₂ and one-dimensional NiTiO₃ for high performance electrode of electrochemical supercapacitor,” (*Communicated*).

LIST OF PUBLICATIONS (Other than the thesis)

PAPER-1

N. Kitchamsetti, R. S. Kalubarme, P. R. Chikate, C. J. Park, Y. R. Ma, P. M. Shirage, and R. S. Devan, “An Investigation on the Effect of Li-Ion Cycling on the Vertically Aligned Brookite TiO₂ Nanostructure,” *ChemistrySelect*, **4** (2019) 6620-6626.

PAPER-2

N. Kitchamsetti, M. S. Ramteke, S. R. Rondiya, S. R. Mulani, M. S. Patil, R. W. Cross, N. Y. Dzade, and R. S. Devan, “DFT and experimental investigations on the photocatalytic activities of NiO nanobelts for removal of organic pollutants,” *J. Alloys. Compd.*, **855** (2020) 157337.

PAPER-3

M. S. Patil, **N. Kitchamsetti**, S. R. Mulani, S. R. Rondiya, R. A. Patil, R. W. Cross, N. Y. Dzade, P. S. Patil, Y. R. Ma, and R. S. Devan, “Photocatalytic behavior of Ba(Sb/Ta)₂O₆ perovskite for reduction of organic pollutants: Experimental and DFT correlation,” *J. Taiwan Inst. Chem. Eng.*, **122** (2021) 201-209.

PAPER-4

N. Kitchamsetti, Pravin N. Didwal, Sameena R. Mulani, Madhuri S. Patil, and Rupesh S. Devan, “Photocatalytic activity of MnTiO₃ perovskite nanodiscs for the removal of organic pollutants,” (*Accepted*).

Table of Contents

ACKNOWLEDGEMENTS	vii
LIST OF PUBLICATIONS.....	xi
LIST OF FIGURES	xvii
LIST OF TABLES.....	xxv
NOMENCLATURE	xxvii
Chapter 1: Introduction	
1.1 Overview of energy storage	2
1.2 Mechanism of supercapacitor	4
1.3 Device configuration of the electrochemical supercapacitor.....	5
1.4 Significance of metal oxides for supercapacitor	7
1.4.1 Binary metal oxides	8
1.4.2 Ternary metal oxides	10
1.5 Significance of mesoporous structures	12
1.6 Motivation	14
1.7 Aim of the Thesis	15
1.8 References	16
Chapter 2: Experimental Techniques	
2.1 Introduction.....	32
2.2 Synthesis methods	32
2.2.1 Hydrothermal synthesis.....	32
2.2.2 Sol-gel synthesis.....	34
2.3 Materials characterization techniques.....	37
2.3.1 Drop shape analysis	38
2.3.2 X-ray photoelectron spectroscopy	39
2.3.3 Nitrogen adsorption-desorption isotherm analysis	40
2.3.4 Electrochemical analysis	42
2.4 References	46
Chapter 3: Mesoporous NiO nanostructures	
3.1 Introduction	50
3.2 Experimental Section.....	53
3.3 Results and discussion	54

3.3.1 Field emission scanning electron microscopy	54
3.3.2 Transmission electron microscopy	56
3.3.3 Nitrogen adsorption-desorption Isotherm	56
3.3.4 X-ray Photoelectron Spectroscopy	58
3.3.5 Electrochemical analysis.....	60
3.3.7 Electrochemical Impedance Spectroscopy	68
3.3.8 Ragone Plot.....	69
3.4 Conclusion	71
3.5 References.....	72

Chapter 4: Mesoporous CoTiO₃ nanostructures

4.1 Introduction.....	80
4.2 Experimental section.....	82
4.3 Results and discussion	83
4.3.1 Fourier transform infrared spectroscopy.....	83
4.3.2 X-ray diffraction and Raman spectroscopy	84
4.3.3 Field emission scanning electron microscopy	85
4.3.4 Nitrogen adsorption-desorption isotherm	88
4.3.5 X-ray photoelectron spectroscopy	90
4.3.6 Contact angle measurements.....	92
4.3.7 Electrochemical performance	93
4.3.8 Electrochemical impedance spectroscopy	98
4.3.9 Ragone plot	100
4.4 Conclusions.....	101
4.5 References.....	101

Chapter 5: Mesoporous NiTiO₃ nanostructures

5.1 Introduction	108
5.2 Experimental section	110
5.3 Results and discussion.....	111
5.3.1 Field emission scanning electron microscopy	111
5.3.2 X-ray photoelectron spectroscopy	114
5.3.3 X-ray diffraction	116
5.3.4 Nitrogen adsorption-desorption isotherm	117

5.3.5	Contact angle measurements	118
5.3.6	Electrochemical analysis	120
5.3.7	Electrochemical impedance spectroscopy	127
5.3.8	Ragone plot	128
5.4	Conclusion	130
5.5	References	131
Chapter 6: Mesoporous 1D NiTiO₃@2D MnO₂ core-shell heterostructure		
6.1	Introduction	138
6.2	Experimental section	141
6.3	Results and discussion.....	143
6.3.1	Field emission scanning electron microscopy	143
6.3.2	Transmission electron microscopy	144
6.3.3	X-ray photoelectron spectroscopy	145
6.3.4	Nitrogen adsorption-desorption isotherm	147
6.3.5	Contact angle measurements	148
6.3.6	Electrochemical analysis	149
6.3.7	Electrochemical impedance spectroscopy	155
6.3.8	Ragone plot.....	157
6.3.9	Computational analysis.....	158
6.4	Conclusion.....	161
6.5	References	162
Chapter 7: Summary and Conclusions		
7.1	Summary and Conclusions	172
7.2	Future scope.....	178

LIST OF FIGURES

Figure 1.1. The plot of Power density vs. Energy density, also called a Ragone plot, for various electrical energy storage devices.....	3
Figure 1.2. Schematic representation of the types of Electrochemical supercapacitors.....	5
Figure 1.3. Schematic representation of the construction of (a) three-electrode, (b) two-electrode supercapacitor.....	6
Figure 2.1. Teflon lined stainless steel autoclave used for the synthesis of nanomaterials	33
Figure 2.2. Schematic diagram showing the sol-gel method and its desired products	35
Figure 2.3. Schematic representation of wetting behavior.....	39
Figure 2.4. Principle of X-ray photoelectron spectroscopy.....	40
Figure 2.5. Different types of adsorption isotherms as classified by IUPAC	42
Figure 2.6. Typical representation of cyclic voltammogram (CV) of pseudocapacitive based materials existence of oxidation and redox peaks.....	42
Figure 2.7. Typical representation of Galvanostatic charge-discharge (GCD) of pseudocapacitive materials.....	45
Figure 2.8. Typical Nyquist plot representation of pseudocapacitive materials.....	46
Figure 3.1. Schematic diagram of the mesoporous NiO nanostructure-based supercapacitor.....	53
Figure 3.2. FESEM images of controlled surface morphological features of the NiO nanostructures. The upper panel shows the top view of the nanostructures obtained at a reaction time of (a) 6 h, (b) 12 h, and (c) 48 h. Inset of the	

Fig. shows their respective high-magnification FESEM image. The lower panel shows the side view of those nanostructures (d-f), respectively. (g) The high-magnification TEM image of the single nanobelts extracted from the large area array of nanobelts in (b).....55

Figure 3.3. High-Resolution TEM image of the single nanobelts extracted from the large area array confirming (a) the mesoporous nature of nanobelts and (b) interplanar spacing of the well-separated NiO nanoparticles of the nanobelts. The nanoparticles are traced with the dotted red lines.....56

Figure 3.4. (a) N₂ adsorption-desorption isotherm and (b) BJH pore size distribution of the NiO nanobelts obtained after the reaction time of 12 h.....57

Figure 3.5. XPS peak intensity contours of the (a) Ni(2p) and (b) O(1s) core levels obtained for the reaction-time dependent NiO nanostructures. The high-resolution XPS spectra of the (c) Ni(2p) and (d) O(1s) core levels of the NiO nanobelts synthesized at a reaction time of 1 h. The XPS spectra were deconvoluted using Voigt curve fitting function.....58

Figure 3.6. CV curves of NiO (a) thin film, (b) mesoporous nanobelts, and (c) nanoflakes at various scan rates.....60

Figure 3.7. CV curves of the nanoflakes obtained at a reaction time of (a) 18 and (b) 24 h62

Figure 3.8. The variation of the peak current density (i_p) of the anodic reduction peak with the square root of the scan rate ($v^{1/2}$) observed in CV curves.....62

Figure 3.9. GCD curves of NiO (a) thin film, (b) mesoporous nanobelts, and (c) nanoflakes at various current densities. (d) Graph of current density dependent variation in the specific capacitance of thin films, mesoporous nanobelts, and nanoflakes prepared at a various reaction time of 6, 12, 18, 24, and 48 h, respectively.....63

Figure 3.10. GCD curves of NiO nanoflakes synthesized at a reaction time of (a) 18 and (b) 48 h, respectively, at various current densities.....	64
Figure 3.11. Cycling stability and capacitance retention of perforated mesoporous NiO analyzed from CV at scan range of 100 mV/s, and GCD at the current density of 4 mA/g. The percentage indicated the Cs retention with the consistent increment in the number of cycles.....	67
Figure 3.12. Nyquist plot of the mesoporous nanobelts and nanoflakes (prepared at a reaction time of 18 and 48 h) acquired at a potential of 0.30 V. Inset shows the best fitted equivalent circuit model and the expanded high-frequency region of the EIS spectra.....	69
Figure 3.13. Ragone plot of thin films composed of irregular morphologies, perforated mesoporous nanobelts, and nanoflakes (obtained at reaction times of 18, 24, and 48 h) of NiO determined at various current densities.....	71
Figure 4.1. FTIR spectra of (a) CTO microrod obtained after annealing (b) as-prepared Co-Ti-EG polymer chain precursor.....	83
Figure 4.2. (a) XRD pattern and (b) Raman spectrum of mesoporous CTO microrods	84
Figure 4.3. FESEM image of (a) as-synthesized and (b) annealed CoTiO ₃ microrod. (c) The high-magnification FESEM image confirms the formation of mesoporous CoTiO ₃ microrod composed of hierarchically interlinked nanoparticles.....	86
Figure 4.4. (a, and b) statistical histogram of the width distribution microrods and nanoparticles, respectively, and (c) EDS spectra of mesoporous CTO microrods.....	87
Figure 4.5. (a) N ₂ adsorption-desorption isotherm, and (b) BJH pore size distribution of the mesoporous CTO microrod.....	89

Figure 4.6. Typical high-resolution XPS spectra of the (a) Co(2p), (b) Ti(2p), and (c) O(1s) core levels of the mesoporous CTO microrods90

Figure 4.7. Contact angle measurement showing the interface of the aqueous KOH electrolyte of (a) 0.5 M, (b) 1 M, (c) 1.5 M, and (d) 2 M concentration on the surface of the working electrode of mesoporous CTO microrods....92

Figure 4.8. (a) Cyclic voltammograms and (b) specific capacitance of mesoporous CTO microrod observed at various scan rates in 2 M aq. KOH electrolyte. (c) The graphical illustration of the anodic peak current density (i_p) with the square root of the scan rate ($v^{1/2}$).....94

Figure 4.9. (a) GCD curves and (b) evaluated specific capacitance of mesoporous CTO rods at various current densities. (c) Specific capacitance retention analyzed for 1950 GCD cycles at the current density of 100 mA/g. The inset figure shows the first 10 cycles.....97

Figure 4.10. (a) Nyquist (EIS) plot of the mesoporous CTO microrods obtained before and after cyclic stability studies. Inset shows the best fitted equivalent circuit model. (b) Evaluated specific energy and specific power of mesoporous CTO microrods.....99

Figure 5.1. FESEM image of as (a) synthesized NiTiO₃ rods (i.e., before annealing) transformed in to (b) mesoporous structure retaining rod morphology after annealing. (c) and (d) shows their respective high magnification FESEM images. (d) Mesoporous NTO rods are composed of interlocked nanoparticles.....111

Figure 5.2. Statistical histogram showing the diameter distribution of the nanoparticles forming the mesoporous hexagonal NiTiO₃ rods.....112

Figure 5.3. EDX spectra of as-synthesized and mesoporous (i.e., annealed) NTO rods113

Figure 5.4.	Typical high resolution XPS spectra of the (a) Ni (2p), (b) Ti (2p), and (c) O (1s) core levels of the mesoporous NTO rods. The XPS spectra were deconvoluted via Voigt function within Shirley background	114
Figure 5.5.	Rietveld refined XRD pattern of NTO rods along with the residual curve located at the bottom	117
Figure 5.6.	(a) N ₂ adsorption-desorption isotherm, and (b) BJH pore size distribution of the mesoporous NTO rods.....	118
Figure 5.7.	Contact angle measurement showing the interface of the aqueous KOH electrolyte of (a) 0.5 M, (b) 1M, (c) 1.5 M, and (d) 2 M concentration on the surface of the working electrode of mesoporous NTO rods	119
Figure 5.8.	(a) Cyclic voltammograms of mesoporous NTO rods at various scan rates in 2 M aq. KOH electrolyte. The graphical illustration of (b) the anodic peak current density (i_p) with the square root of the scan rate ($v^{1/2}$) and (c) specific capacitance at various scan rates, evaluated from the CV curve	120
Figure 5.9.	(a) GCD curves, and (b) evaluated specific capacitance of mesoporous NTO rods at various current densities	124
Figure 5.10.	(a) Cycling stability and capacitance retention of mesoporous NTO rods analyzed from GCD at the current density of 80 mA/g for 2100 cycles. The inset figure shows the first 10 cycles. The percentage number signifies the retention of the C_s with GCD cycles. (b) Nyquist (EIS) plot of the mesoporous NTO rods obtained before and after cyclic stability, and its best fitted equivalent circuit model	126
Figure 5.11.	Evaluated energy and power density of mesoporous NTO rods determined at various current densities	129
Figure 6.1.	Schematic representation of the distinct arrangements of 2D nanoflakes and 1D rods for the formation of core-shell heteroarchitecture. Scheme 1	

represents the core-shell heteroarchitecture of interlinked 2D nanoflakes and single-crystalline 1D rods. Scheme 2 illustrates the synergistic core-shell heteroarchitecture of interlinked 2D nanoflakes and 1D mesoporous rods of interconnected nanoparticles. Scheme 2 provides a relatively larger surface area and access for the ions to diffuse deep inside the core-shell structure compare to scheme 1. Red dotted circles indicate the interfacial and cross-sectional view of the core-shell heteroarchitecture140

Figure 6.2. (a) Low-magnification FESEM image of MnO₂@NiTiO₃ core-shell heterostructure. (b) High-resolution FESEM image of the portion of MnO₂@NiTiO₃ core-shell heterostructure showing the shell of interlocked 2D MnO₂ nanoflakes. The (c) EDS spectra and (d) X-ray diffraction pattern of mesoporous NiTiO₃@MnO₂ core-shell heterostructure143

Figure 6.3. TEM images of (a) MnO₂ nanoflakes and (b) NTO nanoparticles extracted from the MnO₂@NTO core-shell heterostructure. (c) HRTEM image of NTO nanoparticles showing clear lattice fringes.....145

Figure 6.4. Typical high-resolution XPS spectra of the (a) Mn(2p) and (b) O(1s) core levels of the mesoporous MnO₂@NiTiO₃ core-shell heterostructure. The XPS spectra were deconvoluted via the Voigt function within Shirley's background145

Figure 6.5. (a) N₂ adsorption-desorption isotherm, and (b) BJH pore size distribution of the mesoporous MnO₂@NiTiO₃ core-shell heterostructure147

Figure 6.6. Contact angle measurement showing the interface of the aqueous KOH electrolyte of (a) 0.5 M, (b) 1 M, (c) 1.5 M, and (d) 2 M concentration on the surface of the mesoporous MnO₂@NiTiO₃ core-shell heterostructure working electrode148

- Figure 6.7.** Steady-state cyclic voltammograms of (a) Ni-foam, NiTiO₃, and mesoporous MnO₂@NiTiO₃ core-shell heterostructure recorded at a scan rate of 5 mV/s, and (b) mesoporous MnO₂@NiTiO₃ core-shell heterostructure recorded at various scan rates from 5 to 50 mV/s in 2 M aq. KOH electrolyte. (c) The variation in the peak current density (*i_p*) and the square root of the scan rate (*s*) of the cathodic peak current, and (d) the specific capacitance of mesoporous MnO₂@NiTiO₃ core-shell heterostructure evaluated from the CV curves in (b)149
- Figure 6.8.** GCD analysis of (a) NiTiO₃ and MnO₂@NiTiO₃ core-shell heterostructure recorded at a current density of 40 mA/g. (b) GCD curves and (c) specific capacitance of mesoporous MnO₂@NiTiO₃ core-shell heterostructure measured at various current densities154
- Figure 6.9.** (a) Electrochemical impedance spectra (i.e., Nyquist plot) of the mesoporous NiTiO₃ rods and MnO₂@NiTiO₃ core-shell heterostructure. (b) The capacitance retention of MnO₂@NiTiO₃ core-shell heterostructure analyzed from 5000 continuous GCD cycles at a current density of 80 mA/g155
- Figure 6.10.** (a) FESEM image and (b) EDS of MnO₂@NTO core-shell heterostructure after 5000 continuous GCD cycles for the stability study.....155
- Figure 6.11.** Ragone plot of MnO₂@NiTiO₃ core-shell heterostructure. The Ragone plot comprises another Mn, Ni, and Ti based metal oxides are in their pure or hetero-structure form.....157
- Figure 6.12.** (a, b) Crystal structures and (c, d) the corresponding partial density of states of the ilmenite hexagonal NiTiO₃ and tetragonal α-MnO₂.....159
- Figure 6.13.** Optimized structures of (a) MnO₂(100), (b) NiTiO₃(001), and (c) the equilibrium structure of the MnO₂/NiTiO₃ heterostructure.....160

Figure 6.14. (a) Charge density difference iso-surface contours of the $\text{MnO}_2/\text{NiTiO}_3$ heterostructure, where the cyan and yellow regions denote electron density accumulation and depletion by $0.03 \text{ e}/\text{\AA}^3$, respectively. PDOS of (b) isolated $\text{NiTiO}_3(001)$ and (c) $\text{MnO}_2/\text{NiTiO}_3$ heterostructure.....161

Figure 7.1. 1D nanobelts (right panel) and 2D nanosheets (left panel) morphology of NiO has significantly controlled the pseudocapacitive performance in the KOH electrolyte. The perforated and interlocked mesoporous structure of NiO nanobelts have delivered higher power density and energy density (middle panel) than that of nanosheets.174

Figure 7.2. The interconnection of CTO nanoparticles resulted in the formation of mesoporous CTO rods with increased textural boundaries (left panel), offered significantly larger diffusion of OH^- ions deep inside the rod structure, and delivered a specific capacitance of 608.4 F/g (right panel), the specific power of 4835.7 W/kg , and specific energy of 9.77 Wh/kg 175

Figure 7.3. Mesoporous nickel titanate rods encompassing hierarchically interlocked nanoparticles (inset of left panel) provided diffusion-controlled easy/faster and enhanced access to the OH^- ions deep inside the rod body (inset of right panel) and delivered highly stable long-life cycle (left panel) up to 2100 cycles with partial reduction in the charge diffusion mechanism (right panel)176

Figure 7.4. The mesoporous heteroarchitecture of 2D MnO_2 nanoflakes decorated over 1D NiTiO_3 rods delivered excellent energy storage performance as the electrode for electrochemical supercapacitor.....177

LIST OF TABLES

Table 5.1. Comparative analysis of the specific capacitance (C_s) values of various materials reported in the literature.....	122
Table 5.2. Comparative analysis of the power density of various materials reported in the literature.....	130
Table 7.1 Comparison of performance of the electrode materials.....	177

NOMENCLATURE

B

B.E.	Binding Energy
BET	Brauner-Emmett-Teller
BJH	Barrett-Joyner-Halenda

C

CE	Counter Electrode
CPE	Constant Phase Element
C _s	Specific Capacitance
CoTiO ₃	Cobalt Titanate
CTO	Cobalt Titanate
CV	Cyclic Voltammetry

D

DSA	Drop Shape Analyzer
-----	---------------------

E

E	Energy density
EDLC	Electric Double layer Capacitor
EDS	Energy Dispersive Spectroscopy
EG	Ethylene Glycol
EIS	Electrochemical Impedance Spectroscopy
ESR	Equivalent Series Resistance
eV	Electron Volt

F

FESEM	Field Emission Scanning Electron Microscopy
-------	---

G

GCD	Galvanostatic charge-discharge
GofF	Goodness of fit factor

H

HCS	Hybrid Capacitors
-----	-------------------

I

ITO	Indium Tin Oxide
IUPAC	International Pure and Applied Chemistry

J

JCPDS	Joint Committee for Powder Diffraction Standards
-------	--

M

MnO₂ Manganese oxide
MOF Metal Organic Framework

N

NiO Nickel Oxide
NHE Normal Hydrogen Electrode
NMP N-Methyl 2-Pyrrolidone
NTO Nickel Titanate
NiTiO₃ Nickel Titanate

O

OECD Organization for Economic Cooperation and
Development

P

P Power density
PCs Pseudo Capacitors
PVDF Polyvinylidene fluoride

R

R_{ct} Charge transfer resistance
RE Reference Electrode
Re Electrolyte resistance

S

SCE Saturated Calomel Electrode

T

TEM Transmission electron microscopy
TiO₂ Titanium dioxide
TMO Transition Metal Oxide

U

UPS Uninterrupted Power Supply

W

WE Working Electrode

X

XPS X-Ray photoelectron spectroscopy
XRD X-Ray diffraction

Z

Z_w Warburg resistance

Chapter 1

Introduction

The overview of the energy storage, mechanism, and device configuration of the supercapacitor is briefly discussed in this chapter. The significance of binary and ternary metal oxides and mesoporous structures is discussed in detail, which has helped to understand the research gaps and perform research on mesoporous metal oxides electrode material for supercapacitor. The motivation and objectives of the research work are briefed at the end of this chapter.

1.1 Overview of energy storage

Global industrialization and enriched living standards consumed 610 Quads of energy in 2020, and this demand is expected to rise by 50 % until 2050. Most of the increase will be due to the energy requirement of the developing countries fall outside of the Organization for Economic Cooperation and Development (OECD) called non-OECD to drive their economic growth. Notably, India is expected to driven half of this increase along with China. Although fossil fuels are dominant primary energy resources providing nearly 20 % of the global electricity need (IEO-2019 report), they have significantly contaminated the environment by CO₂ emissions. Therefore, renewable energy sources have attracted significant attention and are expected to collectively contribute 30 % of electricity needs. However, the risks involved and limitation of energy generation in both cases demand an urgent hunt for excellent energy storage technologies.

Of the several available electrical energy storage systems, fuel cells, Li-ion batteries, capacitors, and supercapacitors attract the scientific and industrial community for various usage. These systems exhibit distinct specific energy and specific power, as shown in Figure 1.1, [1] and restrict themselves for particular functions. However, Li-ion batteries and supercapacitors have attracted the scientific and industrial community and become the foremost choices for most applications. In general, batteries offer the highest specific energy in the range of 120 to 200 Wh/kg with a relatively low specific power of 0.4 to 3 kW/kg. Conventional capacitors deliver relatively lower specific energy (i.e., < 0.1 Wh/kg) and high specific power (i.e., <100 kW/kg). Conversely, the electrochemical supercapacitors deliver a relatively much higher specific power in the range of 5 to 55 kW/kg and a reasonable specific energy of 4 to 8 Wh/kg. Therefore, the electrochemical supercapacitors are likely to bridge the energy-power gap between the batteries and conventional capacitors and dominate to lead various technological development in the near future. The battery stores energy electrochemically, where the chemical reaction between electrode-electrolyte during the charge-discharge process releases electrical carriers. The slow charging-discharging process in the batteries can degrade the chemical compounds or working electrode materials over time and lose their ability to retain energy throughout their lifetime. However, in the supercapacitors, energy is stored electrostatically on the surface of the material without any chemical reaction. They can

be charged quickly and do not lose their storage capabilities over time. The main limitation of the supercapacitor is the amount of energy stored per unit weight, called energy density. The very small energy density and cost involved in preparing high-performing supercapacitor materials often direct the utilization of cost-effective batteries. However, the recent development in producing novel supercapacitor materials and enhancing their energy storage performance may soon bridge the energy density gap commercially. The complementary utilization of supercapacitor and battery can expand their usage in practical applications.

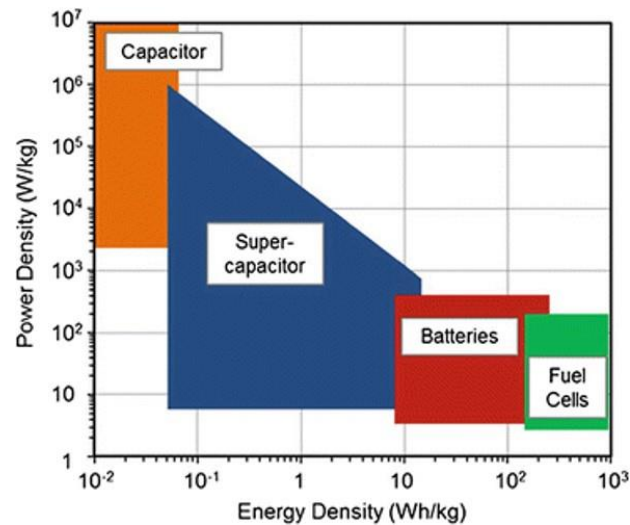


Figure 1.1. The plot of Power density vs. Energy density, called a Ragone plot, for various electrical energy storage devices. [1]

Supercapacitors have several practical applications, which includes

Transportation: The most promising market for supercapacitors is the transportation industry. They can be used in automobiles by coupling with batteries. They can also improve fuel efficiency by storing energy when an automobile is braking and releasing energy while accelerating. Automobiles powered by coupling fuel cells with supercapacitors are ideal choices for stop-and-go traffic, where supercapacitors provide sudden bursts of energy during start-up, and fuel cells provide sustained energy. Supercapacitors also perform well at extremely low temperatures (-40 °C).

Consumer electronics: Supercapacitors are widely used in consumer electronics as backup energy sources for system memories, microcomputers, toys, clocks, mobile phones, and system boards. They are ideal for devices requiring quick charges.

Uninterrupted power supply systems (UPS): Supercapacitors can be used for temporary backup power in UPS systems, providing an instantaneous supply of power without delays and preventing malfunctions of missions. Supercapacitors quickly bridge the power applications for stationary UPS systems that are augmented with fuel cells.

Other applications: Supercapacitors show promise for critical-load operations such as banking centers, hospitals, cell phone towers, airport control towers. The critical time between a power outage and the start of a generator can be bridged effectively by supercapacitors because they provide power within milliseconds to a few seconds after an outage.

1.2 Mechanism of supercapacitor

Based on the charge storage mechanism and electrode material used, the supercapacitors can be classified into three categories, such as (i) Electrical Double-layer Capacitors (EDLCs), (ii) Pseudocapacitors (PCs), and (iii) hybrid capacitors (HCs), as shown in Figure 1.2. EDLCs mainly employ carbon electrode materials, such as graphene, activated carbon, and carbon aerogels, [2] to accumulate charge via reversible adsorption/desorption of ions at the electrode-electrolyte interface. The charge-discharge process in EDLC is equivalent to the dielectric behavior of conventional capacitors, as no faradaic reactions occurred during the energy storage process. EDLC materials have been studied extensively due to their high specific surface area, good electrical conductivity, and excellent mechanical stability, but they suffer from low specific capacitance. The pseudocapacitors (or redox capacitors) store the energy via fast and reversible faradaic redox reactions at the surface of the electrode material. Transition metal oxides (TMO) and conducting polymers (CPs) are the most preferred electrode materials for pseudocapacitors. [2,3] The TMO offers relatively high specific capacitance and superior energy density, while CPs are unique candidates for high-performance supercapacitors due to their excellent intrinsic conductivity. Unfortunately, the lower conductivity of TMOs significantly hinders them from reaching the high theoretical specific capacitance value. On the other hand, CPs suffer from poor cycling stability performance due to the repeated swelling and shrinking of the polymer chains during the ion diffusion and extraction process. Due to these specific constraints of individual material, many attempts

have been made to fabricate hybrid supercapacitors (HCs) that combine the advantages of both EDLC and pseudocapacitors and enhance the overall electrochemical performance.

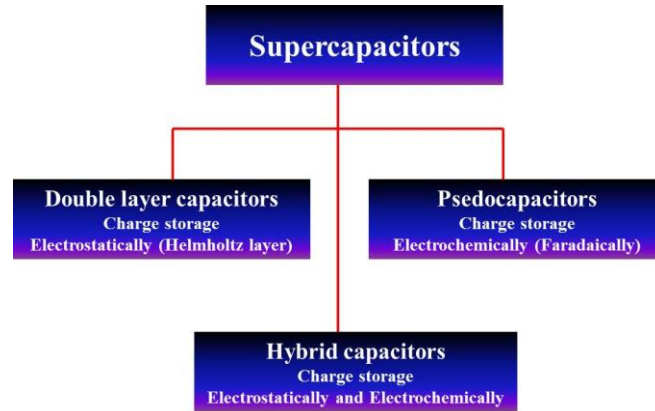


Figure 1.2. Schematic representation of the types of Electrochemical supercapacitors.

1.3 Device configuration of the electrochemical supercapacitor

Generally, the electrochemical properties of supercapacitors are evaluated in three or two electrode systems. The three-electrode system employed to investigate the electrochemical performance of the active materials is composed of a working electrode (WE), reference electrode (RE), and counter electrode (CE), as illustrated in Figure 1.3(a). The working electrode comprises active materials, and the voltage across it is measured with respect to the reference electrode. [4] The working electrode is generally made by coating the active material onto the surface of stable electrodes such as Ni foam, carbon paper, glassy carbon, etc. The active material was added with NMP and isopropanol solvents to form a viscous ink, and subsequently mixed with activated carbon to make the active material conductively efficient. Moreover, PVDF/PTFE, added to it, acts as a binder and keeps the active material attached very strongly on the electrode surface in the electrolyte solution. A reference electrode with stable and reproducible potential is preferably reversible in nature, where a small anodic current produces the oxidation reaction and a cathodic current produces the reduction reaction. Most commonly used reference electrodes are Ag/AgCl electrode, Saturated Calomel Electrode (i.e., SCE), normal hydrogen electrode (i.e., NHE). Finally, an auxiliary electrode, also known as a counter electrode, is made up of exceptionally conductive materials like

graphite or platinum foil, stabilizes the electrochemical reaction at the working electrode by calibrating its potential.

The two-electrode system is composed of a pair of closely spaced electrodes isolated from electrical contact by a porous separator, as shown in Figure 1.3(b). [5] The electroactive material is attached to the current collector from where the electrical current conducts and acts as either a positive or negative electrode. The separator, an ion-permeable but electrically insulating dielectric porous membrane, allows the migration of electrolyte ions while keeping both electrodes electrically apart. The separator and the electrodes are impregnated with an electrolyte, allowing ionic current to flow between the electrodes while preventing electronic current from discharging the cell. The supercapacitor with a two-electrode configuration is categorized as symmetric and asymmetric devices based on the nature of electrode materials. [6]

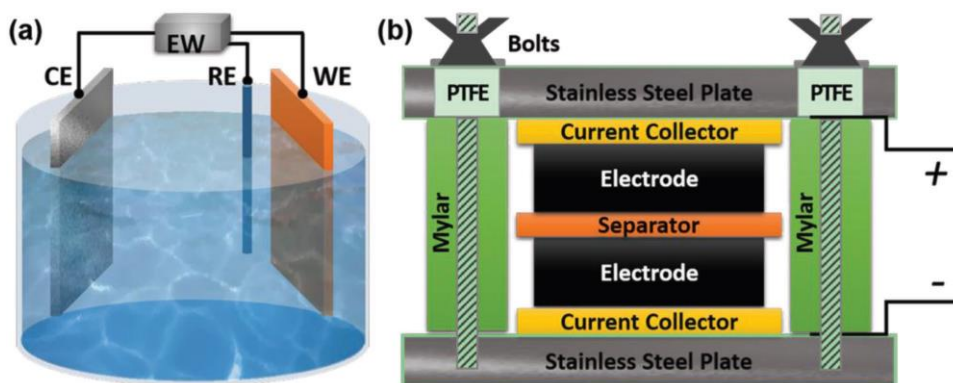


Figure 1.3. Schematic representation of the construction of (a) three-electrode, (b) two-electrode supercapacitor. [4,5]

The same material loaded with the equal mass for both the positive and negative electrodes configure a symmetric supercapacitor, where the applied voltage is distributed equally on two electrodes. It possesses both electrical double-layer capacitance and pseudocapacitance. The electrical double-layer capacitance type devices store electrostatic charges from the accumulation and separation of ions at the electrode and electrolyte interface. [7] However, the pseudocapacitive type device reveals the faradic charge transfer originated from the progression of reversible redox or intercalation process on the electrode surface. The Pseudocapacitance is accompanied by electron charge transfer between the electrode and electrolyte to absorbed ions. Asymmetric

supercapacitors, consisting of one pseudocapacitive electrode and other electric double layer capacitive electrodes, achieve a wider operating potential window and deliver a high energy and power density. [8] Therefore, an asymmetric supercapacitor employing dissimilar electrode materials that can be operated at different potential windows can be manufactured with the cell voltages extending to 2 V in an aqueous electrolyte. [9] However, the reformed electrode materials architectures and the optimized mass ratio of positive and negative electrodes should be considered for smart supercapacitors configuration. [10]

Likewise, more extended cycling stability, retainability, and flexibility are crucial parameters in assessing the supercapacitor performance. The longer cyclic stability of ≥ 10000 cycles while retaining the initial C_s value is expected from the best performing device. The higher electrical conductivity generates a higher charge carrier mobility, and a high surface area promotes charge absorption or provides more redox reaction sites. Therefore, the good electrical conductivity and larger surface area of the electrode materials contribute to high specific capacitance and hence to the energy and power density. All these properties are highly dependent not only on the electrode material itself but also on the electrolyte used. To date, the supercapacitors offered much higher specific power but suffering for specific energy compared to Li-ion batteries. Consequently, the biggest challenge is improving energy density while maintaining high specific capacitance, higher power density, and excellent cycling ability for their widespread utilization to replace/compete with the batteries.

1.4 Significance of metal oxides for supercapacitor

Transition metal oxides are a unique class of solid functional materials that usually consist of multiple oxidation states and ionic bonding and exhibit semiconducting properties. Most metal oxides actively participate in faradaic redox reactions and are thereby extensively utilized as electrode materials for supercapacitors. Unlike conducting polymers, the metal oxide never suffers from swelling and shrinkage. [11] Therefore, metal oxides are known for more extended cyclic stability and better retentivity. So far, several research groups across the globe have explored different classes of metal oxides as a working electrode for supercapacitors, which are discussed below.

1.4.1 Binary metal oxides

Metal oxides are crystalline solids that hold a metal cation and an oxide anion. Oxides of the transition metals with +1, +2, and +3 oxidation states are an ionic mixture, and those oxides with +4, +5, +6, and +7 oxidation numbers behave as covalent compounds containing covalent metal-oxygen bonds. Redox transition metal compounds, in particular oxides of several metals like Mn, Co, Ni, Ti, Fe, Cu, and Mo, are emerging as promising electrode materials for supercapacitors. [12] Metal sites act as an active redox center and sustain processes involving different valence states, a property that enables increased charge storage capacity. Furthermore, their valence changes at different potentials, e.g., valence changes of $\text{Co}^{2+}/\text{Co}^{+3}$ and $\text{Ni}^{2+}/\text{Ni}^{+3}$ obtained in a potential window of $\sim 0 - 0.6$ V; $\text{Ti}^{3+}/\text{Ti}^{4+}$, and $\text{Mn}^{3+}/\text{Mn}^{4+}$ obtained in the potential range of $\sim 0-1.0$ V in aqueous electrolytes. [13] Furthermore, crystal structure, crystallinity, morphology, and specific surface area are the key parameters to decide the electrochemical performance of metal oxides. [14] The high crystallinity enhances the conductivity but reduces the specific surface area. Therefore, the heat treatments at optimum temperature are essential to achieve better electrochemical performance from metal oxides.

Various binary metal oxides have been explored for application in supercapacitor. RuO_2 is the first well explored pseudocapacitive material [19] exhibiting high theoretical capacitance (i.e., 1400-2000 F/g), [20] higher conductivity (i.e., $35.2 \mu\Omega\cdot\text{cm}$), [21] rich redox activity, and more significant reversibility (up to 10000 cycles). [22] However, the high cost of RuO_2 diverted the scientific and industrial community to explore the inexpensive and abundant oxides of transition metals like Ni, Co, Mn, Cu, Fe, Ti, etc., as working electrodes for supercapacitors. [15-18] Manganese oxide is another well-explored electrode material that exists in MnO , MnO_2 , Mn_2O_3 , and Mn_3O_4 forms. [11] In which, MnO_2 has gained considerable attention for the theoretically predicated capacitance of 1370 F/g. [14] The amorphous MnO_x exhibiting Mn^{3+} and Mn^{4+} states displayed the specific capacitance of 174 F/g and best cycling stability (up to 300 Cycles), which eventually decreased due to morphological transformation

after heat treatment at 300 °C and disappeared after the formation of crystalline Mn₂O₃ at 500 °C. [14,23] The porous MnO₂ nanotubes exhibited a specific capacitance of 365 F/g in a three-electrode system and 50 F/g after accompanied with activated graphene in a two-electrode system but delivered excellent cyclic stability with capacitance retention of 76.3 % after 10000 cycles. [24]

The highly abundant and low toxic nickel oxide existing in NiO, Ni₂O₃, and NiO₂ forms have appealed to the scientist with its rich redox electrochemical mechanism. [25] Moreover, NiO becomes a more popular electrode material after theoretical prediction on gaining capacitance of 2573 F/g. [25] The distinct controlled morphologies such as nanoflower, nanoparticle, nanoslice of NiO ascertain that the surface area, chemical composition, and openness of morphologies determine the supercapacitor performance. [26] Moreover, NiO is known to tailor the ionic distribution and ion diffusion at the interface after forming the core-shell morphologies with other metal oxides. [27] Cobalt oxide has gained the crown as another promising electrode material for supercapacitor due to its environmentally benign and low-cost nature. Its theoretical specific capacitance of 3560 F/g has triggered lots of excitement among scientists and industries hunting for the best performing supercapacitor. [28] Cobalt oxides exist in CoO and Co₃O₄ forms. Its electrochemical supercapacitive performance has been explored in its pristine, [29] composite [28] and core-shell forms [30] to reach the theoretically predicted specific capacitance. Recently, a well-aligned CoO nanowire array grown on 3D Ni foam coated with polypyrrole exhibited a specific capacitance of 2223 F/g at 1 mA/cm². The conducting polypyrrole might have assisted CoO nanowires in gaining such high specific capacitance and good cyclic stability. Iron oxide exists in α -Fe₂O₃, and Fe₃O₄ forms is another electrode material of choice. The low intrinsic conductivity and aggregated morphology restrict their use as electrode material despite their rich redox reaction by tailoring Fe⁺³/Fe²⁺. Other metal oxides have accompanied it to form composites electrodes or asymmetric devices searching for better supercapacitive performance. [31] An asymmetric supercapacitor fabricated using Fe₂O₃ nanowires as an anode and NiO as a cathode exhibited a considerably high energy density of 105 Wh/kg at a power

density of 1400 W/kg, which retained up to 72.6 Wh/kg at a power density of 12700 W/kg. [32]

Titanium dioxide is one of the fascinating electrode materials for supercapacitors due to its high chemical stability, low processing cost, non-toxic nature compare to available alternative materials. [33] TiO_2 existing in TiO_2 , TiO , Ti_2O_3 , Ti_3O_5 , Ti_4O_7 , Ti_5O_9 , Ti_7O_{13} , and Ti_9O_{17} forms, [11,34] and crystallize in anatase, rutile, and brookite phase. [11,35] The transition of Ti^{4+} and Ti^{3+} during diffusion of ions from electrolyte ensure the electric double-layer capacitor (EDLC) behavior for TiO_2 . The better conductivity of TiO_2 offers excellent electrochemical stability and hence can provide long cyclic stability and retentivity. [16] Therefore, TiO_2 can be one of the best choices for forming the composite or core-shell structure with other performing metal oxides and improve the total energy storage performance. [36,37].

1.4.2 Ternary metal oxides

The ternary transition metal oxides in the form of spinel or perovskite compounds are a new class of electrode materials exciting the scientific community. The existence of +2 ($\equiv\text{A}$) and +3 ($\equiv\text{B}$) oxidation states at tetrahedral and octahedral sites, respectively, in the AB_2O_4 spinel structure [38] offer rich redox sites as electrode material for energy storage devices. [38] The NiCo_2O_4 , [39] MnCo_2O_4 , [40] ZnCo_2O_4 , [41] CuCo_2O_4 , [42] and CoFe_2O_4 , [43], etc., spinel structures are extensively used as electrode materials for supercapacitors. The plentiful availability of cations, i.e., $\text{Ni}^{2+}/\text{Ni}^{3+}$, $\text{Co}^{2+}/\text{Co}^{3+}$, $\text{Mn}^{2+}/\text{Mn}^{3+}$, Zn^{2+} , Cu^{2+} , $\text{Fe}^{2+}/\text{Fe}^{3+}$, directed the spinel materials to exhibit relatively high pseudocapacitive performance. Their decoration on carbon materials has strengthened the interface and promoted the charge transfer, improving the specific capacitance, capacitance retention, and cyclic stability. [40,44] Moreover, the hybrid devices consist of their composites and activated carbons as working and counter electrodes are observed to demonstrate battery type energy storage mechanism. [45]

Likewise, the perovskite metal oxides with ABO_3 formula consisting of divalent ($\equiv\text{A}$) and tetravalent ($\equiv\text{B}$) metal ions facilitate the redox mechanism owing to their multiple cations, vacancies, and excellent oxygen ion mobility. [46,

47] Selection of metal ions in perovskite oxides is exceptionally important as it determines the cyclic stability, charge storage, and the electrochemical potential window during the electrochemical reaction. Despite the fact that perovskites store charge through bulk and not required high surface area, the charge storage via faradaic redox reactions required nanostructured form cannot be ignored. [62,63] The post-heat treatment of smooth textured SrMnO₃ nanofibers converted into the porous structure after post heat treatment at > 700 °C showed relatively better electrochemical performance. [58] The oxygen deficiency to keep the charge neutrality and increment in the surface area possibly causes enhancement in specific capacitance. [65] Structural stability is one of the major problems to be overcome during electrochemical analysis. The surface mitigation through other stable materials can restrict the perovskite from collapse. Therefore, perovskite synthesis with another metal oxide or carbon allotropes has been considered as its solution. [59-61] Cation leaching is also one problem for reducing capacitance during the electrochemical cycling stability. [64] which can be preserved by doping or forming composites. The doping at either A or B site has influenced oxygen deficiency sites for the redox process and charge storage. Partial substitution of Sr²⁺ at A sites in LaNiO₃ (i.e., La_{0.7}Sr_{0.3}NiO_{3-δ}) nanofibers synthesized using electrospinning delivered specific capacitance 719 F/g at 2 A/g, which reduced for increased doping of Sr²⁺ due to uncontrolled oxygen deficiency. [50] The A site doping also influenced the morphology and, therefore, energy storage performance. [51,52] Up to 15 % Sr doping attended uniform particle distribution in the LaMnO₃ but resulted in the agglomeration for further increase in the doping percentage. The reduction in the surface area after agglomeration restricted the ion diffusion, but the individual and uniform particle distribution observed maximum specific capacitance 102 F/g at 1 A/g. [53] SrCoO₃, a highly redox-active electrode material due to various oxidation states of B-site cation (i.e., Co), is not stable at ambient air. [54-56] However, the doping of Mo⁶⁺ at B-sites in SrCoO₃ has made the crystal structure stable and simultaneously created a large number of oxygen vacancies, which enhanced the cycling stability (93.5% capacitance retention after 5000 cycles). [57] Moreover,

perovskite derivatives supplement the perovskite oxides such as Ruddlesden-popper (RP) $\text{Ca}_2\text{MnO}_{4-\delta}$ oxide composed of CaMnO_3 and rock-salt CaO layer [66] were explored to enhance electrochemical anion intercalation and hence energy storage mechanism. Overall, the perovskites are competent supercapacitor electrode material to enhance the specific energy/power density and capacitance by replacing the carbon or polymers.

1.5 Significance of mesoporous structures

Decreasing the particle size to the nanometer scale or incorporating porosity in the material are two approaches to increase the specific surface area of the material. When pores are an integral part of the structure, they do not collapse during the post-synthesis process. The porous materials have gained importance in fuel cells and electrochemical energy storage applications. The porous nanomaterial morphology offers more open channels for the electroactive species (i.e., electrolyte) to percolate deep inside and get adsorbed/intercalated on the surface of the material. Creating porosity in nanostructures successfully diminishes the ion diffusion length. The empty spaces available in porous materials can accommodate the volume changes associated with the electrochemical reactions, limiting the structure degradation during charging-discharging cycles. The pores or hollow regions available in the porous materials can act as a host for filling with the other materials and enable multifunctional applications. Such porous materials classified as microporous (pore size < 2 nm), mesoporous (2 nm $>$ pore size > 50 nm), and macroporous (pore size > 50 nm). The mesoporous structure with a uniform and balanced pore size is more suitable for the quick transport of electrolytes.

Several techniques/routes have been reported to prepare meso/macro-porous materials for the application in energy storage and conversion, sensing, and catalysis. Initially, the template filling was exploited to obtain the mesoporous structures. The ligand-assisted soft template synthesis protocol was adopted to prepare the ordered mesoporous metal oxides, such as Nb_2O_5 , Ta_2O_5 , VO_x , and ZrO_2 . [68-70]. Which was modified further to gain semicrystalline mesoporous oxides from self-assembling induced evaporation of most metals such as Ti, Al, Zr, Ta, Nb, W, Hf, Sn, and Si. [71-73] However, these soft template methods always demand careful removal of the template

material eventually to gain pure metal oxides. After the first report on the synthesis of ordered single-crystalline porous Cr₂O₃ nanowire array via a hard templating method, [74] various hard templating methods are explored to obtain the pore size between 15 to 150 nm. [75-82] The template filling contributed to limited morphological form and uncontrolled porous growth. Therefore, researchers explored various physical and chemical routes in search of optimistic porous structures. The chemical methods, such as sol-gel, hydrothermal, solvothermal, micro-emulsion, and sol-gel processes, have been employed to develop porous materials with micropores or mesopores in different shapes and sizes. Electrospinning is also used to make a large variety of porous nanofibers. However, the heat treatment for expelling gaseous components by decomposition or carbonization is often the final step in synthesizing nanoporous material.

The ratio of closed to open pores (i.e., accessibility of pores), amount of pores, interconnectivity, shapes (i.e., fiber, thin film, etc.) and chemical composition were controlled to make porous transition metal oxide materials [83,84] suitable for attaining the desired electrochemical performance. Metal-organic frameworks (MOFs) offering larger surface area, tunable porosity, and controllable composition have come up as a good template for obtaining porous metal oxide. [85] The oxidation of metal ions and release of CO₂ and NO₂ gases from the decomposition of organic linkers during annealing at ambient atmosphere give rise to the porous metal oxides. The shape and porosity of MOF templates inculcate the favorable and desired surface area in the metal oxide. To date, numerous porous transition metal oxides such as NiO, [86,87] Co₃O₄, [88,89] CuO, [90] Fe₂O₃, [91,92] Mn₂O₃, [93,94] TiO₂, [95,96] and ZnO, [97] have been extracted from MOF, which are further expanded to ternary metal oxides such as CuCo₂O₄, [98] ZnCo₂O₄, [99] and NiCo₂O₄. [100] These MOFs are also used for the synthesis of different core-shell heterostructures and metal oxide nanocomposites. However, hydrothermal and sol-gel synthesis routes have gained importance for the synthesis of porous nanomaterials. The mesoporous NiO nanotubes synthesized using the hydrothermal method offered larger surface area than nanowire bundles, dandelions, and hollow spheres and provided better specific capacitance (i.e., 405 F/g at a 0.5 A/g) and good cycling stability (i.e., 91 % after 1500 charge-discharge cycles). [105] Ding et al. [106] investigated the effect of experimental conditions on the growth of mesoporous

Co₃O₄ nanostructures. The morphology controlled flower-like mesoporous Co₃O₄ nanosheets exhibited higher specific capacitance (i.e., 327.3 F/g at 0.5 A/g) and outstanding retention (i.e., 96 % at 5 A/g) for 10000 charging-discharging cycles. Moreover, doping and composite formation of mesoporous nanomaterials have shown excellent improvement in energy storage performance. [107] Likewise, La, Mn, Fe, and Ni based perovskite materials such as LaNiO₃, LaMnO₃, LaFeO₃, LaCrO₃, and NiMnO₃ have attracted attention by delivering high specific capacitance and good long term cycling stability. [109,110]

1.6 Motivation

- (a) The environmentally friendly and easy processable transition metal oxides are promising electrode material for energy storage devices due to their wise nanostructure morphology, high surface area, and high theoretical specific capacitance. [2,112,113] Moreover, their energy storage performance can be enhanced by modifying and controlling their defects and interfaces under nanoscale. [114] Nevertheless, their energy density has shown an increment to a certain degree; the low electrical conductivity and slow ions diffusion in bulk have hampered their practical usage. [115,116] Moreover, the nanostructured morphology of transition metal oxides enhances the specific capacitance and rate capability by improving the reaction sites and reducing the ion diffusion length. [2] Especially, well-designed mesoporous morphologies that hold two or three-dimensional (3D) interconnected pores of 2-50 nm diameter have been accepted as the most promising. The ordered mesoporous metal oxides have numerous advantages over the bulk form in the electrochemical field, [4,111] such as high surface area furnishes numbers of charge storage sites.
- (b) Interconnected mesopores facilitate the diffusion of electrolyte ions.
- (c) Nanometer-sized walls develop small crystallites and grain boundaries.
- (d) Porous structures act as a host for loading high capacitance guest materials.

Therefore, investigation of the electrochemical properties of mesoporous transition metal oxides is essential and urgent to improve their performance in energy storage. In recent years, the synthesis of the nanobelts of transition metal oxides has

fascinated researchers due to their high specific surface area, excellent mesoporous structural stability, and outstanding transport properties than those of their high-dimensional counterparts. Many methods have been utilized to prepare nanobelts of metal oxides, [11] such as SnO₂, ZnO, TiO₂, V₂O₅, Bi₂O₃, Fe₂O₃; however, no reports have focused on the synthesis of perforated mesoporous NiO nanobelts using cost-effective synthesis techniques.

The nanosized perovskite metal oxides with ABO₃ formula are considered a replacement for binary metal oxides in the stipulated application and are under comprehensive investigation for their applications in catalysis, water splitting, super capacitance, and batteries, etc., demonstrate their capabilities as a promising candidate for supercapacitor. The structural stability of the cations, oxygen ion mobility, and vacancies mediate the redox mechanism in the perovskite. Moreover, the presence of multiple transition metal ions in the perovskite structure shall apprehend distinct charge storing mechanisms and hence capable of delivering the breakthrough performance of the supercapacitor. However, most of the studies are focused on Lanthanum based perovskites, which might be owing to their better electrical conductivity. Even though few reports are available on the synthesis of Ni, Co, Mn, and Ti based perovskite nanostructures, none of them are focused on synthesizing one-dimensional mesoporous nanostructure for utilization as the working electrode in the supercapacitor. One-dimensional nanostructural morphologies provide direct pathways for electron/ion transfer at the electrode-electrolyte interface. Moreover, the mesoporous form adds a larger surface area to the 1D morphology, which may contribute to improving the electrochemical performance. Therefore, mesoporous 1D morphologies of NiTiO₃ and CoTiO₃ are explored for their electrochemical energy storage performance.

1.7 Aim of the Thesis

This thesis work reports the investigation with the following aims to answer the questions pertaining to the literature survey. The mesoporous nanostructured oxides of Ni, Ti, Co, and Mn metal elements are studied for electrochemical energy storage applications. The mesoporous 1D nanostructures of the binary and ternary metal oxides

are explored to understand their redox reaction mechanism and further subjected to form the core-shell structure

The aims are:

- Morphology controlled synthesis of NiO nanostructures employing the cost-effective technique. Optimization of synthesis condition to gain the mesoporous NiO nanostructures and understand their surface morphology, crystalline nature, chemical composition, pore size distribution, etc.
- To investigate the influence of morphology and mesoporous nature on the electrochemical performance of NiO nanostructures.
- To design mesoporous ATiO_3 (where A = Ni and Co) one-dimensional nanostructures using cost-effective chemical routes.
- To investigate the crystalline nature, electronic structure, surface morphology, pore size distribution, surface wettability, etc., of the ATiO_3 (where A = Ni and Co) one-dimensional nanostructures.
- To investigate the influence of mesoporous nature on the electrochemical performance of ATiO_3 nanostructures.
- To synthesize the heteroarchitecture of 2D MnO_2 shell and 1D NiTiO_3 perovskite core and study the influence of their morphology and physicochemical properties on the electrochemical performance.

1.8 References

- [1.] Li X., Wei B., (2013), Supercapacitors based on nanostructured carbon, *Nano Energy*, 2, 159-173, (DOI:10.1016/j.nanoen.2012.09.008).
- [2.] Wang G., Zhang Li., Zhang J., (2012), A review of electrode materials for electrochemical supercapacitors, *Chem. Soc. Rev.*, 41, 797-828, (DOI:10.1039/C1CS15060J).
- [3.] Hu Y., Wu Y., Wang J., (2018), Manganese-oxide-based electrode materials for energy storage applications: How close are we to the theoretical capacitance, *Adv Mater.*, 2018, 1802569, (DOI:10.1002/adma.201802569).
- [4.] Nguyen T. V., Son L. T., Thuy V. V., Thao V. D., Hatsukano M., Higashimine K., Maenosono S., Chun S. E., Thu T. V., (2020), Facile synthesis of Mn-doped

- NiCo₂O₄ nanoparticles with enhanced electrochemical performance for a battery-type supercapacitor electrode, *Dalton Trans.*, 49, 6718-6729, (DOI:10.1039/d0dt01177k).
- [5.] Forouzandeh P., Kumaravel V., Pillai S. C., (2020), Electrode materials for supercapacitors: A review of recent advances, *Catalysts*, 10, 969, (DOI:10.3390/catal10090969).
- [6.] Bai XWang Z., Luo J., Wu W., Liang Y., Tong X., Zhao Z., (2020), Hierarchical porous carbon with interconnected ordered pores from biowaste for high performance supercapacitor electrodes, *Nanoscale Res. Lett.*, 15, 1-10, (DOI:10.1186/s11671-020-03305-0).
- [7.] Ishaq S., Moussa M., Kanwal F., Ehsan M., Saleem M., Van T. N., Losic D., (2019), Facile synthesis of ternary graphene nanocomposites with doped metal oxide and conducting polymers as electrode materials for high performance supercapacitors, *Sci. Rep.*, 9, 5974, (DOI:10.1038/s41598-019-41939-y).
- [8.] Shewale P. S., Yun K. S., (2021), NiCo₂O₄/RGO hybrid nanostructures on surface-modified Ni core for flexible wire shaped supercapacitor, *Nanomater.*, 11, 852, (DOI:10.3390/nano11040852).
- [9.] Wu D., Xie X., Zhang Y., Zhang D., Du W., Zhang X., Wang B., (2020), MnO₂/carbon composites for supercapacitor: synthesis and electrochemical performance, *Front. Mater.*, 7, 1-6, (DOI:10.3389/fmats.2020.00002).
- [10.] Makkar P., Ghosh N.N., (2020), Facile synthesis of MnFe₂O₄ hollow sphere-reduced graphene oxide nanocomposites as electrode materials for all-solid state flexible high-performance asymmetric supercapacitors, *ACS Appl. Energy Mater.*, 3, 2653-2664, (DOI:10.1021/acsaem.9b02360).
- [11.] Devan R. S., Patil R. A., Lin J. H., Ma Y. R., (2012), One-dimensional metal-oxide nanostructures: recent developments in synthesis, characterization, and applications, *Adv. Funct. Mater.*, 22, 3326-3370, (DOI:10.1002/adfm.201201008).
- [12.] Nguyen T., Montemor M.F., (2017), Redox active materials for metal compound based hybrid electrochemical energy storage: a perspective view, *Appl. Surf. Sci.*, 422, 492-497, (DOI:10.1016/j.apsusc.2017.06.008).

- [13.] An C. H., Zhang Y., Guo H., Wang Y., (2019), Metal oxide-based supercapacitors: progress and perspectives, *Nanoscale Adv.*, 1, 4644-4658, (DOI:10.1039/c9na00543a).
- [14.] Hu Y., Wu Y., Wang J., (2018), Manganese-oxide based electrode materials for energy storage applications: How close are we to the theoretical capacitance?, *Adv. Mater.*, 30, 1802569, (DOI:10.1002/adma.201802569).
- [15.] Patil R. A., Chang C. P., Devan R. S., Liou Y., (2016), Impact of nanosize on supercapacitance: study of 1D nanorods and 2D thin-films of nickel oxide, *ACS Appl. Mater. Interfaces*, 8, 9872-9880, (DOI:10.1021/acsami.6b00487).
- [16.] Devan R. S., Ma Y. R., Patil R. A., Lukas S. M., (2016), Highly stable supercapacitive performance of one-dimensional (1D) brookite TiO₂ nanoneedles, *RSC Adv.*, 6, 62218-62225, (DOI:10.1039/C6RA11348F).
- [17.] Bhojane P., Sinha L., Devan R. S., Shirage P. M., (2018), Mesoporous layered hexagonal platelets of Co₃O₄ nanoparticles with (111) facets for battery applications: high performance and ultra-high rate capability, *Nanoscale*, 10, 1779-1787, (DOI:10.1039/C7NR07879J).
- [18.] Li J., Hu B., Nie P., Shang X., Jiang W., Xu K., Yang J., Liu J., (2021), Fe-regulated δ -MnO₂ nanosheet assembly on carbon nanofiber under acidic condition for high performance supercapacitor and capacitive deionization, *Appl. Surf. Sci.*, 542, 148715, (DOI:10.1016/j.apsusc.2020.148715).
- [19.] Vijayabala V., Senthilkumar N., Nehru K., Karvembu R., (2018), Hydrothermal synthesis and characterization of ruthenium oxide nanosheets using polymer additive for supercapacitor applications, *J. Mater. Sci.: Mater. Electron.*, 29, 323-330, (DOI:10.1007/s10854-017-7919-x).
- [20.] Han Z. J., Pineda S., Murdock A. T., Seo D. H., Ostrikov K., Bendavid A., (2017), RuO₂-coated vertical graphene hybrid electrodes for high performance solid state supercapacitors, *J. Mater. Chem. A*, 5, 17293-17301, (DOI:10.1039/c7ta03355a).
- [21.] Majumdar D., Maiyalagan T., Jiang Z.Q., (2019), Recent progress in ruthenium oxide-based composites for supercapacitor applications, *ChemElectroChem*, 6, 4343-4372, (DOI:10.1002/celec.201900668).

- [22.] Kong S. Y., Cheng K., Ouyang T., Gao Y., Ye K., Wang G., Cao D., (2017), Facile electrodeposition processed of RuO₂-graphene nanosheets-CNT composites as a binder-free electrode for electrochemical supercapacitors, *Electrochim. Acta*, 246, 433-442, (DOI:10.1016/j.electacta.2017.06.019).
- [23.] Chang J. K., Chen Y. L., Tsai W. T., (2004), Effect of heat treatment on material characteristics and pseudo-capacitive properties of manganese oxide prepared by anodic deposition, *J. Power Sources*, 135, 344-353, (DOI:10.1016/j.jpowsour.2004.03.076).
- [24.] Huang M., Zhang Y., Li F., Zhang L., Ruoff R. S., Wen Z., Liu Q., (2014), Self-assembly of mesoporous nanotubes assembled from interwoven ultrathin birnessite-type MnO₂ nanosheets for asymmetric supercapacitors, *Sci. Rep.*, 4, 8, (DOI:10.1038/srep03878).
- [25.] Chime U. K., Nkele A. C., Ezugwu S., Nwanya A. C., Shinde N. M., Kebede M., Ejikeme P. M., Maaza M., Ezema F. I., (2020), Recent progress in nickel oxide based electrodes for high performance supercapacitors, *Curr. Opin. Electrochem.*, 21, 175-181, (DOI:10.1016/j.coelec.2020.02.004).
- [26.] Kim S. I., Lee J. S., Ahn H. J., Song H. K., Jang J. H., (2013), Facile route to an efficient NiO supercapacitor with a three-dimensional nanonetwork morphology, *ACS Appl. Mater. Interfaces* 5, 1596-1603, (DOI:10.1021/am3021894).
- [27.] Schiavi P. G., Altimari P., Marzolo F., Rubino A., Zanoni R., Pagnanelli F., (2021), Optimizing the structure of Ni-Ni(OH)₂/NiO core-shell nanowire electrodes for application in pseudocapacitors: The influence of metallic core, Ni(OH)₂/NiO ratio and nanowire length, *J. Alloys Compds.*, 856, 157718, (DOI:10.1016/j.jallcom.2020.157718).
- [28.] Ali F., Khalid N. R., (2020), Facile synthesis and properties of chromium-doped cobalt oxide (Cr-doped Co₃O₄) nanostructures for supercapacitor applications, *Appl. nanosci.*, 10, 1481-1488, (DOI:10.1007/s13204-020-01266-5).
- [29.] Mirzaeian M., Akhanova N., Gabdullin M., Kalkozova Z., Tulegenova A., Nurbolat S., Abdullin K., (2020), Improvement of the pseudocapacitive performance of cobalt oxide-based electrodes for electrochemical capacitors, *Energies.*, 13, 5228, (DOI:10.3390/en13195228).

- [30.] Jadhav S. M., Kalubarme R. S., Suzuki N., Terashima C., Mun J., Kale B. B., Gosavi S. W., Fujishima A., (2021), Cobalt-doped manganese dioxide hierarchical nanostructures for enhancing pseudocapacitive properties, *ACS Omega*, 6, 5717-5729, (DOI:10.1021/acsomega.0c06150).
- [31.] Yu S., Hong Ng V. M., Wang F., Xiao Z., Li C., Kong L. B., Que W., Zhou K., (2018), Synthesis and application of iron based nanomaterials as anodes of lithium-ion batteries and supercapacitors, *J. Mater. Chem. A*, 6, 9332-9367, (DOI:10.1039/c8ta01683f).
- [32.] Tang Q. Q., Wang W. Q., Wang G. C., (2015), The perfect matching between the low-cost Fe₂O₃ nanowire anode and the NiO nanoflake cathode significantly enhances the energy density of asymmetric supercapacitors, *J. Mater. Chem. A*, 3, 6662-6670, (DOI:10.1039/c5ta00328h).
- [33.] Nguyen N. T., Ozkan S., Hwang I., Zhou X., Schmuki P., (2017), Spaced TiO₂ nanotube arrays allow for a high performance hierarchical supercapacitor structure, *J. Mater. Chem. A*, 5, 1895-1901, (DOI:10.1039/c6ta10179h).
- [34.] Noman M. T., Ashraf M. A., Ali A., (2019), Synthesis and applications of nano-TiO₂: a review, *Environ. Sci. Pollut. Res.*, 26, 3262-3291, (DOI:10.1007/s11356-018-3884-z).
- [35.] Kitchamsetti N., Kalubarme R. S., Chikate P. R., Park C. J., Ma Y. R., Shirage P. M., Devan R. S., (2019), An investigation on the effect of li-ion cycling on the vertically aligned brookite TiO₂ nanostructure, *ChemistrySelect*, 4, 6620-6626, (DOI:10.1002/slct.201900395).
- [36.] Ahirrao D. J., Wilson H. M., Jha N., (2019), TiO₂-nanoflowers as flexible electrode for high performance supercapacitor, *Appl. Surf. Sci.*, 491, 765-778, (DOI:10.1016/j.apsusc.2019.05.076).
- [37.] Rajagopal R., Ryu K. S., (2020), Homogeneous MnO₂@TiO₂ core-shell nanostructure for high performance supercapacitor and Li-ion battery applications, *J. Electroanal. Chem.*, 856, 113669, (DOI:10.1016/j.jelechem.2019.113669).
- [38.] Abdel Maksoud M. I. A., Fahim R. A., Shalan A. E., Elkodous M. A., Olojede S. O., Osman A. I., Farrell C., Al-Muhtaseb A. H., Awed A. S., Ashour A. H.,

- Rooney D. W., (2021), Advanced materials and technologies for supercapacitors used in energy conversion and storage: a review, *Environ. Chem. Lett.*, 19, 375-439, (DOI:10.1007/s10311-020-01075-w).
- [39.] Waghmode R. B., Maile N. C., Lee D. S., Torane A.P., (2020), Chemical bath synthesis of NiCo₂O₄ nanoflowers with nanorods like thin film for flexible supercapacitor application-effect of urea concentration on structural conversion, *Electrochim. Acta*, 350, 136413, (DOI:10.1016/j.electacta.2020.136413).
- [40.] Saravanakumar B., Ravi G., Ganesh V., Guduru R. K., Yuvakkumar R., (2019), MnCo₂O₄ nanosphere synthesis for electrochemical applications, *Mater. Sci. Energy Tech.*, 2, 130-138, (DOI:10.1016/j.mset.2018.11.008).
- [41.] Sharma M., Gaur A., (2020), Designing of carbon nitride supported ZnCo₂O₄ hybrid electrode for high performance energy storage applications, *Sci. Rep.*, 10, 2035, (DOI:10.1038/s41598-020-58925-4).
- [42.] Pawar S. M., Pawar B. S., Babar P. T., Ahmed A. T. A., Chavan H. S., Jo Y., Cho S., Kim J., Hou B., Inamdar A. I., Cha S., Kim J. H., Kim T. G., Kim H., Im H., (2019), Nanoporous CuCo₂O₄ nanosheets as a highly efficient bifunctional electrode for supercapacitors and water oxidation catalysis, *Appl. Surf. Sci.*, 470, 360-367, (DOI:10.1016/j.apsusc.2018.11.151).
- [43.] Acharya J., Sundara Raj B. G., Ko T. H., Khil M. S., Kim H. Y., Kim B. S., (2019), Facile one pot sonochemical synthesis of CoFe₂O₄/MWCNTs hybrids with well dispersed MWCNTs for asymmetric hybrid supercapacitor applications, *Int. J. Hydrog. Energy*, 45, 3073-3085, (DOI:10.1016/j.ijhydene.2019.11.169).
- [44.] Bhagwan J., Nagaraju G., Ramulu B., Sekhar S. C., Yu S. Y., (2019), Rapid synthesis of hexagonal NiCo₂O₄ nanostructures for high performance asymmetric supercapacitors, *Electrochim. Acta*, 299, 509-517, (DOI:10.1016/j.electacta.2018.12.174).
- [45.] Pan J., Li S., Li F., Yu T., Liu Y., Zhang L., Ma L., Sun M., Tian X., The NiFe₂O₄/NiCo₂O₄/GO composites electrode material derived from dual-MOF for high performance solid state hybrid supercapacitors, *Colloids Surf. A Physicochem. Eng. Asp.*, 609, 125650, (DOI:10.1016/j.colsurfa.2020.125650).

- [46.] Zhu L., Ran R., Tade M., Wang W., Shao Z., (2016), Perovskite materials in energy storage and conversion, *Asia-Pac. J. Chem. Eng.*, 11, 338-369, (DOI:10.1002/apj.2000).
- [47.] Tan P., Liu M., Shao Z. P., Ni M., (2017), Recent advances in perovskite oxides as electrode materials for nonaqueous lithium-oxygen batteries, *Adv. Energy Mater.*, 7, 1602674, (DOI:10.1002/aenm.201602674).
- [48.] King G., Woodward P. M., (2010), Cation ordering in perovskites, *J. Mater. Chem.*, 20, 5785-5796, (DOI:10.1039/b926757c).
- [49.] Zhou W., Shao Z. P., Liang F., Chen Z. G., Zhu Z. G., Jin W. Q., (2011), A new cathode for solid oxide fuel cells capable of in situ electrochemical regeneration, *J. Mater. Chem.*, 21, 15343-15351, (DOI:10.1039/c1jm12660a).
- [50.] Cao Y., Lin B., Sun Y., Yang H., Zhang X., (2015), Sr-doped lanthanum nickelate nanofibers for high energy density supercapacitors, *Electrochim. Acta*, 174, 41-50, (DOI:10.1016/j.electacta.2015.05.131).
- [51.] Cao Y., Lin B., Sun Y., Yang H., Zhang X., (2015), Symmetric/asymmetric supercapacitor based on the perovskite-type lanthanum cobaltate nanofibers with sr-substitution, *Electrochim. Acta*, 178, 398-406, (DOI:10.1016/j.electacta.2015.08.033).
- [52.] Cao Y., Lin B., Sun Y., Yang H., Zhang X., (2015), Structure, morphology and electrochemical properties of $\text{La}_x\text{Sr}_{1-x}\text{Co}_{0.1}\text{Mn}_{0.9}\text{O}_{3-\delta}$ perovskite nanofibers prepared by electrospinning method, *J. Alloys Compds*, 624, 31-39, (DOI:10.1016/j.jallcom.2014.10.178).
- [53.] Lang X. Q., Mo H., Hu X., Tian H. W., (2017), Supercapacitor performance of perovskite $\text{La}_{1-x}\text{Sr}_x\text{MnO}_3$, *Dalton Trans.*, 46, 13720-13730, (DOI:10.1039/c7dt03134c).
- [54.] Nagai T., Ito W., Sakon T., (2007), Relationship between cation substitution and stability of perovskite structure in $\text{SrCoO}_{3-\delta}$ -based mixed conductors, *Solid State Ion.*, 177, 3433-3444, (DOI:10.1016/j.ssi.2006.10.022).
- [55.] Petrie J. R., Jeon H. J., Barron S. C., Meyer T. L., Lee H. N., (2016), Enhancing perovskite electrocatalysis through strain tuning of the oxygen deficiency, *J. Am. Chem. Soc.*, 138, 7252-7255, (DOI:10.1021/jacs.6b03520).

- [56.] Alexander C. T., Forslund R. P., Johnston K. P., Stevenson K. J., (2019), Tuning redox transitions via the inductive effect in $\text{LaNi}_{1-x}\text{Fe}_x\text{O}_{3-\delta}$ perovskites for high-power asymmetric and symmetric pseudocapacitors, *ACS Appl. Energy Mater.*, 2, 6558-6568, (DOI:10.1021/acsaem.9b01117).
- [57.] Tomar A. K., Singh G., Sharma R. K., (2018), Fabrication of a Mo-doped strontium cobaltite perovskite hybrid supercapacitor cell with high energy density and excellent cycling life, *ChemSusChem*, 11, 4123-4130, (DOI:10.1002/cssc.201801869).
- [58.] George G., Jackson S. L., Luo C. Q., Fang D., Luo D., Hu D., Wen J., Luo Z., (2018), Effect of doping on the performance of high-crystalline SrMnO_3 perovskite nanofibers as a supercapacitor electrode, *Ceram. Int.*, 44, 21982-21992, (DOI:10.1016/j.ceramint.2018.08.313).
- [59.] Galal A., Hassan H. K., Atta N. F., Jacob T., (2019), Energy and cost-efficient nano-Ru-based perovskites/RGO composites for application in high performance supercapacitors, *J. Colloid Interface Sci.*, 538, 578-586, (DOI:10.1016/j.jcis.2018.12.018).
- [60.] Lang X. Q., Sun X., Liu Z., Nan H., Li C., Hu X., Tian H. W., (2019), Ag-nanoparticles decorated perovskite $\text{La}_{0.85}\text{Sr}_{0.15}\text{MnO}_3$ as electrode materials for supercapacitors, *Mater. Lett.*, 243, 34-37, (DOI:j.matlet.2019.02.002).
- [61.] He L., Shu Y., Li W. S., Liu M. C., (2019), Preparation of $\text{La}_{0.7}\text{Sr}_{0.3}\text{CoO}_{3-\delta}$ @ MnO_2 core/shell nanorods as high-performance electrode materials for supercapacitors, *J. Mater. Sci-Mater. Electronics*, 30, 17-25, (DOI:10.1007/s10854-018-0331-3).
- [62.] Huang X. B., Zhao G., Wang G., Irvine J. T. S., (2018), Synthesis and applications of nanoporous perovskite metal oxides, *Chem. Sci.*, 9, 3623-3637, (DOI:10.1039/c7sc03920d).
- [63.] Shafi P. M., Joseph N., Thirumurugan A., Bose A. C., (2018), Enhanced electrochemical performances of agglomeration-free LaMnO_3 perovskite nanoparticles and achieving high energy and power densities with symmetric supercapacitor design, *Chem. Eng. J.*, 338, 147-156, (DOI:j.cej.2018.01.022).

- [64.] Xu Z. Y., Liu Y., Zhou W., Tade M. O., Shao Z. P., (2018), B-site cation-ordered double-perovskite oxide as an outstanding electrode material for supercapacitive energy storage based on the anion intercalation mechanism, *ACS Appl. Mater. Interfaces*, 10, 9415-9423, (DOI:10.1021/acsami.7b19391).
- [65.] Tomar A. K., (2020), Zero-dimensional ordered Sr₂CoMoO_{6-δ} double perovskite as high-rate anion intercalation pseudocapacitance, *ACS Appl. Mater. Interfaces*, 12, 15128-15137, (DOI:10.1021/acsami.9b22776).
- [66.] Forslund R. P., Pender J., Alexander C. T., Johnston K. P., Stevenson K. J., (2019), Comparison of perovskite and perovskite derivatives for use in anion-based pseudocapacitor applications, *J. Mater. Chem. A*, 7, 21222-21231, (DOI:10.1039/c9ta06094d).
- [67.] Liu Y., Jiang S. P., Shao Z., (2020), Intercalation pseudocapacitance in electrochemical energy storage: recent advances in fundamental understanding and materials development, *Mater. Today Adv.*, 7, 32, (DOI:j.mtadv.2020.100072).
- [68.] Rathnayake D., Perera I., Shirazi-Amin A., Kerns P., Dissanayake S., Suib S. L., (2020), Mesoporous crystalline Niobium oxide with a high surface area: A solid acid catalyst for alkyne hydration, *ACS Appl. Mater. Interfaces*, 12, 47389-47396, (DOI:10.1021/acsami.0c10757).
- [69.] Wong M. S., Antonelli D. M., Ying J. Y., (1997), Synthesis and characterization of phosphated mesoporous zirconium oxide, *Nanostructured Mater.*, 9, 165-168, (DOI:10.1016/S0965-9773(97)00044-5).
- [70.] Mei P., Kaneti Y. V., Pramanik M., Takei T., Dag O., Sugahara Y., Yamauchi Y., (2018), Two-dimensional mesoporous vanadium phosphate nanosheets through liquid crystal templating method toward supercapacitor application, *Nano Energy*, 52, 336-344, (DOI:10.1016/j.nanoen.2018.07.052).
- [71.] Brinker C. J., (2004), Evaporation-induced self-assembly: functional nanostructures made easy, *MRS Bull.*, 29, 631-640, (DOI:10.1557/mrs2004.183).
- [72.] Yang P. D., Zhao D. Y., Margolese D. I., Chmelka B. F., Stucky G. D., (1999), Block copolymer templating syntheses of mesoporous metal oxides with large

- ordering lengths and semicrystalline framework, *Chem. Mater.*, 11, 2813-2826, (DOI:10.1021/cm990185c).
- [73.] Yang P. D., Zhao D., Margolese D., (1998), Generalized syntheses of large-pore mesoporous metal oxides with semicrystalline frameworks, *Nature*, 396, 152-155, (DOI:10.1038/24132).
- [74.] Zhu K. K., Yue B., Zhou W., He H., (2003), Preparation of three-dimensional chromium oxide porous single crystals templated by SBA-15, *Chem. Commun.*, 2003, 98-99, (DOI:10.1039/b210065g).
- [75.] Yang H. F., Zhao D.Y., (2005), Synthesis of replica mesostructures by the nanocasting strategy, *J. Mater. Chem.*, 15, 1217-1231, (DOI:10.1039/b414402c).
- [76.] Lu A. H., Schuth F., (2006), Nanocasting: a versatile strategy for creating nanostructured porous materials, *Adv. Mater.*, 18, 1793-1805, (DOI:10.1002/adma.200600148).
- [77.] Schuth F., (2003), Endo- and exotemplating to create high-surface-area inorganic materials, *Angew. Chem. Int. Ed.*, 42, 3604-3622, (DOI:10.1002/anie.200300593).
- [78.] Tiemann M., (2008), Repeated templating, *Chem. Mater.*, 20, 961-971, (DOI:10.1021/cm702050s).
- [79.] Yoo W. C., Lee J. K., (2004), Field-dependent growth patterns of metals electroplated in nanoporous alumina membranes, *Adv. Mater.*, 16, 1097-1101, (DOI:10.1002/adma.200306595).
- [80.] Wu P. R., Liu Z., Cheng Z. L., (2018), Growth of MoS₂ nanotubes templated by halloysite nanotubes for the reduction of friction in oil, *ACS Omega*, 3, 15002-15008, (DOI:10.1021/acsomega.8b02349).
- [81.] Li D., Thompson R. S., Bergmann G., Lu J.G., (2008), Template based synthesis and magnetic properties of cobalt nanotube arrays, *Adv. Mater.*, 20, 4575-4578, (DOI:10.1002/adma.200801455).
- [82.] Banerjee P., Perez I., Lecordier L. H., Lee S. B., Rubloff G. W., (2009), Nanotubular metal-insulator-metal capacitor arrays for energy storage, *Nature Nanotech.*, 4, 292-296, (DOI:10.1038/nnano.2009.37).

- [83.] Tiwari S. K., Thakur A. K., Adhikari A. D., Zhu Y., Wang N., (2020), Current research of graphene-based nanocomposites and their application for supercapacitors, *Nanomater.*, 10, 2046, (DOI:10.3390/nano10102046).
- [84.] Zhao J., Burke A. F., (2020), Electrochemical capacitors: performance metrics and evaluation by testing and analysis, *Adv. Energy Mater.*, 2020, 2002192, (DOI:10.1002/aenm.202002192).
- [85.] Kaneti Y. V., Tang J., Salunkhe R. R., Jiang X., Yu A., Wu K. C. W., Yamauchi Y., (2017), Nanoarchitected design of porous materials and nanocomposites from metal-organic frameworks, *Adv. Mater.*, 29, 1604898, (DOI:10.1002/adma.201604898).
- [86.] Shin S., Shin M. W., (2021), Nickel metal-organic framework (Ni-MOF) derived NiO/C@CNF composite for the application of high performance self standing supercapacitor electrode, *Appl. Surf. Sci.*, 540, 148295, (DOI:10.1016/j.apsusc.2020.148295).
- [87.] Han Y., Zhang S., Shen N., Li D., Li X., (2017), MOF-derived porous NiO nanoparticle architecture for high performance supercapacitors, *Mater. Lett.*, 188, 1-4, (DOI:10.1016/j.matlet.2016.09.051).
- [88.] Haldorai Y., Choe S. R., Huh Y. S., Han Y. K., (2018), Metal-organic framework derived nanoporous carbon/Co₃O₄ composite electrode as a sensing platform for the determination of glucose and high performance supercapacitor, *Carbon*, 127, 366-373, (DOI:10.1016/j.carbon.2017.11.022).
- [89.] Wang M. X., Zhang J., Fan H. L., Liu B. X., Yi X. B., Wang J. Q., (2019), ZIF-67 derived Co₃O₄/carbon aerogel composite for supercapacitor electrodes, *New. J. Chem.*, 43, 5666-5669, (DOI:10.1039/c8nj05958f).
- [90.] Aljaafari A., Parveen N., Ahmad F., Alam M. W., Ansari S. A., (2019), Self-assembled cube like copper oxide derived from a metal organic framework as a high performance electrochemical supercapacitive electrode material, *Sci. Rep.*, 9, 9140, (DOI:10.1038/s41598-019-45557-6).
- [91.] Zhou Z., Zhang Q., Sun J., He B., Guo J., Li Q., Li C., Xie L., Yao Y., (2018), Metal-organic framework derived spindle like incorporated α -Fe₂O₃ grown on

- carbon nanotube fiber as anodes for high performance wearable asymmetric supercapacitors, *ACS Nano*, 12, 9333-9341, (DOI:10.1021/acsnano.8b04336).
- [92.] Yu Z., Zhang X., Wei L., Guo X., (2019), MOF-derived porous hollow α -Fe₂O₃ microboxes modified by silver nanoclusters for enhanced pseudocapacitive storage, *Appl. Surf. Sci.*, 463, 616-625, (DOI:10.1016/j.apsusc.2018.08.262).
- [93.] Nagamuthu S., Ryu K. S., (2019), MOF-derived microstructural interconnected network porous Mn₂O₃/C as negative electrode material for asymmetric supercapacitor device, *Cryst. Eng. Comm.*, 21, 1442-1451, (DOI:10.1039/c8ce01683f).
- [94.] Liu P. P., Zheng Y. Q., Zhu H. L., Li T. T., (2019), Mn₂O₃ hollow nanotube arrays on Ni foam as efficient supercapacitors and electrocatalysts for oxygen evolution reaction, *ACS Appl. Nano Mater.*, 2, 744-749, (DOI:10.1021/acsanm.8b01918).
- [95.] Shrivastav V., Sundriyal S., Kim K. H., Sinha R. K., Tiwari U. K., Deep A., (2020), Metal organic frameworks derived titanium dioxide -carbon nanocomposite for supercapacitor applications, *Int. J. Energy Res.*, 44, 1-16, (DOI:10.1002/er.5328).
- [96.] Zhang X. J., Wang M., Zhu G., Li D. S., Yan D., Lu T., Pan L., (2017), Porous cake-like TiO₂ derived from metal-organic frameworks as superior anode material for sodium ion batteries, *Ceram. Int.*, 43, 2398-2402, (DOI:10.1016/j.ceramint.2016.11.028).
- [97.] Park J., Ju J. B., Choi W., Kim S. O., (2019), Highly reversible ZnO@ZIF-8 derived nitrogen-doped carbon in the presence of fluoroethylene carbonate for high-performance lithium-ion battery anode, *J. Alloys Compds.*, 773, 960-969, (DOI:10.1016/j.jallcom.2018.09.298).
- [98.] Sun J., Xu C., Chen H., (2021), A review on the synthesis of CuCo₂O₄-based electrode materials and their applications in supercapacitors, *J. Materiomics.*, 7, 98-126, (DOI:10.1016/j.jmat.2020.07.013).
- [99.] Zhang D., Wang Z., Li J., Hu C., Zhang X., Jiang B., Cao Z., Zhang J., Zhang R., (2020), MOF-derived ZnCo₂O₄ porous micro rice with enhanced electrocatalytic activity for the oxygen evolution reaction and glucose oxidation, *RSC Adv.*, 10, 9063-9069, (DOI:10.1039/c9ra08723k).

- [100.] Kibona T. E., (2020), Synthesis of NiCo₂O₄/mesoporous carbon composites for supercapacitor electrodes, *J. Solidstate Electrochem.*, 24, 1587-1598, (DOI:10.1007/s1008-020-04673-4).
- [101.] Hu H., Guan B., Xia B., Lou X. W., (2015), Designed formation of Co₃O₄/NiCo₂O₄ double-shelled nanocages with enhanced pseudocapacitive and electrocatalytic properties, *J. Am. Chem. Soc.*, 137, 5590-5595, (DOI:10.1021/jacs.5b02465).
- [102.] Guo W. X., Sun W. W., Wang Y., (2015), Multilayer CuO@NiO hollow spheres: microwave-assisted metal organic-framework derivation and highly reversible structure-matched stepwise lithium storage, *ACS Nano*, 9, 11462-11471, (DOI:10.1021/acsnano.5b05610).
- [103.] Zhu D. Q., Zheng F., Xu S. H., Zhang Y. G., Chen Q. W., (2015), MOF-derived self-assembled ZnO/Co₃O₄ nanocomposite clusters as high-performance anodes for lithium-ion batteries, *Dalton Trans.*, 44, 16946-16952, (DOI:10.1039/c5dt02271a).
- [104.] Hu L., Huang Y., Zhang F., Chen Q. W., (2013), CuO/Cu₂O composite hollow polyhedrons fabricated from metal-organic framework templates for lithium-ion battery anodes with a long cycling life, *Nanoscale*, 5, 4186-4190, (DOI:10.1039/c3nr00623a).
- [105.] Xiong S. L., Yuan C. Z., Zhang X. G., Qian Y., (2011), Mesoporous NiO with various hierarchical nanostructures by quasi-nanotubes/nanowires/nanorods self-assembly: controllable preparation and application in supercapacitors, *CrystEngComm*, 13, 626-632, (DOI:10.1039/c002610g).
- [106.] Ding K., Zhang X., Yang P., Cheng X., (2016), A precursor-derived morphology-controlled synthesis method for mesoporous Co₃O₄ nanostructures towards supercapacitor application, *CrystEngComm*, 18, 8253-8261, (DOI:10.1039/c6ce01921h).
- [107.] Xiao H., Guo W. J., Sun B., Pei M., Zhou G. W., (2016), Mesoporous TiO₂ and Co-doped TiO₂ nanotubes/reduced graphene oxide composites as electrodes for supercapacitors, *Electrochim. Acta*, 190, 104-117, (DOI:10.1016/j.electacta.2016.01.040).

- [108.] Nayak P. K., Munichandraiah N., (2012), Rapid sonochemical synthesis of mesoporous MnO₂ for supercapacitor applications, *Mater. Sci. Eng. B*, 177, 849-854, (DOI:10.1016/j.mseb.2012.04.004).
- [109.] Arjun N., Pan G. T., Yang T. C. K., (2017), The exploration of lanthanum based perovskites and their complementary electrolytes for the supercapacitor applications, *Res. Phys.*, 7, 920-926, (DOI:10.1016/j.rinp.2017.02.013).
- [110.] Kim H. Y., Shin J. Y., Jang I. C., Ju Y. W., (2020), Hydrothermal synthesis of three-dimensional perovskite NiMnO₃ oxide and application in supercapacitor electrode, *Energies*, 13, 11, (DOI:10.3390/en13010036).
- [111.] Zu L., Zhang W., Qu L., Liu L., Li W., Yu A., Zhao D., (2020), Mesoporous materials for electrochemical energy storage and, *Adv. Energy Mater.*, 10, 2002152, (DOI:10.1002/aenm.202002152).
- [112.] Liu Y., Xu X., Shao Z., Jiang S. P., (2020), Metal-organic frameworks derived porous carbon, metal oxides, and metal sulfides-based compounds for supercapacitors application, *Energy Storage Mater.*, 26, 1-22, (DOI:10.1016/j.ensm.2019.12.019).
- [113.] Lv H., Pan Q., Song Y., Liu X. X., Liu T., (2020), A review on nano/microstructured materials constructed by electrochemical technologies for supercapacitors, *Nano-Micro Lett.*, 12, 118, (DOI:10.1007/s40820-020-00451-z).
- [114.] Yu Z. N., Tetard L., Zhai L., Thomas J., (2015), Supercapacitor electrode materials: nanostructures from 0 to 3 dimensions. *Energy Environ. Sci.*, 8, 702-730, (DOI:10.1039/c4ee03229b).
- [115.] Raj S., Kar P., Roy P., (2018), Facile synthesis of flower-like morphology Cu_{0.27}Co_{2.73}O₄ for a high-performance supercapattery with extraordinary cycling stability, *Chem. Commun.*, 54, 12400-12403, (DOI:10.1039/c8cc04625e).
- [116.] Kumar L., Chauhan H., Yadav N., Yadav N., Hashmi S. A., Deka S., Faster Ion switching NiCo₂O₄ nanoparticle electrode-based supercapacitor device with high performances and long cycling stability, *ACS Appl. Energy Mater.*, 1, 6999-7006, (DOI:10.1021/acsaem.8b01427).

Chapter 2

Experimental Techniques

Chapter 2 is focused on synthesis and characterization techniques, which are utilized to complete the thesis work. The sol-gel and hydrothermal methods used for the synthesis of mesoporous 1D nanostructures are briefly discussed. Most relevant characterization techniques, such as XPS, Nitrogen adsorption-desorption isotherm analysis, contact angle measurements, and electrochemical analysis, are discussed in this chapter.

2.1 Introduction

Size reduction of the material to the nanoscale and integrating porosity are two tactics to increase the surface area of the material for their prominent use in electrochemical energy storage. The porous morphology offers more open channels for the electrolyte ions to penetrate deep inside and reduce the ion diffusion length. Moreover, it can accommodate the volume changes and control the structure degradation due to swelling and shrinkage during electrochemical reactions. The mesoporous structures with moderate dimensions in the range of 2 to 50 nm are more appropriate for observing better electrochemical performance. Various techniques have been explored to synthesize and characterization of mesoporous materials of uniform dimensions.

2.2 Synthesis methods

Hydrothermal and sol-gel synthesis methods have gained prominence for obtaining porous nanostructures with optimized dimensions, morphology, interconnectivity, and chemical composition. Therefore, I have considered these techniques to achieve the mesoporous structure of NiO, CoTiO₃, NiTiO₃, and MnO₂@NiTiO₃.

2.2.1 Hydrothermal synthesis

The hydrothermal method was explored for geographical studies to explain the development of minerals by hot water solutions jumping from cooling lava. Subsequently, substantial studies have been carried out to evolve the hydrothermal method and understand the mechanism behind the reactions and synthesis of new materials. This method includes the chemical reactions of substances in the presence of an aqueous solution or organic solvent in a sealed container at a suitable temperature (50-1000 °C) and pressure (1-100 MPa). Generally, the sealed container is made up of Teflon liner or high-pressure autoclave under supercritical conditions of used solvent (Figure 2.1). The size, morphologies, and structure of nanomaterials can be tuned easily by adjusting the reaction temperature, reaction time, pH of the solution, and the concentration of the reactants. This is one of the best suitable methods widely adopted for the growing distinct nanostructures morphologies in various forms. Moreover, post

and pre hydrothermal synthesis treatments may lead to the fabrication of materials with extended porosity, improved meso/micro-scopic nature, and better stability. Nevertheless, systematic studies on the synthesis of mesoporous nanostructure morphologies using the hydrothermal technique are yet to be explored thoroughly to understand the effect of reaction temperature and time and solution concentration on the mesoporous morphology. Therefore, this method is employed to synthesize mesoporous NiO nanostructures and the formation of MnO₂@NiTiO₃ core-shell nanostructures.

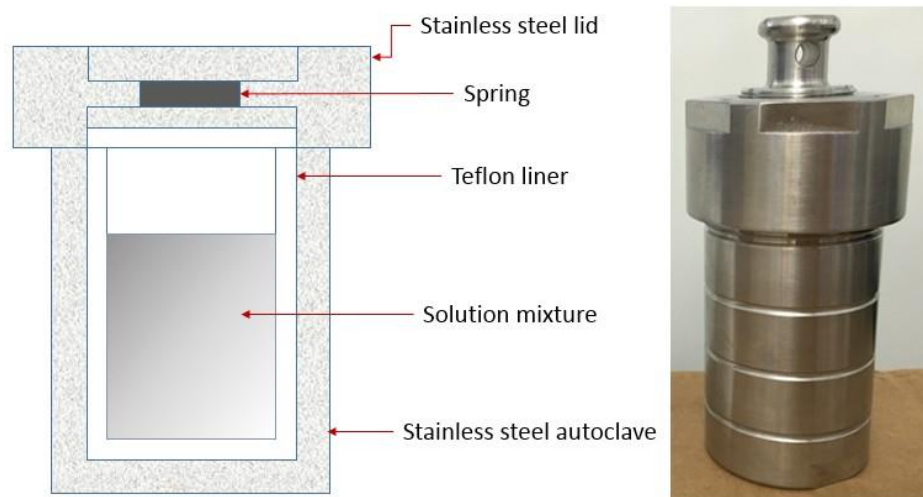


Figure 2.1. Teflon lined stainless steel autoclave used for the synthesis of nanomaterials. [1]

Mesoporous NiO nanostructures

The large area arrays of morphology-controlled NiO nanostructures were synthesized on ITO coated glass substrates via a hydrothermal synthesis approach. 0.234 g of nickel Sulfate (NiSO₄ · 6H₂O, 99.9%, Sigma Aldrich) dissolved in the 5 ml of de-ionized water was reacted with the 15 ml of ethanol (C₂H₅OH, 99.9%, SRL chemicals) solution for 10 min to form a 1:1 solution. The pH of the solution was maintained to 12 after reacting the 3 ml of aqueous ammonia solution (NH₃ · H₂O, Extra pure, 25%, SRL chemicals) for 30 min. at room temperature and then transferred to the autoclave containing well-aligned ITO coated glass substrates. The hydrothermal reaction was carried out at 180 °C for different time intervals of 6, 12, 18, 24, and 48 h to understand the effect of reaction time on the

growth of NiO nanostructures. After the reaction, the autoclave was cooled down to room temperature. The NiO nanostructures deposited ITO coated glass substrate was cleaned gently with deionized water to remove the unreacted precursors and further dried on a hot plate. The variation in the reaction time has altered the morphology from nanobelts to nanosheets of NiO over the ITO coated glass substrate. The NiO nanostructure morphologies were further analyzed to understand their electrochemical performance. The details on the synthesis and characterization of NiO nanostructures are discussed in Chapter 3.

2.2.2 Sol-gel synthesis

The sol-gel method has been widely studied for the tunable nanostructural dimensions of various materials with remarkable electrical, optical, mechanical, and magnetic properties. [2] This method is recognized for its cost-effectiveness, high yield, high surface to volume ratio, reproducibility, and low-temperature chemistry of prepared materials. [3] It allows the synthesis of any type of oxide/non-oxide composition and hybrid organic-inorganic materials, which does not exist obviously (Figure 2.2). Generally, the sol-gel route involves the formation of sol from a homogeneous mixed solution, its conversion into a gel by polycondensation method, and finally heat treatment. Typically, metal alkoxides or chlorides type precursors form colloids after the hydrolysis and polycondensation and produce the discrete colloidal particles network. The size, morphology, and composition of the materials can be tuned by varying the capping agent and metal precursor concentration and selecting a suitable reducing agent and thermal treatment. However, it is often challenging to attain the desired structure due to fracture generated by large capillary forces created after shrinkage of a wet gel upon vacuum drying, and also observe unavoidable existence of residual porosity and OH groups in sol-gel synthesized materials due to precipitation of alkoxide precursors during the sol formation. Therefore, the sol-gel synthesis technique is employed under well-optimized reaction conditions to synthesize mesoporous CoTiO_3 and NiTiO_3 nanostructures.

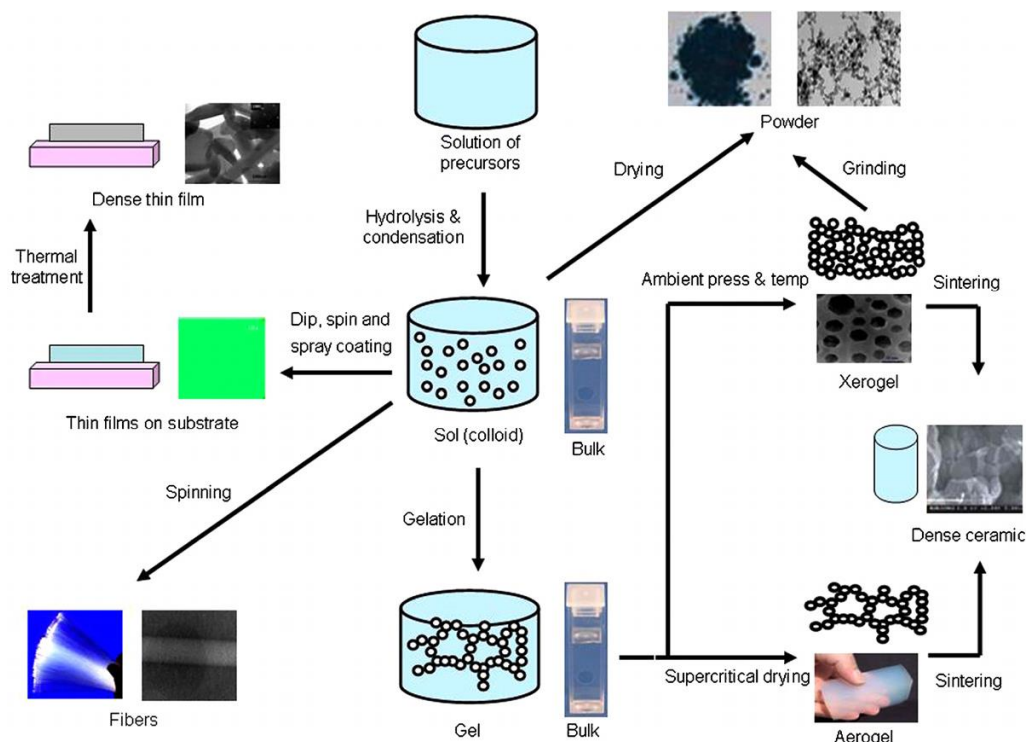


Figure 2.2. Schematic diagram showing the sol-gel method and its desired products. [4]

(a) Mesoporous CoTiO_3 nanostructures

The mesoporous CoTiO_3 microrods were synthesized via a sol-gel method utilizing Cobalt (II) acetate tetrahydrate ($\text{Co}(\text{CH}_3\text{COO})_2$; 99.999 %), Tetrabutyl titanate polymer ($\text{Ti}(\text{OBU})_4$), ethylene glycol (AR grade), and ethanol (ACS reagent, 96 %). 2.49 g of cobalt acetate tetrahydrate and 3.4 ml of tetrabutyl titanate were dissolved successfully for 60 min. in a 60 ml EG at room temperature under constant magnetic stirring to form a red solution. The red solution gradually turns to light pink after the further stirring of 5 hr. This indicates the formation of Co-Ti-EG polymer chain precursor after the reaction of EG with Co^{2+} and Ti^{4+} .

The Co-Ti-EG solution was reacted for various reaction times, i.e., 5, 6, 7, and 8 hr under constant magnetic stirring. The obtained Co-Ti-EG powder was washed several times with ethanol and deionized water, which was further subjected to annealing at 600 °C for 5 hr at a heating rate of 2 °C/min in the ambient atmosphere to remove the organic component. The change in reaction time has altered the morphological features. The observed rod-like mesoporous

morphology has collapsed into the independent particle formation after increasing the reaction time from 5 to 8 hr. Therefore, only rod-like mesoporous morphologies were considered for further electrochemical studies. The details on the synthesis of mesoporous CoTiO_3 rods are discussed in Chapter 4.

(b) Synthesis of Mesoporous NiTiO_3

The analytical grade chemicals were used to synthesize mesoporous NiTiO_3 rods using the sol-gel method. A typical preparation of NiTiO_3 nanorods was as follows: 2.48 g of nickel acetate ($\text{Ni}(\text{CH}_3\text{COO})_2 \cdot 4\text{H}_2\text{O}$, 99.999 %) and 3.4 ml of titanium butoxide ($\text{Ti}(\text{OC}_4\text{H}_9)_4$) were dissolved in 60 ml of ethylene glycol (EG) to form a green solution. Ethylene glycol acts as a solvent, and it reacts with the transition metal ions to form a metal-glycolate polymer through a chain-like structure. In the green solution of nickel acetate, titanium butoxide, and ethylene glycol, ethylene glycol reacts with nickel and titanium metal precursors to form Ni-Ti-EG polymer chain-like structure. After stirring at room temperature for 10 min., the green solution changes to light blue. Further, this reaction was continued for 1, 2, 3, and 4 hr. This has resulted in the agglomeration of the Ni-Ti-EG polymer chain-like structure due to the van der Waals interactions. The light blue residue was gathered and cleaned by centrifugation and redispersion cycles with ethanol and dried at 60 °C for 4 hr. under vacuum. Lastly, it was annealed at 600 °C for 2 hr at ambient atmosphere to obtain NiTiO_3 microrod structure. The reaction at ambient atmosphere was carried out for 1, 2, 3, and 4 h to observe the controlled mesoporous morphology. The increase in reaction time delivered diverse nanostructure morphology. The desired mesoporous rod-like morphology was observed for 1 h reaction time, and an increase in the reaction time (i.e., 2 to 4 h) resulted in the collapsing of the rod morphology. The collapsed morphologies were not considered for further electrochemical studies. The details on the synthesis of mesoporous NiTiO_3 rods are discussed in Chapter 5.

(c) Mesoporous $\text{NiTiO}_3@ \text{MnO}_2$ core-shell heterostructure

The well-optimized mesoporous NiTiO_3 rods were subjected to forming a core-shell structure with MnO_2 nanosheets using the hydrothermal method. The 10 mg of NiTiO_3 rods were dispersed in 30 mL of deionized water under

ultrasonic treatment for 10 min., which was subsequently reacted with 80 mg of KMnO_4 (99 %, alfa aesar) at 90 °C under constant magnetic stirring for another 30 min. The whole solution was transferred to Teflon lined stainless steel autoclave and reacted at 140 °C for 4 h to form MnO_2 over the NiTiO_3 rods. This as-synthesized core-shell $\text{MnO}_2@ \text{NiTiO}_3$ was rinsed thoroughly with deionized water and ethanol after centrifugation and further dried under vacuum at 60 °C for 4 h. Additionally, some more reactions have been carried out by varying the KMnO_4 concentration from 90 and 100 mg for the same amount of NiTiO_3 rods (i.e., 10 mg in 30mL). The increased amount of 90 or 100 mg has resulted in the formation of MnO_2 nanoflakes independently, leading to the formation of nanocomposites rather than core-shell structures. Therefore, the core-shell hetero-architecture of $\text{MnO}_2@ \text{NiTiO}_3$ was further analyzed to understand the electrochemical performance. The details on the synthesis and characterization of $\text{MnO}_2@ \text{NiTiO}_3$ nano-heterostructures is discussed in Chapter 6.

2.3 Materials characterization techniques

The synthesized mesoporous NiO , CoTiO_3 , NiTiO_3 , and $\text{MnO}_2@ \text{NiTiO}_3$ materials were further characterized to investigate their physicochemical and electrochemical properties. The surface morphology and mesoporous appearance were confirmed from Field emission scanning electron microscopy (FESEM, JEOL JSM-6500F). The crystal structure was confirmed from X-ray diffraction (XRD) studies. The XRD measurements were performed in the range from 20 to 80° at a step size of 2 °/min on a D2-phase Bruker equipped with $\text{CuK}\alpha$ radiation ($\lambda = 1.54 \text{ \AA}$). The elemental analysis was done using energy dispersive spectroscopy (EDS, OXFORD X-MAX 20 mm). These more generalized equipment are vastly utilized and explained in the literature. Therefore, their experimental details are not included in this thesis. Moreover, characterization techniques, such as X-ray photoelectron spectroscopy (XPS), contact angle measurements, nitrogen adsorption-desorption isotherm, and electrochemical measurements, which are crucial to understanding the effect of morphology, porous nature, and chemical composition in the electrochemical energy storage performance, are discussed below.

2.3.1 Drop shape analysis

In supercapacitors, specific capacitance (C_s) or energy density depends on the physical adsorption of electrolyte ions on the surface of the electrode. Therefore, appropriate electrode materials and electrolyte selection are important to improve electrolyte adsorption and storage ability. Furthermore, the potential window and charging-discharging rate, key factors for high-performance supercapacitors relying on the suitability of electrolytes such as organic, aqueous, and ionic liquids. The good ion fluidity of aqueous electrolytes leads to a high charging rate, but the potential window is limited to ~ 1 V before water decomposes. The ionic liquids with operating potential windows of 4 V maximum suffer from slower ionic transport and poorer electrochemical performance. The most widely used organic electrolytes where salts dissolved in organic solvents provide a good balance of operating voltages (approximately 2.5 V) and ionic conductivities (approximately 20-60 mS/cm). However, ionic concentration is a tricky and critical problem in organic electrolytes. A high ionic concentration enhances the specific capacitance of supercapacitors, but its improved viscosity results in a low charging rate. Therefore, significant trial and error testing is a prerequisite to optimizing the proper concentration of electrolytes.

An essential surface property of the electrode is its wetting phenomena that is how the aqueous electrolyte makes an interface with the electrode material. The electrode-electrolyte interface, which will be either hydrophobic or hydrophilic, plays a significant role in energy storage performance through electrolyte ion diffusion. Better wettability (i.e., hydrophilicity) is one of the prerequisites for improved energy storage performance. Therefore, contact angle measurement is the best way to quantify the wetting performance of the electrode materials in the desirable electrolytes. Quantitatively, the contact angle varies between $> 0^\circ$ to $< 180^\circ$ (Fig. 2.3), and the 90° angle is considered to define the hydrophilic ($< 90^\circ$) and hydrophobic ($> 90^\circ$) nature of the working electrode materials with electrolyte. Various concentrations/molarities of the aqueous KOH electrolyte (i.e., 0.5, 1, 1.5, and 2 M) were considered to measure the contact angle using a drop shape analyzer (DSA-25, Kruss GmbH, Germany). The

concentration of aq. KOH electrolyte showing a lower contact angle was considered to evaluate the electrochemical performance of the materials under study. The contact angle of the electrolyte with the mesoporous materials is estimated from the contact between the tangent of the electrolyte drop surface and the upper layer of materials placed on a flat surface (i.e., substrate) to study the wettability of electrolytes.

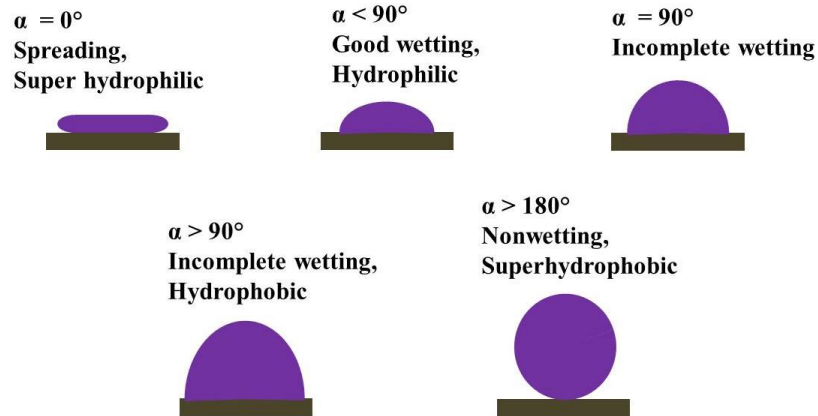


Figure 2.3. Schematic representation of wetting behavior.

2.3.2 X-ray photoelectron spectroscopy

X-ray photoelectron spectroscopy is a surface-sensitive technique that quantifies the chemical and electronic states and the chemical composition of the elements that exist within the material. [5] In XPS, soft X-rays of energy between 100-2500 eV are generally used under ultra-high vacuum to examine the core-levels of the sample. XPS spectra are acquired by irradiating a material with an X-ray beam and evaluating the kinetic energy of the number of secondary electrons escaped from the initial atomic layers up to 10 nm. The irradiation of sample surface with X-rays of enough energy guides ionization and emission of core electrons, as shown in Figure 2.4. A hemispherical electron analyzer collects these emitted photoelectrons to calculate their kinetic energy and constructs an energy spectrum of an ejected photoelectrons vs. binding energy using equation 2.1. [6]

$$\text{B.E.} = h\nu - \text{K.E.} - \phi \quad \dots\dots(2.1)$$

Where, B.E. is the binding energy of the photoelectron, K.E. is the kinetic energy of the emitted photoelectrons, $h\nu$ is the energy of the photon, and ϕ is the work function.

The experimental setup of XPS is well reported in the various literature, therefore, not included in the current thesis. The X-ray photoelectron spectrometer (XPS, Thermo Scientific Inc. K-alpha) with microfocus monochromated Al $K\alpha$ X-rays was used to study the chemical stoichiometry and electronic structure of the mesoporous NiO, CoTiO₃, NiTiO₃, and NiTiO₃@MnO₂ materials. The observed XPS results are correlated with the electrochemical performance. The related details are available in their respective chapters.

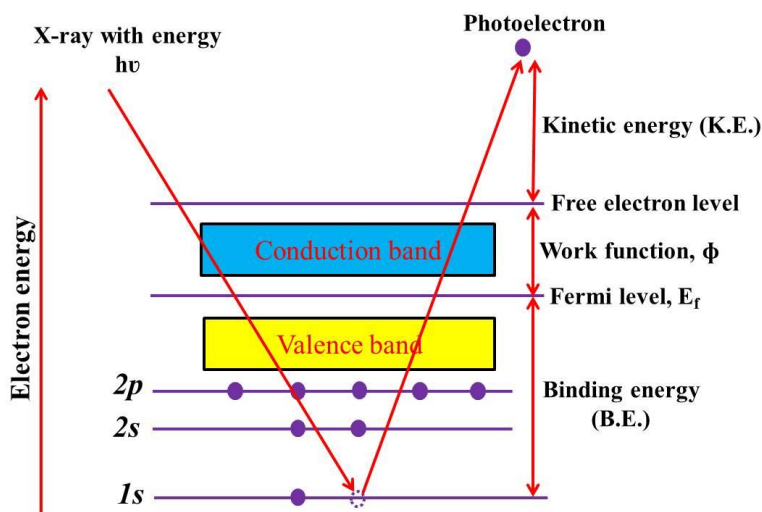


Figure 2.4. Principle of X-ray photoelectron spectroscopy.

2.3.3 Nitrogen adsorption-desorption isotherm analysis

Adsorption is a phenomenon of adhesion of molecules, ions, gas, and solids on a surface. The material on which surface the adsorption happens is known as the adsorbate. The adsorption-desorption properties are affected by the surface area of material, adsorbent activation, nature of adsorbent and adsorbate, and experimental conditions such as reaction temperature and pressure. Our adsorption studies mostly concentrate on physisorption (i.e., physical adsorption), which usually observes at low temperatures (i.e., ~ 77 K) in the presence of an N₂ gas atmosphere and lower heat of adsorption (i.e., 20-40 kJ/mol). The adsorption process materializes through the following steps. [7]

1. At initial low temperature and pressure, the gas molecules try to get adsorbed on the sample surface.

2. As the gas pressure rises, numbers of gas molecules get adsorbed on the sample surface in the monolayer form, and the smaller pores will get occupied first.
3. The rise in the gas pressure occupies relatively larger pores by developing multilayers of the gas molecules.
4. Afterward, a further rise in the gas pressure gives total coverage of the sample specimen and fills nearly all the pores.

Several models have been suggested to study the adsorption-desorption phenomena, such as the Langmuir adsorption isotherm model, Freundlich adsorption isotherm model, linear adsorption isotherm model, and Brauner-Emmett-Teller (BET) adsorption isotherm model. Out of all these, the BET model is used in our research work to study the nitrogen adsorption-desorption isotherm. The adsorption-desorption isotherm can be divided into six types (Figure 2.5). [8] Type I isotherm is usually obtained in microporous solids having minimal external surfaces (i.e., Metal-organic frameworks, zeolites, and activated carbon). It comes up with the monolayer adsorption phenomena, which the Langmuir Isotherm model can describe. Type II isotherm that shows macroporous nature is a reversible isotherm constitutes the unimpeded monolayer-multilayer adsorption. Although Type III isotherm indicates unimpeded multilayer formation, it is the vapor based adsorption. Type IV and V isotherms with distinct hysteresis loops specify the presence of capillary condensation in mesoporous materials. The starting part in the Type IV isotherm is allocated to monolayer-multilayer adsorption. The Type VI isotherm constitutes the stairwise multilayer adsorption on a macroporous surface, and the sharpness of the stair depends on the temperature. The shape of the hysteresis (i.e., H1 to H4) is governed by agglomerated or spherical particles organized uniformly (H1), the pore with confined openings showing constant channel-like pores (H2), loose plate-like particles set up a slit-like pore (H3), and confined slit-like pores with non-uniform internal shape and broad size distribution (H4). The mesoporous nature plays a significant role in enhancing ion diffusion; therefore, the role of porosity and surface area in energy storage performance cannot be neglected. Therefore, isotherm studies were carried out at 180 °C using a nitrogen adsorption-desorption

study with an automated gas adsorption analyzer Quantachrome Autosorb iQ2. The Liquid N₂ gas mixed with 5 % H₂ was soaked in 1-3 mg of material for 8 h to know the pore size distribution and surface area accessible for ion diffusion in the synthesized materials.

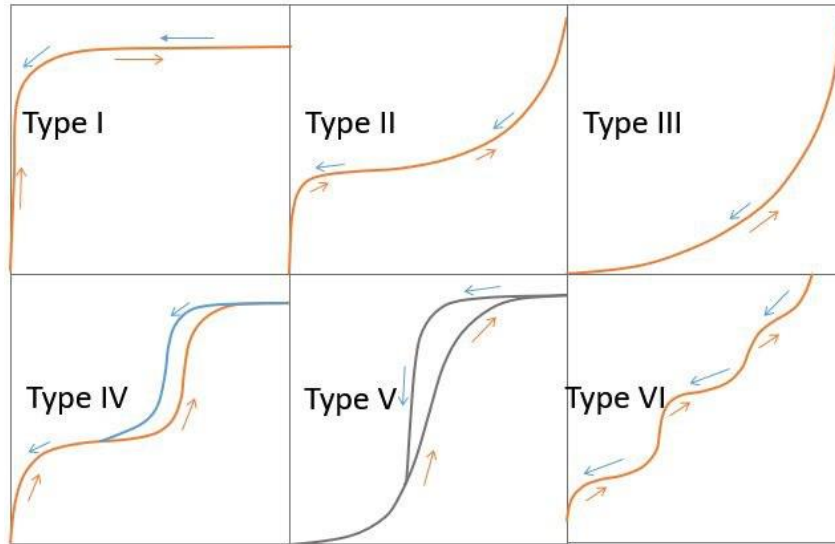


Figure 2.5. Different types of adsorption isotherms as classified by IUPAC. [9]

2.3.4 Electrochemical analysis

The electrochemical performance of the materials as a working electrode for supercapacitor is evaluated from cyclic voltammetry (CV), galvanostatic charge-discharge (GCD), and electrochemical impedance spectroscopy (EIS) in terms of specific capacitance (C_{sp}), energy density (E), and power density (P).

(a) *Cyclic voltammetry (CV)*

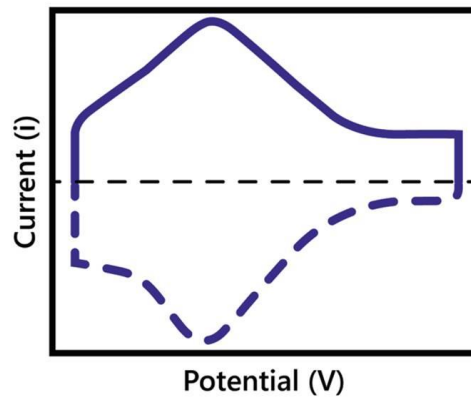


Figure 2.6. Typical representation of cyclic voltammogram (CV) of pseudocapacitive based materials existence of oxidation and redox peaks. [10]

Cyclic voltammetry is one of the most basic electroanalytical characterization methods used to investigate electroactive species. In cyclic voltammetry, a fixed potential of active working electrode materials is employed as a ramp signal with some known sweep rate (i.e., mV/s) and is calculated with respect to a reference electrode. The voltage is varied at a constant sweep rate between two initial ($\equiv V_i$) and final ($\equiv V_f$) values, but when the potential reaches V_f , the scan is reversed to achieve the potential to V_i . In the forward scan, potential scans start at a greater negative potential (V_i) and end at a lower potential (V_f), whereas in the reverse scan, it is the opposite (i.e., from V_f to V_i). The potential V_f at extreme conditions, called switching potential, is sufficient enough to have originated oxidation and reduction of the material. Figure 2.6 shows the schematic of the distinctive cyclic voltammetry graph plotted between current (i) and voltage (V). The CV provides quantitative and qualitative insights such as charge transport, ion diffusion, redox behavior, polarization, reversibility, etc., related to the electrochemical reaction of the electrode material. It also helps to understand the nature of charge storage in materials under investigation.

Cyclic voltammetry (CV) measurements for mesoporous NiO, CTO, NTO, and MnO₂@NTO were performed in an aqueous KOH electrolyte within the optimized operating potential range at various scan rates. The CV plots gave a distinct pair of anodic and cathodic peaks independent of variation in the scan rates. The positive and negative currents observed in the operating potential range explain their oxidation and reduction peaks. The CV analysis and diffusion coefficient, and specific capacitance (C_s) evaluated from CV measurements using the following equations, are detailed in the respective chapters.

The scan rate dependent variation in the current density was interpreted by the Randles-Sevcik equation

$$i_p = 2.69 \times 10^5 C_o n^{3/2} \nu^{1/2} D^{1/2} \dots\dots (2.2)$$

Where, the peak current density (i_p) of the electrochemical reaction is proportional to the square root of the scan rate (ν), i_p is the peak current density (mA/g), C_o is the concentration of ions in the electrolyte solution (mol/cm²), n is the number of

electrons, v is the scan rate (mV/s), and D is the diffusion coefficient for ions in the electrode material.

The specific capacitance (C_s) was measured from the cyclic voltammetry (CV) using the following equation

$$C_s = \frac{\int idV}{2m v \Delta V} \dots\dots (2.3)$$

Where, m is the mass of the active electrode material (g), v is the scan rate in mV/s, $\int idV$ is the area under the CV curve, and ΔV is the potential window.

(b) Galvanostatic charge-discharge (GCD)

The galvanostatic charge-discharge analysis is also called chronopotentiometry. GCD is a method where a constant current is applied between the counter and working electrode, and the potential of the active working electrode is calculated with respect to the reference electrode. The supercapacitor is charged with respect to the particular current density, and once it touches the desired value, it discharges with the same current density till achieving the original potential. During the GCD analysis, the electrode material will undergo different charge and discharge cycles at various current densities to explore the charge storage performance. The charge storage (i.e., specific capacitance) is expected to be in close approximation at the lower and higher current density for reasonable rate capable electrode materials. The specific capacitance, IR drop, energy density, power density, cycling stability, and coulombic efficiency can be evaluated from the GCD analysis. Figure 2.7 shows the schematic GCD plot of electrochemical pseudocapacitive material. The specific capacitance of the electrode material was calculated from the GCD plot by taking care of the mass of the active material (m), potential window (ΔV), discharge time (Δt), and current density (I). The specific capacitance (C_s), energy density (E), and power density (P) were evaluated from GCD measurements using the following equations and are detailed in the respective chapters.

The specific capacitance of the electrode material was evaluated from the equation,

$$C_s = I \cdot dt / m \cdot dv \dots\dots(2.4)$$

Besides the specific capacitance (C_s), power and energy density are highly crucial for supercapacitors. The energy density and power density were calculated by the equations,

$$E = \frac{1}{2} \times C_s \times (\Delta V)^2 \quad \dots\dots (2.5)$$

$$P = \frac{E}{\Delta t} \times 3600 \quad \dots\dots (2.6)$$

Where, C_s is the specific capacitance (F/g), m is the mass of the active electrode material (g), I is the current density (A/g), dV/dt is the slope of the discharge curve, E is the specific energy (Wh/kg), ΔV is the potential operating range (V), P is the specific power (W/kg), and Δt is discharge time (sec) corresponding to the specific capacitance (C_s) value calculated from galvanostatic charge-discharge measurements.

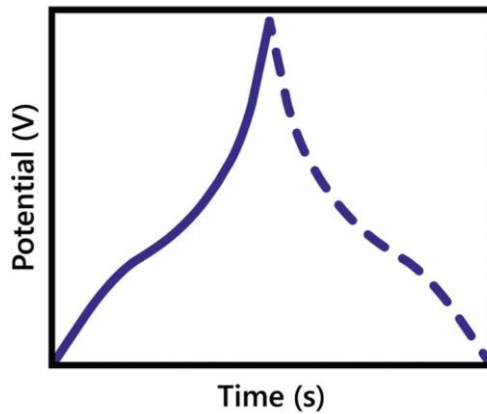


Figure 2.7. Typical representation of Galvanostatic charge-discharge (GCD) of pseudocapacitive materials. [10]

(c) Electrochemical impedance spectroscopy (EIS)

Electrochemical impedance spectroscopy (EIS) is a powerful analytical method in characterizing electrochemical supercapacitor in different frequency regions. EIS analyses are accomplished on systems in an equilibrium position. Usually, a small sinusoidal voltage (based on CV measurements) is covered at the open circuit potential to calculate the frequency (between 20 Hz to 10 MHz) dependent impedance of a cell. The Bode and Nyquist plots are the methods to illustrate the impedance data. The Bode plot signifies the phase angle (ϕ) and modulus of impedance (Z) as a function of frequency, and the Nyquist plot

displays the real and imaginary part of impedance at various frequencies. Typically, impedance is documented and planned from the higher frequency region to the lower frequency region to illustrate the distinct behaviors observed for the different frequency regions. The resistance offered by the electrolyte solution is often a significant contributor to the impedance of the three-electrode cell. A modern potentiostat compensates for the solution resistance between the reference and counter electrodes. However, the resistance between the working and reference electrodes must be considered when the cell is modeled. The point intercepting the X-axis of impedance at the uppermost calculated frequency in a Nyquist plot provides the equivalent series resistance (ESR) (Figure 2.8). Subsequently, semicircles witness the charge storage mechanism for pseudocapacitive materials. The straight line in the lower frequency region is assigned to the ion diffusion resistance (i.e., Warburg resistance, Z_w). In this thesis, electrochemical impedance spectroscopic measurements are performed to understand the charge transfer behavior at the electrode-electrolyte interface and its effect on energy storage performance.

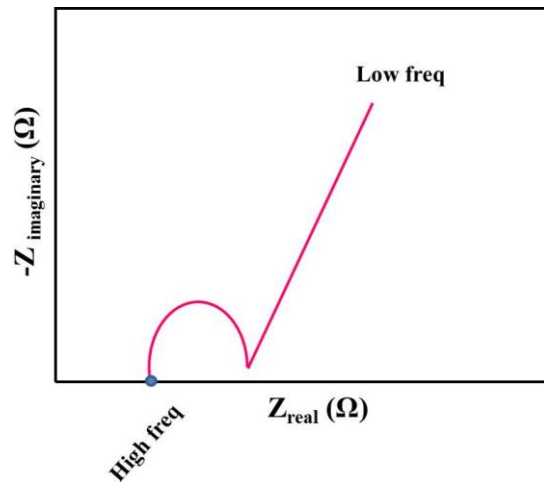


Figure 2.8. Typical Nyquist plot representation of pseudocapacitive material. [10]

2.4 References

- [1.] Ahmad W. R. W., Mamat M. H., Zoolfakar A. S., Khusaimi Z., Rusop M., (2016), A review on hematite α -Fe₂O₃ focusing on nanostructures, synthesis methods and applications, IEEE Student Conf. Res. Devt. (SCORED), (DOI:10.1109/SCORED.2016.7810090).

- [2.] Parashar M., Shukla V. K., Singh R., (2020), Metal oxides nanoparticles via sol-gel method: a review on synthesis, characterization and applications, *J. Mater. Sci: Mater Electron.*, 31, 3729-3749, (DOI:10.1007/s10854-020-02994-8).
- [3.] Parashar M., Shukla V. K., Singh R., (2020), Metal oxide nanoparticles via sol-gel method: a review on synthesis, characterization and applications, *J. Mater. Sci.: Mater. Electron.*, 31, 3729-3749, (DOI:10.1007/s10854-020-02994-8).
- [4.] Gupta R., Kumar A., (2008), Bioactive materials for biomedical applications using sol-gel technology, *Biomed. Mater.*, 3, 034005, (DOI:10.1088/1748-6041/3/3/034005).
- [5.] Brundle C. R., Crist B. V., (2020), X-Ray photoelectron spectroscopy: A perspective on quantitation accuracy for composition analysis of homogeneous materials, *J. Vac. Sci. Technol. A*, 38, 041001, (DOI:10.1116/1.5143897).
- [6.] Stevie F. A., Donley C. L., (2020), Introduction to x-ray photoelectron spectroscopy, *J. Vac. Sci. Technol. A*, 38, 063204, (DOI:10.1116/6.0000412).
- [7.] Groen J. C., Peffer L. A., Pérez-Ramírez J., (2003), Pore size determination in modified micro-and mesoporous materials. Pitfalls and limitations in gas adsorption data analysis, *Micropor. Mesopor. Mater.*, 60, 1-17, (DOI:10.1016/S1387-1811(03)00339-1).
- [8.] Sing K. S., Everett D. H., Haul R. A. W., Moscou L., Pierotti R. A., Rouquerol J., Siemieniewska T., (1985), Reporting physisorption data for gas/solid systems with special reference to the determination of surface area and porosity. *Pure Appl. Chem.*, 57, 603-619, (DOI:10.1002/9783527610044.hetcat0065).
- [9.] Kumar V. K., Srinivas G., Wood B., Ramisetty K. A., Stewart A. A., Howard C. A., Brett D. J. L., Reinoso F. R., (2019), Characterization of adsorption site energies and heterogeneous of porous materials, *J. Mater. Chem. A*, 7, 10104-10137, (DOI:10.1039/C9TA00287A).
- [10.] Mathis T. S., Kurra N., Wang X. H., Pinto D., Simon P., Gogotsi Y., (2019), Energy storage data reporting in perspective-guidelines for interpreting the performance of electrochemical energy storage systems, *Adv. Energy Mater.*, 9, 1902007, (DOI:10.1002/aenm.201902007).

Chapter 3

Mesoporous NiO nanostructures

We report the morphology-controlled approach to improve the specific capacitance (C_s) and energy/power density of the supercapacitor. The irregular morphologies of NiO are transformed into the perforated mesoporous nanobelts and further altered into the nanoflakes. The nanobelts and nanoflakes of NiO with an average width of ~74 nm and ~215 nm forms the film of thickness ~5.8 and 2.7 μm , respectively. The mesoporous NiO nanobelts deliver higher C_s values (i.e., 794 F/g) than the nanoflakes (146 F/g) and irregular morphologies (742 F/g). Moreover, nanobelts show 88.6 % retention after continuous 2500 charging-discharging cycles. The NiO nanobelts exhibit a power density of 2963 W/kg, and energy density of 57 Wh/kg is significantly higher than the pristine NiO nanoflakes, nanorods, 2D thin films porosity tunned nanowalls, nanofibers, and its heterostructures with NiCo_2O_4 and Ni_3S_2 nanosheets. The perforated mesoporous NiO nanobelts with clearly visible textural boundaries provide a relatively larger surface area and excellent interconnecting network than irregular morphologies and nanoflakes, which provide easy access to the OH⁻ ions for diffusion.

3.1 Introduction

The global need for new energy storage technologies is leading to an increasing interest in the advancement of energy storage systems with ultra-high-rate capabilities, especially because worldwide demand might proliferate as batteries and electrochemical supercapacitors are increasingly used in portable electronics, hybrid electric vehicles, and power quality devices. Among these energy storage devices, much attention has been given lately to supercapacitors. Moreover, the quest for high-power density and energy density has led to significant efforts in developing supercapacitors to either assist or compete with batteries. Compared to conventional batteries, supercapacitors have high specific capacitance (C_s), longer cycle life, and excellent pulse charge-discharge properties. Recently, numerous studies are engrossed in improving the power and energy density of supercapacitors for portable power supplies and hybrid electric vehicles. [1] Among various explored morphologies and materials, nanomaterials have triggered a lot of excitement owing to their high aspect ratio and large textural boundaries. Researchers are currently focusing on developing porous layered and hollow structures to achieve optimized chemical and physical properties, as in the case of graphene. However, the highly porous structure and interconnectivity of the nanomaterials remains a great challenge in the development of supercapacitor. [1] Although designing perforated nanostructure morphologies with control over shape and size are promising scientific community, efforts are limited to carbon-based materials or short-ranged morphologies. [2] The porous carbon or polymer electrochemical double-layer capacitor (EDLC) materials provide high C_s , nevertheless suffer from high energy density and faster deterioration. [3] Their shrinking and swelling during the discharging and charging, respectively, results in a short lifetime. Therefore, transition metal oxides of mutable valencies are the better alternative as an electrode material providing higher energy density in conjunction with the stability. The larger surface area, reduction in ion diffusion resistance, and efficient exchange of ions in the network of metal oxides are asking for further improvement to reach the theoretical predictions on the energy and power density. Various metal oxides of titanium, [4] manganese [5] and cobalt, [6] etc. are explored, but higher theoretical capacitance value (i.e., 2573 F/g), faster ion intercalation mechanism (< 2 s), high chemical/thermal stability and large current density

of Nickel oxide (NiO) is attracting scientific community. [7,8] The NiO thin films and nanostructures in the form of nanotubes, [9] pine-cone, [10] nanofiber, [11] nanoparticulated spheres, [12] nanorods, [13] nanospheres, [14] nanoflakes, [15] and nanosheets [16] are explored for electrochemical activities, but their C_s was limited in the range of 46.74 to 463 F/g.

The microwave-assisted NiO particles synthesized using cetyltrimethyl ammonium bromide (CTAB) surfactant grew in particular crystal orientation and agglomerated in the form of nanoflakes. The resistive textural boundaries/contact of the individually nucleated nanoparticle might have limited the C_s of nanoflakes to 401 F/g. [17] The CuO nanoflowers decorated with the NiO nanoflakes were expected to improve the ion conduction by means of synergistic effect but constrained the access to the ion inside the pores of nanoflowers, and C_s reduced further to 280 F/g. [18] Moreover, the C_s of 94 F/g of the polycrystalline NiO microtubes improved to 266.7 F/g after forming overlayers of MnO₂ nanoflakes. [7] The heat treated two-dimensional (2D) round slices of NiO nanoflakes delivered C_s of 407 F/g, which was reduced to 89 F/g for asymmetric combination with activated carbon. [15] The carbonization of polymerized NiO nanofibers resulted in the thick coating of carbon along the fiber body, restricted the efficient penetration of the electrolyte, and resulted in the C_s of 288 F/g. [19] Owing to the significant contribution of porous morphology, the porous composites of ZnO-NiO micro-polyhedrons ($C_s = 649$ F/g), [20] porous 3D NiO/Ni flower-like morphology of irregular nanoflakes composed of nanoparticles ($C_s = 363.7$ F/g), [21] NiO fibers ($C_s = 175$ F/g) and Ni/NiO composite fibers ($C_s = 526$ F/g) [11] were explored to achieve high specific capacitance, power density, and energy density. However, the dense and closed packed morphologies limited access to ion diffusion within. Recent efforts of Mondal et al. [22] on tailoring the hole dimension within the randomly arranged NiO nanoflakes by variation in the calcinated temperature resulted in the C_s of 738 F/g at a temperature of 900 °C. The 2D NiO nanoflake array solvothermally grown on Ni foam sintered in air at 300 °C delivered inflated C_s values of 2013.7 F/g, but the energy and power density was restricted to 45.3 Wh/kg and 1081.9 W/kg, respectively. [23] Likewise, Ci et al. [24] reported smaller energy density values of 15.9 Wh/kg for the combination of 3D, 2D, and 1D nanostructures in the NiO microflower, where 3D NiO microflowers were constructed

of 2D nanosheet framework derived from the weaving of 1D NiO nanowires. Further, the decoration of sulfur over the 2D NiO structures expected to deliver rapid diffusion of ions and fast electron transport due to the higher electrical conductive could achieve the highest C_s of 386.7 F/g. Overall, 2D NiO nanoflakes and their decoration with sulfides and metal particles did not come up to the expectation. The well-defined single crystalline nature and the density-controlled alignment of nanostructures have attracted scientific attention. Despite that, controlled porous architecture with uniform pore distribution in long-range nanostructures has triggered lots of excitement in energy storage. Therefore, the synthesis of perforated mesoporous NiO nanostructure with a larger surface and interconnecting network is of scientific and technological importance.

In recent years, the synthesis of nanobelts of transition metal oxides has fascinated researchers due to their high specific surface area, excellent mesoporous structural stability, and outstanding transport properties than that of their high-dimensional counterparts. Many methods have been utilized to prepare nanobelts of metal oxides [1] such as SnO₂, ZnO, TiO₂, V₂O₅, Bi₂O₃, and Fe₂O₃ but, no reports are focused on the synthesis of perforated mesoporous NiO nanobelts using cost-effective synthesis technique. In this article, we report the controlled synthesis of the various morphologies of NiO, including perforated mesoporous untraceable nanobelts and nanoflakes on the ITO coated conducting glass substrate. The structural morphologies and chemical composition of the NiO nanostructures were examined using field-emission scanning electron microscopy (FESEM) and X-ray photoemission spectroscopy (XPS), respectively. The effect of nanostructure morphology on the electrochemical performances of NiO was systematically investigated utilizing cyclic voltammetry (CV), galvanostatic charge-discharge (GCD) method, and electrochemical impedance spectroscopy (EIS) in the 2 M KOH aqueous electrolyte. The results strongly suggest that the perforated mesoporous NiO nanobelts possess ultra-high-rate capabilities with C_s of 794.12 F/g, energy density of 32.81 Wh/kg, and power density of 2962.9 W/kg, then irregular morphologies and nanoflakes of NiO. Therefore, perforated mesoporous NiO nanobelts are competent electrode material to fabricate highly stable supercapacitors with ultra-high rate and a long cycle lifetime.

3.2 Experimental Section

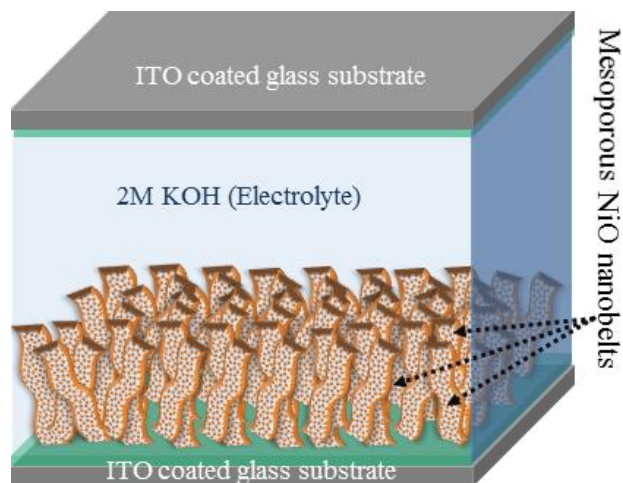


Figure 3.1. Schematic diagram of the mesoporous NiO nanostructure-based supercapacitor.

The large area arrays of morphology-controlled NiO nanostructures were synthesized on ITO coated glass substrates via a hydrothermal synthesis approach. 1M Nickel sulfate ($\text{NiSO}_4 \cdot 6\text{H}_2\text{O}$, 99.9%, Sigma Aldrich) dissolved in the de-ionized water was reacted with the Ethanol ($\text{C}_2\text{H}_5\text{OH}$, 99.9%, SRL chemicals) for 10 min to form a 1:1 solution. The pH of the solution was maintained to 12 after reacting the aqueous ammonia solution ($\text{NH}_3 \cdot \text{H}_2\text{O}$, Extra pure, 25%, SRL chemicals) for 30 min. at room temperature and then transferred to the autoclave containing well-aligned ITO coated glass substrates. The hydrothermal reaction was carried out at 180 °C for different time intervals, such as 6, 12, 18, 24, and 48 h, to grow morphology-controlled NiO nanostructures over the ITO coated glass substrate. After that, the effect of reaction time on the surface morphology was studied utilizing field-emission scanning electron microscopy (FESEM, JEOL JSM-6500F) and Transmission electron microscopy (TEM, JEOL JEM 3010). The electronic structure and chemical states of the NiO nanostructures were analyzed using an X-ray photoelectron spectrometer (XPS, Thermo Scientific Inc. $\text{K}\alpha$) with a microfocus monochromated Al $\text{K}\alpha$ X-ray. The surface area and pore size distribution analysis of the NiO nanobelts were performed adopting N_2 adsorption-desorption isotherm (BET) and Barrett-Joyner-Halenda (BJH) methods in an automated gas sorption analyzer (Quantachrome Autosorb iQ_2). Figure 3.1 shows the schematic of the prototype supercapacitor composed of NiO nanostructures grown on conducting glass (ITO/glass)

substrate as a working electrode, saturated calomel electrode as a reference electrode, and pristine ITO/glass as a counter electrode, was used to evaluate the electrochemical properties. The electrochemical measurements were accomplished at room temperature with the potentiostat (Autolab PGSTAT302N) in 2M KOH aqueous electrolyte to investigate the effect of controlled morphology of NiO nanostructures on the pseudocapacitive performance of electrochemical supercapacitor. The capacitance values, cyclic stability, and energy/power density performance of the prototype device were confirmed with two terminal measurement approach.

3.3 Results and discussion

3.3.1 Field emission scanning electron microscopy

The FESEM images in Figure 3.2 show the controlled surface morphological features of the NiO nanostructures. Time-dependent synthesis performed to control the growth of desired morphology and mesoporous features in the nanostructures. The clearly visible and randomly oriented irregular morphologies of NiO resulted in the thin film formation at the initial stage of the 6 h reaction (Figure 3.2(a)). The high-magnification FESEM image in the inset confirmed the presence of compact nanoparticles like appearance beneath the irregular morphologies in the compact NiO thin film. The increase in the reaction time to 12 h has resulted in the nanobelts growth of the NiO (Figure 3.2(b)), which was further resulted in the flake-like two-dimensional (2D) structure at 48 h. The close observation of high magnification FESEM images in the inset of Figure 3.2(b) shows the appearance of untraceable long nanobelts. No much alteration in the thickness of nanobelts has been observed with further increase in the reaction time (i.e., 48 h), but the width increased apparently. The prominent expansion of the width conceived the formation of protracted nanoflakes like morphology (inset of Figure 3.2(c)). The increase in reaction time to 48 h has resulted in the formation of nano-flakes at the expense of nanobelts. Even though the length of both nanobelts and nanoflakes remains untraceable, their width is ~74 nm and ~215 nm, respectively. Moreover, the time-dependent change in the morphology of NiO nanostructures has resulted in the alteration of the film thickness. The irregular morphologies accompanied by nanoparticles formed the film of a

thickness of $\sim 2.2 \mu\text{m}$ (Figure 3.2(d)). Which was further increased (i.e., owing to the evolution of well-aligned NiO nanobelts. The well-separated nanobelts with clearly visible textural boundaries delivered porous thin film (Figure 3.2(e)). The randomly oriented but fairly vertically aligned NiO nanobelts have resulted in the thin film of thickness $\sim 5.8 \mu\text{m}$. Nevertheless, the film thickness was reduced to $\sim 2.7 \mu\text{m}$ after converting NiO nanobelts into nanoflakes (Figure 3.2(f)). The increased width of NiO nanoflakes drives to decrease the film porosity and hence thickness than that of NiO nanobelts. This leads to the compact film formation for the nanoflakes morphologies. The numbers of pores of the size 5 to 10 nm observed over the nanobelt extracted from the large area array corroborate the highly mesoporous nature of the NiO nanobelts (Figure 3.2(g)) synthesized at a reaction time of 12 h. The crystal structure of the NiO nanobelts is confirmed from HRTEM, and details are provided in Figure 3.3. This indicates that a fairly vertical arrangement of highly mesoporous NiO nanobelts is competent in offering the larger accessible surface area to facilitate the ion intercalation/ deintercalation and therefore improve the charge storage mechanism.

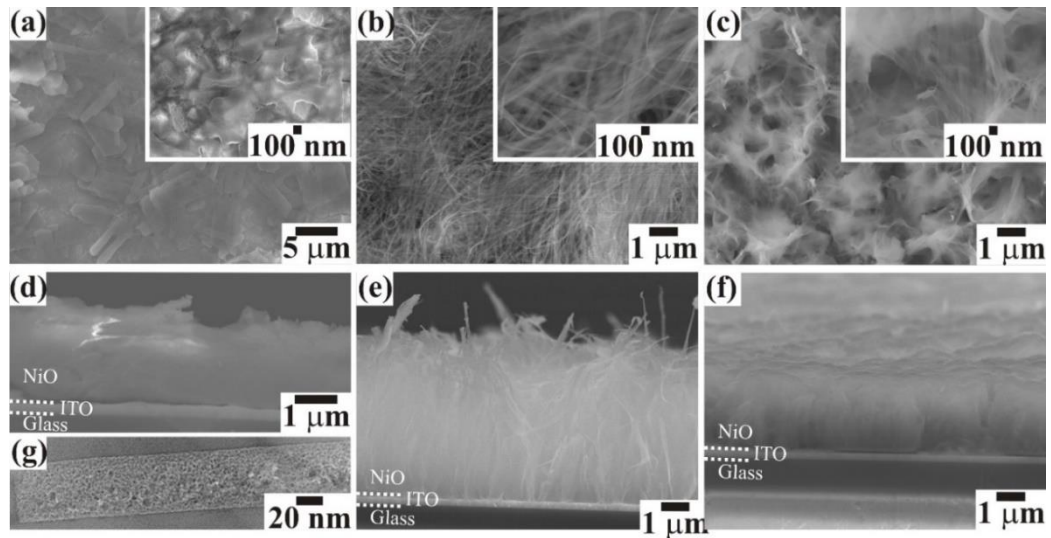


Figure 3.2. FESEM images of controlled surface morphological features of the NiO nanostructures. The upper panel shows the top view of the nanostructures obtained at a reaction time of (a) 6 h, (b) 12 h, and (c) 48 h. Inset of the Fig. shows their respective high-magnification FESEM image. The lower panel shows the side view of those nanostructures (d-f), respectively. (g) The high-magnification

TEM image of the single nanobelts extracted from the large area array of nanobelts in (b).

3.3.2 Transmission electron microscopy

The morphology and crystal structure of mesoporous NiO nanobelts were further characterized by High-Resolution TEM. The TEM image in Figure 3.3 shows that the NiO nanobelts are composed of interlinked nanoparticles with well-defined crystal structures. The interlinking of the NiO nanoparticles has resulted in the formation of mesoporous nanobelts (Figure 3.3(a)). These observations are in good agreement with the FESEM and BET analysis discussed in Figure 3.1 and Figure 3.4. The interplanar spacing of ~ 0.15 nm observed from the HRTEM pattern (Figure 3.3(b)) is assigned to the (220) plane is in well agreement with the Rhombohedral crystal structure defined for NiO (JCPDs: 43740).

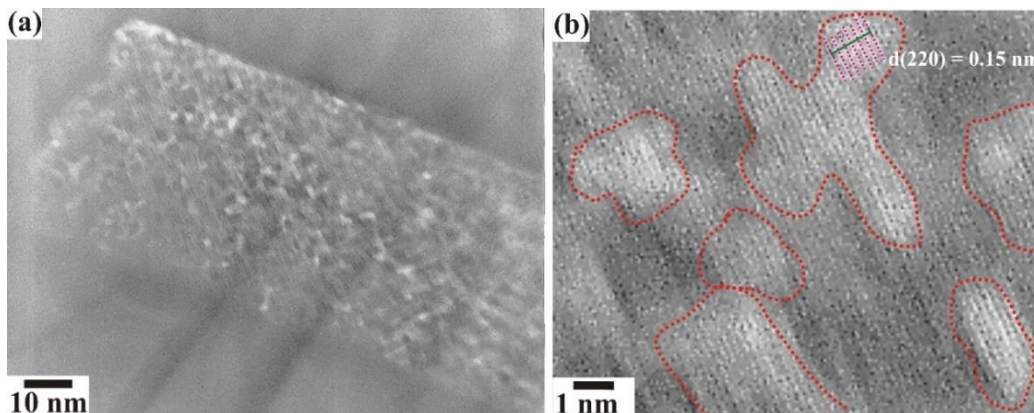


Figure 3.3. High-Resolution TEM image of the single nanobelts extracted from the large area array confirming (a) the mesoporous nature of nanobelts and (b) interplanar spacing of the well-separated NiO nanoparticles of the nanobelts. The nanoparticles are traced with the dotted red lines.

3.3.3 Nitrogen adsorption-desorption Isotherm

N_2 adsorption-desorption isotherm measurements were performed to confirm the mesoporous appearance of the NiO nanobelts in high-magnification TEM images (i.e., Figure 3.2(g)). Figure 3.4 shows the BET analysis confirming the mesoporous nature of the NiO nanobelts. Figure 3.4(a) shows a type IV isotherm with a distinct broad hysteresis loop, confirming the extensive

distribution of internal voids throughout the nanobelt body. The interconnected existence of broad range voids along the nanobelts body has led to the formation of ordered mesoporous NiO nanobelts. The specific surface area of $40.572 \text{ m}^2/\text{g}$ and pore volume $0.352 \text{ cm}^3/\text{g}$ were observed for the nanobelts synthesized at the reaction of 12 h. Although the larger pore size of 1828 nm is observed from the BJH pore size distribution, most of the pores range from 15 to 100 nm. The maximum pores are of width $\sim 19 \text{ nm}$, and the mean (average) pore size distribution is 19.67 nm (Figure 3.4(b)). The improved surface area due to the mesoporous nature of NiO nanobelts not only provides abundant sites for ion accumulation but also expected to improve the electrode-electrolyte interaction at the interface. Moreover, an easily accessible larger mesoporous surface facilitates better electrolyte/ion penetration and further enhances the faradaic charge storage mechanism.

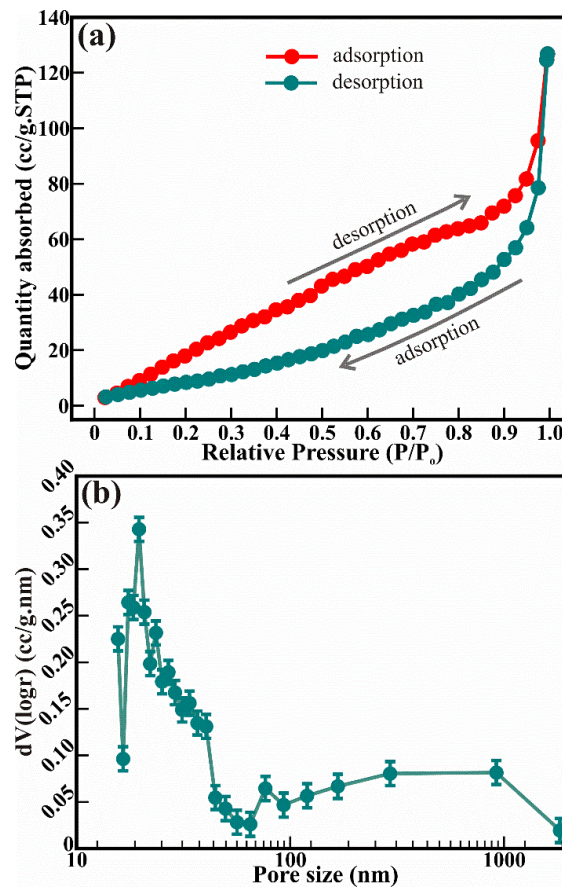


Figure 3.4. (a) N_2 adsorption-desorption isotherm and (b) BJH pore size distribution of the NiO nanobelts obtained after the reaction time of 12 h.

3.3.4 X-ray Photoelectron Spectroscopy

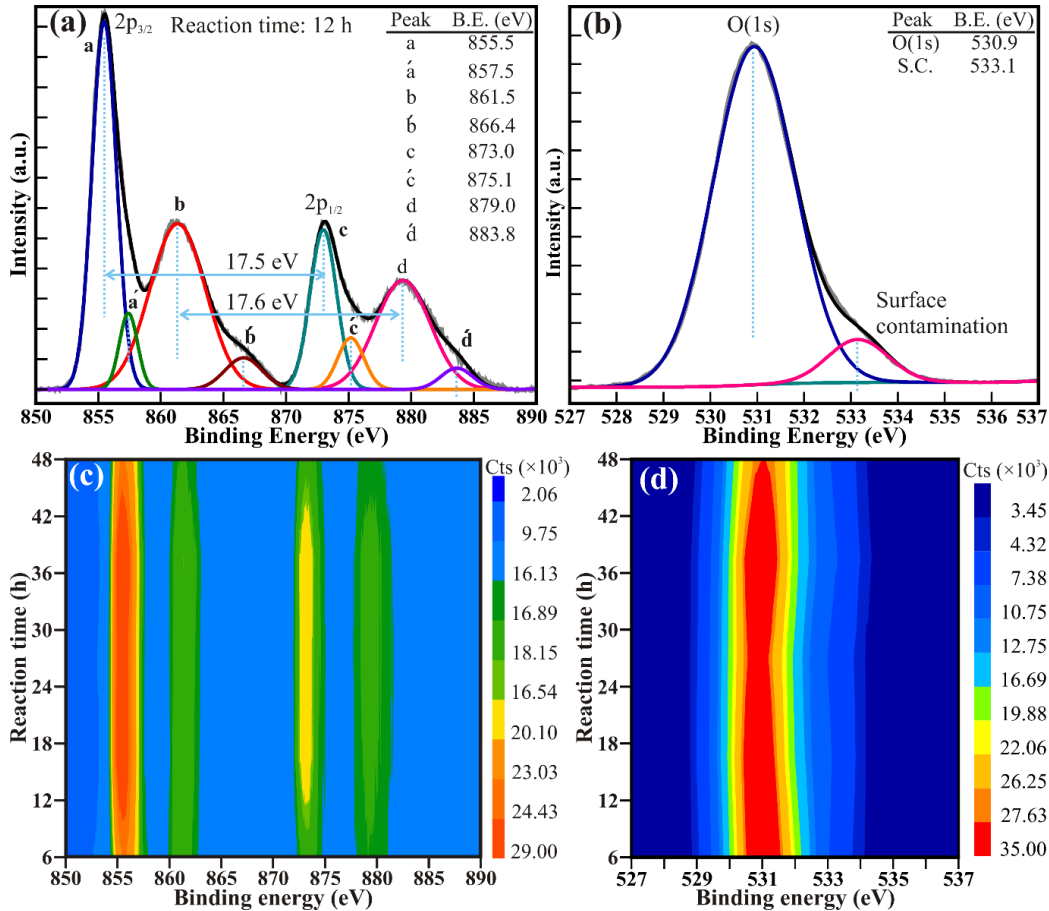


Figure 3.5. XPS peak intensity contours of the (a) Ni(2p) and (b) O(1s) core levels obtained for the reaction-time dependent NiO nanostructures. The high-resolution XPS spectra of the (c) Ni(2p) and (d) O(1s) core levels of the NiO nanobelts synthesized at a reaction time of 12 h. The XPS spectra were deconvoluted using the Voigt curve fitting function.

XPS was employed to understand the effect of reaction time on the chemical stoichiometry and electronic states of NiO nanostructures. Figure 3.5 shows the XPS analysis of time-dependent morphology controlled NiO films, nanobelts, and nanoflakes. Figure 3.5(a) shows the intensity contour plots of Ni(2p) core levels for the samples synthesized at various reaction times. The four distinctive peaks identified as a, b, c, and d are located at the binding energy of 855.5, 861.5, 873.0, and 879.0 eV. Highly intense two peaks (i.e., a \equiv 855.5 eV and c \equiv 873.0 eV) are assigned to the Ni(2p) core levels, and the other two (i.e., b

$\equiv 861.5$ and $d \equiv 879.0$ eV) are their respective shake-up satellite peaks. The double peak features of Ni(2p) along with their concomitant shake-up satellite peaks revealed the paramagnetic chemical states of Ni²⁺. [13] Figure 3.5(b) shows the intensity contour plot of the O(1s) core level. A broad peak located at a binding energy of 530.9 eV is accompanied by the adjacent smaller shoulder peak located at 533.1 eV and are assigned to the O(1s) core-level and surface contamination, respectively.

The peak position of Ni(2p) core level and O(1s) remain akin to each other independent of reaction time. Even though the variation in reaction time has transformed the NiO thin film of irregular morphologies to nanobelts and further to nanoflakes morphology, it has not laded for the alteration in the stoichiometric of NiO. Further, the Ni(2p) and O(1s) high-resolution XPS spectra of mesoporous nanobelts shown in Figure 3.5(c and d), respectively, were deconvoluted using the Voigt curve fitting function within the Sherly background to confirm their electronic states and chemical stoichiometry. The double peak feature of Ni(2p_{3/2}) and Ni(2p_{1/2}) in Figure 3.5(c) represents the Ni(2p) core level of mesoporous nanobelts and revealed the presence of the concomitant shake-up satellite peaks.

The close observation of deconvoluted XPS spectra show the presence of eight peaks in total identified as a, a', b, b', c, c', and d, d' at the binding energy of 855.5, 857.5, 861.5, 866.4, 873.0, 875.1, 879.0, and 883.8 eV, respectively, are assigned to Ni²⁺(2p_{3/2}), Ni³⁺(2p_{3/2}), Ni²⁺(2p_{3/2} Shake-up satellite), Ni³⁺(2p_{3/2} Shake-up satellite), Ni²⁺(2p_{1/2}), Ni³⁺(2p_{1/2}), Ni²⁺(2p_{1/2} Shake-up satellite), and Ni³⁺(2p_{1/2} Shake-up satellite), respectively. A highly intense peak of the Ni²⁺(2p_{3/2}) core level of Ni²⁺ cations confirms the presence of stoichiometric NiO nanobelts. However, the peak observed at ~ 2.0 (± 0.1) eV higher in binding energy than that of Ni²⁺(2p_{1/2}) peak is assigned to the Ni³⁺(2p_{3/2}) core level of Ni³⁺ cations. The intensities and area of the Ni(2p_{1/2}) and Ni(2p_{3/2}) peaks of the Ni²⁺ cations are much higher than those assigned to the Ni³⁺ cations confirmed that the mesoporous nanobelts are composed of stoichiometric NiO extensively, while non-stoichiometric Ni₂O₃ could be a subsidiary phase with minor traces. The energy separation of 17.5 (± 0.1) eV between the Ni(2p_{1/2}) and Ni(2p_{3/2}) peaks

and their shake-up satellite peaks remain unaffected. These observations are akin to that reported for NiO branchlike nanocrystals, [25] nanorods and thin films, [13] nanoflakes assembled 3D flowers, [21] hierarchical nanotubes, [26] and ultrathin porous nanoflakes morphologies. [23] Likewise, the O(1s) XPS spectrum shows the perfect fit to two peaks located at a binding energy of 530.0 and 533.1 eV, respectively. The highly intense lower binding energy peak at 530.0 eV corresponds to the O(1s) core level of O²⁻ anions associated with the stoichiometric NiO. However, the less intense higher binding energy peak at 533.1 eV attributed to the surface contaminations, [4,8,27-29] such as nickel hydroxide along with sub-oxidized Ni, [25,30] and defects sites on the surface [31] of mesoporous nanobelts. The peak intensity of both resolved peaks and area under curves for O(1s) and SC peak indicates the dominance of NiO over Ni₂O₃. Moreover, the absence of the independent peak at a binding energy of 531.2 eV assigned to Ni³⁺ ions [32,33] in the decomposed O (1s) XPS spectrum confirmed the absence of Ni₂O₃ in the nanobelts. Moreover, the binding energy difference (ΔE) of 324.6 eV between the Ni(2p_{3/2}) and O(1s) is very close to that of 322.8 eV for NiO and significantly smaller than 326.2 eV for Ni₂O₃, and larger than the pure metallic Ni (i.e., 321.7 eV). [13] These observations confirmed that the mesoporous nanobelts composed of stoichiometric NiO would improve the specific capacitance, energy density, and power density of the supercapacitor.

3.3.5 Electrochemical analysis

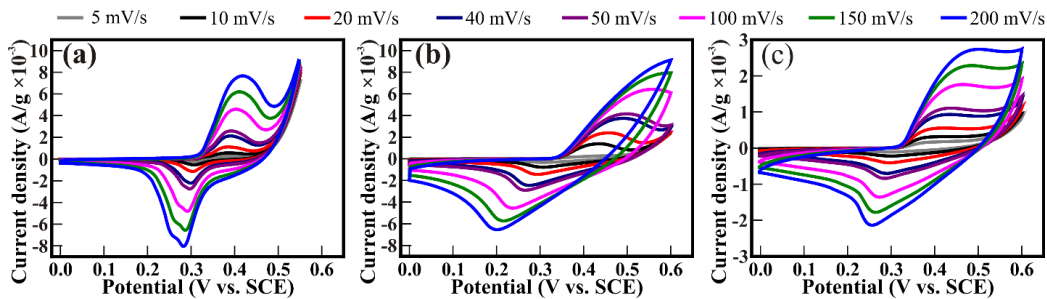
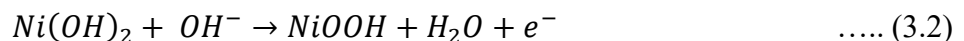


Figure 3.6. CV curves of NiO (a) thin film, (b) mesoporous nanobelts, and (c) nanoflakes at various scan rates.

The electrochemical properties of the morphology controlled NiO thin films, mesoporous nanobelts, and nanoflakes as electrode materials for

supercapacitor were confirmed from CV, GCD, and EIS measurements. CV measurements were performed in a 2M KOH aqueous electrolyte within the potential range of between 0 to 0.6 V at various scan rates (i.e., 5 to 200 mV/s). Figure 3.6 shows the cyclic voltammograms of the NiO thin film, mesoporous nanobelts, and nanoflakes synthesized at a reaction time of 6, 12, and 48 h, respectively (Figure 3.7 for nanoflakes obtained at 18 and 24 h). The CV graphs show a distinct pair of cathodic and anodic peaks independent of variation in the scan rate. The positive and negative current densities observed in the operating potential range of 0 to 0.6 V elucidate oxidation and reduction of the NiO nanostructures, respectively. Relatively more positive current density is observed than that of negative current density (i.e., the difference in current density) for the thin film and nanoflakes morphologies, which is a bit larger in the mesoporous nanobelts. The improved surface area of the nanostructures acts as a trap for ions passing through. The mesoporous nanobelts provided a relatively larger surface area than the thin film and nanoflakes and, hence, could possibly deliver large numbers of trap levels. Trapping-detrapping of free electrons/holes improves the ionic conductivity and consequence in more positive current density for mesoporous nanobelts. The variation in the scan rate exhibits the negligible shifting in the peak positions for the mesoporous nanobelts and nanoflakes synthesized at various reaction times. However, the intensity has enhanced with an increase in the scan rate. Consequently, the area under the CV graph was improved too. On the other hand, the current density has decreased significantly from nanobelts to nanoflakes morphology attained with the increased reaction time from 6 to 48 h (Figure 3.6 & 3.7). The redox reaction mechanism of NiO in an aqueous KOH is a two-step process, involves the reaction of OH⁻ ions followed by the formation of hydroxide layer of Ni(OH)₂ to attend the thermodynamic equilibrium, a typical characteristic of a pseudocapacitor. The reaction mechanism for the formation of hydroxide and an oxy-hydroxide layer of Ni is given as



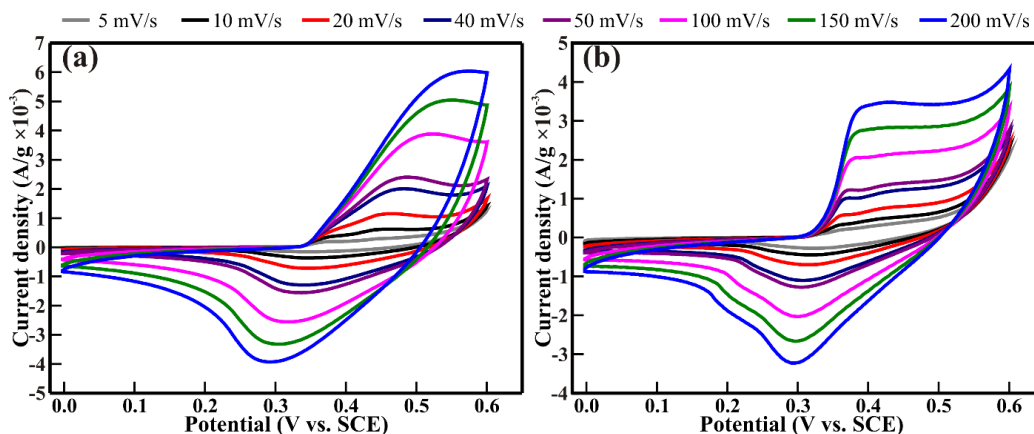


Figure 3.7. CV curves of the nanoflakes obtained at a reaction time of (a) 18 and (b) 24 h.

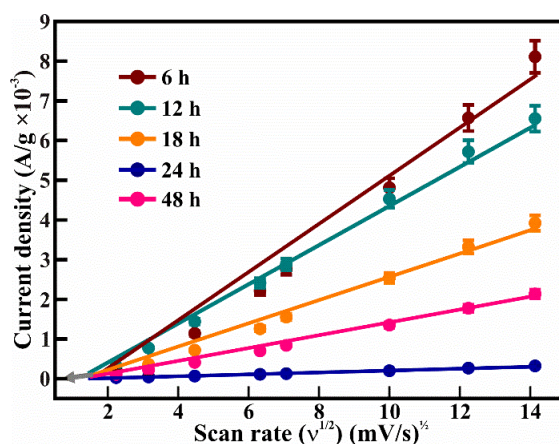


Figure 3.8. The variation of the peak current density (i_p) of the anodic reduction peak with the square root of the scan rate ($v^{1/2}$) observed in CV curves.

The surface area accessible for the ion to contribute to the charge storage mechanism is more abundant in the nanobelts than nanoflakes. The vertical alignment of mesoporous nanobelts provided significantly porous enlarged thin film (Figure 3.2(e)) than that of nanoflake (Figure 3.2(f)). Moreover, the interlocked emergence of nanoflakes forms dense and compressed film might be accountable for the inattentive accessibility of ions.

The variation in the current density of the peaks can be well estimated from the Randles-Sevcik equation,

$$i_p = 2.69 \times 10^5 C_o n^{3/2} \nu^{1/2} D^{1/2} \quad \dots(3.3)$$

Where, i_p is the current density (mA/g), C_o is the concentration of OH^- ions in the electrolyte (mol/cm^2), n is the number of electrons, v is the scan rate (mV/s), and D is the diffusion coefficient of the OH^- ions in the electrode. The dependence of anodic peak current density on the scan rate (Figure 3.8) shows linear behavior. The extrapolated (dotted line) line passing through the origin confirms the diffusion-controlled insertion and deinsertion of OH^- ions along the surface of NiO nanostructures. [4,34]

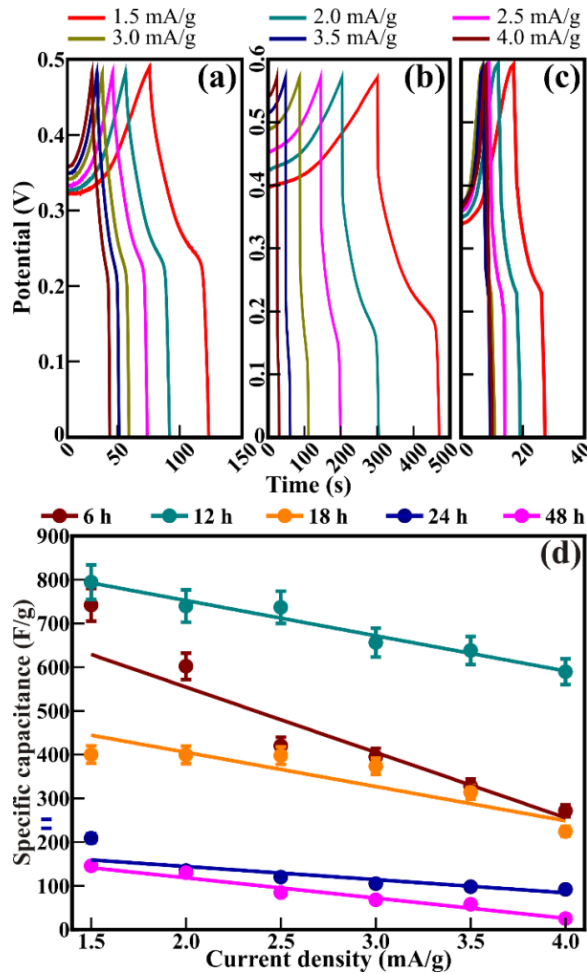


Figure 3.9. GCD curves of NiO (a) thin film, (b) mesoporous nanobelts, and (c) nanoflakes at various current densities. (d) Graph of current density dependent variation in the specific capacitance of thin films, mesoporous nanobelts, and nanoflakes prepared at various reaction times of 6, 12, 18, 24, and 48 h, respectively.

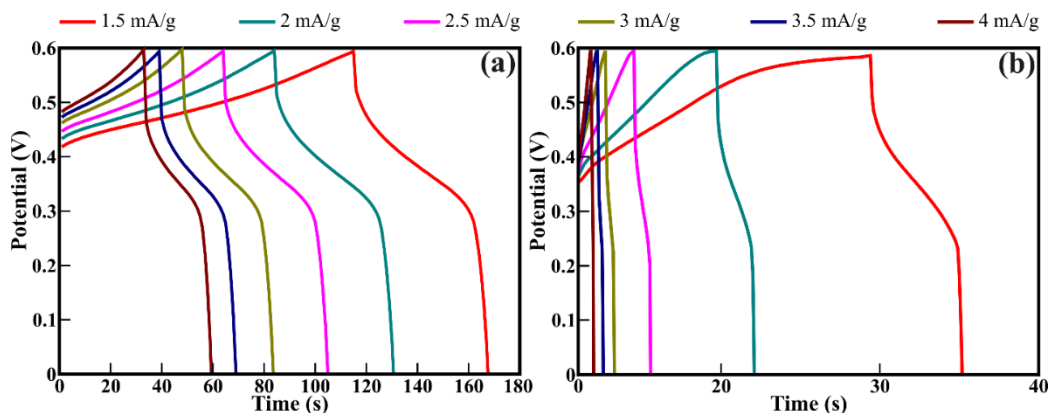


Figure 3.10. GCD curves of NiO nanoflakes synthesized at a reaction time of (a) 18 and (b) 48 h, respectively, at various current densities.

The current density significantly influences the ion exchange mechanism of the working electrode. The GCD at various current densities of 1.5, 2, 2.5, 3, 3.5, and 4 mA/g is shown in Figure 3.9 illustrates declined charging-discharging time with an increase in the current density. The variation in the GCD curves of NiO thin film (Figure 3.9(a)), mesoporous nanobelts (Figure 3.9(b)), and nanoflakes (Figure 3.9(c)) confirm that the charging curve is not entirely symmetric with discharging counterparts. The charging-discharging time (@1.5 mA/g) of ~76 and ~47 s observed for NiO thin film has increased further (~301 and ~170 s) for mesoporous nanobelts but reduced prominently to 17 and 10 s in the case of nanoflakes. The charging-discharging time for nanoflakes prepared at a reaction time of 18 and 24 h was ~115 and ~54 s, ~28 and ~11 s, respectively (Figure 3.10). This reduction tendency is followed for all current densities under investigation since the ion accessibility is limited to the surface.

The specific capacitance (C_s) of the NiO thin film, mesoporous nanobelts, and nanoflakes shown in Figure 3.9(d) is calculated from GCD curves at different current densities using the equation

$$C_s = I \cdot dt / m \cdot dV \quad \dots\dots\dots(3.4)$$

Where, C_s (\equiv F/g) is the specific capacitance of the NiO nanostructures, I (\equiv A) is the applied current, m (\equiv g) is the mass of the active material (i.e., NiO) on the working electrode, and dV/dt (\equiv V/s) is the slope of the discharge curve. The value of C_s reduced linearly with the enhancement of current densities. Higher C_s of

~794 F/g is obtained at a current density of 1.5 mA/g for mesoporous nanobelts than that of the thin film (~742 F/g) and nanoflakes (i.e., ~146 F/g). Moreover, the C_s of ~794 F/g obtained (at a current density of 1.5 mA/g) for mesoporous nanobelts is retained to ~590 F/g after increasing the current density to 4 mA/g. The 25% reduction in the C_s of NiO nanobelts is relatively excellent than that ascertained for vertically aligned NiO nanorods, and 2D thin films [13] randomly distributed NiO nanorods [35] and template-assisted NiO nanotubes. [36] It also corroborates the reversible ion transport along the textural boundaries on the mesoporous nanobelts. OH^- ions propagate effectively to the entire accessible surfaces at a lower current density and suffers from diffusing insider surface at higher current density. Moreover, the maximum diffusion of OH^- ions through the inner walls/surface of the mesoporous nanobelts ensures the proceeding of efficient faradic reactions for energy storage. Nevertheless, at high current density, OH^- ions easily diffuse along the outer and easily accessible surface of NiO nanostructures. The largest reduction of ~ 65 % in C_s was observed for NiO nanoflakes, and the irregular morphological thin film is akin to the hydrothermally synthesized nanoporous pine-cone structured NiO powder. [10] Nevertheless, it is relatively better than the reduction (i.e., 70%) observed for NiO nanoflakes calcinated at 300 °C in CTAB surfactant. [17] The increased asymmetric of the charging and discharging curves and the larger reduction in C_s for NiO nanoflakes substantiate the irreversible kinetics of OH^- ions relative to the NiO nanobelts. Moreover, the small voltage drop at the initial stage of discharge suggests effective charge transfer kinetics. [10,13] The close compact nature of the irregularly shaped nanostructures and nanoflakes offered resistance for the diffusion path of the OH^- ions and resulted in the enormous reduction in the values of C_s with an increase in the current density. Overall, the enhanced C_s of NiO nanobelts is attributed to the improved diffusion of OH^- ions over the enormous accessible surface by virtue of their mesoporous nature. The C_s value of ~794 F/g achieved for mesoporous NiO nanobelts is significantly larger than the values reported for microwave assisted NiO nanoflakes (i.e., 209 F/g). [16] pine-cone structured nanoporous NiO powder (i.e., 337 F/g), [10] NiO nanotubes (i.e. ~80

F/g), [9] agglomerated MnO₂ nanoparticles (i.e. 258.7 F/g), [5] NiO nanoflowers (i.e. 364 F/g), [37] spray deposited NiO thin film (i.e. 405 F/g), [38] 2D NiO nanosheets (i.e. 407 F/g), [15] cobalt oxide aerogels (i.e. 623 F/g), [6] anodized-brass-templated NiO nanostructures (i.e. ~91 F/g), [39] tailor-made porous NiO nanotubes (i.e. 675 F/g), [26] NiO nanosheets obtained with trisodium citrate assisted route (i.e. 463 F/g), [14] and porous hollow nanospheres of NiO nanosheets (i.e. 560 F/g); [40] but akin to the active carbon templated NiO mesoporous structure over Ni-gauge (i.e., 805 F/g), [41] and 1D NiO nanorods (i.e., 746 F/g). [13] Moreover, NiO nanocolumns composed of stacking porous 2D NiO nanoplates (i.e., 285 F/g) derived from annealing Ni(OH)₂ nanoslices (i.e., 176 F/g) delivered C_s of 390 F/g. [42] The increased textural boundaries and the contact resistance between successive nanoplates in the nanocolumns perhaps restricted the C_s, which is circumvented in the largely extended mesoporous NiO nanobelts obtained in the present study. Even though Zhang et al. [43] reported the C_s of 960 F/g for the porous NiO film obtained from solvothermal synthesis, the selection of restricted potential window for electrochemical investigations might be one of the sources for this inflated value. Furthermore, it is reasonably better than the NiO@MnO₂ core-shell nanocomposites (i.e., 266.7 F/g), [7] shranked/wrinkled Co₃O₄/NiO nanofilms (i.e., 565 F/g), [44] two-dimensional NiO nanosheets hybridized with NiS nanoparticles (i.e., ~387 F/g), [45] and heterostructures of α -Fe₂O₃ nanorods supporting NiO nanosheets (i.e., 361 F/g). [46] Moreover, the C_s of the core-shell structure of NiO spheres with Co₃O₄ (i.e., 510 F/g) did not improve due to the polycrystalline nature of hollow NiO spheres composed of nanoparticulated nanowires. [47] Though micro-polyhedrons of NiO-ZnO delivered C_s of ~643 F/g, at higher current density, the porous micropolyhedrons structure collapsed with the diffusion of ions and further reduced drastically. [20] Nevertheless, the carbon known for delivering higher C_s values than metal oxide, not upsurge the supercapacitive performance after forming the core-shell structure in amorphous form along the NiO nanofibers (i.e., 288 F/g), [19] owing to its swelling and shrinkage during electrochemical diffusion of ions. The La³⁺ ions expected to serve as ion buffering reservoirs

created remarkable crystal defects by replacing Ni atoms in the lattice and restricted the C_s of NiO nanospheres to 253 F/g. [12] Likewise, V doped NiO porous structure delivered C_s of 386 F/g. [48] This indicates that the mesoporous and perforated NiO nanobelts are more suitable as an electrode material to achieve ultra-high rate C_s , rather than creating defected porous structure after doping of ions.

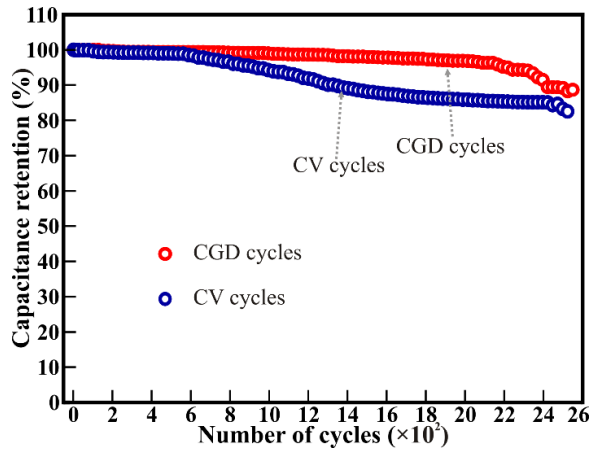


Figure 3.11. Cycling stability and capacitance retention of perforated mesoporous NiO analyzed from CV at scan range of 100 mV/s, and GCD at the current density of 4 mA/g. The percentage indicated the C_s retention with the consistent increment in the number of cycles.

The longer cyclic stability, better lifetime, and durability are important aspects for the performance of the supercapacitor. The mesoporous perforated NiO nanobelts were tested at a scan rate of 100 mV/s (CV cycles) and the current density of 4 mA/g (GCD cycles) for 2500 cycles, respectively (Figure 3.11). The C_s values obtained from CV measurements illustrate long-term stability with only 17.5 % drop after 2500 continuous charging-discharging cycles. Likewise, C_s values measurements were accomplished for 2500 galvanostatic continuous charging-discharging cycles. Significantly, perforated mesoporous NiO nanobelts exhibit only 11.4 % reduction after 2500 continuous GCD cycles, have excellent electrochemical cyclic stability. This 88.6 % retention of C_s of NiO nanobelts after 2500 cycles is much better than the values of NiO pine-cone nanostructures (i.e., 92 % after 100 cycles), [10] NiO nanotubes (i.e., ~55 % after 1000 cycles), which

were further converted in to Ni@NiO core-shell nanoparticle tube array (i.e., ~90 % after 1000 cycles) via template-assisted electrodeposition method, [36] NiO@MnO₂ core-shell nanocomposites (81.7 % after 2000 cycles) composed of NiO porous microtubes (77.4 % after 2000 cycles) and MnO₂ nanosheets (73.5 % after 2000 cycles), [7] nanocrystalline NiO-CeO₂ binary oxide composites (~86 % after 1200 cycles), [49] porous and 3D nanostructures of electrodeposited Ni(OH)₂ forming 200 nm layer on nickel foam (52 % after 300 cycles), [50] and mesoporous layered hexagonal platelets of Co₃O₄ nanoparticles (~81 % after 2020 cycles). [2] Moreover, it is akin to the cyclability and capacitance retention of mesoporous NiO nanoarrays (~89.6 %) prepared by self-generated sacrificial template approach of ZnO/NiO, where ZnO removed by an alkali etching method. [51] The perforated mesoporous morphology of NiO nanobelts experiences the least structural damage and a crystallographic modification during repetitive and continuous insertion and extraction of OH⁻ ions. The excellent electrochemical stability and long cycle life of NiO nanobelts in the KOH electrolyte are ascribed to their perforated mesoporous nanostructure morphology, larger surface area, clearly visible textural boundaries, interconnecting network, and well separated vertical alignment.

3.3.7 Electrochemical Impedance Spectroscopy

The electrical properties and textural boundaries of active material along with the electrolyte play a critical role in the electrochemical charge storage mechanism. Therefore, EIS measurements were performed to understand the involvement of surface morphology and its resistance in the electron transfer and diffusion of the ion. Typical Nyquist plots of the NiO nanobelts and nanoflakes at an applied electrochemical potential of 0.3 V are shown in Figure 3.12. Each EIS spectra consists of a semicircle at a higher frequency followed by a straight line at a lower frequency. The semicircle at a higher frequency region represents the interfacial electron-transfer resistance (R_{ct}), and the relatively straight line at the lower frequency region is assigned to the ion diffusion resistance (i.e., Warburg resistance, Z_w). The intercept of the semicircle yields the electrolyte resistance (R_e). The smaller semicircle observed for the mesoporous NiO nanobelts than

nanoflakes obtained at a reaction time of 24 and 48 h confirms that the nanobelts offer the lowest charge-transfer resistance at the interface. Moreover, the reduced diameter of the semicircle corroborates the improvement in the values of C_s . Likewise, the slope of the straight line observed in the lower frequency region has reduced from nanobelts to nanoflakes. The highest slope observed for NiO nanobelts implies the lower diffusion resistance of OH^- ions along the accessible surface and the textural boundaries of the perforated mesoporous NiO nanobelts. These observations are found supportive of the calculated values of C_s . Moreover, the nature of EIS spectra is in accordance with those illustrated for amorphous carbon-coated NiO nanofibers, [19] hierarchical bulk nanostructured NiO micro bouquets with trimodal pore size, [52] electrospun NiO nanofibers, [53] ZnO-NiO micro-polyhedrons, [20] and hierarchical NiO nanoflakes coated CuO flowers. [18] The lower diffusion and charge-transfer resistance of the NiO nanobelts contributed to the enhanced electrochemical performance.

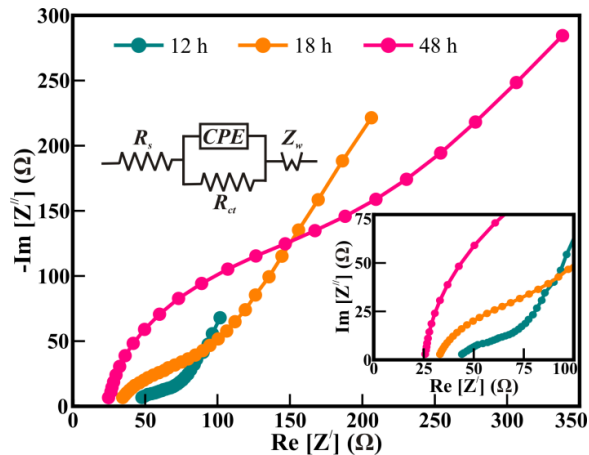


Figure 3.12. Nyquist plot of the mesoporous nanobelts and nanoflakes (prepared at a reaction time of 18 and 48 h) acquired at a potential of 0.30 V. Inset shows the best fitted equivalent circuit model and the expanded high-frequency region of the EIS spectra.

3.3.8 Ragone Plot

The Ragone plot, the correlation between energy and power density, was utilized to evaluate the overall performance of the NiO nanostructures. Figure 3.13 shows the Ragone plot for the NiO nanostructures. The power density of 563

W/kg obtained (at a current density of 4 mA/g) for NiO thin film of irregular morphologies enhanced further to 2963 W/kg for the perforated mesoporous NiO nanobelts. The alteration of nanobelts to nanoflakes conceived the power density in the range of 1896 to 2043 W/kg. Furthermore, the maximum largest energy density of 57 Wh/kg gained for mesoporous NiO nanobelts was reduced to 8 Wh/kg for nanoflake morphology formed at a reaction time of 48 h. Thus, perforated mesoporous NiO nanobelts achieved the maximum power and energy density of 2963 W/kg and 33 Wh/kg, respectively, at a higher current density of 4 mA/g. This confirms that the perforated mesoporous NiO nanobelts possess higher energy and power density than compactly arranged nanoflakes. The energy density of NiO nanobelts is significantly higher compared to the ultrathin porous NiO nanoflakes, [23] 1D nanorods and 2D thin-films of NiO (i.e., 11.93 Wh/kg), [13] porosity tuned NiO nanowalls/nanoflakes (i.e., 12.9 Wh/kg), [22] electrospun NiO fibers (i.e., 20 Wh/kg), [11] hierarchical NiO micro bouquets (i.e., 17 Wh/kg), [52] hierarchical NiO mesocrystals with cuboctahedral morphology (i.e., 18 Wh/kg), [54] coral-like nanoporous β -Ni(OH)₂ nanobars (i.e., 25.9 Wh/kg), [55] and porous hollow NiO spheres composed of nanosheets (i.e., 19.44 Wh/kg). [40] Hierarchical 3D NiO microflowers constructed of 2D ultrathin nanosheets and visualized as an interlaced network of 1D nanowires appeared to be promising electrode materials; nevertheless, 3D NiO microflowers delivered a much smaller energy density (i.e., 15.9 Wh/kg) than the present perforated mesoporous NiO nanobelts, might be owing to their isolated flower-like appearance and discontinues ion traveling paths. [24] On the other hand, the energy density of mesoporous NiO nanobelts is also competitively greater than those observed for the asymmetric supercapacitor composed of NiO/NiCo₂O₄ nanosheets (i.e., 25.99 Wh/kg), [15] NiO/Ni₃S₂ hetero-nanosheets (i.e., 26.3 Wh/kg), [33] ultrathin porous NiO nanoflakes with reduced GO (i.e., 30.7 Wh/kg), [23] ZnO/NiO hybrid nanoarrays (i.e., 50.6 Wh/kg), [51] and corn flake like NiO nanostructure hybridized with activated carbon (i.e., 16 to 44 Wh/kg). [56] The improved energy and power density of NiO nanobelts are attributed to the well established interconnecting network, highly perforated mesoporous

morphology, large accessible surface area, well-aligned textural boundaries, and individual dispersion of nanobelt; altogether highly favored for easy admittance for ion diffusion in depth.

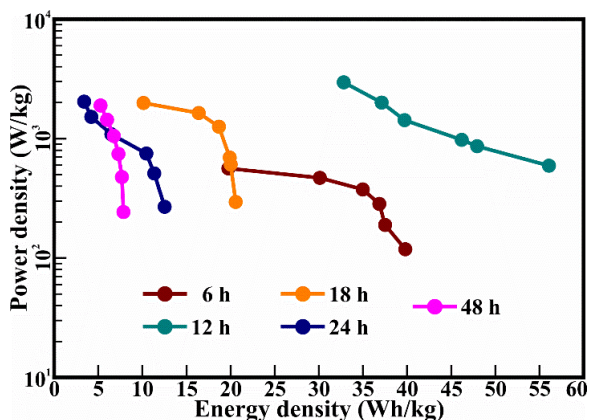


Figure 3.13. Ragone plot of thin films composed of irregular morphologies, perforated mesoporous nanobelts, and nanoflakes (obtained at reaction times of 18, 24, and 48 h) of NiO determined at various current densities.

3.4 Conclusion

The perforated mesoporous NiO nanobelts and nanoflakes synthesized on conducting glass substrates employing a controlled hydrothermal approach. The width of the perforated mesoporous NiO nanobelts (i.e., ~74 nm) increased to ~215 nm and lead to the formation of nanoflakes. The variation in the morphology delivered the thin film of thickness ~5.8 & 2.7 μm , respectively. The XPS analysis revealed that the alteration of morphology from nanobelts to nanoflakes had not altered the stoichiometry of the NiO. The average pore size distribution of ~19.7 nm and larger specific surface area of 40.572 m^2/g of the perforated mesoporous NiO nanobelts provided larger surface-active sites and facilitated the significant diffusion of OH^- ions and transfer of charges. The mesoporous NiO nanobelts showed excellent GCD performance in an aq. KOH electrolyte and delivered C_s of 794 F/g, power density of 2963 W/kg, energy density of 57 Wh/kg, and higher stability with retention of 88.6 % after continuous 2500 charging-discharging cycle. The interconnecting network of well-aligned perforated mesoporous NiO nanobelts provided excellent electrochemical reversibility and propose its potential as electrode materials for the supercapacitor with ultra-high-rate capabilities. Overall, the controlled approach of transforming mesoporous nanobelts from irregular morphologies

and further converting them to the 2D nanoflakes has opened a new path towards improving the charge storage mechanism for supercapacitor and its implementation in the hybrid supercapacitor.

3.5 References

- [1.] Devan R. S., Patil R. A., Lin J. H., Ma Y. R., (2012), One-dimensional metal-oxide nanostructures: recent developments in synthesis, characterization, and applications, *Adv. Funct. Mater.*, 22, 3326-3370, (DOI: 10.1002/adfm.201201008).
- [2.] Bhojane P., Sinha L., Devan R. S., Shirage P. M., (2018), Mesoporous layered hexagonal platelets of Co_3O_4 nanoparticles with (111) facets for battery applications: high performance and ultra-high rate capability, *Nanoscale*, 10, 1779-1787, (DOI: 10.1039/c7nr07879j).
- [3.] Wu Z. S., Parvez K., Feng X. L., Mullen K., (2013), Graphene-based in-plane micro-supercapacitors with high power and energy densities, *Nat. Commun.*, 4, 2487, (DOI: 10.1038/ncomms3487).
- [4.] Devan R. S., Ma Y. R., Patil R. A., Lukas S. M., (2016), Highly stable supercapacitive performance of one-dimensional (1D) brookite TiO_2 nanoneedles, *RSC Adv.*, 6, 62218-62225, (DOI: 10.1039/c6ra11348f).
- [5.] Zhang Y., Li G. Y., Lv Y., Wang L. Z., Zhang A. Q., Song Y. H., Huang B. L., (2011), Electrochemical investigation of MnO_2 electrode material for supercapacitors, *Int. J. Hydrog. Energy*, 36, 11760-11766, (DOI: 10.1016/j.ijhydene.2011.06.020).
- [6.] Wei T. Y., Chen C. H., Chang K. H., Lu S. Y., Hu C. C., (2009), Cobalt oxide aerogels of ideal supercapacitive properties prepared with an epoxide synthetic route, *Chem. Mater.*, 21, 3228-3233, (DOI: 10.1021/cm9007365).
- [7.] Chen J. J., Huang Y., Li C., Chen X. F., Zhang X., (2016), Synthesis of $\text{NiO}@\text{MnO}_2$ core/shell nanocomposites for supercapacitor application, *Appl. Surf. Sci.*, 360, 534-539, (DOI: 10.1016/j.apsusc.2015.10.187).
- [8.] Patil R. A., Devan R. S., Lin J. H., Ma Y. R., Patil P. S., Liou Y., (2013), Efficient electrochromic properties of high-density and large-area arrays of one-dimensional NiO nanorods, *Sol. Energy Mater. Sol. Cells*, 112, 91-96, (DOI: 10.1016/j.solmat.2013.01.003).

- [9.] Pang H., Lu Q. Y., Lia Y. C., Gao F., (2009), Facile synthesis of nickel oxide nanotubes and their antibacterial, electrochemical and magnetic properties, *Chem. Commun.*, 48, 7542-7544, (DOI: 10.1039/b914898a).
- [10.] Meher S. K., Justin P., Rao G. R., (2010), Pine-cone morphology and pseudocapacitive behavior of nanoporous nickel oxide, *Electrochim. Acta*, 55, 8388-8396, (DOI: 10.1016/j.electacta.2010.07.042).
- [11.] Zhang Y., Park M., Kim H. Y., Park S. J., (2017), Moderated surface defects of Ni particles encapsulated with NiO nanofibers as supercapacitor with high capacitance and energy density, *J. Colloid Interface Sci.*, 500, 155-163, (DOI: 10.1016/j.jcis.2017.04.022).
- [12.] Han D. D., Jing X. Y., Wang J., Yang P. P., Song D. L., Liu J. Y., (2012), Porous lanthanum doped NiO microspheres for supercapacitor application, *J. Electroanal. Chem.*, 682, 37-44, (DOI: 10.1016/j.jelechem.2012.06.016).
- [13.] Patil R. A., Chang C. P., Devan R. S., Liou Y., Ma Y. R., (2016), Impact of nanosize on supercapitance: study of 1D nanorods and 2D thin-films of nickel oxide, *ACS Appl. Mater. Interfaces*, 8, 9872-9880, (DOI: 10.1021/acsami.6b00487).
- [14.] Han D. D., Xu P. C., Jing X. Y., Wang J., Yang P. P., Shen Q. H., Liu J. Y., Song D. L., Gao Z., Zhang M. L., (2013), Trisodium citrate assisted synthesis of hierarchical NiO nanospheres with improved supercapacitor performance, *J. Power Sources*, 235, 45-53, (DOI: 10.1016/j.jpowsour.2013.01.180).
- [15.] Zhang L. X., Zheng W. H., Jiu H. F., Ni C. H., Chang J. X., Qi G. S., (2016), The synthesis of NiO and NiCo₂O₄ nanosheets by a new method and their excellent capacitive performance for asymmetric supercapacitor, *Electrochim. Acta*, 215, 212-222, (DOI: 10.1016/j.electacta.2016.08.099).
- [16.] Babu G. A., Ravi G., Mahalingam T., Kumaresavanji M., Hayakawa Y., (2015), Influence of microwave power on the preparation of NiO nanoflakes for enhanced magnetic and supercapacitor applications, *Dalton Trans.*, 44, 4485-4497, (DOI: 10.1039/c4dt03483j).
- [17.] Vijayakumar S., Nagamuthu S., Muralidharan G., (2013), Supercapacitor studies on NiO nanoflakes synthesized through a microwave route, *ACS Appl. Mater. Interfaces*, 5, 2188-2196, (DOI: 10.1021/am400012h).

- [18.] Huang M., Li F., Zhang Y. X., Li B., Gao X., (2014), Hierarchical NiO nanoflake coated CuO flower core-shell nanostructures for supercapacitor, *Ceram. Int.*, 40, 5533-5538, (DOI: 10.1016/j.ceramint.2013.10.143).
- [19.] Shin D. H., Lee J. S., Jun J., Jang J., (2014), Fabrication of amorphous carbon-coated NiO nanofibers for electrochemical capacitor applications, *J. Mater. Chem. A*, 2, 3364-3371, (DOI: 10.1039/c3ta14900e).
- [20.] Pang H., Ma Y. H., Li G. C., Chen J., Zhang J. S., Zheng H. H., Du W. M., (2012), Facile synthesis of porous ZnO-NiO composite micropolyhedrons and their application for high power supercapacitor electrode materials, *Dalton Trans.*, 41, 13284-13291, (DOI: 10.1039/c2dt31916k).
- [21.] Liu X., Liu F., (2018), Nanoflakes-assembled 3D flower-like nickel oxide/nickel composites as supercapacitor electrode materials, *Eur. J. Inorg. Chem.*, 8, 987-991, (DOI: 10.1002/ejic.201701306).
- [22.] Mondal M., Das B., Howli P., Das N. S., Chattopadhyay K. K., (2018), Porosity-tuned NiO nanoflakes: effect of calcination temperature for high performing supercapacitor application, *J. Electroanal. Chem.*, 813, 116-126, (DOI: 10.1016/j.jelechem.2018.01.049).
- [23.] Wu S. X., Hui K. S., Hui K. N., Kim K. H., (2016), Ultrathin porous NiO nanoflake arrays on nickel foam as an advanced electrode for high performance asymmetric supercapacitors, *J. Mater. Chem. A*, 4, 9113-9123, (DOI: 10.1039/c6ta02005d).
- [24.] Ci S. Q., Wen Z. H., Qian Y. Y., Mao S., Cui S. M., Chen J. H., (2015), NiO-microflower formed by nanowire-weaving nanosheets with interconnected Ni-network decoration as supercapacitor electrode, *Sci. Rep.*, 5, 11919, (DOI: 10.1038/srep11919).
- [25.] Liu D., Li D. S., Yang D. R., (2017), Size-dependent magnetic properties of branchlike nickel oxide nanocrystals, *AIP Adv.*, 7, 015028, (DOI: 10.1063/1.4974307).
- [26.] Cao F., Pan G. X., Xia X. H., Tang P. S., Chen H. F., (2014), Synthesis of hierarchical porous NiO nanotube arrays for supercapacitor application, *J. Power Sources*, 264, 161-167, (DOI: 10.1016/j.jpowsour.2014.04.103).

- [27.] Devan R. S., Thakare V. P., Antad V. V., Chikate P. R., Khare R. T., More M. A., Dhayal R. S., Patil S. I., Ma Y. R., Schmidt-Mende L., (2017), Nano-heteroarchitectures of two-dimensional MoS₂@ one-dimensional brookite TiO₂ nanorods: prominent electron emitters for displays, ACS Omega, 2, 2925-2934, (DOI: 10.1021/acsomega.7b00345).
- [28.] Chikate P. R., Daware K. D., Gayhane D. S., Ma Y. R., Choudhary R. J., Patil S. I., More M. A., Phase D. M., Gosavi S. W., Shirage P. M., Devan R. S., (2018), Controlled hetero-architectures of Au-nanoparticles-decorated ZnO nanowires for enhanced field electron emission displays, ChemistrySelect, 3, 7891-7899, (DOI: 10.1002/slct.201801282).
- [29.] Chikate P. R., Bankar P. K., Choudhary R. J., Ma Y. R., Patil S. I., More M. A., Phase D. M., Shirage P. M., Devan R. S., (2018), Spitzer shaped ZnO nanostructures for enhancement of field electron emission behaviors, RSC Adv., 8, 21664-21670, (DOI: 10.1039/c8ra03282c).
- [30.] Han S. Y., Lee D. H., Chang Y. J., Ryu S. O., Lee T. J., Chang C. H., (2006), The growth mechanism of nickel oxide thin films by room-temperature chemical bath deposition, J. Electrochem. Soc., 153, C382-C386, (DOI: 10.1149/1.2186767).
- [31.] Zhao B., Ke X. K., Bao J. H., Wang C. L., Dong L., Chen Y. W., Chen H. L., (2009), Synthesis of flower-like NiO and effects of morphology on its catalytic properties, J. Phys. Chem. C, 113, 14440-14447, (DOI: 10.1021/jp904186k).
- [32.] Dalavi D. S., Devan R. S., Patil R. S., Ma Y. R., Kang M. G., Kim J. H., Patil P. S., Electrochromic properties of dandelion flower like nickel oxide thin films, J. Mater. Chem. A, 1, 1035-1039, (DOI: 10.1039/c2ta00842d).
- [33.] Liu S. D., Lee S. C., Patil U. M., Ray C., Sankar K. V., Zhang K., Kundu A., Kang S., Park J. H., Jun S. C., (2017), Controllable sulfuration engineered NiO nanosheets with enhanced capacitance for high rate supercapacitors, J. Mater. Chem. A, 5, 4543-4549, (DOI: 10.1039/c6ta11049e).
- [34.] Hazzazi O. A., Zaky A. M., Amin M. A., El Rehim S. S. A., (2008), Passivation and Cl⁻ induced depassivation of Cu-Ag alloys in borate buffer solutions, Int. J. Electrochem. Sci., 3, 489-508.

- [35.] Lu Z. Y., Chang Z., Liu J. F., Sun X. M., (2011), Stable ultrahigh specific capacitance of NiO nanorod arrays, *Nano Res.*, 4, 658-665, (DOI: 10.1007/s12274-011-0121-1).
- [36.] Li Q., Liang C. L., Lu X. F., Tong Y. X., Li G. R., (2015), Ni@NiO core-shell nanoparticle tube arrays with enhanced supercapacitor performance, *J. Mater. Chem. A*, 3, 6432-6439, (DOI: 10.1039/c4ta06921h).
- [37.] Yang Y. Y., Liang Y. R., Zhang Z. Y., Zhang Y. D., Wu H. Y., Hu Z. A., (2016), Morphology well-controlled synthesis of NiO by solvothermal reaction time and their morphology-dependent pseudocapacitive performances, *J. Alloys Compds.*, 658, 621-628, (DOI: 10.1016/j.jallcom.2015.10.253).
- [38.] Yadav A. A., Chavan U. J., (2016), Influence of substrate temperature on electrochemical supercapacitive performance of spray deposited nickel oxide thin films, *J. Electroanal. Chem.*, 782, 36-42, (DOI: 10.1016/j.jelechem.2016.10.006).
- [39.] Al-Osta A., Jadhav V. V., Zate M. K., Mane R. S., Hui K. N., Han S. H., (2015), Electrochemical supercapacitors of anodized-brass-templated NiO nanostructured electrodes. *Scri. Mater.*, 99, 29-32, (DOI: 10.1016/j.scriptamat.2014.11.019).
- [40.] Yu W., Jiang X. B., Ding S. J., Li B. Q., (2014), Preparation and electrochemical characteristics of porous hollow spheres of NiO nanosheets as electrodes of supercapacitors, *J. Power Sources*, 256, 440-448, (DOI: 10.1016/j.jpowsour.2013.12.110).
- [41.] Yao M. M., Hu Z. H., Xu Z. J., Liu Y. F., Liu P. P., Zhang Q., (2015), Template synthesis and characterization of nanostructured hierarchical mesoporous ribbon-like NiO as high performance electrode material for supercapacitor, *Electrochim. Acta*, 158, 96-104, (DOI: 10.1016/j.electacta.2014.12.058).
- [42.] Zhang X. J., Shi W. H., Zhu J. X., Zhao W. Y., Ma J., Mhaisalkar S., Maria T. L., Yang Y. H., Zhang H., Hng H. H., Yan Q. Y., (2010), Synthesis of porous NiO nanocrystals with controllable surface area and their application as supercapacitor electrodes, *Nano Res.*, 3, 643-652, (DOI: 10.1007/s12274-010-0024-6).
- [43.] Zhang Y. B., Guo Z. G., (2014), Green synthesis of open porous NiO films with an excellent capacitance performance, *Chem. Commun.*, 50, 3443-3446, (DOI: 10.1039/c3cc47547f).

- [44.] Zuo Y., Ni J. J., Song J. M., Niu H. L., Mao C. J., Zhang S. Y., Shen Y. H., (2016), Synthesis of $\text{Co}_3\text{O}_4/\text{NiO}$ nanofilms and their enhanced electrochemical performance for supercapacitor application, *Appl. Surf. Sci.*, 370, 528-535, (DOI: 10.1016/j.apsusc.2016.02.193).
- [45.] Kim S. Y., Gopi C., Reddy A. E., Kim H. J., (2018), Facile synthesis of a NiO/NiS hybrid and its use as an efficient electrode material for supercapacitor applications, *New J. Chem.*, 42, 5309-5313, (DOI: 10.1039/c7nj05145j).
- [46.] Jiao Y., Liu Y., Yin B. S., Zhang S. W., Qu F. Y., Wu X., (2014), Hybrid $\alpha\text{-Fe}_2\text{O}_3@/\text{NiO}$ heterostructures for flexible and high performance supercapacitor electrodes and visible light driven photocatalysts, *Nano Energy*, 10, 90-98, (DOI: 10.1016/j.nanoen.2014.09.002).
- [47.] Fan M. Q., Ren B., Yu L., Song D. L., Liu Q., Liu J. Y., Wang J. Jing X. Y., Liu L. H., (2015), Facile synthesis of Co_3O_4 nanowires grown on hollow NiO microspheres with superior electrochemical performance, *Electrochim. Acta*, 166, 168-173, (DOI: 10.1016/j.electacta.2015.03.090).
- [48.] Park H. W., Na B. K., Cho B. W., Park S. M., Roh K. C., (2013), Influence of vanadium doping on the electrochemical performance of nickel oxide in supercapacitors, *Phys. Chem. Chem. Phys.*, 15, 17626-17635, (DOI: 10.1039/c3cp52498a).
- [49.] Padmanathan N., Selladurai S., (2014), Electrochemical capacitance of porous NiO- CeO_2 binary oxide synthesized via sol-gel technique for supercapacitor, *Ionics*, 20, 409-420, (DOI: 10.1007/s11581-013-0989-8).
- [50.] Yang G. W., Xu C. L., Li H. L., (2008), Electrodeposited nickel hydroxide on nickel foam with ultrahigh capacitance, *Chem. Commun.*, 48, 6537-6539, (DOI: 10.1039/b815647f).
- [51.] Meng G., Yang Q., Wu X. C., Wan P. B., Li Y. P., Lei X. D., Sun X. M., Liu J. F., (2016), Hierarchical mesoporous NiO nanoarrays with ultrahigh capacitance for aqueous hybrid supercapacitor, *Nano Energy*, 30, 831-839, (DOI: 10.1016/j.nanoen.2016.09.012).
- [52.] Anjali P., Sonia T. S., Shakir I., Nair S. V., Balakrishnan A., (2015), On the synthesis and electrochemical characterization of ordered hierarchical NiO micro

- bouquets with trimodal pore size distribution, *J. Alloys Compds.*, 618, 396-402, (DOI: 10.1016/j.jallcom.2014.08.133).
- [53.] Hosseini S. R., Ghasemi S., Karnali-Rousta M., Nabavi S. R., (2017), Preparation of NiO nanofibers by electrospinning and their application for electro-catalytic oxidation of ethylene glycol, *Int. J. Hydrog. Energy*, 42, 906-913, (DOI: 10.1016/j.ijhydene.2016.09.116).
- [54.] Zheng M. T., Dong H. W., Xiao Y., Hu H., He C. L., Lei B. F., Sun L. Y., Liu Y. L., (2017), Hierarchical NiO mesocrystals with tuneable high-energy facets for pseudocapacitive charge storage, *J. Mater. Chem. A*, 5, 6921-6927, (DOI: 10.1039/c7ta00978j).
- [55.] Li J., Luo F. L., Tian X. Q., Lei Y., Yuan H. Y., Xiao D., (2013), A facile approach to synthesis coral-like nanoporous β -Ni(OH)₂ and its supercapacitor application, *J. Power Sources*, 243, 721-727, (DOI: 10.1016/j.jpowsour.2013.05.172).
- [56.] Kumbhar V. S., Cho M. H., Lee J., Kim W. K., Lee M., Lee Y. R., Shim J. J., (2017), Electrosynthesis of a corn flake-like NiO nanostructure on nickel foam for polymer gel electrolyte-based high performance asymmetric supercapacitors, *New J. Chem.*, 41, 10584-10591, (DOI: 10.1039/c7nj00686a).

Chapter 4

Mesoporous CoTiO₃ nanostructures

We synthesized mesoporous cobalt titanate (CTO) microrods via the sol-gel method as an outstanding working electrode for the supercapacitor. The mesoporous CTO microrods were amassed in hexagonal shapes of an average width of ~670 nm and were composed of nanoparticles of average diameter ~41 nm. The well crystalline CTO microrods of the hexagonal phase to the R3 space group possessed an average pore size distribution of 3.92 nm throughout the microrod. The mesoporous CTO microrods with increased textural boundaries played a vital role in the diffusion of ions, and they provided a specific capacitance of 608.4 F/g and specific power of 4835.7 W/kg and specific energy of 9.77 Wh/kg in an aqueous 2M KOH electrolyte, which was remarkably better than those of Ti, La, Cr, Fe, Ni, and Sr based perovskites or their mixed heterostructures supplemented by metal oxides as an impurity. Furthermore, the diffusion-controlled access to the OH⁻ ions (0.27 μs) deep inside the microrod conveyed the high stability, a long life cycle for up to 1950 continuous charging-discharging cycles, and excellent capacitance retention of 82.3%. Overall, the mesoporous CTO shows its potential as an electrode for a long-cycle supercapacitor and provides opportunities for additional enhancement after developing the core-shell hetero-architecture with other metal oxide materials such as MnO₂ and TiO₂.

4.1 Introduction

The fast growth of the global population and massive industrialization of human civilization have induced enormous pressure on the environment and have also brought forward a severe concern about the energy crisis. Continuous improvement in energy generation and storage is essential to meet worldwide energy challenges for a sustainable supply of low-cost and clean energy. The amalgamation of abundant renewable energies (i.e., biofuels and solar energy) and versatile electrochemical energy conversion and storage devices like supercapacitors, [1] fuel cells, [2] and batteries [3] may offer an ideal energy system for the future. Still, it is not yet functionalized efficiently to serve the need of society. Batteries known for their specific energy fail to provide improved specific power and compete with a supercapacitor. Balancing the specific energy and specific power of supercapacitors is vital to support the daily energy needs and overcome the sudden power loss. The automotive and power electronics industry continues to hint that supercapacitors have the potentials to replace the batteries in the coming future upon reducing the short circuits and self-discharge and maintaining the long cycle lifetime. Therefore, hierarchical and mesoporous hybrid nanostructures have attracted considerable attention due to the largest accessible surface area and good interconnections for energy storage. The pore size and specific surface area accessible for ion diffusion significantly influence the energy storage mechanism.

Nanostructured transition metal oxides have shown tremendous electrochemical performance due to their high surface area and short ion diffusion length than bulk. Among the well-studied various metal oxides such as TiO_2 , MnO_2 , Fe_2O_3 , NiO , Ta_2O_5 , MoO_2 , V_2O_5 , Nb_2O_5 , and Co_3O_4 , [4] the oxide of Co and Ti exhibited decent and long cycling electrochemical performance. [5-8] Among these various pseudocapacitive materials, TiO_2 is widely used in energy storage and conversion, i.e., supercapacitors, Li-ion batteries, solar cells, photocatalysis, and sensors, etc. due to its chemical and thermal stability, high aspect ratio structure, excellent ionic or electronic charge transfer, and wide bandgap, etc., and environmental friendliness. Moreover, TiO_2 resembles the conventional electric double-layer capacitor, which contributes to the non-faradaic mechanism with very low specific capacitance (C_s). [9] Although pristine TiO_2 reveals low electrochemical performance, it shows excellent stability for continuous charging-

discharging of 10,000 cycles [5] than any other metal oxide in its pristine form. Likewise, Co_3O_4 is explored as electrode material for supercapacitors due to its tuneable morphology, chemical and thermal stability, redox activity, and high theoretical C_s . [8] However, very limited efforts are made to utilize the hetero-architectures of TiO_2 and Co_3O_4 as an electrode material for supercapacitor. [9-11] Perovskite, with the generalized formula of ABO_3 (where A and B are Ti and Co), have involved great interest owing to their excellent optical, [12,13] electronic, [14] catalytic, [15] ferroelectric, [12] and magnetic properties. [16] Recently, Imani et al. [17] reported microwave irradiated NiTiO_3 nanoparticles as an electrode for supercapacitor applications. The results indicated an acceptable C_s of 257 F/g at a scan rate of 10 mV/s with a good reversible redox reaction and the capacitance retention of ~ 92 % after 1000 cycles. In addition to this, Pejman et al. [18] synthesized NiMnO_3/C nanocomposite electrode for supercapacitors exhibit C_s of 285 F/g at a current density of 1 A/g and excellent cycling stability with 93.5 % capacitance retention over 1000 cycles. Recently, Huang et al. derived CTO mesoporous micro-prisms from the bimetal-organic framework as anode material for sodium-ion batteries and observed 90.1 % (@ 5 A/g) capacity retention for 2000 cycle in Na^+ ion. [19] However, to the best of our knowledge, literature not reports the utilization of CoTiO_3 as an electrode for supercapacitor. Therefore, we report here the utilization of the CoTiO_3 compound as the electrode for the supercapacitor. Highly porous CTO microrods were synthesized via the sol-gel route. The effect of functional groups on the synthesis of mesoporous CTO microrods is examined by FTIR. The structural properties are analyzed from Raman and X-ray diffraction. The surface morphologies and chemical composition of the CTO microrods were examined using field emission scanning electron microscopy (FESEM) and X-ray photoemission spectroscopy (XPS). The molar ratio dependent diffusion of OH^- ions from aq. KOH electrolyte along the surface of mesoporous CTO rods is examined from the drop shape analyzer. The effect of mesoporous morphology of CTO rods constitute of interconnected nanoparticles on the electrochemical properties of CTO was investigated systematically utilizing cyclic voltammetry (CV), galvanostatic charge-discharge (GCD), and impedance spectroscopy (EIS) in KOH electrolyte. The mesoporous CTO rods delivered C_s of 608.4 F/g, the

specific power of 4835.7 W/kg, the specific energy of 9.77 Wh/kg, and long cyclic stability.

4.2 Experimental section

Mesoporous CTO microrods were synthesized via a simple sol-gel method utilizing Cobalt (II) acetate tetrahydrate ($\text{Co}(\text{CH}_3\text{COO})_2$; 99.999 %), Tetrabutyl titanate polymer ($\text{Ti}(\text{OBU})_4$), ethylene glycol (AR grade), and ethanol (ACS reagent, 96 %). Stoichiometric amounts of $\text{Co}(\text{CH}_3\text{COO})_2$ and $\text{Ti}(\text{OBU})_4$ in 1:1 molar proportion were dissolved in the ethylene glycol (EG) at room temperature under constant stirring to synthesize the CoTiO_3 precursor. The red-colored solution gradually turned in to a light pink solution of metal-glycolate polymer chain-like structure, was further stirred for the next 1 h to obtain the Co-Ti-EG powder. Co-Ti-EG powder was washed with ethanol and deionized water several times and further annealed at 600 °C in ambient conditions for 5 h to ensure the formation of crystalline CoTiO_3 green powder. The crystalline and structural properties of the annealed CTO powder were characterized using XRD (D2-phaser Bruker) equipped with Cu $K\alpha$ radiation ($\lambda = 1.54 \text{ \AA}$) and Raman spectroscopy (Renishaw in Via reflex spectrometer, 532 nm laser) respectively. The effect of functional groups on the features of CTO rods is examined from FTIR spectroscopy (Perkin-Elmer Spectrum, one FTIR spectrometer). The surface morphological features were identified utilized field-emission scanning electron microscopy (FESEM, JEOL JSM-6500F). The elemental analysis was carried out using energy dispersive spectroscopy (OXFORD EDS X-MAX 20 mm). The chemical states and electronic structure of mesoporous CTO rods were identified using an X-ray photoelectron spectrometer (XPS, Thermo Scientific Inc. K-alpha) with a microfocus monochromated Al $K\alpha$ X-ray. The surface area and pore size distribution of the powder were calculated from nitrogen adsorption and desorption isotherms based on the Brunauer-Emmett-Teller and Barret-Joyner-Halenda methods, respectively. Surface wettability was evaluated for different concentrations of KOH electrolyte using a drop shape analyzer (DSA-25, Kruss GmbH, Hamburg, Germany). The electrochemical performance of the mesoporous CoTiO_3 microrod was examined using an electrochemical workstation (Autolab PGSTAT302N). The supercapacitor constituted of CTO coated Ni foam as the working electrodes, a platinum foil as the counter electrode, saturated calomel electrode as the reference electrode, and aqueous

KOH as an electrolyte was examined at room temperature to investigate the potentials of mesoporous CTO rods in the electrochemical performance.

4.3 Results and discussion

4.3.1 Fourier transform infrared spectroscopy

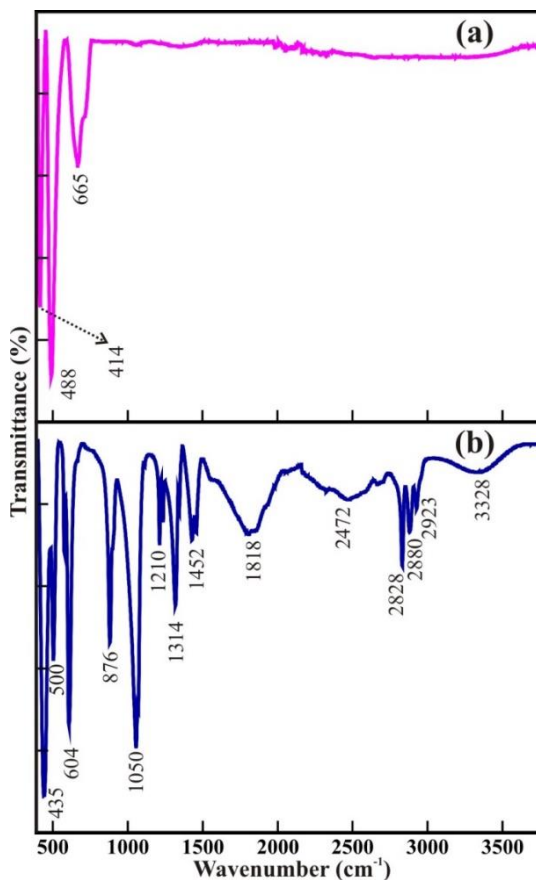


Figure 4.1. FTIR spectra of (a) CTO microrod obtained after annealing (b) as-prepared Co-Ti-EG polymer chain precursor

The FTIR spectra in Figure 4.1 indicate the effect of metal-organic Co-Ti-EG glycolate on the synthesis of mesoporous CTO rods. More number of peaks observed for the as-synthesized Co-Ti-EG glycolate powder (Figure 4.1(b)) were disappeared after annealing at a temperature of 600 °C (Figure 4.1(a)). The peaks centered at 3328, 1452, 1050, and 876 /cm are assigned to the ν_{OH} , δ_{OH} , ν_{CO} , and γ_{OH} bands of C-O and O-H bonding in the $-\text{CH}_2\text{-OH}$, respectively. [19] Whereas the peaks centered at 2472, 1818, 1314, and 1210 /cm are assigned to the ν_{OH} , $\nu_{C=O}$, δ_{OH} , and ν_{CO} bands of C=O, C-O, and O-H bonding in the $-\text{COOH}$ group,

respectively. [19] The peaks centered at 2828 and 2923 /cm are indexed to the symmetry and antisymmetry stretching vibrations, respectively, of C-H bonding in the -CH₂- group instead of the -CH₃ group. [20] However, all these peaks assigned to the various organic components might have decomposed into CO, CO₂, and H₂O and disappeared after annealing as-synthesized CTO powder at a temperature of 600 °C. Therefore, the presence of weak bands only between 400 to 800 /cm is assigned to the stretching vibrations of metal ions of mesoporous CTO rods (Figure 4.1(a)). [20]

4.3.2 X-ray diffraction and Raman spectroscopy

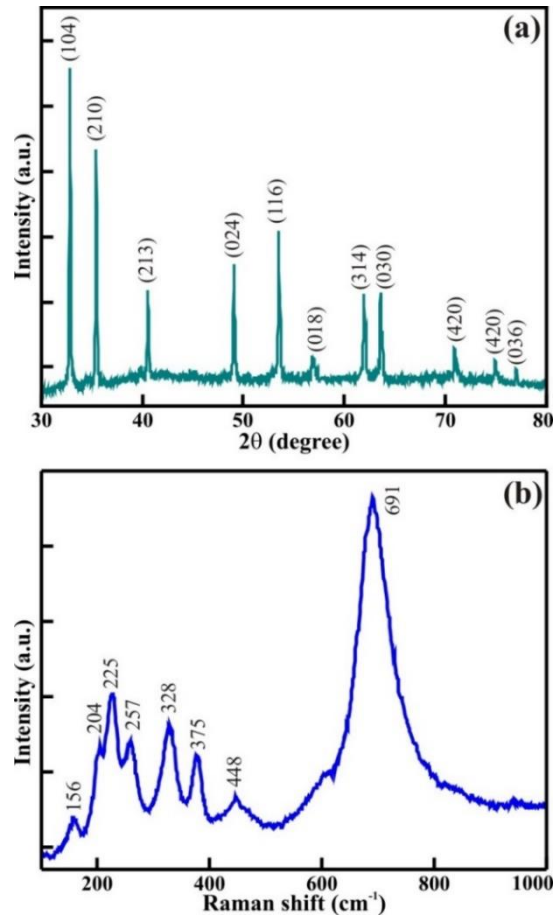


Figure 4.2. (a) XRD pattern and (b) Raman spectrum of mesoporous CTO microrods.

Figure 4.2(a) shows the X-ray diffraction pattern of the annealed CTO microrod. The hexagonal crystal structure of the space group R-3 with the lattice

parameters $a = b = 5.0654$, $c = 13.9209$ Å; $\alpha = \beta = 90^\circ$ and $\gamma = 120^\circ$ (JCPDS: 72-1069) is assigned to the mesoporous CTO microrods. The diffraction peaks identified at $2\theta = 32.8, 35.4, 40.5, 49.08, 53.5, 56.9, 61.9, 63.6, 70.9, 74.9,$ and 77.1° are indexed as (104), (210), (213), (024), (116), (018), (314), (030), (1010), (420), and (036) lattice planes, respectively. The well indexing of all diffraction peaks confirms the formation of pure crystalline mesoporous CTO microrods without impurity phases such as TiO_2 and Co_3O_4 . Furthermore, Raman spectroscopic analysis shown in Figure 4.2(b) was executed to understand the structural properties of CTO rods. A total of 8 significant Raman bands observed at 691, 448, 375, 328, 257, 225, 204, and 156 /cm are well consistent with the earlier reported values for CTO nanoparticles and micro-prisms. [19,21] The strongest Raman mode observed at 691 /cm is assigned to the large frequency vibrational mode of CoO_6 octahedra known as the symmetry stretching mode, and the rest of other Raman modes are assigned to the lattice vibrations of phonon modes. [19,21] The observed Raman spectrum confirms the absence of other additional bands corresponding to Co_3O_4 , TiO_2 , and D/G bonds of carbon. Thus, the consistency of Raman spectra with the XRD analysis also confirms the formation of pristine CTO rods.

4.3.3 Field emission scanning electron microscopy

The surface morphology was examined using FESEM to understand the effect of EG in the growth of mesoporous CTO microrods. Figure 4.3(a) shows the surface morphology of as-synthesized CTO rods. The hexagonal-shaped rods with a smooth surface and clearly visible textural boundaries were composed of Co-Ti-EG glycolate chains and grown to the average diameter of ~ 1.1 μm . These rods of Co-Ti-EG chains were further subjected to the annealing at 600°C . The smooth surface converted into a particle-like appearance without altering the hexagonal morphology of the rods (Figure 4.3(b)). Co-Ti-EG glycolate has converted into intact CTO nanoparticles after selective removal of EG glycolate on annealing. The well crystalline CTO nanoparticles are interconnected with adjacent nanoparticles while maintaining the hexagonal morphological feature of as-synthesized samples (Figure 4.3(c)). The CTO nanoparticles of the average

diameter of $40.7 (\pm 0.5)$ nm resulted in the mesoporous rods of the average diameter of $0.67 (\pm 0.2)$ μm . Moreover, the formation of CTO nanoparticles culminated in the mesoporous rods might be owing to the evaporation of glycolate precursors.

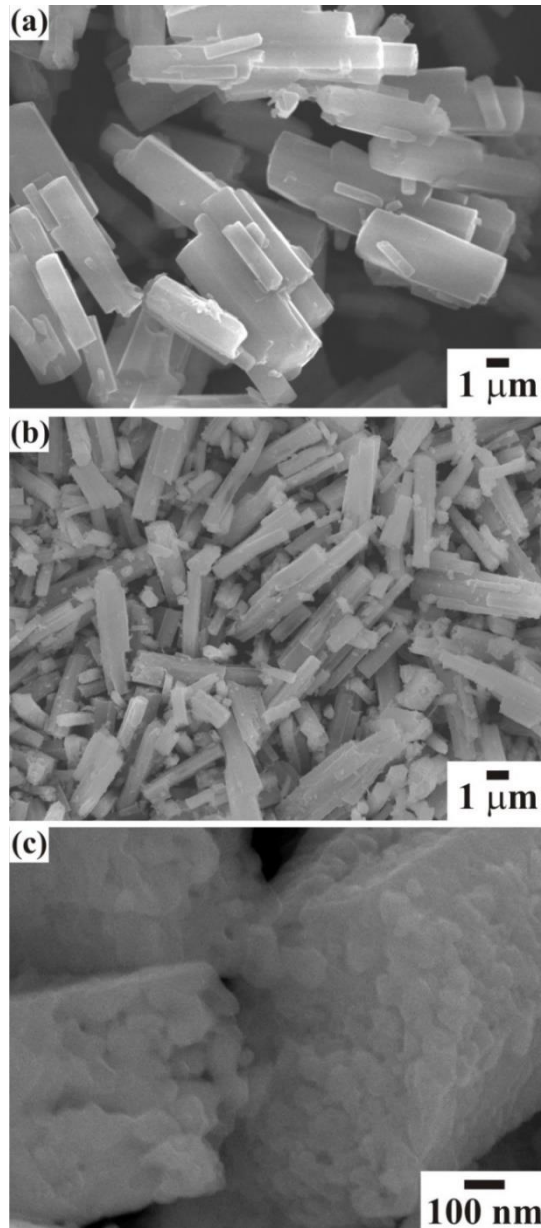


Figure 4.3. FESEM image of (a) as synthesized and (b) annealed CoTiO₃ microrod. (c) The high-magnification FESEM image confirms the formation of mesoporous CoTiO₃ microrod composed of hierarchically interlinked nanoparticles.

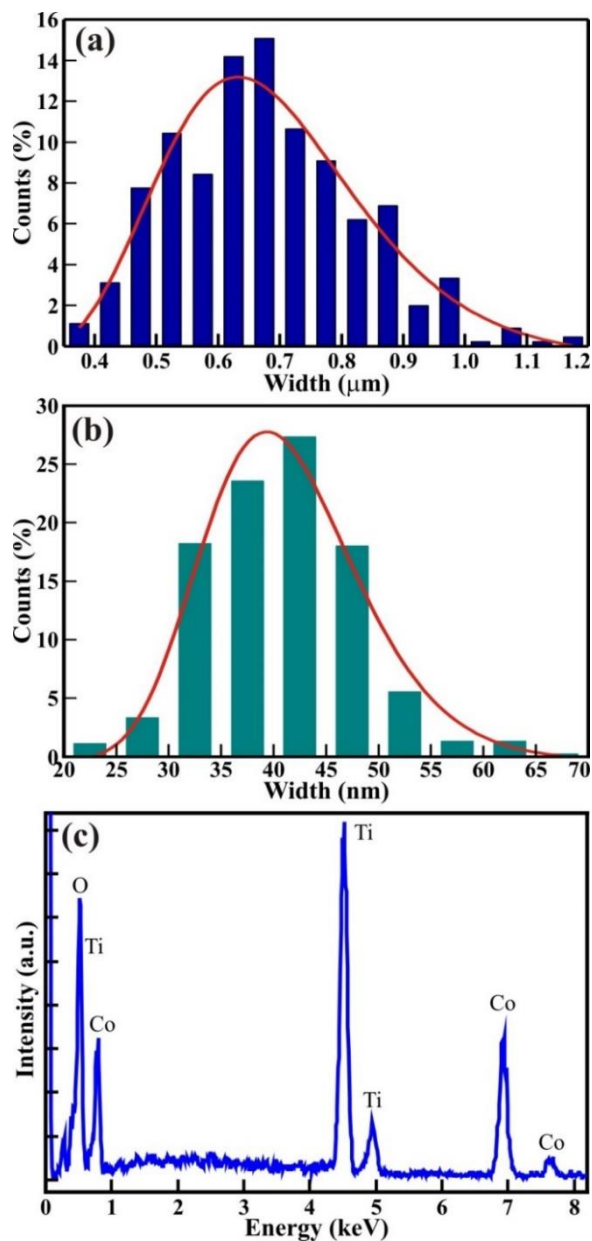


Figure 4.4. (a, and b) statistical histogram of the width distribution microrods and nanoparticles, respectively, and (c) EDS spectra of mesoporous CTO microrods.

A statistical histogram of the width distribution of the hexagonal rods and the nanoparticles diameter is shown in Figure 4.4(a) and (b), respectively. It depicts that all the nanoparticles and rods are smaller than 70 nm and 1.2 μm, but most of them fall in the range of 30 to 50 nm and 0.6 to 0.75 μm, respectively.

The variation of the widths can be fitted by the log-normal distribution function [22,23]

$$f_N = \frac{A}{w\sigma\sqrt{2\pi}} \exp\left[-\frac{\ln(w/\bar{w})^2}{2\sigma^2}\right] \quad \dots (4.1)$$

Where, w is the width of nanoparticles and rods, \bar{w} is mean width of the nanoparticles ($\equiv 40.7 \pm 0.5$ nm) and rods ($\equiv 0.67 \pm 0.02$ nm), A is the initial constant for nanoparticles ($\equiv 5.56 \pm 0.59$) and rods, and σ is the standard deviation of the width distribution of the nanoparticles ($\equiv 0.18 \pm 0.02$) and rods ($\equiv 0.24 \pm 0.02$). The log-normal distribution of the width is asymmetrical for both CTO nanoparticles and rods. The small standard deviation of the width distribution ($\sigma \leq 0.25$) illustrates that the CTO nanoparticles and rods are well confined to the limited width range. Further, energy dispersive spectroscopy (EDS) measurements were performed on annealed CTO samples to confirm the removal of the EG precursor at a temperature of 600 °C. The EDS spectra in Figure 4.4(c) confirm the presence of the elements Co, Ti, and O only, further confirms the high purity of CTO samples.

4.3.4 Nitrogen adsorption-desorption isotherm

Nitrogen adsorption-desorption isotherm measurements for the sol-gel synthesized CTO microrod shown in Figure 4.5 were performed to evaluate the pore structure. The distinctive hysteresis loop, mainly observed for the higher pressure, i.e., 0.0-1.0 P/P_0 indicating type IV isotherm for the CTO microrod (Figure 4.5(a)), reveals a mesoporous structure. The pore volume and specific surface area of the CTO microrods measured from the N_2 adsorption-desorption isotherm using the Brunauer-Emmett-Teller (BET) method are 0.142 cm^3/g and 126.89 m^2/g , respectively. The higher surface area of the CTO microrods is attributed to the mesoporous hexagonal structure constituted after the linkage of the distinct CTO nanoparticles. Furthermore, the pore size distribution as a function of pore diameter for the CTO shown in Figure 4.5(b) was analyzed from the desorption curve using the Barret-Joyner-Halenda (BJH) method. The broad peak of the pore size distribution curve confirmed the presence of a wide range of pores throughout the hexagonal CTO rods. A specific surface area and total pores volume of 126.89 m^2/g and 0.142 cm^3/g , respectively, was observed for the hexagonal rods composed of CTO nanoparticles.

The pore size distribution was confined to the range of 4 to 285 nm, with the average (mean) pore diameter distribution of 3.919 nm. Even though the largest pore diameter distribution of 285.3 nm was observed, most pores lie in the range of 4-100 nm. The maximum number of pores attended a diameter of 30.6 nm. The mesoporous CTO rods offered a larger surface area and provided plenty of accessible sites deep inside the rod morphology to collect ions. Hence, they were expected to increase the interaction at the electrode-electrolyte interface. Moreover, the interconnection of the nanoparticles provided easy transportation for ions penetrated deep inside the mesoporous structure and further assisted in the significant improvement in the faradaic charge storage mechanism.

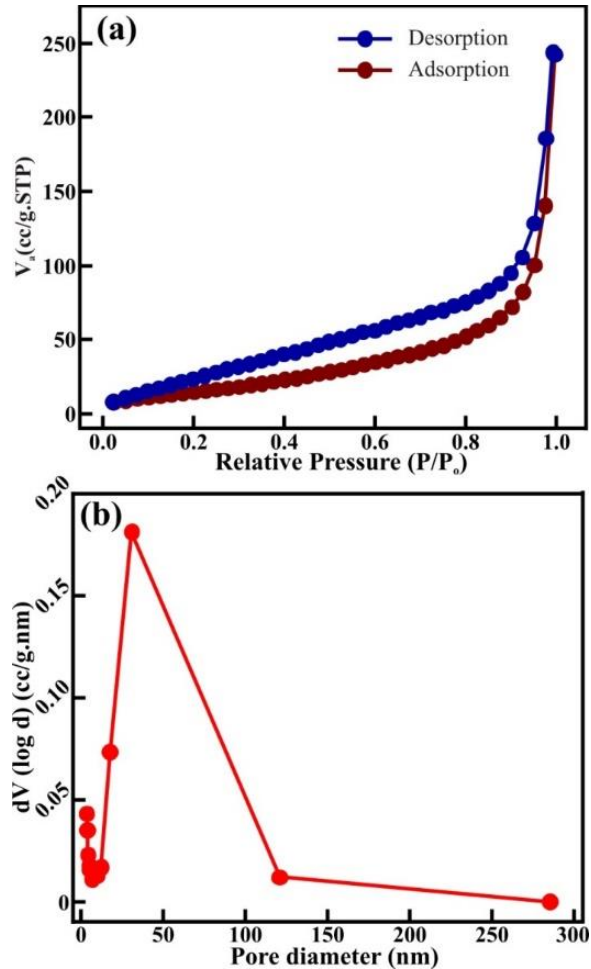


Figure 4.5. (a) N₂ adsorption-desorption isotherm, and (b) BJH pore size distribution of the mesoporous CTO microrod.

4.3.5 X-ray photoelectron spectroscopy

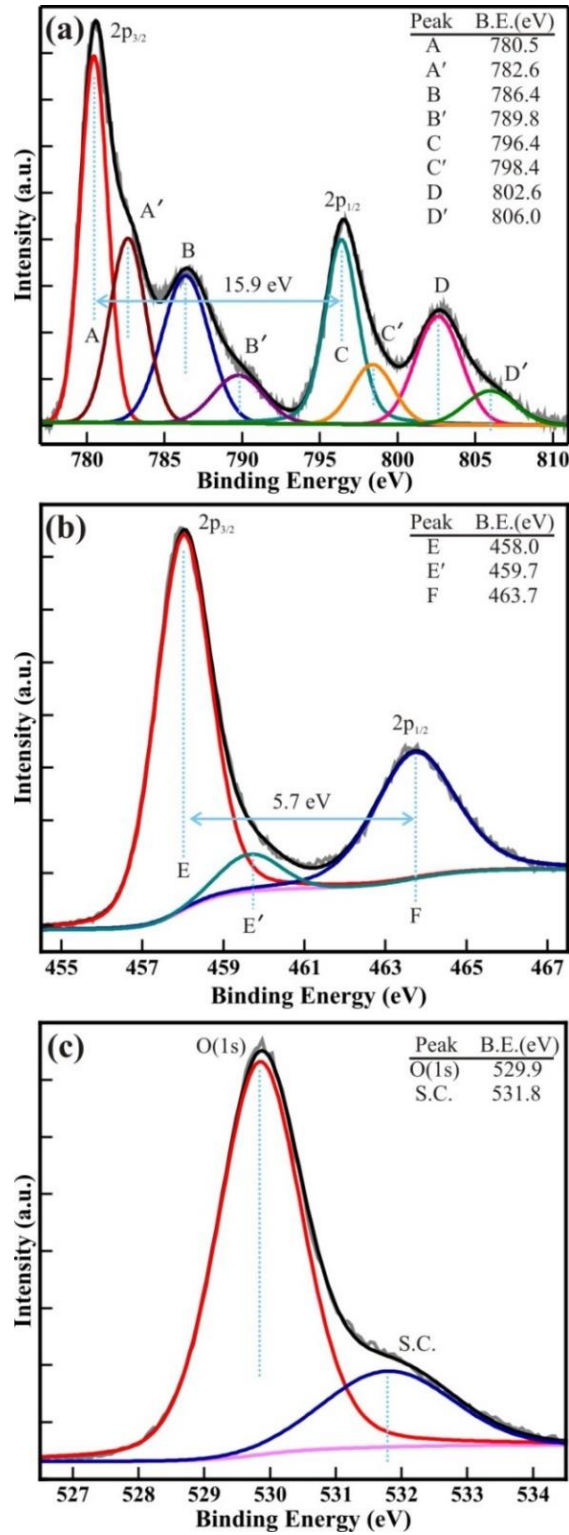


Figure 4.6. Typical high-resolution XPS spectra of the (a) Co(2p), (b) Ti(2p), and (c) O(1s) core levels of the mesoporous CTO microrods.

X-ray photoelectron spectroscopy (XPS) studies were carried out for the quantitative analysis of the electronic structure and chemical properties of mesoporous CTO microrod. Figure 4.6 shows the high-resolution XPS spectra of the core levels of Co(2p), Ti(2p), and O(1s). The dual-peak feature of Co(2p) is shown in Figure 4.6(a). The peaks correspond to Co(2p_{3/2}) and Co(2p_{1/2}) are located at a binding energy of 780.5 and 796.4 eV, respectively. The shake-up satellite peaks are observed at 786.4 and 802.6 eV, which are 5.9 and 6.2 eV higher in binding energy than Co(2p_{3/2}) and Co(2p_{1/2}) peaks, respectively. The double peak feature of Co(2p) observed along with their associated shake-up satellite peaks reveal the paramagnetic chemical state of Co²⁺ and open 3d⁹ shell of Co²⁺, usually observed in divalent magnetic elements like Cu and Ni. [24] Further to precisely determine the double peak feature of Co(2p) and their shake-up satellite peak, Co(2p) XPS spectra are decomposed via Voigt curve fitting function followed by a Shirley background. The Co(2p_{3/2}) and Co(2p_{1/2}) peaks deconvoluted in the four distinct peaks, labeled as A, A', C, and C' are located at a binding energy of 780.5, 782.6, 796.4, and 798.4 eV represents the Co²⁺(2p_{3/2}), Co³⁺(2p_{3/2}), Co²⁺(2p_{1/2}), and Co³⁺(2p_{1/2}), peaks respectively. The peak intensity of Co²⁺(2p_{3/2}) is significantly (i.e., >2 times) larger than that of Co³⁺(2p_{3/2}), indicates the presence of a substantially larger amount of Co²⁺ in the CTO. Moreover, the shake-up satellite peaks of Co(2p_{3/2}) and Co(2p_{1/2}) also decomposed in the four discrete peaks, identified as B, B', D, and D', are located at the binding energy of 786.4, 789.8, 802.6, and 806.0 eV. represents shake-up satellite peaks of Co²⁺(2p_{3/2}), Co³⁺(2p_{3/2}), Co²⁺(2p_{1/2}), and Co³⁺(2p_{1/2}), respectively. The spin-orbit splitting between the Co(2p_{3/2}) and Co(2p_{1/2}) core levels and their shakeup satellite peaks is 15.9 and 16.2 eV, respectively, is assigned for the presence of the larger amount of Co²⁺ than that of Co⁰ or Co³⁺ ions. [15,25,26] Figure 4.6(b) shows the XPS spectra of Ti(2p) core levels deconvoluted via Voigt curve fitting function within the Shirley background to precisely determine the double peak features of Ti(2p_{3/2}) and Ti(2p_{1/2}) core levels. The decomposed peaks observed at binding energy of 458.0 eV (i.e., E), 459.8 eV (i.e., E'), and 463.7 eV (i.e., F) are assigned to the Ti⁴⁺(2p_{3/2}), Ti³⁺(2p_{3/2}) and Ti⁴⁺(2p_{1/2}), core level, respectively.

[3,5,27] The intensity of the $\text{Ti}^{4+}(2p_{3/2})$ is 12 times larger than that of $\text{Ti}^{3+}(2p_{3/2})$ confirm the presence of the larger amount of Ti^{4+} along with very minor traces of Ti^{3+} . This confirms that a very minor quantity of Co^{3+} and Ti^{3+} is present in the CTO compound to achieve stoichiometry. Furthermore, O(1s) XPS spectra of CTO microrod decomposed via Voigt curve fitting function within the Shirley background (Figure 4.6(c)) shows the perfect fits to two peaks located at 529.84 and 531.74 eV represents the O(1s) core level of the O^{2-} anions and the surface contamination, such as carbon oxides or hydroxides [5] in the mesoporous CTO rods. Moreover, the BE separation (ΔE) of 71.8 eV between O(1s) and $\text{Ti}(2p_{3/2})$ is very close to the enthalpy of formation of CoTiO_3 . [3] Overall, the XPS analysis confirms the formation of stable mesoporous CTO microrods consisting of the significantly larger amount of Co^{2+} and Ti^{4+} cations, albeit minor traces of Co^{3+} and Ti^{3+} cations.

4.3.6 Contact angle measurements

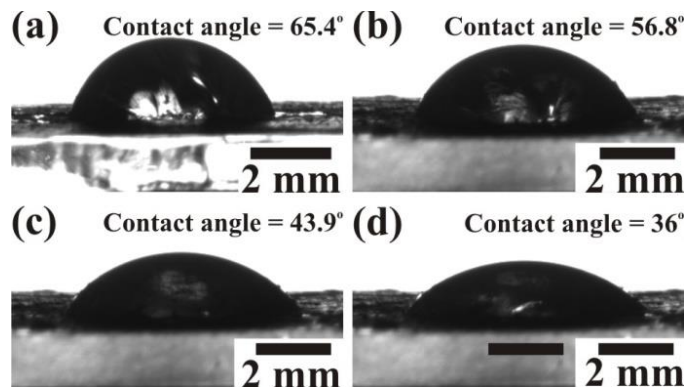


Figure 4.7. Contact angle measurement showing the interface of the aqueous KOH electrolyte of (a) 0.5 M, (b) 1 M, (c) 1.5 M, and (d) 2 M concentration on the surface of the working electrode of mesoporous CTO microrods.

The diffusion of a large number of ions during the charging process is expected to gain maximum C_s . Therefore, wettability studies are carried out to investigate the electrode-electrolyte interface mechanism. The average contact angle determined by the young's relation for various concentrations of aqueous KOH electrolyte (0.5M, 1M, 1.5M, and 2M) on the electrode surface confirmed their inversely proportional relation. The contact angle of CTO microrods

measured for the 0.5 (Figure 4.7(a)), 1 (Figure 4.7(b)), 1.5 (Figure 4.7(c)), and 2 (Figure 4.7(d)) M concentrations of aqueous KOH electrolyte is, 65.4°, 56.8°, 43.9°, and 36°, respectively. The increase in the concentration of KOH electrolyte might have led to the improved cohesive force with CTO microrods and expected to enhance further the diffusion of electrolyte/ions deep inside the mesoporous CTO microrods. Therefore, 2M aq. KOH electrolyte exhibiting a lower contact angle with the CTO electrode is preferred for electrochemical measurements.

4.3.7 Electrochemical performance

The electrochemical performance of mesoporous CTO microrods was analyzed from cyclic voltammetry (CV), galvanostatic charge-discharge (GCD), and electrochemical impedance spectroscopy (EIS) in 2M aq. KOH electrolyte. The CV was performed in the potential range of 0 to 0.6 V at different sweep rates varying from 5, 10, 20, 40, 50, and 100 mV/s (Figure 4.8(a)). The two distinct peaks observed at positive and negative current densities in the potential window of 0 to 0.6 V reveal the oxidation and reduction of CTO rods. Furthermore, these oxidation and reduction peaks have shifted to relatively higher and lower potentials with an increase in the sweep rate. The oxidation peak observed for the potential of 0.36 V at a sweep rate of 5 mV/s has shifted by 0.17 V (i.e., observed at 0.54 V) at the sweep rate of 100 mV/s. Similarly, the reduction peak observed at 0.20 V for a sweep rate of 5 mV/s has shifted by 0.17 V (i.e., observed at 0.03 V) after increasing the sweep rate of 100 mV/s. This shifting in the oxidation and reduction peaks with increased sweep rate is assigned to the redox processes due to the polarization and ohmic resistance at the electrolyte-electrode interface during faradic processes. Which is akin to the observations for Co_3O_4 hexagonal platelets composed of nanoparticles, [28] Co_3O_4 nanorods, [7] LaNiO_3 nanotubes, [29] and core-shell morphology of NiCo_2O_4 nanosheets and hollow microrod arrays. [30] Moreover, the peak intensity and area under the CV graph have increased with an increase in the sweep rate, indicating the more significant diffusion of OH^- ions at the slower scan rates.

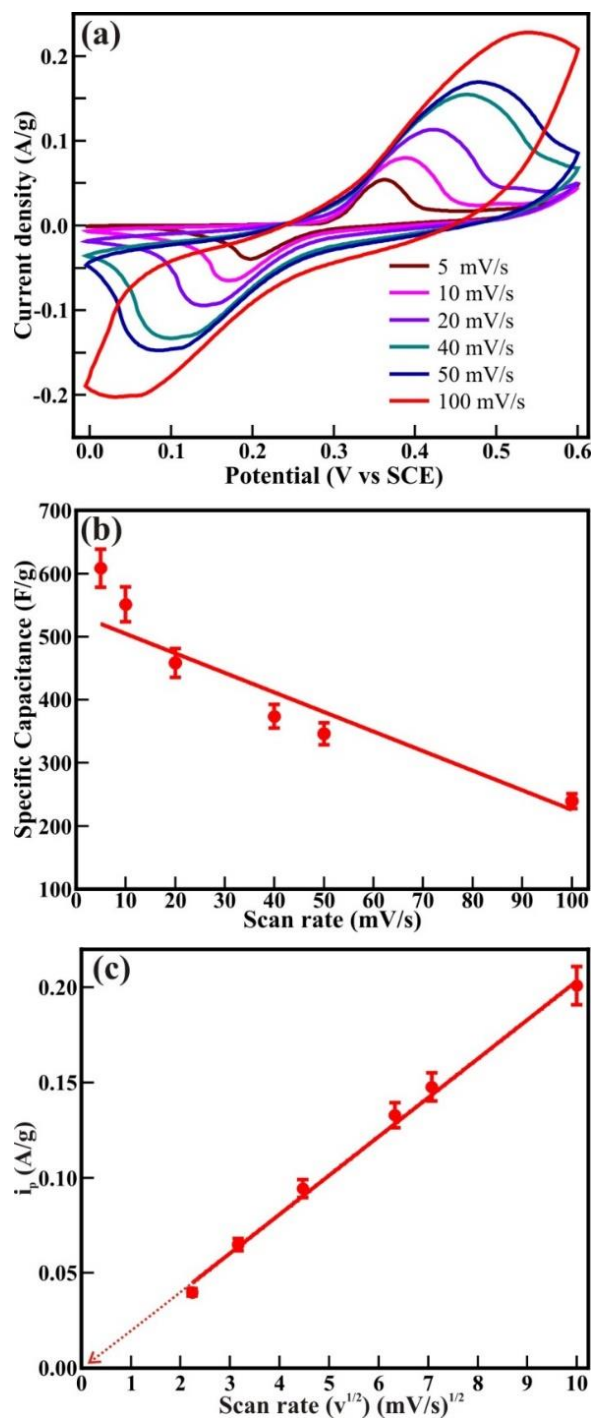


Figure 4.8. (a) Cyclic voltammograms and (b) specific capacitance of mesoporous CTO microrod observed at various scan rates in 2 M aq. KOH electrolyte. (c) The graphical illustration of the anodic peak current density (i_p) with the square root of the scan rate ($v^{1/2}$).

The specific capacitance (C_s) shown in Figure 4.8(b) is evaluated from the CV graphs at various sweep rates (Figure 4.8(a)) using the equation

$$C_s = \frac{\int idV}{2mv\Delta V} \quad \dots\dots (4.2)$$

Where, C_s is the specific capacitance (F/g), m is the mass of the CTO microrods loaded in the working electrode (g), v is the scanning rate (mV/s), ΔV is the applied potential range (V), and $\int idV$ is the integral area under the CV graph. The evaluated C_s values linearly varied with the sweep rate. The C_s value of 608.4 F/g (at a sweep rate of 5 mV/s) was retained to 239.4 F/g even after increasing the sweep rate to 100 mV/s. The significantly easy access of electrolyte deep inside the mesoporous CTO microrods might have provided preeminent diffusion of the large number of OH^- ions at a slower sweep rate along the textural boundaries of nanoparticles assembled in mesoporous microrods and further resulted in the larger C_s value of 608.4 F/g. The increased sweep rate is expected to restrict the easy access of larger amounts of OH^- ions in a short time and hence reduce the C_s relatively. The C_s value of 608.4 F/g conceived from the mesoporous CTO rods is relatively larger than the pristine Co_3O_4 and TiO_2 nanostructure morphologies such as hexagonal platelet Co_3O_4 particles (i.e., 476 F/g), [28] Co_3O_4 nanorods (i.e., 351 F/g), [31] mesoporous Co_3O_4 nanosheets (i.e., 92 F/g), [32] brookite TiO_2 nanoneedles (i.e., 34.1 mF/g), [5] selectively dealloyed Ti/ TiO_2 network nanostructures (i.e., 35.5 F/g), [31] and $\text{NiO}@\text{Co}_3\text{O}_4$ core-shell nanofibers (i.e., 437 F/g). [10] Moreover, present mesoporous CTO microrods deliver significantly larger C_s values than the hetero-architectures of Co or Ti oxides formed with other compatible metal oxides or pristine/doped graphene oxides. A hierarchical 3D flowers of $\text{Co}_3\text{O}_4@\text{MnO}_2$ grown on nitrogen-doped graphene oxide (NGO) hybrid composite delivered C_s of 347 F/g. Gobal et al. [34] synthesized NiO-ZnO/ TiO_2 nanotubes formed after calcination of the electrodeposited Zn-Ni over the TiO_2 nanotubes provided the C_s of 325 F/g in a 1M NaOH electrolyte. The agglomeration of microwave irradiated NTO nanoparticles restricted the easy access of 0.5M H_2SO_4 electrolyte and hence constrained the redox process, limiting the C_s value to 257 F/g. [17] Likewise, CTO has provided substantially higher C_s value than the other ABO_3 family

members such as LaFeO₃ (i.e., 375.7 F/g), [35] LaNiO₃ (i.e., 280 F/g), [29] and SrMnO₃ (i.e., 321.7 F/g). [36]

Further, the variation of the current density with respect to the sweep rate is estimated by the Randle-Sevcik equation, (Figure 4.8(c))

$$i_p = 2.69 \times 10^5 C_o n^{3/2} \nu^{1/2} D^{1/2} \quad \dots (4.3)$$

Where, i_p is the peak current density in mA/g, C_o is the concentration of OH⁻ ions in the electrolyte solution, n is the number of electrons, ν is the sweep rate in mV/s, and D is the diffusion coefficient of OH⁻ ions in the electrode material. The plot of peak current density with respect to sweep rate shows the linear behavior. The straight line passing through the origin confirms the diffusion-controlled adsorption and desorption of OH⁻ ions along the surface of CTO nanoparticles assembling to form mesoporous microrods.

Figure 4.9(a) shows the charge-discharge curves measured at various current densities ranging from 30 to 120 mA/g. The asymmetric behavior of charge-discharge plots revealed the pseudocapacitive behavior of mesoporous CTO microrods. Figure 4.9(b) shows the specific capacitance (F/g) at different current densities estimated from the equation.

$$C_s = \frac{I \cdot dt}{m \cdot dv} \quad \dots (4.4)$$

The maximum C_s of 299.5 F/g gained for the current density of 30 mA/g is reduced to 230.4 F/g at the current density to 120 mA/g (Figure 4.9(b)). The time provided for the diffusion of ions deep inside the mesoporous microrods along the surface of CTO nanoparticles is relatively small at higher current density; that is why C_s values are reduced with an increase in the current density. The C_s value of 299.5 F/g achieved from mesoporous CTO microrods is significantly higher than the values reported for the other perovskites of di- and tri-valent metal ions such as PVP assisted porous LaCoO₃ nanospheres (i.e., 203 F/g in 6 M KOH), [37] electrodeposited LaMnO₃/MnO nanoarrays on carbon cloth (i.e., 260 F/g in 0.5 M Na₂SO₄), [38] hydrothermally derived nanotube of Co@TiO₂ and RGO composite (i.e., 27.5 F/g), [9] and sol-gel assisted Sr doped LaMnO₃ spheres (i.e., 198 F/g). [39] Moreover, the mesoporous CTO rods have provided better C_s values than the nanocomposite prepared by varying the

composition of constituent phases of Carbon, Fe_2O_3 , and Co_3O_4 . The C_s value of $\text{C}/\text{Fe}_2\text{O}_3$ (i.e., 85.3 F/g) was further improved after the addition of Co_3O_4 (i.e., 144 F/g). [40] This reconfirms that the CTO microrods are excellent electrode materials from the perovskite family in their pristine form.

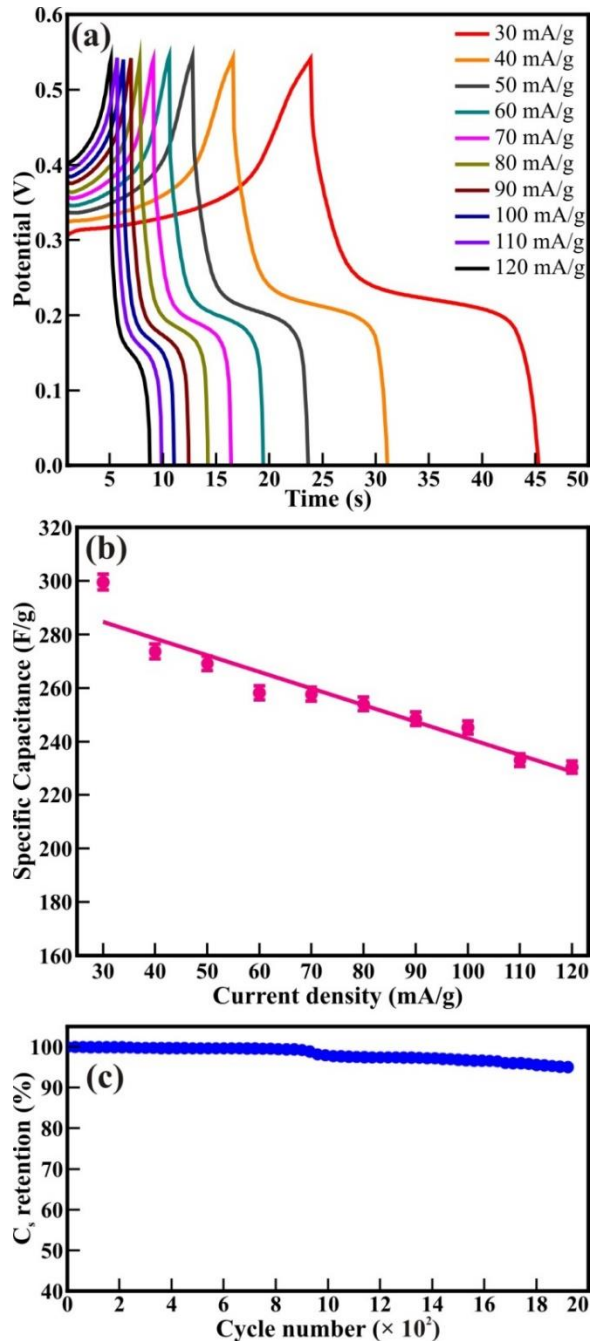


Figure 4.9. (a) GCD curves and (b) evaluated specific capacitance of mesoporous CTO rods at various current densities. (c) Specific capacitance retention analyzed for 1950 GCD cycles at the current density of 100 mA/g. The inset figure shows the first 10 cycles.

Longer cyclic stability is essential for the better durable performance of the supercapacitor. Therefore, the cycling stability of the mesoporous CTO microrods was tested at a current density of 100 mA/g for 1950 charge-discharge cycles (Figure 4.9(c)). The C_s values of 299.5 F/g have reduced by ~2 % for the initial 1000 cycles, which further lowered to ~5 % after the 1950 continuous charge-discharge cycles. The observed capacitance retention for the mesoporous CTO microrods is more impressive than the values attained for microwave irradiated NTO nanoparticles, [17] the electrodeposited LaMnO₃/MnO nanoarrays, [38] compatible with the hierarchical flower-like 3D nanostructure of Co₃O₄@MnO₂/Nitrogen-doped graphene oxide hybrid composite, [41] and mesoporous perovskite of interlocked NiTiO₃ nanoparticles. [42] This distinct cyclic stability of mesoporous CTO microrods confirms the better durability, longer lifetime, and excellent electrochemical stability in 2 M KOH electrolyte.

4.3.8 Electrochemical impedance spectroscopy

The surface morphology, textural boundaries, and electrical properties of the active electrode material play a vital role in diffusing the ions from the electrolyte. Therefore, electrochemical impedance spectroscopy (EIS) was employed to know the contribution of textural boundaries and electrical resistance in the diffusion of OH⁻ ions in the mesoporous CTO microrods. Figure 4.10(a) demonstrates the typical Nyquist plots of the CTO microrods in 2 M KOH electrolyte. The EIS spectrum of mesoporous CTO microrods before stability study is akin to that recorded after stability study for 1950 charging-discharging cycles. The EIS spectra signify a perfect fit for a semi-circular arc analogous to the charge-transfer resistance at the interface of electrolyte and CTO microrods. This semi-circular arc of impedance spectra is similar to the Co₃O₄, [7] TiO₂, [5] LaMnO₃/MnO, [38] and Sr doped LaMnO₃. [39] The intercept and diameter of the semi-circular arc symbolize the charge transfer resistance (R_{ct}) of 92.1 Ω for mesoporous CTO microrods has reduced to 41.2 Ω after 1950 charge-discharge cycles. However, the values of electrolyte resistance (R_s) obtained before the stability study (0.53 Ω) remained the same even after 1950 continuous charging-discharging cycles (0.56 Ω). The equivalent circuit for the EIS consists of

electrolyte resistance (R_s), charge transfer resistance (R_{ct}), and constant phase elements denoted in the inset of Figure 4.10(a). It confirms that larger surface area in conjunction with clearly visible textural boundaries of interconnected nanoparticles of mesoporous CTO microrods providing abundant access to the OH^- ions from the aq. KOH electrolyte. The partial drop in the charge diffusion of the mesoporous CTO microrods after 1950 cycles indicates the increase in the accessibility of surface and textural boundaries of mesoporous CTO rods during repeated charge-discharging cycles, which might be one of the reasons behind excellent stability.

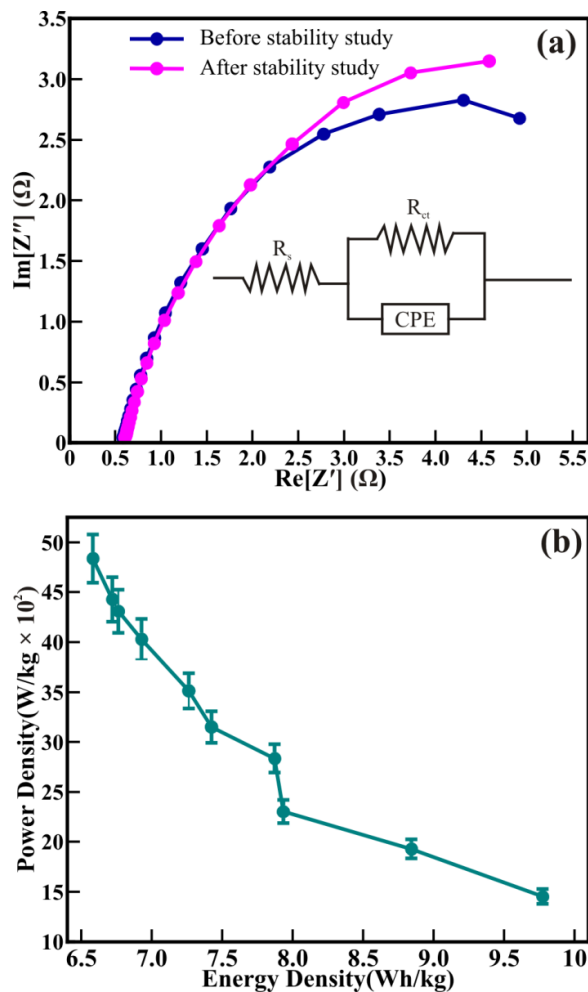


Figure 4.10 (a) Nyquist (EIS) plot of the mesoporous CTO microrods obtained before and after cyclic stability studies. Inset shows the best fitted equivalent circuit model. (b) Evaluated specific energy and specific power of mesoporous CTO microrods.

The time constant was calculated to divulge the reaction kinetics for the transport of OH⁻ ions deep inside the CTO microrods, from the equation

$$\tau = 1/2\pi f^* \quad \dots (4.5)$$

Where, f^* is the frequency corresponds to the maxima of the imaginary component of the semicircle. The time constant of 1.32 μ s measured before stability study confirm the abrupt and easy access for the OH⁻ ions transportation deep inside the CTO microrod along the textural boundaries. The time constant has not reduced ever after 1950 charging-discharging cycles (i.e., 1.59 μ s), reinforce the excellent cyclic stability observed for mesoporous CTO microrods.

4.3.9 Ragone plot

Figure 4.10(b) exhibits the relation of specific power and specific energy evaluated from equations 6 and 7 to interpret the comprehensive performance of CTO,

$$E = \frac{1}{2} \times C_s \times (\Delta V)^2 \quad \dots (4.6)$$

$$P = \frac{E}{\Delta t} \times 3600 \quad \dots (4.7)$$

Where, C_s is the specific capacitance (F/g), ΔV is the potential operating range (volts), Δt is the discharge time in (Sec.), P is the specific power (W/kg), and E is the specific energy (Wh/kg). The specific power reduces with respect to an enhancement in the specific energy as the charge/discharge current density increased from 30 to 120 mA/g. The maximum specific power of 4835.7 W/kg and specific energy of 9.8 Wh/kg is obtained from mesoporous CTO. The specific power of 4835.7 W/kg (at the current density of 30 mA/g) obtained for CTO is significantly higher than the hierarchical flower-like 3D nanostructure of Co₃O₄@MnO₂/nitrogen-doped graphene oxide hybrid composite (i.e., 850 W/kg), [41] 3D TiO₂@ Ni(OH)₂ core-shell nanowire arrays (i.e., 1881.8 W/kg), [11] and 3D nanonet of hollow structured Co₃O₄ (i.e., 100 W/kg). [43] Moreover, the performance of mesoporous CTO is relatively excellent than the perovskites of NiCo₂O₄ nanosheets@ hollow microrod arrays (i.e., 100 W/kg), [30] Sr doped LaMnO₃ nanoparticles (i.e., 120 W/kg), [39] and 3D carbon-fiber network

anchored with metallic Co (i.e., 797 W/kg), [44] and compatible with mesoporous perovskite of interlocked NiTiO₃ nanoparticles (4320 W/kg). [42] The improved electrochemical performance of CTO is attributed to the well-connected network of CTO nanoparticles, well-defined textural boundaries, and highly accessible larger surface area of the perforated mesoporous morphology collectively furnishes easy access for ions diffusion deep inside the mesoporous structure.

4.4 Conclusions

In conclusion, we report the synthesis of mesoporous cobalt titanite (CTO) microrods incorporating interconnected nanoparticles with clearly visible textural boundaries. The CTO nanoparticles of average diameter ~ 59 nm hierarchically organized in the hexagonal form provided mesoporous microrods of average diameter ~ 800 nm and the average pore size distribution of 3.919 nm throughout the rod body. The CTO nanoparticles of mesoporous rods are of the hexagonal crystalline phase to the space group of R-3. XPS analysis showed the consistent presence of Co²⁺/Co³⁺ and Ti⁴⁺/Ti³⁺, confirmed the formation of stoichiometric CTO microrods. The interconnection of CTO nanoparticles resulted in the formation of mesoporous CTO rods with increased textural boundaries offered a larger surface area for significantly larger diffusion of OH⁻ ions, further leading to an increase in C_s in 2 M KOH electrolyte. The diffusion-controlled access to the OH⁻ ions (0.27 μs) deep inside the rod structure provides higher specific power (4835.7 W/kg) and specific energy (9.77 Wh/kg) than the other perovskite family members. Moreover, the excellent stability up to 1950 continuous charging-discharging cycles with the capacitance retention of 82.3 % recommends the mesoporous CTO microrods as a proficient working electrode for the supercapacitor. Furthermore, the morphology-dependent electrochemical performance showed in this study has unlocked a new corridor to explore the core-shell hetero-architectures of CTO rods with other metal oxides like TiO₂, MnO₂, CuO as an electrode for hybrid capacitors, which may further enhance the electrochemical performance.

4.5 References

- [1.] Kitchamsetti N., Chikate P. R., Patil R. A., Ma Y. R., Shirage P. M., Devan R. S., (2019), Perforated mesoporous NiO nanostructures for an enhanced

- pseudocapacitive performance with ultra-high rate capability and high energy density, *Cryst. Eng. Comm.*, 21, 7130-7140, (DOI: 10.1039/c9ce01475f).
- [2.] Duan C., Tong J., Shang M., Nikodemski S., Sanders M., Ricote S., Almansoori A., O'Hayre R., (2015), Readily processed protonic ceramic fuel cells with high performance at low temperatures, *Science*, 349, 1321-1326, (DOI: 10.1126/science.aab3987).
- [3.] Kitchamsetti N., Kalubarme R. S., Chikate P. R., Park C. J., Ma Y. R., Shirage P. M., Devan R. S., (2019), An investigation on the effect of Li-ion cycling on the vertically aligned brookite TiO₂ nanostructure, *ChemistrySelect*, 4, 6620-6626, (DOI: 10.1002/slct.201900395).
- [4.] Devan R. S., Patil R. A., Lin J. H., Ma Y. R., (2012), One-dimensional metal-oxide nanostructures: recent developments in synthesis, characterization, and applications, *Adv. Funct. Mater.*, 22, 3326-3370, (DOI: 10.1002/adfm.201201008).
- [5.] Devan R. S., Ma Y. R., Patil R. A., Lukas S. M., (2016), Highly stable supercapacitive performance of one-dimensional (1D) brookite TiO₂ nanoneedles, *RSC Adv.*, 6, 62218-62225, (DOI: 10.1039/c6ra11348f).
- [6.] Lu X., Wang G., Zhai T., Yu M., Gan J., Tong Y., Li Y., (2012), Hydrogenated TiO₂ nanotube arrays for supercapacitors, *Nano Lett.*, 12, 1690-1696, (DOI: 10.1021/nl300173j).
- [7.] Jiang T., Yang S., Bai Z., Dai P., Yu X., Wu M., Hu H., (2018), Facile fabrication and configuration design of Co₃O₄ porous acicular nanorod arrays on Ni foam for supercapacitors, *Nanotechnol.*, 29, 315402, (DOI: 10.1088/1361-6528/aac3f4).
- [8.] Arun T., Kumar T. K., Udayabhaskar R., Mangalaraja R. V., Fakhrabadi A. A., (2019), Nano hexagonal Co₃O₄ platelets for supercapacitor applications-synthesis and characterization, *Mater. Res. Exp.*, 6, 0850b1, (DOI: 10.1088/2053-1591/ab24e8).
- [9.] Xiao H., Guo W., Sun B., Pei M., Zhou G., (2016), Mesoporous TiO₂ and Co-doped TiO₂ nanotubes/reduced graphene oxide composites as electrodes for supercapacitors, *Electrochim. Acta*, 190, 104-117, (DOI: 10.1016/j.electacta.2016.01.040).

- [10.] Jiang P., Wang Q., Dai J., Li W., Wei Z., (2017), Fabrication of NiO@Co₃O₄ core/shell nanofibres for high-performance supercapacitors, *Mater. Lett.*, 188, 69-72, (DOI: 10.1016/j.matlet.2016.10.098).
- [11.] Ke Q., Zheng M., Liu H., Guan C., Mao L., Wang J., (2015), 3D TiO₂@Ni(OH)₂ core-shell arrays with tunable nanostructure for hybrid supercapacitor application, *Sci. Rep.*, 5, 13940, (DOI: 10.1038/srep13940(2015)).
- [12.] DiDomenico M. Jr., Wemple S. H., (1968), Optical properties of perovskite oxides in their paraelectric and ferroelectric phases, *Phys. Rev.*, 166, 565, (DOI: 10.1103/PhysRev.166.565).
- [13.] Hu F., Zhang H., Sun C., Yin C., Lv B., Zhang C., Yu W. W., Wang X., Zhang Y., Xiao M., (2015), Superior optical properties of perovskite nanocrystals as single photon emitters, *ACS Nano*, 9, 12410-12416, (DOI: 10.1021/acsnano.5b05769).
- [14.] Mizumaki M., Yoshii K., Hinatsu Y., Doi Y., Uruga T., (2005), Investigation of structural and electronic properties in Ru perovskite oxides by XAFS measurements, *Phys. Scr. T*, 115, 513-515, (DOI: 10.1238/Physica.Topical.115a00513).
- [15.] Shilpy M., Ehsan M. A., Ali T. H., Hamid S. B. A., Ali M. E., (2015), Performance of cobalt titanate towards H₂O₂ based catalytic oxidation of lignin model compound, *RSC Adv.*, 5, 79644-79653, (DOI: 10.1039/c5ra14227j).
- [16.] Rao C. N. R., Ganguly P., Singh K. K., Ram R. A. M., (1988), A comparative study of the magnetic and electrical properties of perovskite oxides and the corresponding two-dimensional oxides of K₂NiF₄ structure, *J. Solid State Chem.*, 72, 14-23, (DOI: 10.1016/0022-4596(88)90003-5).
- [17.] Imani M., Radmanesh L., Tadjarodi A., (2019), Synthesis of perovskite-like NiTiO₃ nanoparticles as an electrode material by a rapid solid combustion technique induced by microwave irradiation, *Ceram. Int.*, 45, 18772-18777, (DOI: 10.1016/j.ceramint.2019.06.105).
- [18.] Kakvand P., Rahmanifar M. S., El-Kady M. F., Pendashteh A., Kiani M. L., Hashami M., Najafi M., Abbasi A., Mousavi M. F., Kaner R. B., (2016), Synthesis of NiMnO₃/C nano-composite electrode materials for electrochemical capacitors, *Nanotechnol.*, 27, 315401, (DOI: 10.1088/0957-4484/27/31/315401).

- [19.] Huang Z.-D., Zhang T.-T., Lu H., Yang J., Bai L., Chen Y., Yang X.-S., Liu R.-Q., Lin X.-J., Li Y., Li P., Liu X., Feng X.-M., Ma Y.-W., (2018), Bimetal-organic-framework derived CoTiO_3 mesoporous micro-prisms anode for superior stable power sodium ion batteries, *Sci. China Mater.*, 61, 1057-1066, (DOI: 10.1007/s40843-017-9225-5).
- [20.] Lin Y.-J., Chang Y.-H., Yang W.-D., Tsai B.-S., (2006), Synthesis and characterization of ilmenite NiTiO_3 and CoTiO_3 prepared by a modified Pechini method, *J. Non-cryst. Solids*, 352, 789-794, (DOI: 10.1016/j.jnoncrysol.2006.02.001).
- [21.] Zhou G.-W., Lee D. K., Kim Y. H., Kim C. W., Kang Y. S., (2006), Preparation and spectroscopic characterization of ilmenite-type CoTiO_3 nanoparticles, *Bull. Kr. Chem. Soc.*, 27, 368-372, (DOI: 10.5012/bkcs.2016.27.3.368).
- [22.] Chikate P. R., Daware K. D., Patil S. S., Didwal P. N., Lole G. S., Chaudhary R. J., Gosavi S. W., Devan R. S., (2020), Effects of Au loading on the enhancement of photoelectrochemical activities of the Au@ZnO nano-heteroarchitecture, *New. J. Chem.*, 44, 5535-5544, (DOI: 10.1039/D0nj00004c).
- [23.] Devan R. S., Ho W. D., Wu S. Y., Ma Y. R., (2010), Investigation of high-temperature phase transformation in one-dimensional Ta_2O_5 nanorods, *J. Appl. Crystl.*, 43, 498-503, (DOI: 10.1107/s0021889810026646).
- [24.] Shaikh J. S., Pawar R. C., Devan R. S., Ma Y. R., Salvi P. P., Kolekar S. S., Patil P. S., (2011), Synthesis and characterization of Ru doped CuO thin films for supercapacitor based on Bronsted acidic ionic liquid, *Electrochim. Acta*, 56, 2127-2134, (DOI: 10.1016/j.electacta.2010.11.046).
- [25.] Anirudha J., Rao P. T., Munichandraiah N., Shivashankar S. A., (2016), Flower-like porous cobalt (II) monoxide nanostructures as anode material for Li-ion batteries, *J. Electroanal. Chem.*, 761, 21-27, (DOI: 10.1016/j.jelechem.2015.11.003).
- [26.] Yang G., Yan W., Wang J., Yang H., (2014), Fabrication and characterization of CoTiO_3 nanofibers by sol-gel assisted electrospinning, *Mater. Lett.*, 122, 117-120, (DOI: 10.1016/j.matlet.2014.01.177).
- [27.] Devan R. S., Ma Y. R., More M. A., Khare R. T., Antad V. V., Patil R. A., Thakare V. P., Dhayal R. S., Mende L. S., (2016), Promising field electron emission

- performance of vertically aligned one dimensional (1D) brookite(β) TiO₂ nanorods, RSC Adv., 6, 98722-98729, (DOI: 10.1039/c6ra20747b).
- [28.] Deori K., Ujjain S. K., Sharma R. K., Deka S., (2013), Morphology controlled synthesis of nanoporous Co₃O₄ nanostructures and their charge storage characteristics in supercapacitors, ACS Appl. Mater. Interfaces, 5, 10665-10672, (DOI: 10.1021/am4027482).
- [29.] Ho K. H., Wang J., (2017), Hydrazine reduction of LaNiO₃ for active materials in supercapacitors, J. Am. Ceram. Soc., 100, 4629-4637, (DOI: 10.1111/jace.14997).
- [30.] Lu X.-F., Wu D.-J., Li R.-Z., Li Q., Ye S. -H., Tong Y.-X., Li G. -R., (2014), Hierarchical NiCo₂O₄ nanosheets@ hollow microrod arrays for high-performance asymmetric supercapacitors, J. Mater. Chem. A, 2, 4706-4713, (DOI: 10.1039/c3ta14930g).
- [31.] Manteghi F., Kazemi S. H., Peyvandipour M., Asghari A., (2015), Preparation and application of cobalt oxide nanostructures as electrode materials for electrochemical supercapacitors, RSC Adv., 5, 76458-76463, (DOI: 10.1039/c5ra09060a).
- [32.] Xiong S., Yuan C., Zhang X., Xi B., Qian Y., (2009), Controllable synthesis of mesoporous Co₃O₄ nanostructures with tunable morphology for application in supercapacitors, Chem. Euro. J., 15, 5320-5326, (DOI: 10.1002/chem.200802671).
- [33.] Chen P.-C., Hsieh S.-J., Jou J., Chen C.-C., (2014), Selectively dealloyed Ti/TiO₂ network nanostructures for supercapacitor application, Mater. Lett., 133, 175-178, (DOI: 10.1016/j.matlet.2014.06.165).
- [34.] Gobal F., Faraji M., (2013), Fabrication of nanoporous nickel oxide by de-zincification of Zn–Ni/(TiO₂-nanotubes) for use in electrochemical supercapacitors, Electrochim. Acta, 100, 133-139, (DOI: 10.1016/j.electacta.2013.03.155).
- [35.] Li Z., Zhang W., Yuan C., Su Y., (2017), Controlled synthesis of perovskite lanthanum ferrite nanotubes with excellent electrochemical properties, RSC Adv., 2017, 7, 12931-12937, (DOI: 10.1039/c6ra27423d).
- [36.] George G., Jackson S. L., Luo C. Q., Fang D., Luo D., Hu D., Wen J., Luo Z., (2018), Effect of doping on the performance of high-crystalline SrMnO₃ perovskite nanofibers as a supercapacitor electrode, Ceram. Int., 44, 21982-21992, (DOI: 10.1016/j.ceramint.2018.08.313).

- [37.] Guo Y., Shao T., You H., Li S., Li C., Zhang L., (2017), Polyvinylpyrrolidone-assisted solvothermal synthesis of porous LaCoO₃ nanospheres as supercapacitor electrode, *Int. J. Electrochem. Sci.*, 12, 7121-7127, (DOI: 10.20964/2017.08.47).
- [38.] Ma P., Lei N., Yu B., Liu Y., Jiang G., Dai J., Li S., Lu Q., (2019), Flexible Supercapacitor electrodes based on carbon cloth-supported LaMnO₃/MnO nano-arrays by one-step electrodeposition, *Nanomater.*, 9, 1676, (DOI: 10.3390/nano9121676).
- [39.] Wang X. W., Zhu Q. Q., Wang X. E., Zhang H. C., Zhang J. J., Wang L. F., (2016), Structural and electrochemical properties of La_{0.85}Sr_{0.15}MnO₃ powder as an electrode material for supercapacitor, *J. Alloys Compds.*, 675, 195-200, (DOI: 10.1016/j.jallcom.2016.03.048).
- [40.] Su J., Liu S., Wang J., Liu C., Li Y., Wu D., (2016), Solution-based synthesis of carbon-hematite composite thin films for high-performance supercapacitor applications, *MRS Commun.*, 6, 367-374, (DOI: 10.1557/mrc.2016.60).
- [41.] Ramesh S., Karuppasamy K., Kim H.-S., Kim H., Kim J.-H., (2018), Hierarchical flowerlike 3D nanostructure of Co₃O₄@MnO₂/N-doped Graphene oxide (NGO) hybrid composite for a high-performance supercapacitor, *Sci. Rep.*, 8, 1-11, (DOI: 10.1038/s41598-018-34905-7).
- [42.] Kitchamsetti N., Ma Y. R., Shirage, Devan R. S., (2020), Mesoporous perovskite of interlocked nickel titanate nanoparticles for efficient electrochemical supercapacitor electrode, *J. Alloys. Compd.*, 833, 155134, (DOI: 10.1016/j.jallcom.2020.155134).
- [43.] Wang Y., Lei Y., Li J., Gu L., Yuan H., Xiao D., (2014), Synthesis of 3D-nanonet hollow structured Co₃O₄ for high capacity supercapacitor, *ACS Appl. Mater. Interfaces*, 6, 6739-6747, (DOI: 10.1021/am500464n).
- [44.] Tiwari A. P., Chae S. H., Ojha G. P., Dahal B., Mukhiya T., Lee M., Chhetri K., Kim T., Kim H. Y., (2019), Three-dimensional porous carbonaceous network with in-situ entrapped metallic cobalt for supercapacitor application, *J. Colloid Interface Sci.*, 553, 622-630, (DOI: 10.1016/j.jcis.2019.06.070).

Chapter 5

Mesoporous NiTiO_3 nanostructures

We have synthesized mesoporous nickel titanate (NTO) rods encompassing interlocked nanoparticles with clearly visible textural boundaries via the sol-gel route as an excellent working electrode for the supercapacitor. The mesoporous NTO rods assembled in the hexagonal shape of average diameter $\sim < 1 \mu\text{m}$ and ~ 3 to $6.4 \mu\text{m}$ long are composed of nanoparticles of diameter $\sim 30 \text{ nm}$. The well crystalline NTO rods of the hexagonal phase to the space group of $R\text{-}3\text{H}$ possess average (mean) pore size distribution of 17.48 nm throughout the rod body. The stoichiometric mesoporous NTO rods with increased textural boundaries played a significant role in the larger diffusion of ions and delivered the specific capacitance (C_s) of 542.26 F/g , the energy density of 8.06 Wh/kg , and a power density of 4320 W/kg in an aqueous KOH electrolyte, is significantly better than Ni, Mn, Fe, Cr, and Ti-based perovskites or their mixed-phase accompanied by metal oxides as impurities. Moreover, the diffusion-controlled easy/faster and enhanced access to the OH^- ions ($20.4 \mu\text{s}$) deep inside the rod body delivered a long life cycle, high stability up to 2100 cycles, and excellent retention of 91 %. Overall, mesoporous NTO rods hold potentials as an electrode material for long cycle lifetime supercapacitor and can further improve after forming the nano-hetero-architecture or hybrid structures with other prominent materials such as NiO, and Mn_2O_3 , etc.

5.1 Introduction

Supercapacitors have attracted considerable attention from researchers and industries for their extensive utilization in hybrid electric vehicles, portable devices, industrial uninterruptible power supplies, and military fields due to high power density, long life expectancy, eco-friendliness, and high safety. [1] The pseudocapacitors storing the charges through redox reactions along the textural boundaries deep inside the electrode materials deliver higher capacitance than the electric double-layer capacitors. [2] Carbon materials and conducting polymers with rational porous morphology addresses competitive power density, but the stress induced by shrinkage and swelling during charging-discharging curtail their lifetime and degrade faster. [3] However, transition metal oxides, a better alternative to improve stability and control degradation, are employed in their pure (i.e., NiO, TiO₂, MnO₂, etc.), mixed (i.e., NiO/Co₃O₄, NiO/MnO₂, Co₃O₄ @ MnO₂ or composite (with carbon, graphene, polymer, etc.) [4,5] form to improve the performance of supercapacitors under controlled redox mechanism. Among these, NiO, observed to be the most promising pseudo-capacitive electrode material, offering high specific capacitance (C_s) theoretically of 2584 F/g and providing good electrochemical reaction pathways. Nevertheless, theoretical values for NiO are yet far away to achieve experimentally, [6] the poor electrical conductivity unfavorable to fast ion/electron transport deliver low C_s . The kinetics of electron/ion transport, the electrode/electrolyte interface, and the intrinsic electrochemical pathways of NiO asking for further improvement to enhance the power density and reaction kinetics. [6] TiO₂ is another most fascinating transition metal oxide of vast attraction as electrode material in supercapacitor because of its unique three different morphologies, anatase, brookite, and rutile, providing abundant enough vacant sites to accommodates ion. Even though TiO₂ has delivered better durability and high stability for 10000 cycles, the C_s and power density are a major concern. [7] Therefore, a new approach to blending the properties of Ni and Ti to improve supercapacitive performance is of prime importance. Defect engineering (doping, cationic vacancies, etc.) of oxides of Ni and Ti to increase the overall electrical conductivity of the electrodes [8] can be one approach, and blending both of them in single-phase compounds shall be another excellent approach.

The nanosized perovskite metal oxides with ABO_3 formula, considered to be a replacement for single oxides in the stipulated application, which are under comprehensive investigation for their applications in catalysis, water splitting, supercapacitance, and batteries, etc., [9] demonstrate their capabilities as a promising candidate for supercapacitor. The structural stability of the cations and oxygen ion mobility and vacancies mediate the redox mechanism in the perovskite. [10] Moreover, the presence of multiple transition metal ions in the perovskite structure shall apprehend distinct charge storing mechanisms and hence capable of delivering the breakthrough performance of the supercapacitor. However, most of the studies are focused on Lanthanum based perovskites, which might be owing to their better electrical conductivity. [11] The sol-gel driven $LaFeO_3$ poised into nanotubes under controlled calcination temperature and time delivered the C_s of 313.21 F/g. [11] The Sr doped $LaMnO_3$ provided high electrical conductivity of 44.9 S/cm, but the C_s value was restricted to 56 F/g due to nanoparticle morphologies, [12] expected to improve significantly after realizing nanorods structure. Recently, Arjun et al. [13] explored various Lanthanum based perovskite (i.e., $La(Mn/Fe/Cr/Ni)O_3$) nanoparticles to enhance the C_s by controlling the redox reactions of anion, but only redox reaction involving Ni^{2+} (i.e., $LaNiO_3$) delivered better C_s of 106.58 F/g, which found improved to 280 F/g after hydrazine reduction treatment. [14] Even though few reports are available on the synthesis of NTO one-dimensional nanostructure [15] and nanoparticles, [16,17] none of them are focused on the synthesis of mesoporous rod for utilization as the working electrode in the supercapacitor. Even though Imani et al. [18] have employed microwave irradiation assisted spontaneous combustion for the synthesis of NTO nanoparticles, the presence of the large number of impurity phases of rutile TiO_2 , anatase TiO_2 , and bunsenite NiO restricted their electrochemical performance in aqueous H_2SO_4 and curtailed the C_s to 257 F/g. One of the prerequisites to gain excellent electrochemical performance is the synthesis of pure NTO phase with an enormously larger surface area. One-dimensional morphologies in nanostructural form provide direct pathways for electron/ion transfer at the electrode-electrolyte interface. [5,19]

In this study, we introduced mesoporous NTO rods encompassing interlocked nanoparticles with clearly visible textural boundaries synthesized via sol-gel route as an

excellent working electrode for the supercapacitor. Synthesis of mesoporous NTO rods without any impurity was examined using field-emission scanning electron microscopy (FESEM), BET analysis, X-ray diffraction (XRD), and X-ray photoemission spectroscopy (XPS). The electrochemical mechanism of mesoporous NTO rods was analyzed utilizing contact angle meter, cyclic voltammetry (CV), galvanostatic charging discharging (GCD), and impedance analysis using optimized 2 M aq. KOH electrolyte. Our study corroborates that the mesoporous NTO rods deliver faster/easy access for ion transportation (20.4 μ s), enhanced power density (4320 W/kg), greater retentivity (~91 %), and longer cycles lifetime (2100) with excellent stability.

5.2 Experimental section

The analytical grade chemicals were used for the synthesis of mesoporous NTO rods. 1 M of nickel acetate (Sigma Aldrich, $\text{Ni}(\text{CH}_3\text{COO})_2 \cdot 4\text{H}_2\text{O}$) and 3.4 ml of titanium butoxide (Sigma Aldrich, $\text{Ti}(\text{OC}_4\text{H}_9)_4$) dissolved in ethylene glycol (EG) at room temperature and reacted employing constant stirring for 1 h until obtaining a blue precipitate. It was dried at 60 °C in vacuum for 4 h after cleaning with ethanol by repeated centrifugation and dispersion and subsequently annealed at 600 °C in the ambient atmosphere for 2 h to obtain mesoporous NTO rods encompassing the interlocked nanoparticle. X-ray diffraction (D2-Phaser Bruker, Cu-K α , $\lambda=1.5406 \text{ \AA}$) was utilized to confirm the crystal structure and the nature of the NTO rods. The surface morphological features are confirmed from field emission scanning electron microscopy (FESEM, JEOL JSM-6500F). The surface area and pore size distribution of NTO rods were evaluated using N₂ adsorption-desorption isotherm (BET) and Barrett-Joyner-Halenda (BJH) methods in an automated gas sorption analyzer (Quantachrome Autosorb iQ2). The chemical states and electronic structure of mesoporous NTO rods were explored from an X-ray photoelectron spectrometer (XPS, Thermo Scientific Inc. K-alpha) with a microfocus monochromated Al K α X-rays. The effect of the electrolyte concentration on the ion diffusion was analyzed through the surface wettability studies performed using a drop shape analyzer (DSA-25, Kruss GmbH, Germany). The dilute slurry of a mixture of NTO rods powder, carbon black, and Polyvinylidene fluoride (PVDF) prepared in the N-methyl 2-pyrrolidone (NMP) was drop cast on Ni foam and further dried at 80 °C for 25 h to gain the working electrode. This working electrode of mesoporous NTO rods was

utilized along with pristine ITO/glass as counter electrode and saturated calomel electrode as a reference electrode to investigate the electrochemical properties. The electrochemical measurements were performed at room temperature in 2 M KOH aqueous electrolyte using the electrochemical workstation (Autolab, PGSTAT302N, Metrohm) to investigate the effect of mesoporous morphology, the interlocking of the nanoparticles, and the redox mechanism of Ni and Ti on the pseudocapacitive performance of electrochemical supercapacitor.

5.3 Results and discussion

5.3.1 Field emission scanning electron microscopy

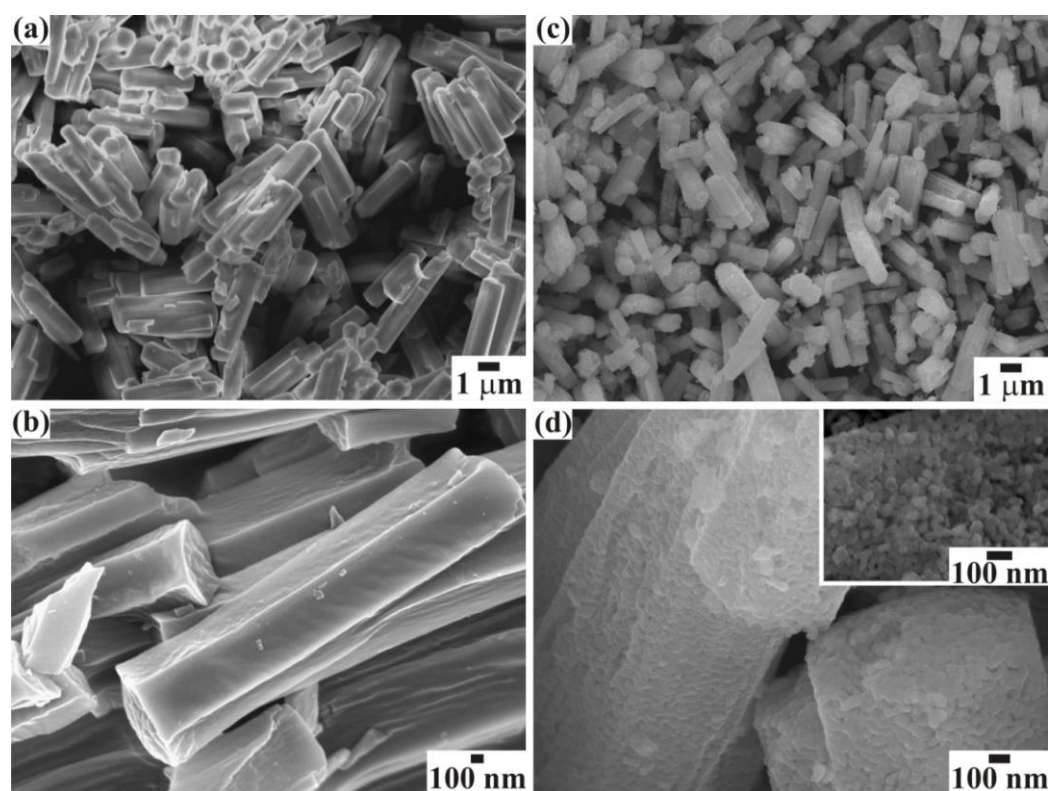


Figure 5.1. FESEM image of as (a) synthesized NiTiO_3 rods (i.e., before annealing) transformed in to (b) mesoporous structure retaining rod morphology after annealing. (c), and (d) shows their respective high magnification FESEM images. (d) Mesoporous NTO rods are composed of interlocked nanoparticles.

FESEM images in Figure 5.1 show the surface morphology of NiTiO_3 nanostructures. The optimized reaction mixture of nickel acetate ($\text{Ni}(\text{CH}_3\text{CO}_2)_2 \cdot 4\text{H}_2\text{O}$), titanium butoxide $\text{Ti}(\text{OCH}_2\text{CH}_2\text{CH}_2\text{CH}_3)_4$ and ethylene

glycol ($C_2H_6O_2$) provided a rod-like structure of length between ~ 3 to $6.4 \mu\text{m}$ and a diameter of $\sim < 1 \mu\text{m}$ (Figure 5.1(a)). Further, the high-magnification FESEM images confirmed that the rods are well separated with clearly visible textural boundaries. The hexagonal-shaped individual rod depicts very smooth facets along the rod body with the nonporous surface (Figure 5.1(b)). The annealing of the as-synthesized NiTiO_3 rods at $600 \text{ }^\circ\text{C}$ for 2 h in an ambient atmosphere has not altered their hexagonal morphology, but the smooth surfaces appear to be coarse in nature (Figure 5.1 (c)). The high magnification FESEM image of the single rods shown in Figure 5.1(d) depicts that the NiTiO_3 rods are composed of numbers of nanoparticles. The numerous nucleation centers activated during the annealing constrained the growth of the nanoparticles along the rod body. The interconnections between every successive nanoparticle retained the hexagonal rod morphology along with their clearly visible facets. However, the textural boundaries of each particle are clearly visible, and the average diameter of the nanoparticles is $\sim 46 \text{ nm}$ (Figure 5.2). The high magnification FESEM image of the single rods shown in Figure 5.1(d) depicts that the NiTiO_3 rods are composed of numbers of nanoparticles. The statistical histogram of the NTO nanoparticle distribution shown in Figure 5.2 confirms that most nanoparticles are distributed in the range of 30-72 nm. However, the maximum number of NTO nanoparticles has a diameter of 42-51 nm.

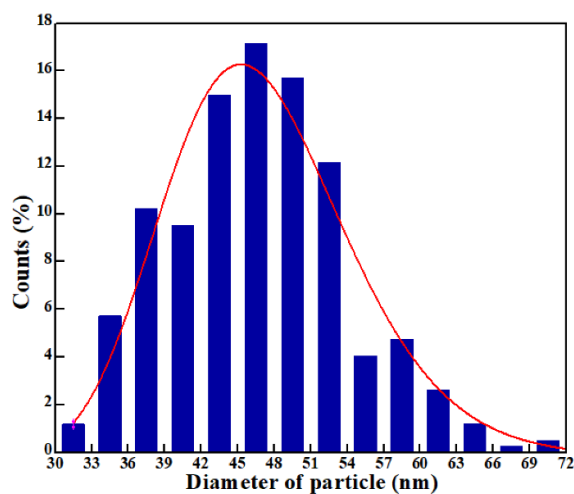


Figure 5.2. Statistical histogram showing the diameter distribution of the nanoparticles forming the mesoporous hexagonal NiTiO_3 rods.

The size distribution of NTO nanoparticles can be fitted using the log-normal size distribution function given below

$$f_N(x) = \frac{A}{x\sigma\sqrt{2\pi}} \exp\left[-\frac{\ln(x/\bar{x})^2}{2\sigma^2}\right] \quad \dots\dots(5.1)$$

Where, x is the diameter of the NTO nanoparticles; \bar{x} ($= 46.49 \pm 0.63$ nm) is the mean diameter of the NTO nanoparticles; A ($= 307.18 \pm 26.71$) is the initial constant; σ ($= 0.16 \pm 0.02$) is the standard deviation of the size of the NTO nanoparticles. The log-normal distribution of the NTO particle diameter is asymmetric. The smaller standard deviation of the diameter ($\sigma \leq 0.25$) confirms that the NTO nanoparticles are well confined to the limited diameter range.

The interconnection between nanoparticles with clearly visible textural boundaries provided the mesoporous nature to NiTiO₃ rods, which confirms that the mesoporous hexagonal NiTiO₃ rods consisting of well-defined nanoparticles were obtained after annealing as-synthesized rods. The EDS analysis was executed on the as-synthesized and annealed mesoporous NTO rods to confirm the effect of annealing on the presence of elements. The EDS spectra of as-synthesized NTO rods is akin to that of mesoporous NTO rods corroborate the existence of Ni, Ti, and O, only, without any impurity (Figure 5.3). This evidenced that the annealing has not altered the elemental concentration of NTO rods but only resulted in the formation of mesoporous NTO rods.

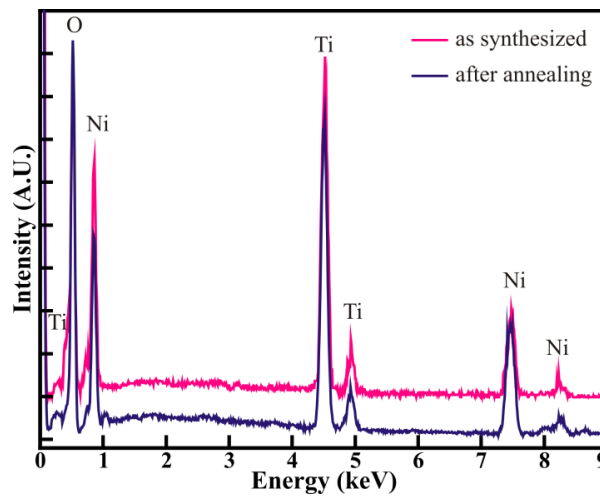


Figure 5.3. EDX spectra of as-synthesized and mesoporous (i.e., annealed) NTO rods.

5.3.2 X-ray photoelectron spectroscopy

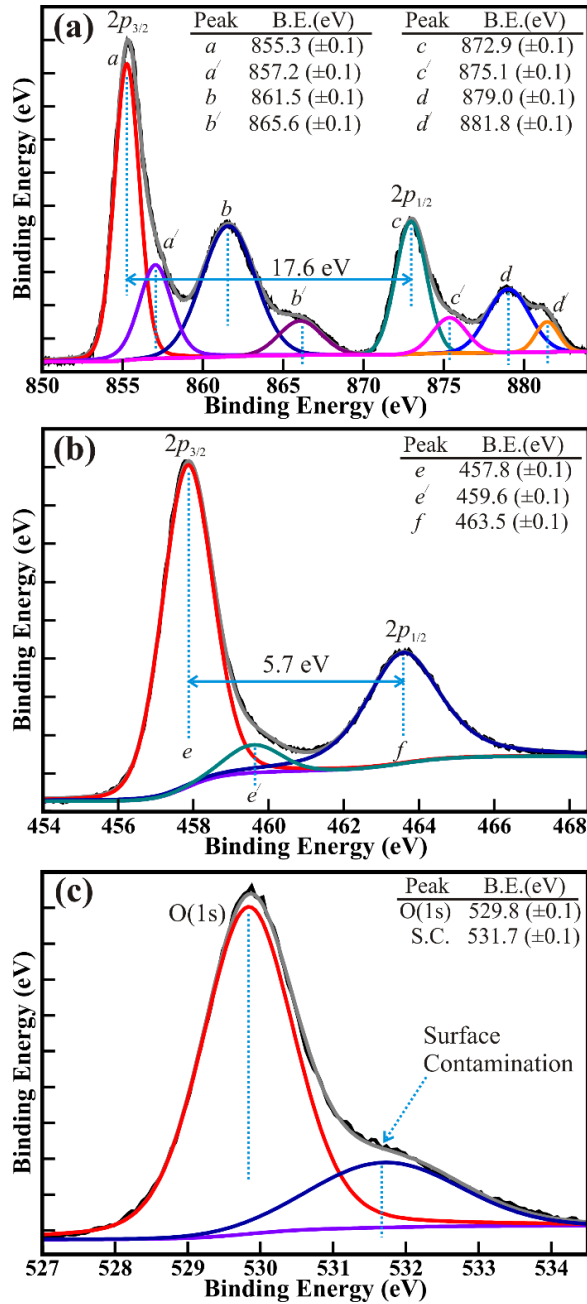


Figure 5.4. Typical high resolution XPS spectra of the (a) Ni (2p), (b) Ti (2p), and (c) O (1s) core levels of the mesoporous NTO rods. The XPS spectra were deconvoluted via the Voigt function within Shirley background.

Further, the quantitative analysis of the electronic structure and chemical properties of NiTiO₃ nanorods was carried out utilizing X-ray photoelectron spectroscopy (XPS). Figure 5.4 shows the XPS spectra of Ni(2p), Ti(2p), and

O(1s) core levels of NiTiO₃ nanorods. The XPS spectrum of the Ni(2p) core levels for the mesoporous NiTiO₃ rods (Figure 5.4 (a)) exhibits four distinctive peaks identified as a, b, c, and d, are located at binding energy (BE) of 855.3, 861.5, 872.9, and 879.0 eV, respectively. The highly intense two peaks located at BE of 855.3 (\equiv a) and 872.9 (\equiv c) eV are assigned to Ni(2p) core levels, and their concomitant peaks at BE of 861.5 (\equiv b), and 879.0 (\equiv d) eV, respectively, are identified as respective shake-up satellite peaks. The Ni(2p) spectrum was fitted via the Voigt function following the Shirley background to precisely determine the double peak features of Ni(2p_{3/2}) and Ni(2p_{1/2}). [20] The decomposed spectra corroborate perfect fit with 8 peaks labeled as a, a', b, b', c, c', d, and d' represents the core levels of the Ni²⁺(2p_{3/2}), Ni³⁺(2p_{3/2}), Ni²⁺(2p_{3/2}) shakeup satellite, Ni³⁺(2p_{3/2}) shakeup satellite, Ni²⁺(2p_{1/2}), Ni³⁺(2p_{1/2}), Ni²⁺(2p_{1/2}) shakeup satellite, and Ni³⁺(2p_{1/2}) shakeup satellite, respectively. The three-fold higher intensity of both the Ni(2p_{3/2}) and Ni(2p_{1/2}) core levels of Ni²⁺ than that of the core levels of Ni³⁺ revealed the significant appearance of Ni²⁺ cations in the mesoporous NiTiO₃ rods and very minor traces of Ni³⁺ formation. The spin-orbit splitting between the Ni(2p_{3/2}) and Ni(2p_{1/2}) core levels and their respective shakeup satellite peaks are 17.6 and 17.5 eV, respectively, is also akin to that assigned for the formation of Ni²⁺, and not for Ni³⁺ or metallic Ni. [6] Likewise, the XPS spectrum of the Ti(2p) core levels for the NiTiO₃ rods illustrate two distinctive peaks identified as e, and f at the BE of 457.8 and 463.5 eV, respectively, represents the core levels of Ti(2p_{3/2}) and Ti(2p_{1/2}) for Ti⁴⁺ cations. However, this spectrum was fitted using the Voigt function following the Shirley background to precisely determine the features of the double peaks of Ti (2p_{3/2}) and Ti (2p_{1/2}) core levels. The deconvoluted spectra perfectly fit for three peaks located at a binding energy of 457.8, 459.6, and 463.5 eV represents the Ti⁴⁺(2p_{3/2}), Ti³⁺(2p_{3/2}), and Ti²⁺(2p_{1/2}) core levels, respectively. Nevertheless, the nine-fold higher intensity of the Ti(2p_{3/2}) core levels of Ti⁴⁺ than that of the core levels of Ti³⁺ confirm the existence of the negligible amount of Ti³⁺ cations. The spin-orbit splitting of 5.7 eV observed between the Ti(2p_{3/2}) and Ti(2p_{1/2}) core levels reflect Ti⁴⁺ cations. [7,21,22] The compound peak feature found for O(1s) XPS spectrum was

decomposed via Voigt fitting function within the Shirley background (Figure 5.4(c)) to reconfirm the oxidation state of the Ni and Ti elements in the mesoporous NTO rods. The deconvolution of the spectra shows the perfect fit for two peaks located at BE of 529.8 and 531.7 eV. The highly intense peak observed at the lower BE of 529.8 eV corresponds to the O(1s) core level of the O²⁻ anions in NiTiO₃ rods. A higher BE peak at 531.7 eV is attributed to surface contamination, such as carbon oxides or hydroxides. [23-25] However, the six-fold higher intensity of the O(1s) core levels of O²⁻ than that of the peak at BE of 531.7 substantiate the significantly lower amount of surface contamination. Moreover, the BE separation of 72.0 eV observed for Ti(2p_{3/2}) and O(1s) core levels of the mesoporous NTO rods is very close to that represents Ti⁴⁺ cations (i.e., 71.5) and significantly smaller than the Ti²⁺ (75.0 eV) and Ti³⁺ (73.4 eV). [26,27] This reconfirms the existence of the significant quantity of Ti⁴⁺ cations in the mesoporous NiTiO₃ rods and a scarcely detectable amount of Ti³⁺ cations. Moreover, the insignificant presence of Ni³⁺ is accompanied by the Ti³⁺ or vice-versa, confirmed the stoichiometric resemblance between Ni and Ti in the mesoporous NTO rods, which further avert the formation of non-stoichiometric or additional phases of Ti₂O₃, and Ni₂O₃, etc. Overall, the XPS analysis confirms the formation of stoichiometric mesoporous NTO rods composed of nanoparticles.

5.3.3 X-ray diffraction

Structural analysis of the mesoporous NiTiO₃ rods is carried out by the Rietveld refinement of XRD spectra (Figure 5.5). The refinement confirmed the well crystalline nature of NTO rods in the hexagonal phase to the space group of R-3H. The XRD peaks of mesoporous NTO rods at 2θ of 24.1°, 33.1°, 35.6°, 39.1°, 41.9°, 43.5°, 49.4°, 53.9°, 57.4°, 62.4°, 64°, 69.4°, 72.1°, 75.5°, and 77.7° are attributed to the (101), (104), (110), (006), (021), (202), (024), (216), (018), (214), (030), (208), (219), (220), and (036) crystal planes, respectively, well-matched with the ICSD code 171584. The x-ray density, R_f factor, Bragg R-factor, χ² value, and the goodness of fit factor (GofF) observed from Rietveld refinement are 5.121 g/cc, 37.4, 12.1, 2.97, and 1.7, respectively. The lattice parameters gained are a =

$b = 5.03 \text{ \AA}$, and $c = 13.82 \text{ \AA}$. This indicates the good agreement of the calculated data with that of experimentally observed patterns. Moreover, no characteristic peaks indicating the formation of NiO, TiO₂, or other impurities phases are observed, confirm the synthesis of pure NTO rods.

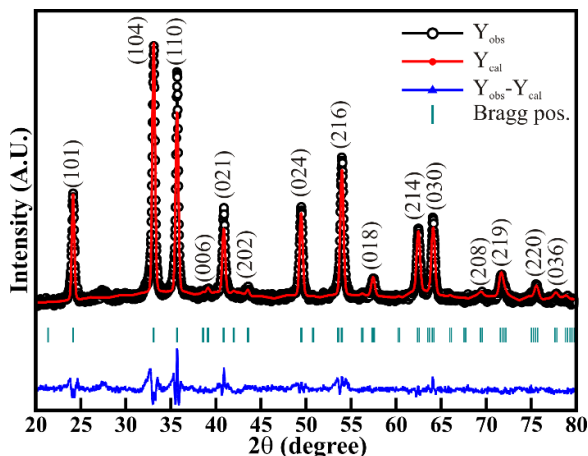


Figure 5.5. Rietveld refined XRD pattern of NTO rods along with the residual curve located at the bottom.

5.3.4 Nitrogen adsorption-desorption isotherm

Nitrogen adsorption-desorption isotherm measurements were performed to evaluate the pore structure of NTO rods and the surface area of the nanoparticles encompassed in their growth. The Brunauer-Emmett-Teller (BET) analysis in Figure 5.6 represents the mesoporous nature of the NTO rods. Figure 5.6(a) shows type IV isotherm with a distinct hysteresis loop in the P/P_0 range of 0.4-1.0, substantiate the extensive distribution of internal voids along the rod body due to the interlocked arrangement of the nanoparticles. The interconnected nanoparticles led the broad range of voids throughout the rods and resulted in the evaluation of hexagonal ordered mesoporous NTO rods. The pore volume and (BET) surface area of the NTO rods is around $0.087 \text{ cm}^3/\text{g}$ and $33.154 \text{ m}^2/\text{g}$, respectively. The maximum distribution of pores was observed in the range of 3.40 to 316.62 nm; nevertheless, the larger pore size of 316.62 nm is perceived (Figure 5.6(b)). The large number of pores are $\sim 0.087 \text{ cc/g}$ nm wide, and the average (mean) pore size distribution is 17.481 nm. The interconnected nanoparticles with the pertinent pores formed the mesoporous NTO rods and

provided ample sites along the enhanced surface area for accumulation of ions, and hence expected to escalate the interaction at the interface of electrode-electrolyte. Furthermore, the easily accessible mesoporous surface inside the microrod encompassing interconnected nanoparticles alleviates the ion/electrolyte penetration deep inside and further enhances the faradaic charge storage mechanism.

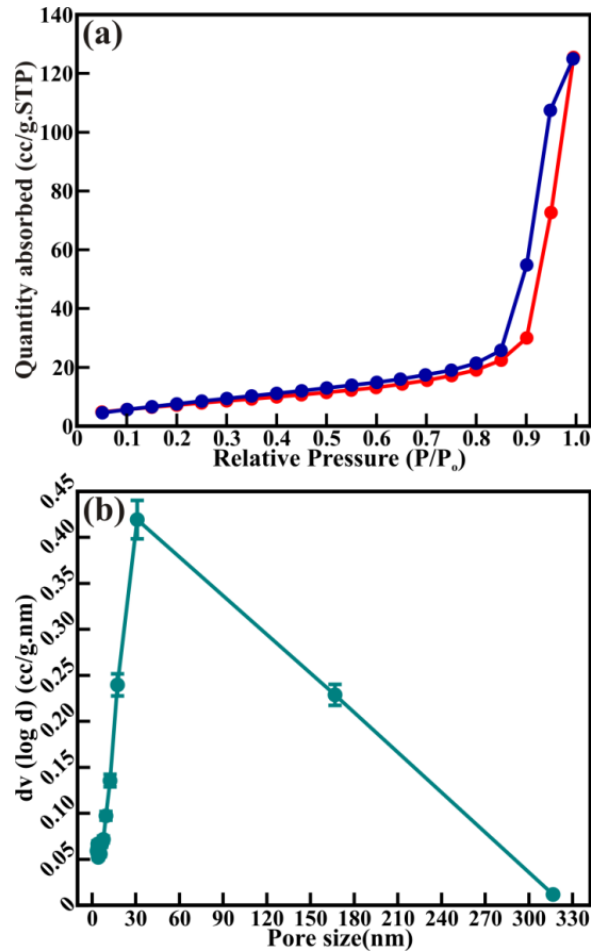


Figure 5.6. (a) N₂ adsorption-desorption isotherm, and (b) BJH pore size distribution of the mesoporous NTO rods.

5.3.5 Contact angle measurements

The electrolyte interface with the NTO controls the intercalation of the ions, thereupon the energy storage ability of NTO rods. Therefore, mesoporous NTO rods were subjected to understand the surface wettability of the electrolyte via contact angle measurement. [18] Figure 5.7 shows the molarity dependent

surface wettability (i.e., contact angle) at the electrolyte-electrode interface. The wettability test was carried under the various molarities of aq. KOH electrolytes. The 0.5, 1, 1.5, and 2 M KOH electrolyte delivered the average contact angle of 82.9°, 78.2°, 56.1°, and 52.4°, respectively. Interestingly, the contact angle of 82.9° observed for 0.5 M KOH was reduced drastically to 56.1° for the 1.5 M KOH. Further increase in the molarity of KOH to 2 M showed a slight reduction to 52.4°, indicate the intimate contact of 2 M KOH with an electrode surface, contributing to easy transfer of electrons at the interface, which further facilitates better energy storage performance of supercapacitor. Therefore, in the quest for better wettability and lower contact angle, the electrochemical measurements were carried out using 2 M KOH electrolyte.

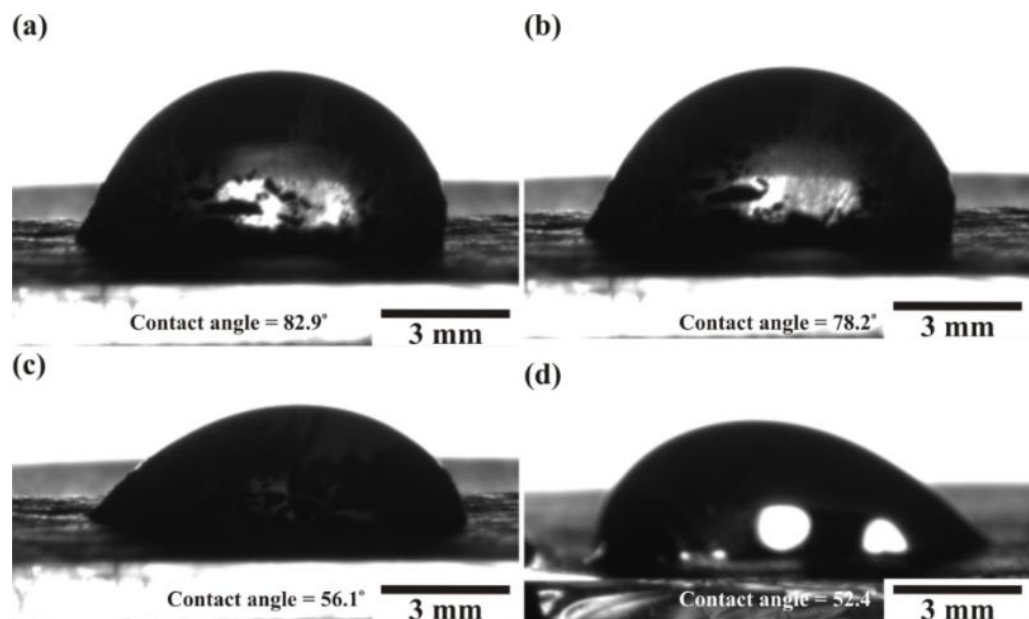


Figure 5.7. Contact angle measurement showing the interface of the aqueous KOH electrolyte of (a) 0.5 M, (b) 1M, (c) 1.5 M, and (d) 2 M concentration on the surface of the working electrode of mesoporous NTO rods.

5.3.6 Electrochemical analysis

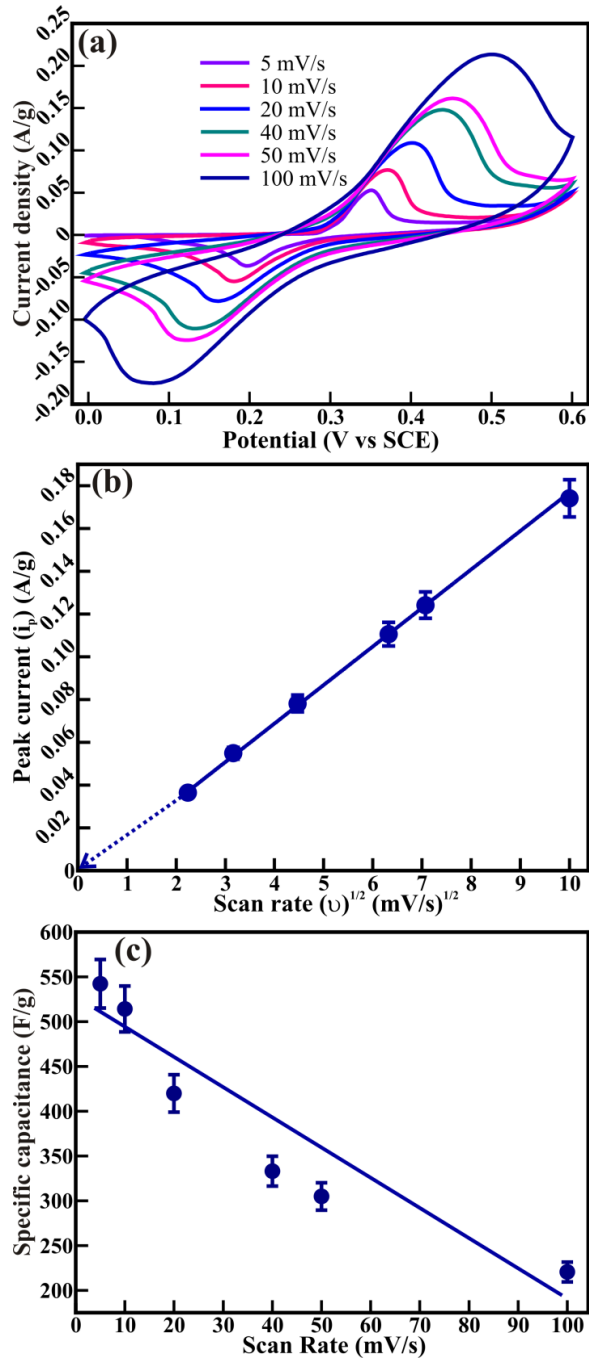


Figure 5.8. (a) Cyclic voltammograms of mesoporous NTO rods at various scan rates in 2 M aq. KOH electrolyte. The graphical illustration of (b) the anodic peak current density (i_p) with the square root of the scan rate ($v^{1/2}$) and (c) specific capacitance at various scan rates, evaluated from the CV curve.

The electrochemical properties of mesoporous NTO rods were confirmed from cyclic voltammetry (CV), galvanostatic charge-discharge (GCD), and electrochemical impedance spectroscopy (EIS) measurements in the 2 M KOH electrolyte. The CV measurement was performed in the potential range of 0 to 0.6 V at various scan rates (Figure 5.8(a)). The two distinct peaks observed at negative and positive current densities in the potential range of 0 to 0.6 V elucidate the reduction and oxidation of NTO rods. Moreover, these oxidation and reduction peaks have shifted to relatively higher and lower applied potentials with an increase in the scan rate. The oxidation peak observed for the potential of 0.351 V at a scan rate of 5 mV/s has shifted by 0.149 V (i.e., observed at 0.5 V) at the scan rate of 100 mV/s. Likewise, the reduction peak observed at 0.195 V for a scan rate of 5 mV/s has shifted by 0.12 V (i.e., observed at 0.075 V) after increasing the scan rate of 100 mV/s. This shifting in the oxidation and reduction peaks with an increase in the scan rate is assigned to the kinetics of carriers and potential of the reference electrode, akin to that observed for NiO nanoparticle, [28] LaFeO₃ nanotubes, [11] and mesoporous (Ni₂(CO₃)(OH)₂ · H₂O) flowers. [29] Furthermore, the area under the CV curve enhanced due to improved peak intensity with an increase in the scan rate. The increase in the scan rate leads to enhancement in the area under the CV curves.

The scan rate dependent variation in the current density can be interpreted from the Randle-Sevcik equation, [30]

$$i_p = 2.69 \times 10^5 C_o n^{3/2} \nu^{1/2} D^{1/2} \dots (5.1)$$

Where, the peak current density (i_p) of the electrochemical reaction is proportional to the square root of the scan rate (ν), i_p is the peak current density (mA/g), C_o is the concentration of OH⁻ ions in the electrolyte solution (mol/cm²), n is the number of electrons, ν is the scan rate (mV/s), and D is the diffusion coefficient for OH⁻ ions in the electrode material. The graphical representation of the peak current density of the anodic reduction peak (i_p) with the square root of the scan rate (ν) demonstrates the linear behavior (Figure 5.8(b)). The straight-line encompassing all the points pass through the origin (extrapolated dotted line) confirms the

diffusion-controlled adsorption and desorption of OH⁻ ions along the surface of mesoporous NTO rods.

The C_s evaluated (Figure 5.8(c)) from the CV curves at various scan rates (Figure 5.8(a)) using the equation

$$C_s = \frac{\int idV}{2m v \Delta V} \dots\dots\dots (5.2)$$

Where, C_s is the specific capacitance (F/g), m is the mass of the NTO rods loaded in the working electrode (g), v is the scanning rate (mV/s), and ΔV is the applied potential range (V), and ∫ idV is the integral area under the CV curve. The evaluated C_s values linearly varied with the scan rate. The C_s value of 542.3 F/g gained at a scan rate of 5 mV/s was retained to 220.5 F/g for the scan rate to 100 mV/s. The larger C_s value of 542.3 F/g might have resulted from the OH⁻ ions easily accessed deep inside the mesoporous NTO rods and further diffusion in a large number along the surface of nanoparticles assembling the mesoporous NTO rods. The slower scan rate paved the more extensive diffusion of ions along the working electrode of mesoporous NTO nanorods. The increased scan rate is expected to restrict the easy access of more significant amounts of OH⁻ ions quickly, hence reducing the C_s relatively.

Table 5.1: Comparative analysis of the specific capacitance (C_s) values of various materials reported in the literature.

S./N.	Materials	C _s	Ref.
1.	Mesoporous NTO	542.3 F/g	Current work
2.	Spray deposited NiO thin films	405 F/g	[31]
3.	Chemically grown porous thin film	69.8 F/g	[9]
4.	Microwave power assisted NiO nanoflakes	252 F/g	[32]
5.	Trisodium citrate assisted NiO nanospheres	463 F/g	[33]
6.	Porous NiO nanocrystals	390 F/g	[8]
7.	Selectively dealloyed Ti/TiO ₂ network nanostructures	35.5 F/g	[34]

8.	One-dimensional brookite TiO ₂ nanoneedles	34.1 mF/g	[7]
9.	NiO@MnO ₂ core-shell nanocomposite	266.7 F/g	[35]
10.	NiO-MnO ₂ /MWCNT composite	193.5 F/g	[36]
11.	LaNiO ₃	280 F/g	[14]
12.	LaFeO ₃	375.7 F/g	[11]
13.	SrMnO ₃	321.7 F/g	[39]
14.	Sr doped LaMnO ₃	102 F/g	[40]

The C_s value of 542.3 F/g obtained for the mesoporous NTO rods is relatively larger than the pristine NiO, and TiO₂ nanostructure morphologies such as spray deposited NiO thin films, [31] chemically grown porous thin film, [9] microwave power-assisted NiO nanoflakes, [32] trisodium citrate assisted NiO nanospheres, [31] porous NiO nanocrystals, [8] selectively dealloyed Ti/TiO₂ network nanostructures, [34] one-dimensional brookite TiO₂ nanoneedles, [7] NiO@MnO₂ core-shell nanocomposite, [35] and NiO-MnO₂/MWCNT composite. (Table 5.1) [36] The TiO₂ crystals grown over the 3D rGO using cellulose as the structure-directing agents for shape control restricted C_s to 397 F/g owing to the composite nature of TiO₂ and rGO. [37] Furthermore, Zhao et al. [38] employed Ti and Ni in combination with rGO to enhance supercapacitor performance. The hydrothermal loading of TiO₂ and Ni(OH)₂ over rGO in different weight proportions expected to improve the electron transfer and conductivity restricted the C_s to 374.3 F/g in 1M KOH electrolyte. Moreover, NTO has provided substantially higher C_s value than the other undoped and doped ABO₃ family members (Table 5.1) such as LaNiO₃, [14] LaFeO₃, [11] SrMnO₃, [39], and Sr doped LaMnO₃. [40] Arjun et al. [13] explored the utilization of Mn, Fe, Cr, and Ni in the Lanthanum based perovskites to improve C_s values. The intrinsic properties of Ni exhibited C_s of 106.58 F/g, but all others were restricted in the range of 16.43 to 56.78 F/g. This indicates that the pure phase formation of Ti and Ni (i.e., NTO) provides improved C_s values than that of pristine Ti and Ni oxides, or their composites, or core-shell structures. Even though Imrani et al. [18] reported the synthesis of microwave irradiated NTO nanoparticles, their

electrochemical performance restricted the values of C_s to 257 F/g, which might be due to the highly agglomerated nanoparticles resulting in the uncontrolled redox mechanism. Overall, interlocked nanosized particles delivering mesoporous NTO rods with increased textural boundaries played a significant role in the larger diffusion of ions, further leading to enhanced C_s .

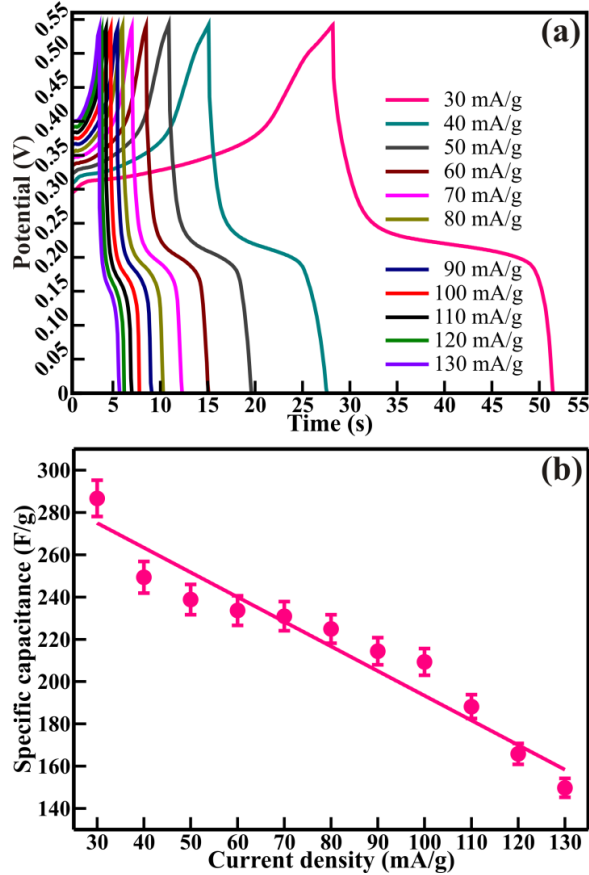


Figure 5.9. (a) GCD curves, and (b) evaluated specific capacitance of mesoporous NTO rods at various current densities.

The current density influences the exchange of ions between the electrolyte and the working electrode. The galvanostatic charging-discharging (GCD) of mesoporous NTO rods studied at various current densities ranging between 30 to 130 mA/g is shown in Figure 5.9. The relatively symmetric nature of charging and discharging curves interprets the highly reversible transportation of ions along the textural boundaries of the NTO nanoparticles encompassed in the mesoporous rods. The nonlinear charge/discharge curves confirmed the pseudocapacitance behavior of the mesoporous NTO rods, which is in close

agreement with the cyclic voltammetry curves showing the redox peaks. The accessibility of ions through porous sites of the electroactive material is vital for an efficient faradaic redox reaction mechanism.

The increase in current density furnishes faster diffusion of ions and hence reduces charging/discharging time (Figure 5.9(a)). The OH⁻ ions have sufficient time to penetrate deep inside the porous surface of the NTO rods electrode at lower current density than that of higher current density. The current density-dependent values of C_s of the mesoporous NTO rods (Figure 5.9(b)) is calculated from the GCD curves using the equation

$$C_s = I \cdot dt / m \cdot dV \quad \dots\dots (5.3)$$

Where, C_s is the specific capacitance of the mesoporous NTO rods (F/g), I is the current density (A/g), m is the mass of the NTO on the working electrode (g), and dV/dt is the slope of the discharge curve. The values of C_s decreased linearly with an increase in the current density. The maximum C_s of 286.6 F/g obtained for the current density of 30 mA/g is reduced to 165.7 F/g after increasing the current density to 130 mA/g (Figure 5.9(b)). The C_s value of 286.6 F/g achieved from mesoporous NTO rods is significantly higher than the values gained from the other perovskites consisting of Ni divalent ions. The nanocomposite powder consisting of NiO, Ni(OH)₂, La₂O₃, and La(OH)₃ (i.e., 70 F/g), which was further reduced to LaNiO₃ by refluxing in the hydrazine for 12 h. (i.e., 280 F/g). [14] Moreover, the sol-gel processed perovskite LaFeO₃ nanoparticles converted in to nanotube morphologies after high-temperature calcination are found greatly oxygen-deficient from XPS analysis for O(1s) peak. The oxygen deficiency might have restricted their supercapacitor performance and hence restrain C_s values. [11] The La³⁺ ions expected to be ion buffering reservoir and particle growth controller created remarkable crystal defects after replacing Ni atoms from the lattice of NiO microspheres and could achieve the maximum C_s of 253 F/g, [41] which is even lesser than the mesoporous NTO rods. Furthermore, it is found to be either better or compatible with the microwave-assisted nanoflake structured NiO (i.e., 209 F/g), [32] metal complex derived NiO nanotubes (i.e., ~80 F/g), [26] porous 2D NiO nanoplates (i.e., 285 F/g) stacked in nanocolumn form after hydrothermal

dehydration and recrystallization, [42] and 1D brookite TiO₂ nanoneedles. [7] This reconfirms that the mesoporous NTO rods are better electrode materials than the other perovskite family members in their pristine or defective form.

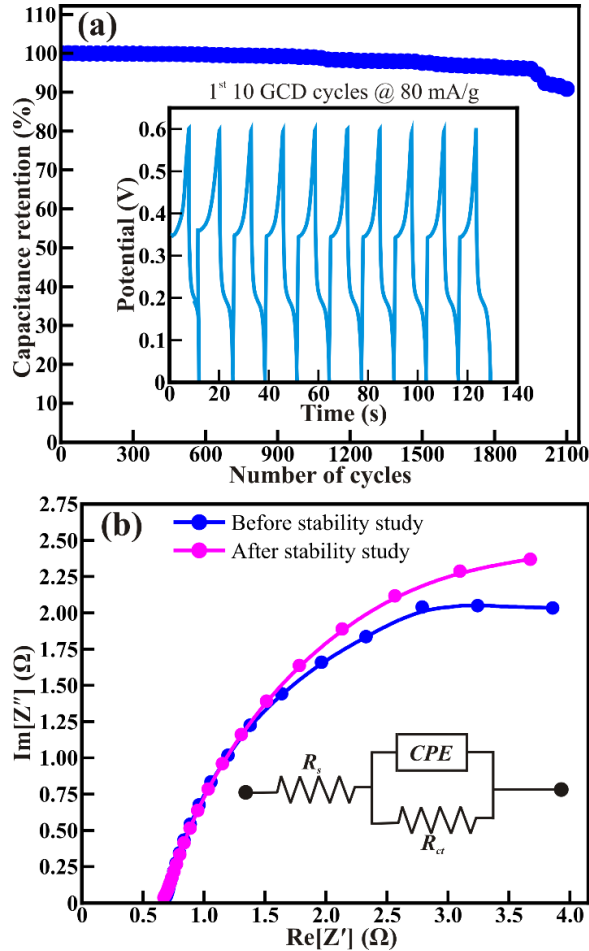


Figure 5.10. (a) Cycling stability and capacitance retention of mesoporous NTO rods analyzed from GCD at the current density of 80 mA/g for 2100 cycles. The inset figure shows the first 10 cycles. The percentage number signifies the retention of the C_s with GCD cycles. (b) Nyquist (EIS) plot of the mesoporous NTO rods obtained before and after cyclic stability and its best fitted equivalent circuit model.

The longer lifetime and excellent cycling stability are the prerequisite features for highly stable supercapacitors. The cyclic stability for long time usage of mesoporous NTO rods was explored for continuous charging-discharging cycles of 2100 at the current density of 100 mA/g (Figure 5.10(a)). The first 10

GCD cycles are shown in the inset of Figure 5.10(a). During the stability study, the GCD curves showed symmetry in the charging, and the discharging process confirmed their stable performance. The evaluated C_s value dropped to ~ 260.8 F/g after the continuous GCD cycles of 2100, which is a relatively very slower reduction. This ~ 91 % retention of C_s attained for the mesoporous NTO rods is more phenomenal than the values obtained for microwave irradiated NTO nanoparticles. [18] Those microwaves irradiated agglomerated nanoparticulate morphology of NTO cultivated an uncontrolled redox process and restricted cyclic performance and stability (~ 92 % retention for 1000). Moreover, the stability performance of mesoporous NTO rods is compatible with the synthesized SrMnO_3 nanofibers delivering 87 % retention for 5000 cycles, [39] and calcination temperature, and time-controlled sol-gel driven LaFeO_3 nanotubes providing 86.1 % retention after 5000 cycles. [11] This distinct stability performance of mesoporous NTO rods confirms the longer lifetime, better durability, better cycling stability, and excellent electrochemical reversibility in 2 M aq. KOH electrolyte.

5.3.7 Electrochemical impedance spectroscopy

The textural boundaries, surface morphology, the core of the nanostructures, and the electrical properties of the active materials play a crucial role in the diffusion of ions from the electrolyte. Therefore, electrochemical impedance spectroscopy (EIS) was utilized to understand the involvement of electrical resistance and textural boundaries in the diffusion of OH^- ions in the mesoporous NTO rods. Figure 5.10(b) illustrates the typical Nyquist plots of the mesoporous NTO rods in 2 M KOH electrolyte. The EIS spectrum recorded on mesoporous NTO rods (i.e., before stability studies) is akin to that recorded after stability study for continuous 2100 charging-discharging cycles. The distinguished impedance spectra represent a perfect fit for semicircular arc corresponding to the charge-transfer resistance at the interface of mesoporous NTO rods and electrolytes. These semicircular arcs of impedance spectra are akin to the experiential for TiO_2 , [7] NiO , [28] Sr doped LaMnO_3 , [12] NiMnO_3 -nitrogen-doped graphene composite, [43] and PIL: RG-O. [44] The intercept and

diameter of the semicircular arc represent the electrolyte resistance (R_e) and charge transfer resistance (R_{ct}), respectively. The R_{ct} of 5.43 Ω for mesoporous NTO rods has increased to 6.94 Ω after 2100 charge-discharge cycles. However, the values of R_e gained before stability studies (0.67 Ω) remained identical even after continuous charging-discharging for 2100 cycles (0.65 Ω). This indicates the partial reduction in the charge diffusion mechanism of the mesoporous NTO rods after 2100 cycles, which was as expected and well supporting the evaluated C_s values after stability studies. The equivalent circuit for the EIS measurements composed of electrolyte resistance (R_e), charge transfer resistance (R_{ct}), and constant phase elements is represented in the inset of Figure 5.10(b). Overall, it revealed that mesoporous NTO rods comprising interconnected nanoparticles offering larger surface area along with clearly visible textural boundaries provided easy and enhanced access to the OH^- ions from the aqueous electrolyte deep inside. The time constant calculated from equation

$$\tau = \frac{1}{2\pi f^*} \quad \text{----- (5.4)}$$

Where, f^* is the frequency corresponding to the maximum of the imaginary component of the semicircle. The calculated values of time constant of 2.04 μs before stability studies reveal the easy access for the transport of OH^- ions along the textural boundaries and also deep inside the mesoporous morphology of the NTO rod. Which is crucial to ensure the fast charging-discharging mechanism of the electrochemical supercapacitor. The time constant further increased slightly by 0.33 μs (i.e., 2.37 μs) signifies persistent easy access for the transport of OH^- ions even after the continuous 2100 charging-discharging cycles, confirms the excellent cyclic stability of mesoporous NTO rods.

5.3.8 Ragone plot

The correlation of the evaluated energy and power density is shown in Figure 5.11. The power density reduced comparably to the energy density with an increase in the GCD current density from 30 to 130 mA/g. The maximum power density of 4320 W/kg and energy density of 8.1 Wh/kg gained from mesoporous NTO rods encompassing interlocked nanoparticles which is significantly better

than other perovskite compounds reported in the literature. The power density of NiTiO₃ is considerably higher than the electrodeposited core-shell structure of Ni(OH)₂ @ 3D Ni, [1] 3D nanonet hollow structured Co₃O₄, [4] template-based synthesis of NiCo₂O₄ nanosheets@ hollow microrod arrays, [5] Co₃O₄ @ Ni(OH)₂ core-shell electrode, [17] KNiF₃ nanocrystal, [45] and Sr doped LaMnO₃ nanoparticles [40] (Table 5.2). The nanocrystal of the KNiF₃ perovskite restricted the power density to 242 W/kg, [45] owing to the nanoparticles of uneven morphologies restricting the easy accesses of electrons for redox species of K and Ni, which was further improved after partial replacement between Ni and Co for the optimal synergistic effect of Ni and Co redox species. Moreover, the performance of mesoporous NTO rods is relatively excellent, then pristine and Sr doped LaMnO₃ nanoparticles. [40] The doping of Sr in the perovskite of LaMnO₃ is expected to provide effective charge storage after assisting the surface redox process of Mn²⁺/Mn³⁺ and Mn³⁺/Mn⁴⁺, deprived the performance of LMO in actual and restricted both the power and energy density to 120 W/kg and 3.9 Wh/kg, respectively. This significant performance is ascribed to the large surface area, mesoporous nature, clearly visible textural boundaries, enhanced/stable electrochemical performance of the 1D morphologies of interlocked NTO nanoparticles.

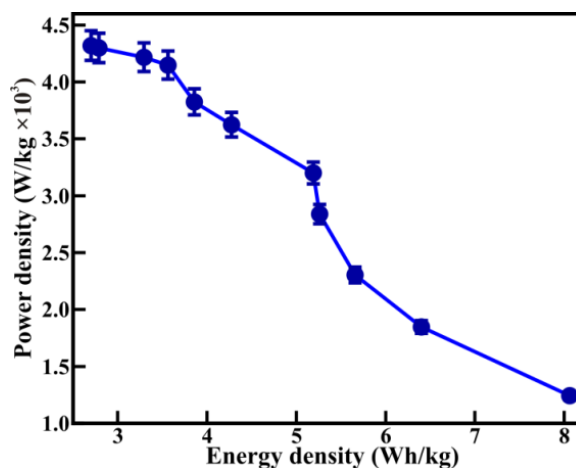


Figure 5.11. Evaluated energy and power density of mesoporous NTO rods determined at various current densities.

Table 5.2: Comparative analysis of the power density of various materials reported in the literature.

S./N.	Materials	Power density	Ref.
1.	Mesoporous NTO	4320 W/kg	Current work
2.	core-shell Ni(OH) ₂ @ 3D Ni	100 W/kg	[45]
3.	3D nanonet hollow structured Co ₃ O ₄	100 W/kg	[46]
4.	NiCo ₂ O ₄ nanosheets@ hollow microrod arrays	100 W/kg	[47]
5.	Co ₃ O ₄ @ Ni(OH) ₂ core-shell structure	33.46 W/kg	[48]
6.	KNiF ₃ nanocrystals	242 W/kg	[49]
7.	Sr doped LaMnO ₃ nanoparticles	120 W/kg	[40]

5.4 Conclusion

In summary, we report the synthesis of mesoporous nickel titanite (NTO) rods encompassing hierarchically interlocked nanoparticles with clearly visible textural boundaries. The NTO nanoparticles of diameter ~ 30 nm hierarchically arranged in the hexagonal form delivered mesoporous rods of the average pore size distribution of 17.481 nm throughout the rod body. The mesoporous NTO rods of average diameter $\sim < 1 \mu\text{m}$, and ~ 3 to $6.4 \mu\text{m}$ long are of hexagonal crystalline phase to the space group of R-3H. XPS analysis revealed the insignificant existence of Ni²⁺/Ni³⁺ and Ti⁴⁺/Ti³⁺, confirmed the formation of stoichiometric NTO rods. The hierarchical interlocking of nanosized NTO particles resulted in the mesoporous NTO rods with increased textural boundaries offered a larger surface area for substantially larger diffusion of OH⁻ ions, further leading to enhanced C_s of 542.26 F/g in optimized 2 M aq. KOH electrolyte. The diffusion-controlled easy/faster access to the OH⁻ ions (20.4 μs) deep inside the rod body through the mesoporous, possess significantly higher power density (4320 W/kg) and energy density (8.06 Wh/kg) than the other perovskite family members in their pristine or defective form incorporating oxide form of Ni, Mn, Fe, Cr, and Ti, etc. Furthermore, the excellent stability of up to 2100 cycles with the retention of 91 % endorses the

mesoporous NTO rods as competent electrode materials for the supercapacitor with stable performance. Moreover, the mesoporous nature and morphology dependent distinctive electrochemical properties revealed in this study have opened a new pathway to explore the nano-hetero-architectures or hybrid structures of NTO with other promising materials like Ni/Mn/Cu-oxides as electrode materials for hybrid supercapacitors, which may further improve the specific capacitance and cyclic stability.

5.5 References

- [1.] Zhi M., Xiang C., Li J., Li M., Wu N., (2013), Nanostructured carbon metal oxide composite electrodes for supercapacitors: a review, *Nanoscale*, 5, 72-78, (DOI: 10.1039/c2nr32040a).
- [2.] Wang G., Zhang L., Zhang J., (2012), A review of electrode materials for electrochemical supercapacitors, *Chem. Soc. Rev.*, 41, 797-828, (DOI: 10.1039/c1cs15060j).
- [3.] Jiang H., Lee P. S., Li C., (2013), 3D carbon based nanostructures for advanced supercapacitors, *Energy Environ. Sci.*, 6, 41-53, (DOI: 10.1039/c2ee23284g).
- [4.] Xia X., Tu J., Zhang Y., Wang X., Gu C., Zhao X.-B., Fan H.J., (2012), High-quality metal oxide core/shell nanowire arrays on conductive substrates for electrochemical energy storage, *ACS Nano*, 6, 5531-5538, (DOI: 10.1021/nn301454q).
- [5.] Devan R.S., Patil R.A., Lin J.H., Ma Y.R., (2012), One-dimensional metal-oxide nanostructures: recent developments in synthesis, characterization, and applications, *Adv. Funct. Mater.*, 22, 3326-3370, (DOI: 10.1002/adfm.201201008).
- [6.] Patil R.A., Chang C.P., Devan R.S., Liou Y., Ma Y.-R., (2016), Impact of nanosize on supercapacitance: study of 1D nanorods and 2D thin-films of nickel oxide, *ACS Appl. Mater. Interfaces*, 8, 9872-9880, (DOI: 10.1021/acsami.6b00487).
- [7.] Devan R.S., Ma Y.R., Patil R.A., Lukas S.M., (2016), Highly stable supercapacitive performance of one-dimensional (1D) brookite TiO₂ nanoneedles, *RSC Adv.*, 6, 62218-62225, (DOI: 10.1039/c6ra11348f).
- [8.] Zheng Z., Chen J., Yoshida R., Gao X., Tarr K., Ikuhara Y.H., Zhou W., (2014), One-step synthesis of TiO₂ nanorod arrays on Ti foil for supercapacitor application, *Nanotechnology*, 25, 435406, (DOI: 10.1088/0957-4484/25/43/435406).

- [9.] Kostopoulou A., Kymakis E., Stratakis E., (2018), Perovskite nanostructures for photovoltaic and energy storage devices, *J. Mater. Chem. A*, 6, 9765-9798, (DOI: 10.1039/c8ta01964a).
- [10.] Mefford J.T., Hardin W.G., Dai S., Johnston K.P., Stevenson K.J., (2014), Anion charge storage through oxygen intercalation in LaMnO_3 perovskite pseudocapacitor electrodes, *Nat. Mater.*, 13, 726-734, (DOI: 10.1038/nmat4000).
- [11.] Li Z., Zhang W., Yuan C., Su Y., (2017), Controlled synthesis of perovskite lanthanum ferrite nanotubes with excellent electrochemical properties, *RSC Adv.*, 7, 12931-12937, (DOI: 10.1039/c6ra27423d).
- [12.] Lü J., Zhang Y., Lü Z., Huang X., Wang Z., Zhu X., Wei B., (2015), A preliminary study of the pseudo-capacitance features of strontium doped lanthanum manganite, *RSC Adv.*, 5, 5858-5862, (DOI: 10.1039/c4ra13583k).
- [13.] Arjun N., Pan G.-T., Yang T.C., (2017), The exploration of lanthanum based perovskites and their complementary electrolytes for the supercapacitor applications, *Respir. Physiol.*, 7, 920-926, (DOI: 10.1016/j.rinp.2017.02.013).
- [14.] Ho K.H., Wang J., (2017), Hydrazine reduction of LaNiO_3 for active materials in supercapacitors, *J. Am. Ceram. Soc.*, 100, 4629-4637, (DOI: 10.1111/jace.14997).
- [15.] Dharmaraj N., Park H., Kim C., Kim H., Lee D., (2004), Synthesis and characterization of zirconium oxide nanofibers by electrospinning, *Mater. Chem. Phys.*, 87, 5-9, (DOI: 10.1080/15533170500471391).
- [16.] Lin Y.-J., Chang Y.-H., Yang W.-D., Tsai B.-S., (2006), Synthesis and characterization of ilmenite NiTiO_3 and CoTiO_3 prepared by a modified Pechini method, *J. Non-Cryst. Solids*, 352, 789-794, (DOI: 10.1016/j.jnoncrysol.2006.02.001).
- [17.] Fang D., Huang K., Liu S., Luo Z., Qing X., Zhang Q., (2010), High-density $\text{NiTiO}_3/\text{TiO}_2$ nanotubes synthesized through sol-gel method using well-ordered TiO_2 membranes as template, *J. Alloys Compd.*, 498, 37-41, (DOI: 10.1016/j.jallcom.2010.02.150).
- [18.] Imani M., Radmanesh L., Tadjarodi A., (2019), Synthesis of perovskite-like NiTiO_3 nanoparticles as an electrode material by a rapid solid combustion technique

- induced by microwave irradiation, *Ceram. Int.*, 45, 18772-18777, (DOI: 10.1016/j.ceramint.2019.06.105).
- [19.] An C. H., Zhang Y., Guo H.N., Wang Y.J., (2019), Metal oxide-based supercapacitors: progress and perspectives, *Nanoscale Adv.*, 1, 4644-4658, (DOI: 10.1039/c9na00543a).
- [20.] Dalavi D.S., Devan R.S., Patil R.S., Ma Y.R., Patil P.S., (2013), Electrochromic performance of sol-gel deposited NiO thin film, *Mater. Lett.*, 90, 60-63, (DOI: 10.1016/j.matlet.2012.08.108).
- [21.] Patil R.A., Devan R.S., Liou Y., Ma Y.-R., (2016), Efficient electrochromic smart windows of one-dimensional pure brookite TiO₂ nanoneedles, *Sol. Energy Mater. Sol. Cells*, 147, 240-245, (DOI: 10.1016/j.solmat.2015.12.024).
- [22.] Kitchamsetti N., Kalubarme R.S., Chikate P.R., Park C.J., Ma Y.R., Shirage P.M., Devan R.S., (2019), An investigation on the effect of Li-ion cycling on the vertically aligned brookite TiO₂ nanostructure, *ChemistrySelect*, 4, 6620-6626, (DOI: 10.1002/slct.201900395).
- [23.] Devan R.S., Lin J.H., Ho W.D., Wu S.Y., Liou Y., Ma Y.R., (2010), Investigation of high temperature phase transformation in one-dimensional Ta₂O₅ nanorods, *J. Appl. Crystallogr.*, 43, 1062-1067, (DOI: 10.1017/S0021889810026646).
- [24.] Devan R.S., Lin C.-L., Gao S.-Y., Cheng C.-L., Liou Y., Ma Y.R., (2011), Enhancement of green-light photoluminescence of Ta₂O₅ nanoblock stacks, *Phys. Chem. Chem. Phys.*, 13, 13441-13446, (DOI: 10.1039/c121283d).
- [25.] Devan R.S., Thakare V.P., Antad V.V., Chikate P.R., Khare R.T., More M.A., Dhayal R.S., Patil S.I., Ma Y.R., Schmidt-Mende L., (2017), Nano-heteroarchitectures of two-dimensional MoS₂@ one-dimensional brookite TiO₂ nanorods: prominent electron emitters for displays, *ACS Omega*, 2, 2925-2934, (DOI: 10.1021/acsomega.7b00345).
- [26.] Pang H., Lu Q., Li Y., Gao F., (2009), Facile synthesis of nickel oxide nanotubes and their antibacterial, electrochemical and magnetic properties, *Chem. Commun.*, 2009, 7542-7544, (DOI: 10.1039/b914898a).
- [27.] Devan R.S., Ma Y.-R., More M.A., Khare R.T., Antad V.V., Patil R.A., Thakare V.P., Dhayal R.S., Schmidt-Mende L., (2016), Promising field electron emission

- performance of vertically aligned one dimensional (1D) brookite (β) TiO_2 nanorods, *RSC Adv.*, 6, 98722-98729, (DOI: 10.1039/c6ra20747b).
- [28.] [Jahromi S.P., Pandikumar A., Goh B.T., Lim Y.S., Basirun W.J., Lim H.N., Huang N.M., (2015), Influence of particle size on performance of a nickel oxide nanoparticle-based supercapacitor, *RSC Adv.*, 5, 14010-14019, (DOI: 10.1039/c4ra16776g).
- [29.] Bhojane P., Sinha L., Goutam U.K., Shirage P.M., (2019), A 3D mesoporous flowers of nickel carbonate hydroxide hydrate for high-performance electrochemical energy storage application, *Electrochim. Acta*, 296, 112-119, (DOI: 10.1016/j.electacta.2018.11.025).
- [30.] Kitchamsetti N., Chikate P.R., Patil R.A., Ma Y.R., Shirage P.M., Devan R.S., (2019), Perforated mesoporous NiO nanostructures for an enhanced pseudocapacitive performance with ultra-high rate capability and high energy density, *CrystEngComm*, 21, 7130-7140, (DOI: 10.1039/c9ce01475f).
- [31.] Yadav A.A., Chavan U., (2016), Influence of substrate temperature on electrochemical supercapacitive performance of spray deposited nickel oxide thin films, *J. Electroanal. Chem.*, 782, 36-42, (DOI: 10.1016/j.elechem.2016.10.006).
- [32.] Babu G.A., Ravi G., Mahalingam T., Kumaresavanji M., Hayakawa Y., (2015), Influence of microwave power on the preparation of NiO nanoflakes for enhanced magnetic and supercapacitor applications, *Dalton Trans.*, 44, 4485-4497, (DOI: 10.1039/c4dt03483j).
- [33.] Meng G., Yang Q., Wu X., Wan P., Li Y., Lei X., Sun X., Liu J., (2016), Hierarchical mesoporous NiO nanoarrays with ultrahigh capacitance for aqueous hybrid supercapacitor, *Nanomater. Energy*, 30, 831-839, (DOI: 10.1016/j.nanoen.2016.09.012).
- [34.] Chen P.C., Hsieh S.J., Zou J., Chen C.C., (2014), Selectively dealloyed Ti/ TiO_2 network nanostructures for supercapacitor applications, *Mater. Lett.*, 133, 175-178, (DOI: 10.1016/j.matlet.2014.06.165).
- [35.] Chen J., Huang Y., Li C., Chen X., Zhang X., (2016), Synthesis of NiO@ MnO_2 core/shell nanocomposites for supercapacitor application, *Appl. Surf. Sci.*, 360, 534-539, (DOI: 10.1016/j.apsusc.2015.10.187).

- [36.] Hwang S.G., Ryu S.H., Yun S.R., Ko J.M., Kim K.M., Ryu K.-S., (2011), Behavior of NiO-MnO₂/MWCNT composites for use in a supercapacitor, *Mater.Chem.Phys.*, 130, 507-512, (DOI: 10.1016/j.matchemphys.2011.07.022).
- [37.] Zhu L., Ran R., Tade M., Wang W., Shao Z., (2016), Perovskite materials in energy storage and conversion, *Asia Pac. J. Chem. Eng.*, 11, 338-369, (DOI: 10.1002/apj.2000).
- [38.] Gabal M., Hameed S., Obaid A., (2012), CoTiO₃ via cobalt oxalate-TiO₂ precursor. Synthesis and characterization, *Mater. Char.*, 71, 87-94, (DOI: 10.1016/j.matchar.2012.06.009).
- [39.] George G., Jackson S.L., Luo C.Q., Fang D., Luo D., Hu D., Wen J., Luo Z., (2018), Effect of doping on the performance of high-crystalline SrMnO₃ perovskite nanofibers as a supercapacitor electrode, *Ceram. Int.*, 44, 21982-21992, (DOI: 10.1016/j.ceramint.2018.08.313).
- [40.] Lang X., Mo H., Hu X., Tian H., (2017), Supercapacitor performance of perovskite La_{1-x}Sr_xMnO₃, *Dalton Trans.*, 46, 13720-13730, (DOI: 10.1039/c7dt03134c).
- [41.] Han D., Jing X., Wang J., Yang P., Song D., Liu J., (2012), Porous lanthanum doped NiO microspheres for supercapacitor application, *J. Electroanal. Chem.*, 682, 37-44, (DOI: 10.1016/j.elechem.2012.06.616).
- [42.] Zhang X., Shi W., Zhu J., Zhao W., Ma J., Mhaisalkar S., Maria T.L., Yang Y., Zhang H., Hng H.H., (2010), Nickel oxide aerogel for high performance supercapacitor electrodes, *Nano Res.*, 3, 643-652, (DOI: 10.1039/c6ra24436j).
- [43.] Giri S., Ghosh D., Das C.K., (2013), One pot synthesis of ilmenite-type NiMnO₃-“nitrogen-doped” graphene nanocomposite as next generation supercapacitors, *Dalton Trans.*, 42, 14361-14364, (DOI: 10.1039/c3dt51807h).
- [44.] Kim T.Y., Lee H.W., Stoller M., Dreyer D.R., Bielawski C.W., Ruoff R.S., Suh K.S., (2010), High-performance supercapacitors based on poly(ionic liquid)-modified graphene electrodes, *ACS Nano*, 5, 436-442, (DOI: 10.1021/nn101968p).
- [45.] Su Y.S., Xiao K., Li N., Liu Z.Q., Qiao S.Z., (2014), Amorphous Ni(OH)₂@ three dimensional Ni core-shell nanostructures for high capacitance Pseudocapacitors and asymmetric supercapacitors, *J. Mater. Chem. A*, 34, 13845-13853, (DOI: 10.1039/c4ta02486a).

- [46.] Wang Y.Y., Lei Y., Li J., Yuan Gu H.Y., Xiao D., (2014), Synthesis of 3D-nanonet hollow structured Co_3O_4 for high capacity supercapacitor, *ACS Appl. Mater. Interfaces*, 6, 6739-6747, (DOI: 10.1021/am500464n).
- [47.] Lu X.F., Wu D.J., Li R.Z., Li Q., Ye S.H., Tong Y.X., Li G.R., (2014), Hierarchical NiCo_2O_4 nanosheets@ hollow microrod arrays for high-performance asymmetric supercapacitors, *J. Mater. Chem. A*, 2, 4706-4713, (DOI: 10.1039/c3ta14930g).
- [48.] Tang C.H., Yin X.S., Gong H., (2013), Superior performance asymmetric supercapacitors based on a directly grown commercial mass 3D Co_3O_4 @ $\text{Ni}(\text{OH})_2$ core-shell electrode, *ACS Appl. Mater. Interfaces*, 5, 10574-10582, (DOI: 10.1021/am402436q).
- [49.] Ding R., Li X., Shi W., Xu Q., Han X., Zhou Y., Hong W., Liu E., (2017), Perovskite $\text{KNi}_{0.8}\text{Co}_{0.2}\text{F}_3$ nanocrystals for supercapacitors, *J. Mater. Chem. A*, 5, 17822-17827, (DOI: 10.1039/c7ta05209j).

Chapter 6

Mesoporous 1D NiTiO₃@2D MnO₂ core-shell heterostructure

The novel hybrid core-shell electrodes of 2D and 1D nanomaterials have the ability to address the relatively lower specific energy of supercapacitors effectively. Therefore, we report the utilization of the core-shell structure of hierarchical MnO₂ nanoflakes and NiTiO₃ (NTO) mesoporous rods as an efficient supercapacitor electrode providing a larger surface area and more pathways for the diffusion of OH⁻ ions. Two-step-chemically processed hybrid porous core-shell structure of MnO₂@NTO delivered a specific capacitance of 1054.7 F/g, specific power of 3892.5 W/kg, and specific energy of 15.7 Wh/kg. Moreover, 85.3 % capacitance retention after 5000 cycles in 2M KOH electrolytes was observed without degradation in the surface morphological features. Complementary first-principles density functional theory (DFT) calculations reveal synergistic interactions between the MnO₂ and NTO in the MnO₂@NTO heterostructure, which gave rise to improved electrical conductivity.

6.1 Introduction

The energy storage devices ask attention for utilization in the new emerging technologies for excellent performance in safely storing green energy. The environmentally friendly supercapacitor has the ability to compete with batteries by offering adequate specific energy, higher specific power, a long-life cycle, and faster charging and dissipation of energy. The carbon allotropes are found to deliver competent energy storage performance but suffer from further improvement because of swelling and shrinkage during the ion diffusion and removal processes. [1-2] Therefore, the researchers have explored the materials known for better ionic and electronic charge transfer to store electric charges through faradaic redox reaction and improve the performance of supercapacitors. [3-5] The fundamental defects, [6] the controlled morphological approaches, [7-8] and porous networking [9-11] in the electrode material influenced electrochemical behavior. However, the formation of heterostructures of either carbon allotropes or metal oxides is the most convincing approach to improving the performance. [12-13] The core-shell structure resulted from microwave-assisted polymerization of PANI, and multiwalled carbon nanotubes delivered relatively larger specific capacitance (i.e., 322 F/g) than the pristine MWCNTs (i.e., 25.4 F/g). [14] The composite of PPy and PANI prepared by the in-situ chemical oxidation polymerization route offered the specific capacitance of 416 F/g. [15] However, the incorporation of metal oxides (i.e., $\text{Zn}_2\text{SnO}_4/\text{MnO}_2$) to form the heterostructure with carbon microfiber has delivered the specific capacitance of 642.2 F/g. [16] Overall, it has been observed that the formation of heteroarchitecture delivers complementary properties for notably excellent ion diffusion compare to the independent existence of both core and shell materials. Among the various oxides of metals like Ru, Co, Sn, Ti, Ni, Mn, etc., Mn is earning importance on account of multi-valence states $\text{Mn}^{2+}/\text{Mn}^{3+}/\text{Mn}^{4+}/\text{Mn}^{5+}$ to form MnO_2 , Mn_3O_4 , and Mn_2O_3 . [3] These multi-valence states provide better control over electron transporting activity, crystallinity, electrical conductivity (i.e., 10^{-8} S/cm), resistivity (i.e., 0.3 Ωcm) and activation energy (i.e., 0.075 eV). [17] The stronger electrochemical activity and richer redox reaction ability appealing the scientific community to explore various nanostructured morphological forms of MnO_2 to gain the theoretical specific capacitance of 1110 F/g. [18] Substantial efforts have been made to improve electrochemical

performance by fabricating nanostructures such as the flakes, belts, wires, flowers, spheres, needles, urchins, rods, particles, and tubes like nanostructure morphologies of MnO_2 and Mn_2O_3 , providing high specific surface areas for ion diffusion are explored as electrode materials for supercapacitor. [3-5] Moreover, the heterostructures of NiO , Co_3O_4 , TiO_2 , $\text{Ni/Mn/Fe/Zn-Co}_2\text{O}_4$, $\text{Ni/Zn-Fe}_2\text{O}_4$, etc., as core and Co_3O_4 , Mn_2O_3 , MnO_2 , NiO , etc. as shell [5,13] are explored to gain better supercapacitive performance. The synergistic effect between distinct metal oxides in two different morphological forms plays a vital role in controlling the interfacial ion-exchange mechanism and the specific capacitance (Fig. 1). Even though the core-shell structure of 2D nanoflakes and single-crystalline 1D rod structures provide a larger surface area (Scheme 1, Fig. 1), the specific capacitance was restricted to the 110-450 F/g [10,19-21] due to limited diffusion of the ions on the surface only. Therefore, we have explored the core-shell heteroarchitecture of the 2D nanoflakes and 1D mesoporous rods, as shown in Scheme 2 of Fig. 1. The mesoporous 1D rods composed of interconnected nanoparticles shall provide a larger accessible surface area, which is aided by the interlinked 2D nanoflakes decorated over it. Such a synergistic heteroarchitecture will provide an enormous surface area in total and furnish tremendous sites for the diffusion of ions deep inside the core-shell morphology, which will improve the specific capacitance and energy/power performance. However, the selection of excellent core and shell materials is of vital importance. Among various 2D morphologies of metal oxides, MnO_2 is observed to help overcome the poor conductivity of various metal oxides and improve the specific capacitance. However, observed specific capacitance values are mostly restricted to the range of 200-500 F/g, owing to the limited accessible activation sites for ion diffusion. [22, 25-27] Still, the decoration of MnO_2 nanosheets on the 3D hierarchical NiCo_2O_4 nanoneedles delivered the specific capacitance of 816 F/g at a current density of 5 mA/cm². [23] Therefore, the utilization of mesoporous and interconnected morphologies of different forms to grow core-shell heteroarchitecture is of scientific importance for improving energy storage performance. However, to the best of our knowledge, the literature does not report the comprehensive electrochemical studies of a core-shell heteroarchitecture of 2D MnO_2 nanoflakes and 1D mesoporous NiTiO_3 rods composed of interconnected nanoparticles. Recently, the poor conductivity of microwave irradiated NiTiO_3 nanoparticles restricted

the specific capacitance to 257 F/g at a scan rate of 10 mV/s even after providing a large surface area for substantially easy, faster, and larger diffusion of ions in aq. electrolyte. [28] Nevertheless, more abundant $\text{Ni}^{3+}/\text{Ni}^{2+}$ and $\text{Ti}^{4+}/\text{Ti}^{3+}$ redox reaction species of mesoporous NTO rods can deliver excellent electrochemical performance after constituting heteroarchitecture with multi-valence Mn-oxide nanostructures.

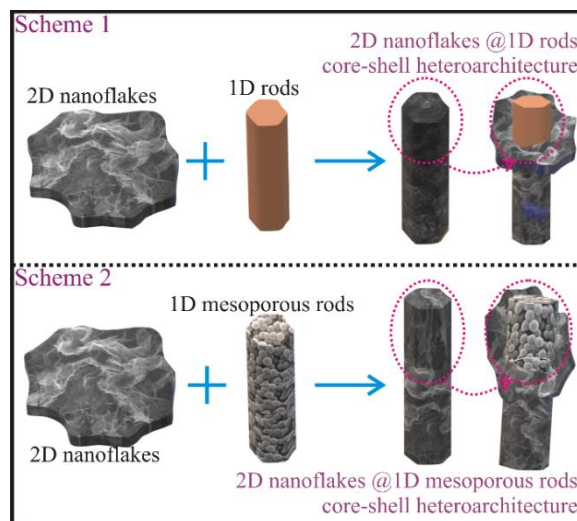


Figure 6.1. Schematic representation of the distinct arrangements of 2D nanoflakes and 1D rods for the formation of core-shell heteroarchitecture. Scheme 1 represents the core-shell heteroarchitecture of interlinked 2D nanoflakes and single crystalline 1D rods. Scheme 2 illustrates the synergistic core-shell heteroarchitecture of interlinked 2D nanoflakes and 1D mesoporous rods of interconnected nanoparticles. Scheme 2 provides a relatively larger surface area and access for the ions to diffuse deep inside the core-shell structure compare to scheme 1. Red dotted circles indicate the interfacial and cross-sectional view of the core-shell heteroarchitecture.

This study reports a core-shell heteroarchitecture of 2D MnO_2 nanoflakes decorated over mesoporous 1D NTO hexagonal rods as the electrode materials for supercapacitor. The formation of core-shell $\text{MnO}_2@\text{NTO}$ heteroarchitecture was examined utilizing field-emission scanning electron microscopy (FESEM), X-ray diffraction (XRD), Brunauer-Emmett-Teller (BET) analysis, Energy Dispersive Spectroscopy (EDS), and X-ray photoemission spectroscopy (XPS). The optimized core-shell structure of 2D MnO_2 nanoflakes and mesoporous 1D NTO rods of hierarchically interlocked nanoparticles has delivered a larger effective surface area for excellent

diffusion and redox mechanism between Mn, Ni, and Ti, deep inside the structure. Therefore, the two-step processed MnO₂@NTO core-shell heteroarchitecture delivered a specific capacitance of 1054.7 F/g, the specific power of 3892.5 W/kg, the specific energy of 15.79 Wh/kg, capacitance retentivity of 85.3 %, and a longer cycle lifetime.

6.2 Experimental section

The mesoporous NiTiO₃ microrods were synthesized using the sol-gel technique, where analytical grade 1 M nickel acetate (i.e., Ni(CH₃COO)₂·4H₂O, 98. %, Sigma Aldrich), 3.4 ml of titanium butoxide (i.e., Ti(OC₄H₉)₄, 97 % Sigma Aldrich) and ethylene glycol (C₂H₆O₂, 99.8.%, Sigma Aldrich,) were reacted at optimized temperature and time. The details on the synthesis of mesoporous NiTiO₃ rods encompassing the interlocked nanoparticle are discussed elsewhere. [28] Further, these mesoporous NiTiO₃ rods were subjected to the formation of a core-shell structure with MnO₂ nanosheets. The 10 mg of NiTiO₃ rods were dispersed in 30 mL of deionized water under ultrasonic treatment for 10 min., which was subsequently reacted with 80 mg of KMnO₄ (99 %, alfa aesar) at 90 °C under constant magnetic stirring for another 30 min. The whole solution was transferred to Teflon lined stainless steel autoclave and reacted at 140 °C for 4 h to form MnO₂ over the NiTiO₃ rods. Thus, the obtained core-shell MnO₂@NiTiO₃ was rinsed thoroughly with deionized water and ethanol after centrifugation and further dried under vacuum at 60 °C for 4 h.

The surface morphological features were of core-shell MnO₂@NiTiO₃ confirmed from field emission scanning electron microscopy (FESEM, JEOL JSM-6500F). The elemental analysis was done using energy dispersive spectroscopy (OXFORD EDX X-MAX 20 mm). The chemical states and electronic structure of mesoporous NiTiO₃@MnO₂ core-shell heteroarchitecture were explored from the X-ray photoelectron spectrometer (XPS, Thermo Scientific Inc. K-alpha) with a microfocus monochromated Al K α X-rays. The surface area and pore size distribution of NiTiO₃@MnO₂ were evaluated using N₂ adsorption-desorption isotherm (BET) and Barrett-Joyner-Halenda (BJH) methods in an automated gas sorption analyzer (Quantachrome Autosorb iQ2). The effect of electrolyte concentration on ion diffusion was investigated through the surface wettability studies performed using a drop shape analyzer (DSA-25, Kruss GmbH, Germany). The MnO₂@NiTiO₃ drop cast on Ni foam

and further dried at 80 °C for 25 h to prepare the working electrode. The electrochemical properties were investigated in a three-electrode setup comprising MnO₂@NiTiO₃ coated on Ni-foam as a working electrode, the platinum foil as a counter electrode, and a saturated calomel electrode as a reference electrode. The electrochemical measurements were performed at room temperature in 2 M KOH aqueous electrolyte using the electrochemical workstation (Autolab, PGSTAT302N, Metrohm) to investigate the effect of redox processes of Ni, Ti, and Mn on the pseudocapacitive performance of MnO₂@NiTiO₃ core-shell structure.

The density functional theory (DFT) calculations were performed using the Vienna Ab initio Simulation Package (VASP). [29] The Project Augmented Wave (PAW) method [30] was used to describe the interactions between the core and valence electrons, whereas the Perdew–Burke–Ernzerhof (PBE) generalized gradient approximation (GGA) functional [31] was used to compute the electronic exchange-correlation potential. Due to the antiferromagnetic nature of both α -MnO₂ and NiTiO₃, all calculations were spin-polarized. To ensure an accurate description of the structural, electronic, and magnetic properties of α -MnO₂ and NiTiO₃, Hubbard U correction (PBE+U) was implemented. [32, 33] An effective U_{eff} of 5.5, 3.5, and 4.5 eV for Mn-3*d*, Ti-3*d*, and Ni-3*d* electrons, respectively, are required to predict the electronic behaviors, in agreement with experimental findings. Geometry optimizations were performed using the conjugate-gradient algorithm until the residual Hellmann–Feynman forces on all relaxed atoms reached 10^{-3} eV Å⁻¹. Dispersion interactions were accounted for using the Grimme DFT-D3 dispersion correction scheme. [34] An energy cut-off of 500 eV was used in all of the calculations, and a Monkhorst-Pack [35] *k*-point mesh of 5×5×3 and 7×7×3 for bulk α -MnO₂ was used to perform the integration over the Brillouin zone of for bulk NiTiO₃ and α -MnO₂, respectively. The MnO₂ (100) and NiTiO₃ (001) used to form the MnO₂/NTO heterostructure were created from their relaxed bulk structures using the METADISE code, which ensures the creation of surfaces with zero dipole moment perpendicular to the surface plane. The isolated surface and heterostructures were optimized using 3×3×1 *k*-point mesh, whereas the electronic structures were obtained with a higher mesh of 5×5×1. A vacuum size of 15 Å was added in the z-direction of the slab to avoid

interactions between periodic slabs. Charge transfers between the MnO₂ and NiTiO₃ layer in the MnO₂@NiTiO₃ heterostructure were quantified using Bader charge analysis. [36]

6.3 Results and discussion

6.3.1 Field emission scanning electron microscopy

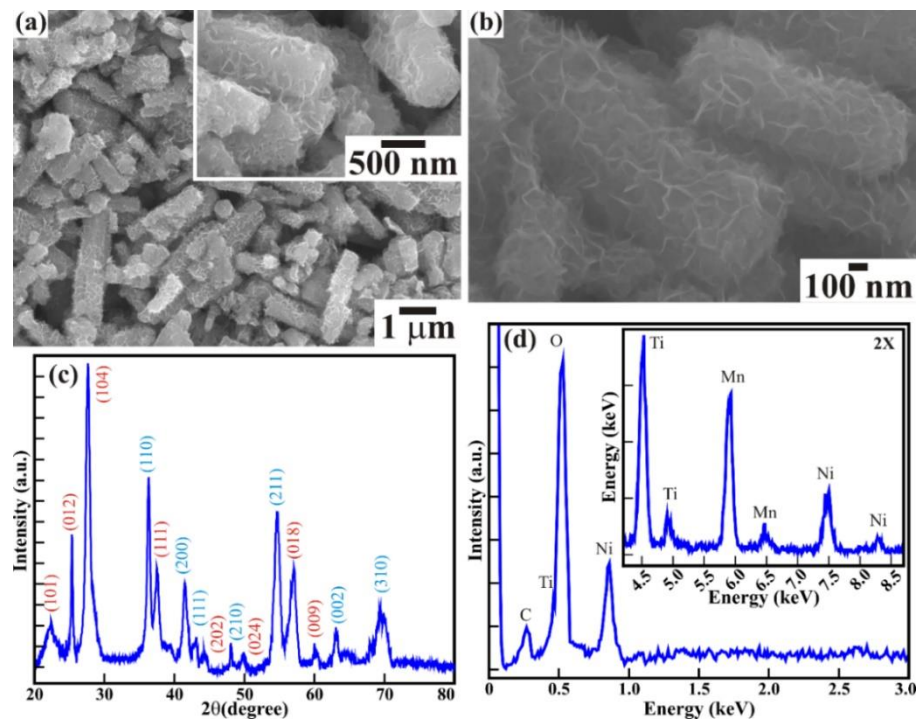


Figure 6.2. (a) Low-magnification FESEM image of MnO₂@NiTiO₃ core-shell heterostructure. (b) High-resolution FESEM image of the portion of MnO₂@NiTiO₃ core-shell heterostructure showing the shell of interlocked 2D MnO₂ nanoflakes. (c) X-ray diffraction pattern and (d) EDS spectra of mesoporous NiTiO₃@MnO₂ core-shell heterostructure.

Figure 6.2 shows the surface morphology of the MnO₂ decorated NiTiO₃ microrods. The surface morphological features of mesoporous NiTiO₃ microrods constituted of interlocked nanoparticles of an average diameter of ~ 59 nm are detailed in our previous report. [28] These well crystalline NiTiO₃ microrods were further subjected to the decoration of MnO₂ to form the core-shell structure with NiTiO₃ rods. Figure 6.2 (a) shows the FESEM image of the large surface area of MnO₂ decorated NiTiO₃ rods. The close observation of Figure 6.2 (a) depicts that NiTiO₃ retained their unique rods like features after the decoration of MnO₂,

which confirms that the hydrothermal treatment to decorate MnO₂ has not altered the surface morphological features of NiTiO₃ rods. The high magnification FESEM image (Figure 6.2 (b)) shows the uniform decoration of MnO₂ over the NiTiO₃ rods surface. The MnO₂ in nanoflakes form is distributed homogeneously without leaving larger voids or gaps on the NiTiO₃ rod surface. The average thickness of the MnO₂ nanoflakes is < 8.5 nm. However, the width of the nanoflakes remains untraceable due to their interconnecting nature. The randomly aligned MnO₂ nanoflakes formed a well-defined interconnected network covering whole NiTiO₃ rods and give the appearance of 2D MnO₂ core and 1D NiTiO₃ shell morphology. The MnO₂@NiTiO₃ core-shell structure surface roughness appears to be relatively larger than pristine NiTiO₃ rods due to the networked MnO₂ nanoflakes. The crystal structures of the NiTiO₃@MnO₂ core-shell heterostructure are characterized by XRD. The XRD pattern of NiTiO₃@MnO₂ was shown in Figure 6.2 (c). All the characteristic peaks coincided perfectly with the standard NiTiO₃ phase (JCPDS card no. 09-4870) and MnO₂ phase (JCPDS card no. 24-0735) without detecting any impurities. Furthermore, the energy-dispersive spectra (Figure 6.2 (d)) confirmed the existence of Ni, Ti, Mn, and O elements in the MnO₂@NiTiO₃ core-shell morphology. Even though C is detected in the EDS, the intensity of the peak assigned to C is much smaller than other observed peaks and confirmed the negligible presence of C. This indicates that the large accessible surface area and well-connected core-shell morphology of 2D MnO₂ nanoflakes and 1D mesoporous NiTiO₃ rods intend to deliver more diffusion channels to boost the ion diffusion and improve the energy storage capacity.

6.3.2 Transmission electron microscopy

The morphology and lattice structure of the MnO₂ and NTO were evaluated from TEM measurements. Figure. 6.3 (a and b) shows the TEM images of MnO₂ and NTO extracted from the core-shell heteroarchitecture of MnO₂@NTO. The MnO₂ grew in ultra-thin nanoflakes form has established well-interconnected networks of few micrometers wide. Whereas the NTO nanorods are formed of well crystalline interconnected nanoparticles with clearly visible

textural boundaries. The average diameter of the NTO nanoparticle is < 50 nm. The interconnected arrangement of these individual nanoparticles provided the mesoporous nanorods morphology, which is identical to the FESEM studies (Figure. 6.3(a, b)). Over this of mesoporous rods of interconnected NTO nanoparticle network, MnO₂ nanoflakes are decorated. The HRTEM image (Figure. 6.3(c)) revealed the single-crystalline nature of the NTO particles with clear domain boundaries and well-oriented lattice fringes. The calculated lattice spacing of 0.27 nm represents the lattice plane of (104) for the hexagonal NTO crystalline phase, which is consistent with the XRD data (Figure. 6.3(c)). This indicates that the large accessible surface area and well-connected morphology of synergistic 2D MnO₂ nanoflakes and 1D mesoporous NTO rods intend to deliver more diffusion channels to boost ion diffusion & improve energy storage capacity.

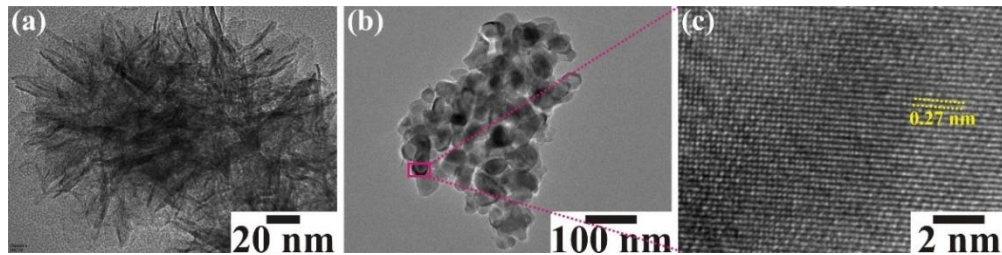


Figure. 6.3. TEM images of (a) MnO₂ nanoflakes and (b) NTO nanoparticles extracted from the MnO₂@NTO core-shell heterostructure. (c) HRTEM image of NTO nanoparticles showing clear lattice fringes.

6.3.3 X-ray photoelectron spectroscopy

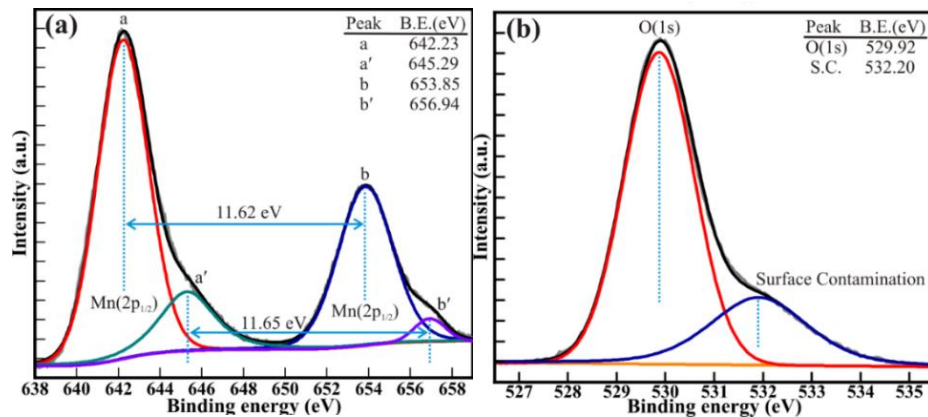


Figure 6.4. Typical high-resolution XPS spectra of the (a) Mn(2p) and (b) O(1s) core levels of the mesoporous MnO₂@NiTiO₃ core-shell heterostructure. The

XPS spectra were deconvoluted via the Voigt function within Shirley's background.

Further, the electronic and chemical properties of MnO₂@NiTiO₃ core-shell heteroarchitecture are confirmed from X-ray photoelectron spectroscopy (XPS) studies. Figure 6.4 shows the high-resolution XPS spectra of Mn(2p) and O(1s) core-levels of the MnO₂ nanoflakes network forming shell over the core of mesoporous NiTiO₃ rods. The thicker shell of MnO₂ suppresses the XPS signal of NiTiO₃ microrods, so XPS spectra of Ni(2p) and Ti(2p) are not collected in the present case. However, the deconvoluted XPS spectra of Ni(2p) and Ti(2p) core-levels of NiTiO₃ microrods discussed elsewhere confirmed the formation of stoichiometric mesoporous NiTiO₃ rods composed of nanoparticles. [28] The XPS spectrum of Mn(2p) core levels for the MnO₂ nanoflakes (Figure 6.4(a)) exhibits two distinctive peaks identified as 'a and b'. The Mn offers several oxidations, leading to considerable asymmetry and broadening of the Mn(2p) spectra consisting of several double peak contributions. Therefore, the Mn(2p) spectrum with double peak features was deconvoluted using the Voigt curve function and Shirley background. The deconvoluted spectra explicitly fit for four peaks located at a binding energy of 642.23 (≡ a), 645.29 (≡ a'), 653.86 (≡ b), and 656.94 (≡ b') eV arbitrate the double peak features of Mn⁴⁺(2p_{3/2}), Mn⁶⁺(2p_{3/2}), Mn⁴⁺(2p_{1/2}), and Mn⁶⁺(2p_{1/2}) core levels, respectively. [37] However, much higher (~ > 5 times) intensity of the Mn⁴⁺(2p_{3/2}) core levels than that of Mn⁶⁺(2p_{3/2}) core levels illustrate the existence of the negligible amount of Mn⁶⁺ cations. The spin-orbit splitting of 11.62 and 11.65 eV was observed between the Mn⁴⁺(2p) and Mn⁶⁺(2p) core levels, respectively. Likewise, the O(1s) XPS spectrum with compound peak feature was decomposed via Voigt fitting function within the Shirley background (Figure 6.4(b)) to confirm the oxidation state of MnO₂ nanoflakes. The deconvoluted spectra perfectly fit for two peaks located at BE of 529.92 and 532.20 eV. The highly intense peak situated at the lower BE of 529.92 eV corresponds to the O(1s) core level of the O²⁻ anions in the MnO₂ nanoflakes shell. Whereas, low intense peak at a higher BE peak of 532.20 eV is attributed to surface contamination, such as carbon oxides or hydroxides. [38-40]

This confirmed that the mesoporous NiTiO₃ rods are covered with stoichiometric MnO₂ nanoflakes to form a core-shell heteroarchitecture, i.e., 2D MnO₂@1D NiTiO₃.

6.3.4 Nitrogen adsorption-desorption isotherm

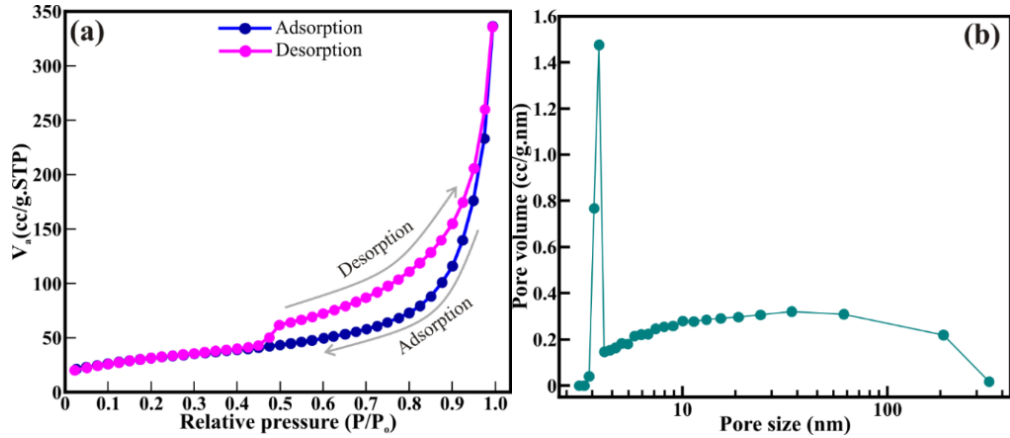


Figure 6.5. (a) N₂ adsorption-desorption isotherm, and (b) BJH pore size distribution of the mesoporous MnO₂@NiTiO₃ core-shell heterostructure.

The specific surface area and pore size distribution play a significant role in the material's energy storage performance. The Brunauer-Emmett-Teller (BET) analysis (Figure 6.5) specifies the mesoporous nature of MnO₂@NiTiO₃ core-shell heteroarchitecture. The nitrogen adsorption and desorption isotherm of the MnO₂@NiTiO₃ core-shell structure (Figure 6.5 (a)) illustrates the type IV isotherm with a distinct hysteresis loop for P/P₀ range of 0.4-1.0. A similar type of behavior was observed for NiTiO₃ rods composed of interlocked nanoparticle morphology. [28] This implies that the MnO₂ nanoflakes have retained the mesoporous nature of NiTiO₃ rods even after forming shells along the rod body. Moreover, the more open hysteresis nature of MnO₂@NiTiO₃ represents the improvement in the total number of mesoporous voids after coating the shell of MnO₂ nanoflakes along the surface of NiTiO₃ rods core, in comparison of pure NiTiO₃ rods. The well-defined interconnected network of 2D MnO₂ nanoflakes added up voids with the mesoporous NiTiO₃ rods while maintaining the hexagonal morphology. The pore volume and BET surface area of MnO₂@NiTiO₃ core-shell structure are 0.54 cm³/g and 157.15 m²/g, respectively (Figure 6.5(b)). Even though the pores are distributed in the 3.50 to 313.96 nm

range, the maximum number of pores are ~ 7.3 nm in size, and the average pore size distribution is ~ 3.92 nm. These values are significant than the NiTiO_3 rods ($33.15 \text{ m}^2/\text{g}$, 17.48 nm). [28] This illustrates that the well-connected network of randomly aligned 2D MnO_2 nanoflakes over the mesoporous NiTiO_3 rods of interconnected nanoparticles effectively improved the mesoporous synergy and delivered a larger surface area for ion accumulation, which shall escalate the ion interactions at the electrolyte-electrode interface deep inside both the shell and core structures. Overall, an interconnected network of 2D MnO_2 nanoflakes and NiTiO_3 microrods delivered a mesoporous core-shell structure and offered a larger specific surface area for easy/smooth interactions of ions at the electrode-electrolyte interface deep inside the heteroarchitecture, which is foreseeable to boost the energy storage capabilities.

6.3.5 Contact angle measurements

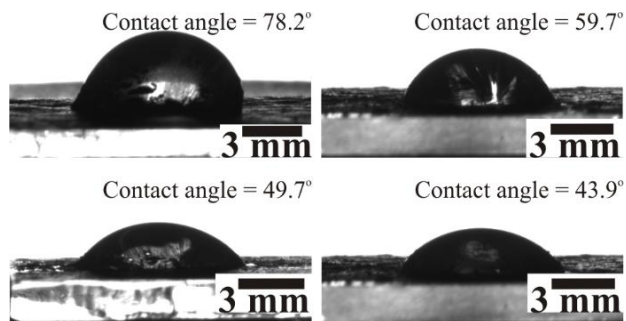


Figure 6.6. Contact angle measurement showing the interface of the aqueous KOH electrolyte of (a) 0.5 M, (b) 1 M, (c) 1.5 M, and (d) 2 M concentration on the surface of the mesoporous $\text{MnO}_2@ \text{NiTiO}_3$ core-shell heterostructure working electrode.

The electrolyte interface with the $\text{MnO}_2@ \text{NiTiO}_3$ controls the intercalation of the ions, and thereupon energy storage ability. Therefore, contact angle measurements were performed employing various molarities of aq. KOH on $\text{MnO}_2@ \text{NiTiO}_3$ to understand the surface wettability of the KOH electrolyte at the electrolyte-electrode interface. Figure 6.6 shows the surface wettability (i.e., contact angle) of the different molarities of aq. KOH electrolytes at the surface of $\text{MnO}_2@ \text{NiTiO}_3$. The 0.5, 1, 1.5, and 2 M KOH electrolyte delivered the average contact angle of 78.2° (Figure 6.6 (a)), 59.7° (Figure 6.6 (b)), 49.7° (Figure 6.6

(c)), and 43.9° (Figure 6.6 (d)), respectively. The contact angle of 78.2° observed for 0.5 M KOH was reduced remarkably to 49.7° for the 1.5 M KOH, and after that, reduced to 43.9° for 2 M KOH. It represents the complying contact of 2 M KOH with an electrode surface, which expedites the easy transfer of electrons at the interface and boosts energy storage performance. Therefore, the electrochemical measurements were carried out using 2 M KOH electrolyte for better wettability and lower contact angle.

6.3.6 Electrochemical analysis

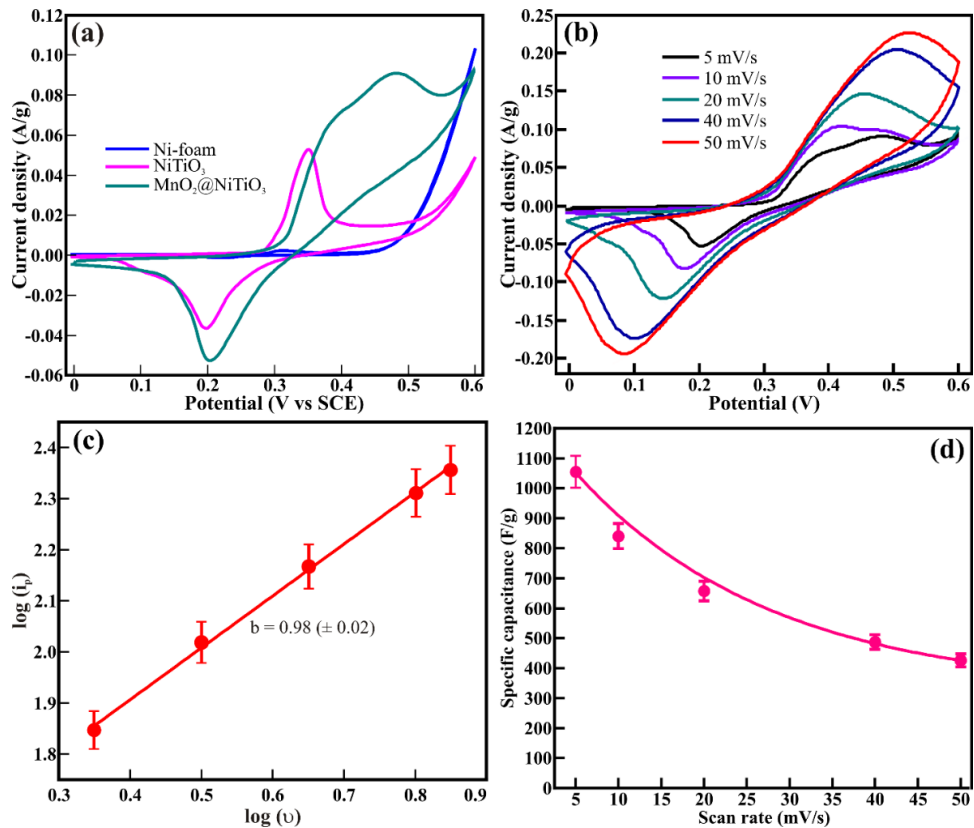


Figure 6.7. Steady-state cyclic voltammograms of (a) Ni-foam, NiTiO₃, and mesoporous MnO₂@NiTiO₃ core-shell heterostructure recorded at a scan rate of 5 mV/s, and (b) mesoporous MnO₂@NiTiO₃ core-shell heterostructure recorded at various scan rates from 5 to 50 mV/s in 2 M aq. KOH electrolyte. (c) The variation in the peak current density (i_p) and the scan rate (v) of the cathodic peak current, and (d) the specific capacitance of mesoporous MnO₂@NiTiO₃ core-shell heterostructure evaluated from the CV curves in (b).

The electrochemical studies of $\text{MnO}_2@\text{NiTiO}_3$ core-shell structure were performed in a three-electrode system to understand their energy storage mechanism in 2 M KOH electrolyte. Figure 6.7 (a) shows the cyclic voltammetry curves of the pristine Ni-foam, mesoporous NiTiO_3 rods composed of nanoparticles, and $\text{MnO}_2@\text{NiTiO}_3$ core-shell heteroarchitecture, recorded at the scan rate of 5 mV/s in the optimized applied potential of 0 to 0.6 V (vs. SCE). The flat natured CV graph of Ni-foam did not show any evidence for the energy storage but confirmed its conducting nature without taking part in the redox mechanism directly. Two redox peaks in the CV graphs of mesoporous NiTiO_3 rods represented the existence of $\text{Ni}^{2+}/\text{Ni}^{3+}$ and $\text{Ti}^{3+}/\text{Ti}^{4+}$ redox couples assisting in the energy storage performance of NiTiO_3 rods. The energy storage performance and mechanism of mesoporous NiTiO_3 rods are detailed elsewhere. [28] Likewise, a pair of well-defined redox peaks in the CV graph of $\text{MnO}_2@\text{NiTiO}_3$ electrode during charging and discharging signifies the reversible faradic redox reaction mechanism in the potential range of 0 to 0.6 V (vs. SCE). Moreover, the close observation of Figure 6.7 (a) indicates that the current density and integral area of the CV curve for the $\text{NiTiO}_3 @\text{MnO}_2$ electrode are apparently larger than the NiTiO_3 rod electrode. This evidences the improved charge storage ability of NiTiO_3 rods after forming its heteroarchitecture with 2D MnO_2 nanoflakes (i.e., $\text{MnO}_2@\text{NiTiO}_3$). Figure 6.7(b) shows the CV curves of $\text{NiTiO}_3@\text{MnO}_2$ recorded at the scan rate from 5 to 50 mV/s and illustrated the pair of distinct redox peaks during charging (i.e., oxidation) and discharging (i.e., reduction) are akin to that observed in Figure 6.7 (a). The oxidation and reduction peak resulted from diffusion and extraction of OH^- ions have shifted at relatively higher and lower applied potentials, respectively, with an increase in the sweep rate. The oxidation and reduction peak observed for a sweep rate of 5 mV/s has red-shifted by 0.13 V (i.e., 0.51 V) and blue-shifted by 0.13 V (i.e., 0.08 V), respectively, for a sweep rate of 50 mV/s. This shifting assigned to the reference electrode potential and carrier kinetics is analogous to that reported for $\text{MnO}_2@\text{ZnFe}_2\text{O}_4$ multilevel nanosheets, [41] hierarchical $\text{NiCo}_2\text{O}_4@\text{NiCo}_2\text{O}_4$

core-shell nanoflakes, [42] hierarchical MoS₂ nanowires/NiCo₂O₄ nanosheets, [43] mesoporous NiTiO₃ microrods, [28] and NiO nanobelt. [10]

The CV graphs indicate the symmetry of both positive and negative current density. Nevertheless, the positive current density appears to be relatively much larger than the mesoporous NiTiO₃ rods. The larger surface area acts as a trap to capture free electrons/ions, which might be the reason for higher current density. This indicates that the decoration of randomly aligned 2D MnO₂ nanoflakes over the mesoporous NiTiO₃ rods to form a MnO₂@ NiTiO₃ core-shell heteroarchitecture provided a larger surface area than the mesoporous NiTiO₃ rods. The large surface area of MnO₂@NiTiO₃ perhaps delivers large numbers of trap level, where trapping-detrapping of free electrons/ions enhance ionic conductivity and hence more current density. The oxidation and reduction peaks have attained higher current density with an increase in the scan rate from 5 to 50 mV/s. The scan rate-dependent current density response of the MnO₂@NiTiO₃ core-shell nanostructure morphologies can be expressed from eq 6.1. [44]

$$i_p = a\nu^b \text{ or } \log(i_p) = \log(a) + b \log(\nu) \quad \text{--(6.1)}$$

Where, a and b are constants, ν is the scan rate, and i_p is the current density. The estimated value of b represents the current controlled capacitive process (if b =1) and semi-infinite diffusion-limited process. Therefore, the relation between the peak current density (i_p) and the scan rate (ν) is illustrated in Figure 6.7 (c) to identify the MnO₂@NiTiO₃ based electrode type. The linear behavior is observed between peak current density and the scan rate. After fitting, the estimated b value of MnO₂@NiTiO₃ for anodic processes was 0.98 (\pm 0.02), close to 1, justifying the capacitive and not diffusion charge storage mechanism in MnO₂@NiTiO₃ core-shell heteroarchitecture. Figure 6.7(d) shows the scan rate-dependent variation in the specific capacitance of MnO₂@NiTiO₃ estimated from their respective CV curves from the equation.

$$C_s = \frac{\int idV}{2m\nu\Delta V} \quad \text{..... (6.2)}$$

Where, C_s is the specific capacitance (F/g), m is the mass of the active electrode materials of NiTiO₃@MnO₂ core-shell heteroarchitecture (g), ν is the scan rate (mV/s), and ΔV is the applied potential range (V), and $\int idV$ is the integral area

of the CV curve. The $\text{MnO}_2@\text{NiTiO}_3$ delivered much larger specific capacitance (i.e., 1054.7 F/g) than the mesoporous NiTiO_3 rods (i.e., 542.3 F/g) at a scan rate of 5 mV/s. This indicates that redox reaction kinetics was more significant in the $\text{MnO}_2@\text{NiTiO}_3$ heteroarchitecture than the mesoporous NiTiO_3 rods. Furthermore, the evaluated specific capacitance for $\text{MnO}_2@\text{NiTiO}_3$ has decreased exponentially with an increase in the scan rate. The calculated specific capacitance values linearly varied with the sweep rate. The specific capacitance of 1054.7 F/g obtained at a scan rate of 5 mV/s was reduced to 425.8 F/g at a higher scan rate of 50 mV/s. The specific capacitance of 1054.7 F/g obtained for $\text{MnO}_2@\text{NiTiO}_3$ is relatively larger or comparative to the Mn, Ti, and Ni based core-shell and composite materials. [9, 20-24, 45-46] The large C_s value for $\text{MnO}_2@\text{NiTiO}_3$ is assigned to the interlaced arrangement of 2D nanoflakes, mesoporous 1D rods of interconnecting nanoparticles, and a larger accessible surface deep inside the core-shell heteroarchitecture. The slow scan rate provided adequate time for the maximum number of OH^- ions (or charges) to propagate deep inside the core-shell morphology along the surface and textural boundaries of both nanoflakes and nanoparticles. Nevertheless, at a high scan rate, the OH^- ion (or charges) encountered a significant barrier for diffusion deep inside the core-shell structure. [7] The larger accessible reaction sites along the well-interconnected pathways created from the mesoporous arrangement of MnO_2 nanosheets shell and nanoparticle embedded NiTiO_3 rods core benefited for easy and larger diffusion of OH^- ions than that of mesoporous NiTiO_3 rods merely.

Galvanostatic charge-discharge (GCD) studies were performed to understand the effect of current density on the energy storage performance of $\text{MnO}_2@\text{NiTiO}_3$. Figure 6.8 (a) shows the GCD curve of mesoporous NiTiO_3 rods and its core-shell structure with MnO_2 nanoflakes at the current density of 40 mA/g. Both GCD curves are akin to each other, indicating a reversible reaction mechanism. The charge-discharge time for $\text{MnO}_2@\text{NiTiO}_3$ core-shell structure (\approx 98 s) is larger than the mesoporous NiTiO_3 rods (\approx 27.6 s). The loading of MnO_2 nanoflakes over the mesoporous NiTiO_3 rods has enhanced C_s value of 547.7 F/g than the NiTiO_3 rods (i.e., 249.3 F/g). The 2 fold larger C_s values of

MnO₂@NiTiO₃ core-shell structure than mesoporous NiTiO₃ rods are ascribed to additional activation sites and conducting paths of interconnected 2D MnO₂ nanoflakes shell over the mesoporous 1D NiTiO₃ rod core. Further, the GCD curves of MnO₂@NiTiO₃ core-shell structure were measured at various current densities. The charging-discharging time showed an inverse relation with the current density (Figure 6.8 (b)). The increased current density resulted in faster/more ion diffusion, reducing charging/discharging time.

The current density dependent specific capacitance values of the mesoporous MnO₂@NiTiO₃ (Figure 6.8 (c)) evaluated from the GCD curves using the equation,

$$C_s = \frac{I dt}{m dV} \quad \dots (6.3)$$

Where, C_s is the specific capacitance of the MnO₂@NiTiO₃ core-shell heteroarchitecture (F/g), I is applied current density (A/g), m is the mass of the MnO₂@NiTiO₃ loaded on working electrode (g), and dV/dt is the slope of the discharge curve in GCD curve.

The current density dependent variation in the C_s values is akin to that observed from CV curves recorded for various scan rates. The specific capacitance of 547.7 F/g observed at the smaller current density of 40 mA/g has decreased to 508.8 F/g after increasing the current density to 110 mA/g, which is ~ 7 % reduction in C_s values against 63 % variation in the current density. This signifies the highly stable nature of MnO₂@NiTiO₃ core-shell heteroarchitecture. Moreover, the C_s values of MnO₂@NiTiO₃ are either analogous or significantly higher than the doped, core-shell, or composite materials consisting of Mn, Ti, O, and Ni, such as nanotube of Co-doped TiO₂ and RGO composite, [47] LaMnO₃/MnO nanoarrays, [26] Sr doped LaMnO₃ spheres, [48] firecrackers like β-MnO₂@NiCo₂O₄ nanostructures, [25] porous MnO₂-modified diatomite structures, [49] and heterostructured MnO₂/PEDOT nanowire arrays. [50] The electrical properties, textural boundaries, and core-shell interface play a vital role, along with the amount of active material and electrolyte in energy storage performance.

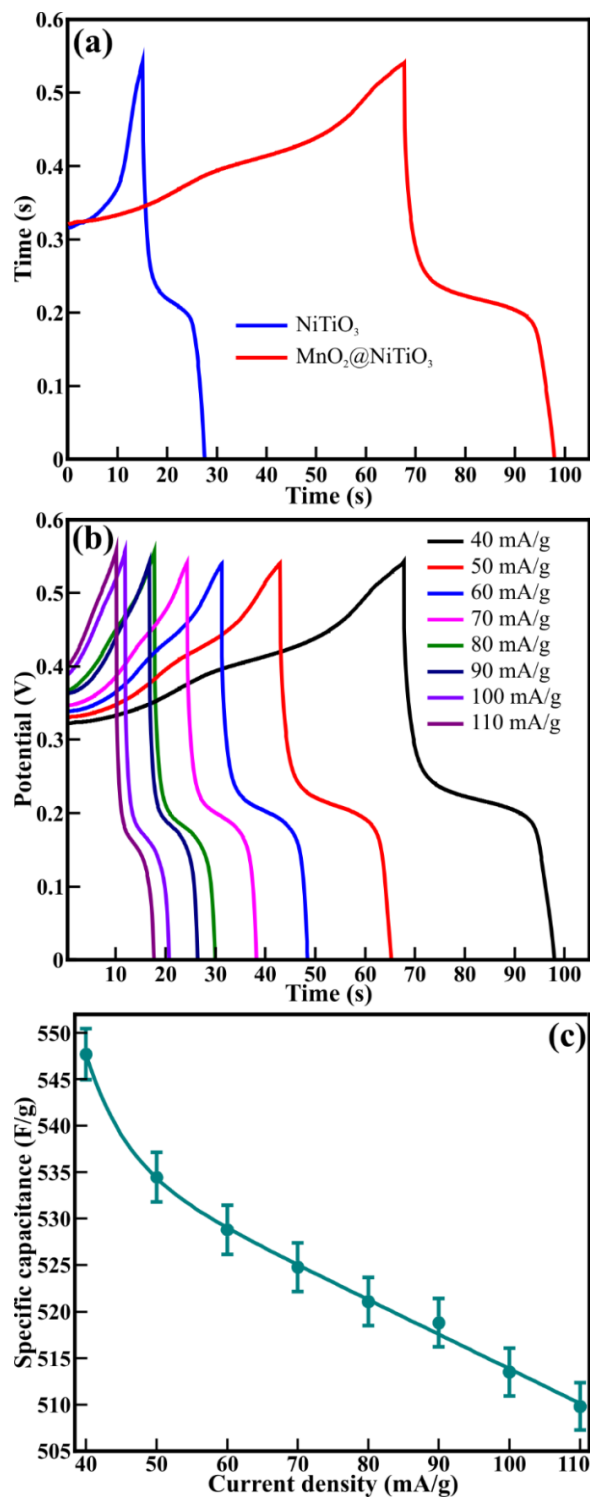


Figure 6.8. GCD analysis of (a) NiTiO₃ and MnO₂@NiTiO₃ core-shell heterostructure recorded at a current density of 40 mA/g. (b) GCD curves and (c) specific capacitance of mesoporous MnO₂@NiTiO₃ core-shell heterostructure measured at various current densities.

6.3.7 Electrochemical impedance spectroscopy

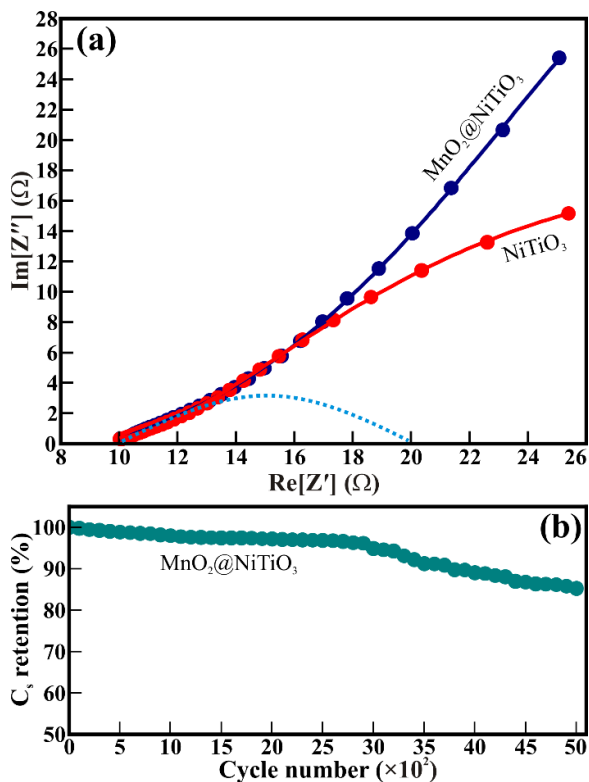


Figure 6.9. (a) Electrochemical impedance spectra (i.e., Nyquist plot) of the mesoporous NiTiO_3 rods and $\text{MnO}_2@\text{NiTiO}_3$ core-shell heterostructure. (b) The capacitance retention of $\text{MnO}_2@\text{NiTiO}_3$ core-shell heterostructure analyzed from 5000 continuous GCD cycles at a current density of 80 mA/g.

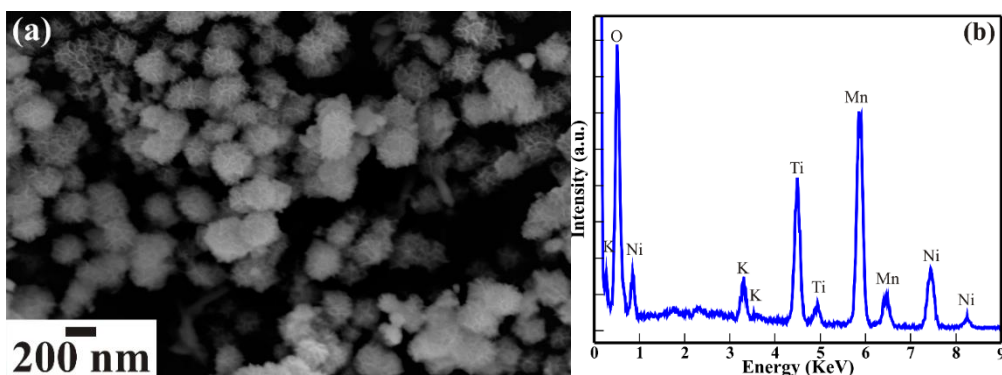


Figure. 6.10. (a) FESEM image and (b) EDS of $\text{MnO}_2@\text{NTO}$ core-shell heterostructure after 5000 continuous GCD cycles for the stability study.

The electrochemical impedance spectroscopic (EIS) studies were performed to understand the effect of electrolyte and material resistance in ion

diffusion on the $\text{MnO}_2@\text{NiTiO}_3$ core-shell structure. The Nyquist plots of the NiTiO_3 and $\text{MnO}_2@\text{NiTiO}_3$ core-shell structure measured in the frequency range from 1 MHz to 10 Hz are shown in Figure 6.9 (a). The impedance spectra of $\text{MnO}_2@\text{NiTiO}_3$ and NiTiO_3 are identical to each other with quasi-semicircle in the high-frequency region, which signifies that electrolyte resistance, interfacial charge transfer resistance, and faradic reaction mechanism are equivalent. Furthermore, the impedance spectrum of $\text{MnO}_2@\text{NiTiO}_3$ core-shell is more linear than NiTiO_3 has shown a quasi-semicircle in the low-frequency region. The straight (or linear) portion of impedance spectra observed in both $\text{MnO}_2@\text{NiTiO}_3$ core-shell and mesoporous NiTiO_3 rods was assigned to the Warburg resistance and attributed to the diffusion-controlled reaction of OH^- ions. The linear portion of impedance spectra of $\text{MnO}_2@\text{NiTiO}_3$ shows a larger angle than the NiTiO_3 , indicative of more significant conductivity in $\text{MnO}_2@\text{NiTiO}_3$. [41] This indicates that the loading of MnO_2 nanoflakes over the NiTiO_3 has not resulted in the further increase in the interfacial charge transfer resistance [43] but improved conductivity by providing a larger accessible surface area in the 2D and 1D structural forms deep inside the core-shell structure, resulting in the significant improvement in the specific capacitance. The long term cycling performance is crucial for the durable performance of the supercapacitors for many practical applications. Figure 6.9 (b) shows the GCD cyclic performance of $\text{MnO}_2@\text{NiTiO}_3$ examined at the current density of 80 mA/g for continuous 5000 cycles in ~ 17 h. The C_s has reduced by ~3.18 % for the initial 2500 cycles, and it decreased further by 14.7 % more till 5000 cycles, which is better than the mesoporous NTO nanorods (i.e., 9 %). [28] The improvement in the stability of $\text{MnO}_2@\text{NiTiO}_3$ electrode material is mainly attributed to their unique combination of interconnected 2D nanosheets encompassing mesoporous 1D NTO rods. Figure. 6.10 shows the FESEM and EDS analysis of $\text{MnO}_2@\text{NTO}$ core-shell heteroarchitectures after stability study for 5000 continuous GCD cycles. The surface morphological features in Figure. 6.10(a) depicts that randomly aligned MnO_2 nanoflakes decorated over NTO rods remained intact without significant alterations even after stability study for 5000 GCD cycles. Furthermore, EDS

(Figure. 6.10(b)) analysis of MnO₂@NTO after stability study showed the existence of K, Ni, Ti, Mn, and O elements. The less intense peak assigned to K represents its minor existent, which might be due to the irreversible diffusion of ions from the KOH electrolyte. This irreversible diffusion has caused a reduction in capacitance retention detailed in Figure. 6.9(b).

6.3.8 Ragone plot

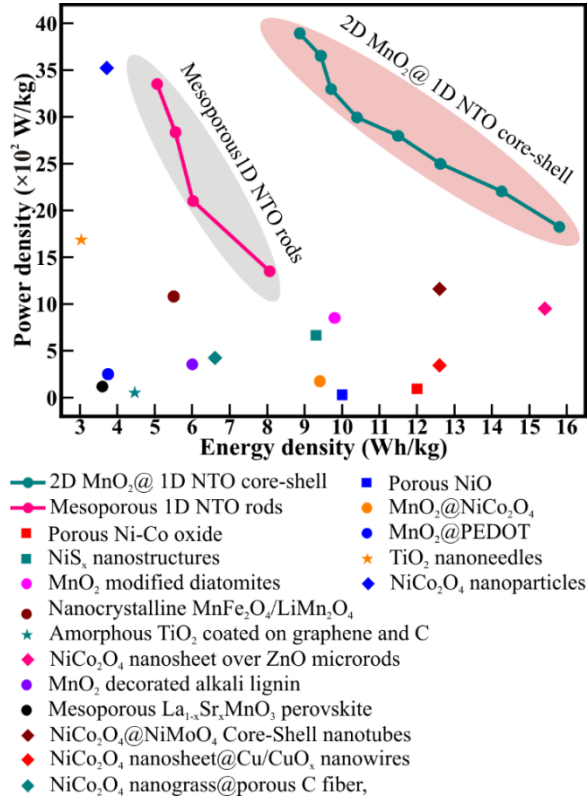


Figure 6.11. Ragone plot of MnO₂@NiTiO₃ core-shell heterostructure. The Ragone plot comprises another Mn, Ni, and Ti based metal oxides are in their pure or hetero-structure form.

Power density and energy density are the two key parameters to characterize the performance of the electrochemical supercapacitors. Although it is challenging to compare all types of supercapacitor's performance due to different working conditions, like charge-discharge rates, material mass loading, and potential window, a rough comparison between the developed electrode and documented work can still be made. The Ragone plots Figure 6.11 is the

comparative evaluation of energy density and power density of the NiTiO₃@MnO₂ core-shell heteroarchitecture electrode. The MnO₂@NiTiO₃ delivered a maximum energy density of 15.8 Wh/kg at a power density of 1822.8 W/kg and maximum power density of 3892.5 W/kg at an energy density of 8.9 Wh/kg, which is a significant improvement in comparison to mesoporous NiTiO₃ rods (i.e., 8.0 Wh/kg @ 1349.9 W/kg). Furthermore, the energy and power density of MnO₂@NiTiO₃ is better than various Mn, Ni, and Ti-based metal oxides in its pure, mixed, core-shell or composite forms, such as firecracker-like MnO₂@NiCo₂O₄ nanostructures, [25] hierarchically porous Ni-Co oxide powder, [51] MnO₂ particle decorated alkali lignin, [52] hierarchical NiCo₂O₄ nanosheets array over ZnO hollow microrods, [53] amorphous TiO₂ thin film conformally coated on the graphene and carbon nanotubes, [54] MnO₂@PEDOT nanowires core-shell structure, [50] hierarchical and porous MnO₂-modified diatomites structure, [49] hierarchical porous NiO, [55] TiO₂ nanoneedles, [8] mesoporous La_{1-x}Sr_xMnO₃ perovskite, [56] NiS_x nanostructure morphologies, [57] NiCo₂S₄@NiMoO₄ Core-Shell nanotube, [58] NiCo₂O₄ nanosheet decorated Cu/CuO_x nanowires, [59] NiCo₂S₄ single-crystalline nanoparticles, [60] NiCo₂O₄ nanograss decorated on bio-waste derived porous Carbon fiber, [61] and nanocrystalline MnFe₂O₄/LiMn₂O₄. [62] The higher specific capacitance, higher energy and power density, high cyclic stability, and better capacitance retention of MnO₂@ NiTiO₃ is assigned to enhanced conductivity, incessantly accessible activation sites, mesoporous nature, the better interface between the interlocked MnO₂ nanoflakes and mesoporous NiTiO₃ rods. Therefore, the mesoporous MnO₂@NiTiO₃ core-shell heteroarchitecture providing abundant and accessible activation sites deep inside holds the potentials to serve as a robust and stable electrode for the supercapacitor.

6.3.9 Computational analysis

Atomic-level insights into the synergistic effect of interactions in the MnO₂@NTO heterostructure were gained from first-principles DFT calculations. The interface structure and its electronic structure are systematically characterized. The NiTiO₃ was modeled in the hexagonal ilmenite phase with

space group $R\bar{3}$ (no. 148) as shown in Figure. 6.12(a). [63] A full unit cell relaxation yielded lattice parameters of $a = b = 5.057 \text{ \AA}$ and $c = 13.759 \text{ \AA}$ in close agreement with previous reports of Preciado et al. [64] and Xin et al. [65] α -MnO₂ was modeled tetragonal crystal structure with space group I4/m (no. 87) as shown in Figure. 6.12(b). The lattice parameters of α -MnO₂ were calculated at $a = b = 9.763 \text{ \AA}$, $c = 2.872 \text{ \AA}$, which compare closely with known experimental and theoretical reports. [66, 67] From the electronic projected density of states (Figure. 6.12(c) & (d)), the bandgap of NiTiO₃ and α -MnO₂ are predicted at 2.56 and 2.42 eV, respectively. Our calculated bandgaps are consistent with previous reports by Xin et al. [65] for NiTiO₃ and Sakai et al. [68] for α -MnO₂.

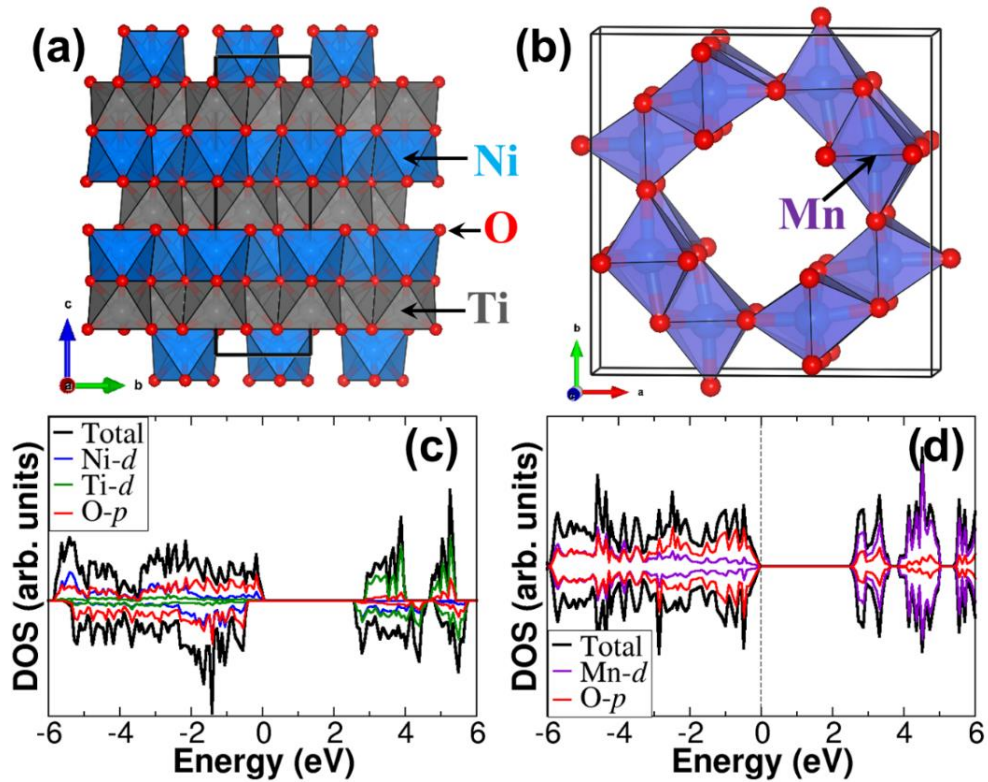


Figure. 6.12. (a, b) Crystal structures and (c, d) the corresponding partial density of states of the ilmenite hexagonal NiTiO₃ and tetragonal α -MnO₂.

The MnO₂/NTO heterostructure was constructed with (2×4)-MnO₂(100) and (2×2)-NTO (001) supercells (Figure. 6.13(a) & (b)), which ensured minimal lattice mismatch at the interface (1.82% in the x-direction and < 0.85% in the y-direction). The optimized geometry of the MnO₂/NTO heterostructure is shown

in Figure. 6.13(c). The interacting O–Ni distances at the interface are calculated to be in the range of 2.034–2.377 Å, indicating strong interface bonding. Differential charge density analyses (Figure. 6.14(a)) reveal electron density redistribution and accumulation within interface regions, especially within the newly formed covalent O–Ni bonds. Overall, a net charge transfer of $1.03 e^-$ was predicted from the NTO to the MnO_2 . As the electrical conductivity and the density of states (DOS) at the Fermi level dictates the material’s quantum capacitance, the partial density of states (PDOS) of the NTO layer without and with MnO_2 decoration has been determined as shown in Figure. 6.14(b-c). Whereas the isolated NTO layer retains the semiconducting characteristics with a bandgap of ~ 2 eV, the MnO_2/NTO heterostructure exhibits metallic conductivity enhanced electron density of states at the Fermi level. The improved electrical conductivity due to the synergistic interaction between MnO_2 and NTO might be responsible for the enhanced performance of the $\text{MnO}_2@\text{NTO}$ nanocomposite as the electrode in the supercapacitance.

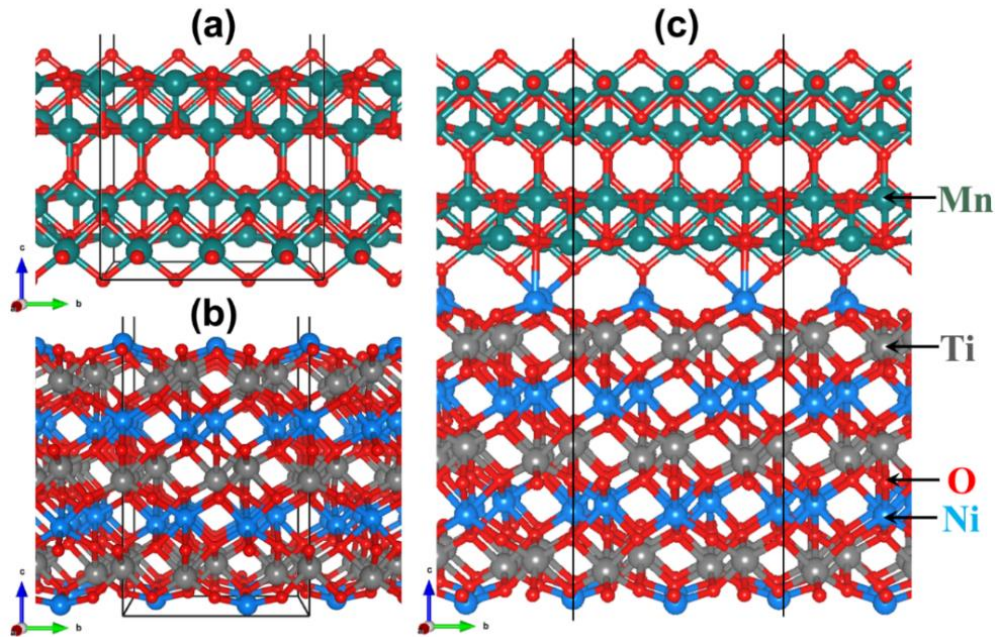


Figure. 6.13. Optimized structures of (a) $\text{MnO}_2(100)$, (b) $\text{NiTiO}_3(001)$, and (c) the equilibrium structure of the $\text{MnO}_2/\text{NiTiO}_3$ heterostructure.

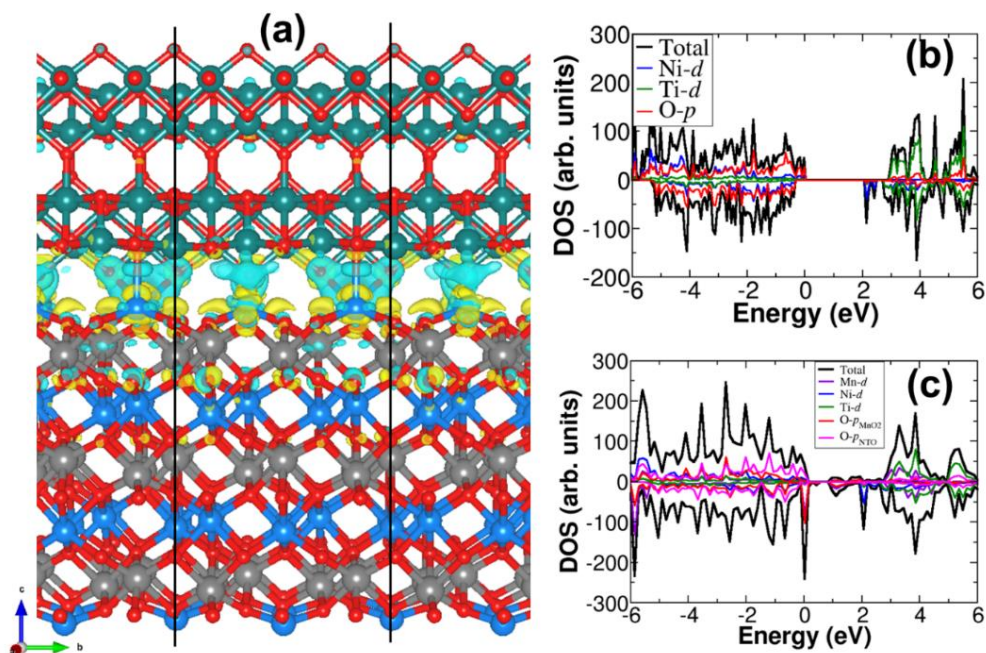


Figure. 6.14. (a) Charge density difference iso-surface contours of the MnO₂/NiTiO₃ heterostructure, where the cyan and yellow regions denote electron density accumulation and depletion by 0.03 e/Å³, respectively. PDOS of (b) isolated NiTiO₃(001) and (c) MnO₂/NiTiO₃ heterostructure.

6.4 Conclusion

In conclusion, we have demonstrated the synthesis and utilization of NTO@MnO₂ core-shell heteroarchitecture as an electrode for supercapacitors. The 1D NTO nanorods synthesized by the sol-gel technique were decorated with randomly arranged 2D MnO₂ nanoflakes utilizing a hydrothermal synthesis protocol. The heteroarchitecture of 2D MnO₂@1D NTO possesses an average pore size distribution of 3.92 nm throughout the structure. XPS analysis revealed the significant existence of Ni²⁺/Ni³⁺, Ti⁴⁺/Ti³⁺, and Mn⁴⁺/Mn⁶⁺ to boost the energy storage performance of the MnO₂@NTO core-shell structure. The large accessible surface area and well-connected morphology of synergistic 2D MnO₂ nanoflakes and 1D mesoporous NTO rods confirmed the sufficient penetration of electrolyte ions deep inside the heteroarchitecture and hence assisted in enhancing the specific capacitance. The working electrode made of NTO@MnO₂ core-shell heteroarchitecture exhibits excellent capacitive performance in terms of specific

capacitance (1054.7 F/g), specific power of 3892.5 W/kg, and specific energy of 15.7 Wh/kg, specific power (1822.8 W/kg), specific energy (i.e., 15.7 Wh/kg), and longer cycle life (85.3 % for 5000 cycles). The intact surface morphological features observed even after continuous 5000 GCD cycles confirmed the stable performance of the MnO₂@MTO core-shell structure. The experimental results were corroborated by DFT calculations, which showed improvement in the electrical conductivity of the MnO₂@MTO heterostructure due to the synergistic interactions between MnO₂ and MTO. Consequently, the large specific energy at a high specific power delivery rate and excellent cycling stability enables the core-shell structure composed of MnO₂ nanoflakes along the mesoporous MTO rods to be a suitable electrode material for supercapacitor applications.

6.5 References

- [1.] Patil D. S., Pawar S., Devan R., Mali S., Gang M., Ma Y., Hong C., Kim J., Patil P., (2014), Polyaniline based electrodes for electrochemical supercapacitor: Synergistic effect of silver, activated carbon and polyaniline, *J. Electroanal. Chem.*, 724, 21-28, (DOI:10.1016/j.jelechem.2014.04.006).
- [2.] Patil D. S., Pawar S. A., Devan R. S., Gang M. G., Ma Y.-R., Kim J. H., Patil P. S., (2013), Electrochemical supercapacitor electrode material based on polyacrylic acid/polypyrrole/silver composite, *Electrochim. Acta*, 105, 569-577, (DOI:10.1016/j.electacta.2013.05.022).
- [3.] Devan R. S., Patil R. A., Lin J. H., Ma Y. R., (2012), One-dimensional metal-oxide nanostructures: recent developments in synthesis, characterization, and applications, *Adv. Funct. Mater.*, 22, 3326-3370, (DOI:10.1002/adfm.201201008).
- [4.] Wang G., Zhang L., Zhang J., (2012), A review of electrode materials for electrochemical supercapacitors, *Chem. Soc. Rev.*, 41, 797-828, (DOI:10.1039/c1cs15060j).
- [5.] Jiang L.-B., Yuan X.-Z., Liang J., Zhang J., Wang H., Zeng G.-M., (2016), Nanostructured core-shell electrode materials for electrochemical capacitors, *J. Power Sources*, 331, 408-425, (DOI:10.1016/j.jpowsour.2016.09.054).
- [6.] Shaikh J., Pawar R. C., Devan R. S., Ma Y.-R., Salvi P. P., Kolekar S. S., Patil P. S., (2011), Synthesis and characterization of Ru doped CuO thin films for

- supercapacitor based on Bronsted acidic ionic liquid, *Electrochim. Acta*, 56, 2127-2134, (DOI:10.1016/j.electacta.2010.11.046).
- [7.] Patil R. A., Chang C.-P., Devan R. S., Liou Y., Ma Y.-R., (2016), Impact of nanosize on supercapacitance: study of 1D nanorods and 2D thin-films of nickel oxide, *ACS Appl. Mater. Interfaces*, 8, 9872-9880, (DOI:10.1021/acsami.6b00487).
- [8.] Devan R. S., Ma Y.-R., Patil R. A., Lukas S.-M., (2016), Highly stable supercapacitive performance of one-dimensional (1D) brookite TiO₂ nanoneedles, *RSC Adv.*, 6, 62218-62225, (DOI:10.1039/c6ra11348f).
- [9.] Gobal F., Faraji M., (2013), Fabrication of nanoporous nickel oxide by de-zincification of Zn–Ni/(TiO₂-nanotubes) for use in electrochemical supercapacitors, *Electrochim. Acta*, 100, 133-139, (DOI:10.1016/j.electacta.2013.03.155).
- [10.] Kitchamsetti N., Chikate P. R., Patil R. A., Ma Y.-R., Shirage P. M., Devan R. S., (2019), Perforated mesoporous NiO nanostructures for an enhanced pseudocapacitive performance with ultra-high rate capability and high energy density, *CrystEngComm*, 21, 7130-7140, (DOI:10.1039/c9ce01475f).
- [11.] Xu K., Li W., Liu Q., Li B., Liu X., An L., Chen Z., Zou R., Hu J., (2014), Hierarchical mesoporous NiCo₂O₄@MnO₂ core-shell nanowire arrays on nickel foam for aqueous asymmetric supercapacitors, *J. Mater. Chem. A*, 2, 4795-4802, (DOI:10.1039/c3ta14647b).
- [12.] Jiang H., Lee P. S., Li C., (2013), 3D carbon-based nanostructures for advanced supercapacitors, *Energy Environ. Sci.*, 6, 41-53, (DOI:10.1039/c2ee23284g).
- [13.] Xia X., Tu J., Zhang Y., Wang X., Gu C., Zhao X.-B., Fan H. J., (2012), High-quality metal oxide core/shell nanowire arrays on conductive substrates for electrochemical energy storage, *ACS Nano*, 6, 5531-5538, (DOI:10.1021/nn301454q).
- [14.] Mi H., Zhang X., An S., Ye X., Yang S., (2007), Microwave-assisted synthesis and electrochemical capacitance of polyaniline/multi-wall carbon nanotubes composite, *Electrochem. Commun.*, 9, 2859-2862, (DOI:10.1016/j.elecom.2007.10.013).

- [15.] Mi H., Zhang X., Ye X., Yang S., (2008), Preparation and enhanced capacitance of core-shell polypyrrole/polyaniline composite electrode for supercapacitors, *J. Power Sources*, 176, 403-409, (DOI:10.1016/j.powsour.2007.10.070).
- [16.] Bao L., Zang J., Li X., (2011), Flexible Zn₂SnO₄/MnO₂ core/shell nanocable-carbon microfiber hybrid composites for high-performance supercapacitor electrodes, *Nano Lett.*, 11, 1215-1220, (DOI:10.1021/nl104205s).
- [17.] Fau P., Bonino J., Rousset A., (1994), Electrical properties of sputtered MnO₂ thin films, *Appl. Surf. Sci.*, 78, 203-210, (DOI:10.1016/0169-4332(94)00111-1).
- [18.] Wu S., Zhang J., Sun C., Chen J., (2020), Synthesis of MnO₂/NiCo-layered double hydroxide hybrid as electrode materials for supercapacitor, *J. Inorg. Organomet. Polym. Mater.*, 30, 3179-3187, (DOI:10.1007/s10904-020-01481-1).
- [19.] Chen J., Huang Y., Li C., Chen X., Zhang X., (2016), Synthesis of NiO@MnO₂ core/shell nanocomposites for supercapacitor application, *Appl. Surf. Sci.*, 360, 534-539, (DOI:10.1016/j.apsusc.2015.10.187).
- [20.] Hu X. W., Liu S., Qu B. T., You X. Z., (2015), Starfish-shaped Co₃O₄/ZnFe₂O₄ hollow nanocomposite: synthesis, supercapacity, and magnetic properties, *ACS Appl. Mater. Interfaces*, 7, 9972-9981, (DOI:10.1021/acsami.5b02317).
- [21.] Zhou H., Zou X., Zhang Y., (2016), Fabrication of TiO₂@MnO₂ nanotube arrays by pulsed electrodeposition and their application for high-performance supercapacitors, *Electrochim. Acta*, 192, 259-267, (DOI:10.1016/j.electacta.2016.01.182).
- [22.] Ramesh S., Karuppasamy K., Kim H. S., Kim H. S., Kim J. H., (2018), Hierarchical flowerlike 3D nanostructure of Co₃O₄@MnO₂/N-doped Graphene oxide (NGO) hybrid composite for a high-performance supercapacitor, *Sci. Rep.*, 8, 11, (DOI:10.1038/s41598-018-34905-7).
- [23.] Ren B., Fan M., Yang X., Wang L., Yu H., (2019), 3D Hierarchical structure electrodes of MnO₂ nanosheets decorated on needle-like NiCo₂O₄ nanocones on ni foam as a cathode material for asymmetric supercapacitors, *ChemistrySelect*, 4, 5641-5650, (DOI:10.1002/slct.201901018).

- [24.] Li L., Hu Z. A., An N., Yang Y. Y., Li Z. M., Wu H. Y., (2014), Facile synthesis of MnO₂/CNTs composite for supercapacitor electrodes with long cycle stability, *J. Phys. Chem. C*, 118, 22865-22872, (DOI:10.1021/jp505744p).
- [25.] Kuang M., Wen Z. Q., Guo X. L., Zhang S. M., Zhang Y. X., (2014), Engineering firecracker-like beta-manganese dioxides@ spinel nickel cobaltates nanostructures for high-performance supercapacitors, *J. Power Sources*, 270, 426-433, (DOI:10.1016/j.jpowsour.2014.07.144).
- [26.] Ma P., Lei N., Yu B., Liu Y., Jiang G., Dai J., Li S., Lu Q., (2019), Flexible supercapacitor electrodes based on carbon cloth-supported LaMnO₃/MnO nanoarrays by one-step electrodeposition, *Nanomater.*, 9, 1676, (DOI:10.3390/nano9121676).
- [27.] Zhang X., Zhang Z., Sun S., Sun Q., Liu X., (2018), Hierarchical 3D NiFe₂O₄@ MnO₂ core-shell nanosheet arrays on Ni foam for high-performance asymmetric supercapacitors, *Dalton Trans.*, 47, 2266-2273, (DOI:10.1039/c7dt04127f).
- [28.] Kitchamsetti N., Ma Y.-R., Shirage P. M., Devan R. S., (2020), Mesoporous perovskite of interlocked nickel titanate nanoparticles for efficient electrochemical supercapacitor electrode, *J. Alloys Compds.*, 833, 155134, (DOI:10.1016/j.jallcom.2020.155134).
- [29.] Kresse G., Furthmüller J., Hafner J., (1994), Theory of the crystal structures of selenium and tellurium: the effect of generalized-gradient corrections to the local-density approximation, *Phys. Rev. B*, 50, 13181, (DOI: 10.1103/PhysRevB.50.13181).
- [30.] Kresse G., Joubert D., (1999), From ultrasoft pseudopotentials to the projector augmented wave method, *Phys. Rev. B*, 59, 1758-1775, (DOI: 10.1103/PhysRevB.59.1758).
- [31.] Perdew J. P., Burke K., Ernzerhof M., (1996), Generalized gradient approximation made simple, *Phys. Rev. Lett.*, 77, 3865-3868, (DOI: 10.1103/physrevlett.77.3865).
- [32.] Himmetoglu B., Floris A., de Gironcoli S., Cococcioni M., (2014), Hubbard-Corrected DFT Energy Functionals: The LDA + U Description of Correlated Systems, *Int. J. Quantum Chem.*, 114, 14-49, (DOI: 10.1002/qua.24521).

- [33.] Rohrbach A., Hafner J., Kresse G., (2003), Electronic correlation effects in transition-metal sulfides, *J. Phys. Condens. Matter*, 15, 979-996, (DOI: 10.1088/0953-8984/15/6/325).
- [34.] Grimme S., Antony J., Ehrlich S., Krieg H., (2010), A consistent and accurate ab initio parametrization of density functional dispersion correction (DFT-D) for the 94 elements H-Pu, *J. Chem. Phys.*, 132, 19, (DOI: 10.1063/1.3382344).
- [35.] Monkhorst H. J., Pack J. D., (1976), Special points for Brillouin-zone integrations. *Phys. Rev. B*, 13, 5188, (DOI: 10.1103/PhysRevB.13.5188).
- [36.] Tang W., Sanville E., Henkelman G., (2009), A grid-based Bader analysis algorithm without lattice bias, *J. Phys. Condens. Matter*, 21, 7, (DOI: 10.1088/0953-8984/21/8/084204).
- [37.] Moulder J. F., Stickle W. F., Sobol P. E., Bomben K. D., (1992), *Handbook of X-ray Photoelectron Spectroscopy*, Perkin-Elmer Corporation, Physical Electronics Division: Minnestoa, 55344, U.S.A., 261.
- [38.] Sun X., Radovanovic P. V., Cui B., (2015), Advances in spinel $\text{Li}_4\text{Ti}_5\text{O}_{12}$ anode materials for lithium-ion batteries, *New J. Chem.*, 39, 38-63, (DOI: 10.1039/C4NJ01390E).
- [39.] Devan R. S., Thakare V. P., Antad V. V., Chikate P. R., Khare R. T., More M. A., Dhayal R. S., Patil S. I., Ma Y. R., Schmidt-Mende L., (2017), Nano-Heteroarchitectures of Two-Dimensional MoS_2 @ One-Dimensional Brookite TiO_2 Nanorods: Prominent Electron Emitters for Displays, *ACS Omega*, 2, 2925-2934, (DOI: 10.1021/acsomega.7b00345).
- [40.] Chikate P. R., Bankar P. K., Choudhary R. J., Ma Y. R., Patil S. I., More M. A., Phase D. M., Shirage P. M., Devan R. S., (2018), Spitzer shaped ZnO nanostructures for enhancement of field electron emission behaviors, *RSC Adv.*, 8, 21664-21670, (DOI: 10.1039/C8RA03282C).
- [41.] Sun S., Zhang X., Wu Y., Liu X., Meng Y., Zhao X., Liu P. X., (2019), Synthesis of ZnFe_2O_4 @ MnO_2 Multilevel Nanosheets Structure and Its Electrochemical Properties as Positive Electrodes for Asymmetric Supercapacitors, *ChemistrySelect*, 4, 5168-5177, (DOI: 10.1002/slct.201900346).

- [42.] Liu X., Shi S., Xiong Q., Li L., Zhang Y., Tang H., Gu C., Wang X., Tu J., (2013), Hierarchical NiCo₂O₄@NiCo₂O₄ core/shell nanoflake arrays as high-performance supercapacitor materials, *ACS Appl. Mater. Interfaces*, 5, 8790-8795, (DOI: 10.1021/am402681m).
- [43.] Wen S., Liu Y., Zhu F., Shao R., Xu W., (2018), Hierarchical MoS₂ nanowires/NiCo₂O₄ nanosheets supported on Ni foam for high-performance asymmetric supercapacitors, *Appl. Surf. Sci.*, 428, 616-622, (DOI: 10.1016/j.apsusc.2017.09.189).
- [44.] Jia H. N., Wang Z. Y., Zheng X. H., Cai Y. F., Lin J. H., Liang H. Y., Qi J. L., Cao J., Feng J. C., Fei W. D., (2019), Controlled synthesis of MOF-derived quadruple-shelled CoS₂ hollow dodecahedrons as enhanced electrodes for supercapacitors, *Electrochim. Acta*, 312, 54-61, (DOI: 10.1016/j.electacta.2019.04.192).
- [45.] Zhao L., Yang M., Zhang Z., Ji Y., Teng Y., Feng Y., Liu X., (2018), Hierarchical micro/nanostructured Co₃O₄@MnCo₂O₄ core-shell nanowire arrays on Ni foam for electrochemical energy storage, *Inorg. Chem. Commun.*, 89, 22-26, (DOI: 10.1016/j.inoche.2018.01.003).
- [46.] Zhu L., Ran R., Tade M., Wang W., Shao Z., (2016), Perovskite materials in energy storage and conversion. *Asia-Pac. J. Chem. Eng.*, 11, 338-369, (DOI: 10.1002/adfm.202003653).
- [47.] Xiao H., Guo W., Sun B., Pei M., Zhou G., (2016), Mesoporous TiO₂ and Co-doped TiO₂ nanotubes/reduced graphene oxide composites as electrodes for supercapacitors, *Electrochim. Acta*, 190, 104-117, (DOI: 10.1016/j.electacta.2016.01.040).
- [48.] Wang X., Zhu Q., Wang X., Zhang H., Zhang J., Wang L., (2016), Structural and electrochemical properties of La_{0.85}Sr_{0.15}MnO₃ powder as an electrode material for supercapacitor, *J. Alloys Compd.*, 675, 195-200, (DOI: 10.1016/j.jallcom.2016.03.048).
- [49.] Zhang Y. X., Huang M., Li F., Wang X. L., Wen Z. Q., (2014), One-pot synthesis of hierarchical MnO₂-modified diatomites for electrochemical capacitor electrodes, *J. Power Sources*, 246, 449-456, (DOI: 10.1016/j.jpowsour.2013.07.115).

- [50.] Duay J., Gillette E., Liu R., Lee S. B., (2012), Highly flexible pseudocapacitor based on freestanding heterogeneous MnO₂/conductive polymer nanowire arrays, *Phys. Chem. Chem. Phys.*, 14, 3329-3337, (DOI: 10.1039/C2CP00019A).
- [51.] Li L., Hu Z. A., An N., Yang Y. Y., Li Z. M., Wu H. Y., (2014), Facile Synthesis of MnO₂/CNTs Composite for Supercapacitor Electrodes with Long Cycle Stability, *J. Phys. Chem. C*, 118, 22865-22872, (DOI: 10.1021/jp505744p).
- [52.] Ma P. P., Lei N., Yu B., Liu Y. K., Jiang G. H., Dai J. M., Li S. H., Lu Q. L., (2019), Flexible Supercapacitor Electrodes Based on Carbon Cloth-Supported LaMnO₃/MnO Nano-Arrays by One-Step Electrodeposition, *Nanomater.*, 9, 15, (DOI: 10.3390/nano9121676).
- [53.] Lu X.-F., Wu D.-J., Li R.-Z., Li Q., Ye S.-H., Tong Y.-X., Li G.-R., (2014), Hierarchical NiCo₂O₄ nanosheets@ hollow microrod arrays for high-performance asymmetric supercapacitors, *J. Mater. Chem. A*, 2, 4706-4713, (DOI: 10.1039/C3TA14930G).
- [54.] Sun X., Xie M., Travis J. J., Wang G. K., Sun H. T., Lian J., George S. M., (2013), Pseudocapacitance of Amorphous TiO₂ Thin Films Anchored to Graphene and Carbon Nanotubes Using Atomic Layer Deposition, *J. Phys. Chem. C*, 117, 22497-22508, (DOI: 10.1021/jp4066955).
- [55.] Wang D. W., Li F., Cheng H. M., (2008), Hierarchical porous nickel oxide and carbon as electrode materials for asymmetric supercapacitor, *J. Power Sources*, 185, 1563-1568, (DOI: 10.1016/j.jpowsour.2008.08.032).
- [56.] Lang X. Q., Mo H. Y., Hu X. Y., Tian H. W., (2017), Supercapacitor performance of perovskite La_{1-x}Sr_xMnO₃, *Dalton Trans.*, 46, 13720-13730, (DOI: 10.1039/C7DT03134C).
- [57.] Patil A. M., Lokhande A. C., Chodankar N. R., Kumbhar V. S., Lokhande C. D., (2016), Engineered morphologies of beta-NiS thin films via anionic exchange process and their supercapacitive performance, *Mater. Des.*, 97, 407-416, (DOI: 10.1016/j.matdes.2016.02.114).
- [58.] Zhang Y., Xu J., Zheng Y. Y., Zhang Y. J., Hu X., Xu T. T., (2017), NiCo₂S₄@NiMoO₄ Core-Shell Heterostructure Nanotube Arrays Grown on Ni Foam as a Binder-Free Electrode Displayed High Electrochemical Performance

- with High Capacity, *Nanoscale Res. Lett.*, 12, 9, (DOI: 10.1186/s11671-017-2180-z).
- [59.] Kuang M., Zhang Y. X., Li T. T., Li K. F., Zhang S. M., Li G., Zhang W., (2015), Tunable synthesis of hierarchical NiCo₂O₄ nanosheets-decorated Cu/CuO_x nanowires architectures for asymmetric electrochemical capacitors, *J. Power Sources*, 283, 270-278, (DOI: 10.1016/j.jpowsour.2015.02.117).
- [60.] Zeng Z. F., Wang D. Z., Zhu J. L., Xiao F. Q., Li Y. D., Zhu X. H., (2016), NiCo₂S₄ nanoparticles//activated balsam pear pulp for asymmetric hybrid capacitors, *CrystEngComm*, 18, 2363-2374, (DOI: 10.1039/C6CE00319B).
- [61.] Senthilkumar S. T., Fu N. Q., Liu Y., Wang Y., Zhou L. M., Huang H. T., (2016), Flexible fiber hybrid supercapacitor with NiCo₂O₄ nanograss@carbon fiber and bio-waste derived high surface area porous carbon, *Electrochim. Acta*, 211, 411-419, (DOI: 10.1016/j.electacta.2016.06.059).
- [62.] Lin Y. P., Wu N. L., (2011), Characterization of MnFe₂O₄/LiMn₂O₄ aqueous asymmetric supercapacitor, *J. Power Sources*, 196, 851-854, (DOI: 10.1016/j.jpowsour.2010.07.066).
- [63.] Anjana P. S., Sebastian M. T., (2006), Synthesis, characterization, and microwave dielectric properties of ATiO₃ (A= Co, Mn, Ni) ceramics, *J. Am. Ceram. Soc.*, 89, 2114-2117, (DOI: 10.1111/j.1551-2916.2006.01004. x).
- [64.] Preciado M. A. R., Kassiba A., Acevedo A. M., Janusik M. M., (2015), Vibrational and electronic peculiarities of NiTiO₃ nanostructures inferred from first principle calculations, *RSC Adv.*, 5, 17396-17404, (DOI: 10.1039/C4RA16400H).
- [65.] Xin C., Wang Y., Sui Y., Wang Y., Wang X., Zhao K., Liu Z., Li B., (2014), Electronic, magnetic and multiferroic properties of magnetoelectric NiTiO₃, *J. Alloys Compds*, 613, 401-406, (DOI: 10.1016/j.jallcom.2014.05.189).
- [66.] Cheng F. Y., Zhang T., Zhang Y., Du J., Han X. P., Chen J., (2013), Enhancing Electrocatalytic Oxygen Reduction on MnO₂ with Vacancies, *Angew. Chem. Int. Ed.*, 52, 2474-2477, (DOI: 10.1002/anie.201208582).
- [67.] Rondiya S. R., Karbhal I., Jadhav C. D., Nasane M. P., Davies T. E., Shelke M. V., Jadkar S. R., Chavan P. G., Dzade N. Y., (2020), Uncovering the origin of enhanced field emission properties of rGO–MnO₂ heterostructures: a synergistic experimental

and computational investigation, *RSC Adv.*, 10, (2020), 25988-25998, (DOI: 10.1039/D0RA03360J).

- [68.] Sakai N., Ebina Y., Takada K., Sasaki T., (2005), Photocurrent generation from semiconducting manganese oxide nanosheets in response to visible light, *J. Phys. Chem. B*, 109, 9651-9655, (DOI: 10.1021/jp0500485).

Chapter 7

Summary and Conclusions

Chapter 7 includes the summary and conclusion of the thesis work. Through my research work, I learned that synthesizing various mesoporous nanostructure morphologies and forming core-shell heterostructures can enhance the performance of the supercapacitor. This thesis work is focused on synthesizing the various mesoporous 1D nanostructures of the binary, ternary metal oxides and further subjected to form the core-shell heterostructure. The prime importance is given to synthesizing a variety of nanostructures and utilization of electrochemical energy storage performance. This thesis enabled me to explore unique NiO nanobelts and their application to electrochemical supercapacitors. Further, this thesis enabled the design of unique mesoporous $ATiO_3$ ($A=Ni$ and Co) one-dimensional perovskite nanostructures using a cost-effective chemical route, which is helpful for a variety of industrial applications. The materials are unique because these types of materials are not well explored for energy storage applications. This thesis also enabled the synthesis of the heteroarchitecture of 2D MnO_2 shell and 1D $NiTiO_3$ perovskite core and studied the electrochemical performance.

7.1 Summary and Conclusions

The low electrical conductivity and slow ions diffusion in bulk have hampered the practical usage of transition metal oxides as electrode material for supercapacitor. However, the variety of nanostructure morphology, high surface area, and high theoretical specific capacitance of transition metal oxides has attracted the scientific community to explore their compatibility for further enhancement. The introduction of defects and control over the interface at the nanoscale are explored approaches to enhance energy storage performance. The nanostructured morphology of transition metal oxides has been observed to enhances the reaction sites and reduce the ion diffusion length. Especially, well-designed mesoporous morphologies that hold two or three-dimensional (3D) interconnected pores of 2-50 nm diameter have been accepted as the most promising. The ordered mesoporous metal oxides have numerous advantages over the bulk form in the electrochemical field, such as high surface area furnishes numbers of charge storage sites, interconnected mesopores facilitate the diffusion of electrolyte ions, nanometer-sized walls develop small crystallites and grain boundaries, and porous structures act as a host for loading high capacitance guest materials. Therefore, investigation of the electrochemical properties of mesoporous transition metal oxides is essential and urgent to improve energy storage performance. The nanosized perovskite metal oxides with the ABO_3 formula are considered a promising replacement for binary metal oxides in the supercapacitor. The structural stability of the cations, oxygen ion mobility, and vacancies mediate the redox mechanism in the perovskite. Moreover, the presence of multiple transition metal ions in the perovskite structure shall apprehend distinct charge storing mechanisms and hence capable of delivering the breakthrough performance of the supercapacitor. However, most of the studies are focused on Lanthanum based perovskites owing to their better electrical conductivity. Even though few reports are available on the synthesis of Ni, Co, Mn, and Ti-based perovskite nanostructures, none of them are focused on synthesizing one-dimensional mesoporous nanostructure for utilization as the working electrode in the supercapacitor. 1D nanostructural morphologies provide direct pathways for electron/ion transfer at the electrode-electrolyte interface. The mesoporous form adds a larger surface area to the 1D morphology and may improve the electrochemical performance. Therefore, mesoporous

1D morphologies of $ATiO_3$ (where $A = Ni$ and Co) are explored for their electrochemical energy storage performance. Therefore, I have focused on synthesizing the mesoporous 1D nanostructures of the binary and ternary metal oxides consisting of Ni, Ti, Co, and Mn elements. The prime importance is given for the optimized synthesis of 1D mesoporous structures comprised of nanostructure morphologies, which were further subjected to confirm their electrochemical energy storage performance. The unique NiO nanobelts are explored as a working electrode for electrochemical supercapacitors. Further, $CoTiO_3$ and $NiTiO_3$ perovskites are explored to gain better energy storage performance. The 1D mesoporous morphologies of these perovskites were synthesized using a cost-effective chemical route. Moreover, heteroarchitecture of best performing $NiTiO_3$ perovskites as core and the 2D MnO_2 nanosheets as the shell has been explored to enhance energy storage performance. Thus, the thesis work is divided into three major parts such as the mesoporous 1D NiO nanostructures, mesoporous 1D $ATiO_3$ ($A = Ni$ and Co) perovskite nanostructures, and 2D $MnO_2@1D NiTiO_3$ as core-shell heteroarchitecture. The summarized conclusions of my research are as follows

The large area arrays of morphology-controlled NiO nanostructures were synthesized on ITO coated glass substrates via a hydrothermal synthesis approach. The irregular morphologies of nickel oxide (NiO) are transformed into the mesoporous nanobelts and further altered into the nanoflakes by controlling the hydrothermal reaction for different time intervals such as 6, 12, 18, 24, and 48 h. This morphology-controlled methodology is explored to enhance the specific capacitance (C_s) and the energy density of the NiO nanostructures (Figure 7.1). The nanobelts and nanoflakes of NiO with an average width of ~ 74 nm and ~ 215 nm organizes the thickness of film ~ 5.8 and 2.7 μm , respectively. The mesoporous NiO nanobelts with clearly visible textural boundaries deliver reasonably higher surface area (i.e., 40.572 m^2/g) and pore size distribution (i.e., ~ 19.7 nm) than that of nanoflakes and irregular morphologies, which offer easy access to larger surface-active sites and assisted the substantial diffusion of OH^- ions. Therefore, perforated mesoporous NiO nanobelts offer a higher specific capacitance of 794 F/g than the nanoflakes of 146 F/g and asymmetrical morphologies of 742 F/g. Moreover, mesoporous NiO nanobelts exhibited exceptional charge-discharge performance in an aq. $2M$ KOH electrolyte and delivered energy density of 57 Wh/kg, power density of 2963

W/kg, and 88.6 % retention in capacitance even after continuous 2500 charge-discharge cycles. The interlocking network of well-associated mesoporous NiO nanobelts provided excellent electrochemical reversibility and recommends its potential as electrode material for the supercapacitor with ultra-high rate capabilities and high energy density. Overall, the well-ordered methodology of altering mesoporous nanobelts from asymmetrical morphologies and further transforming them into 2D nanoflakes have unlocked a new path towards enhancing the charge storage mechanism and its employment in the hybrid supercapacitor.

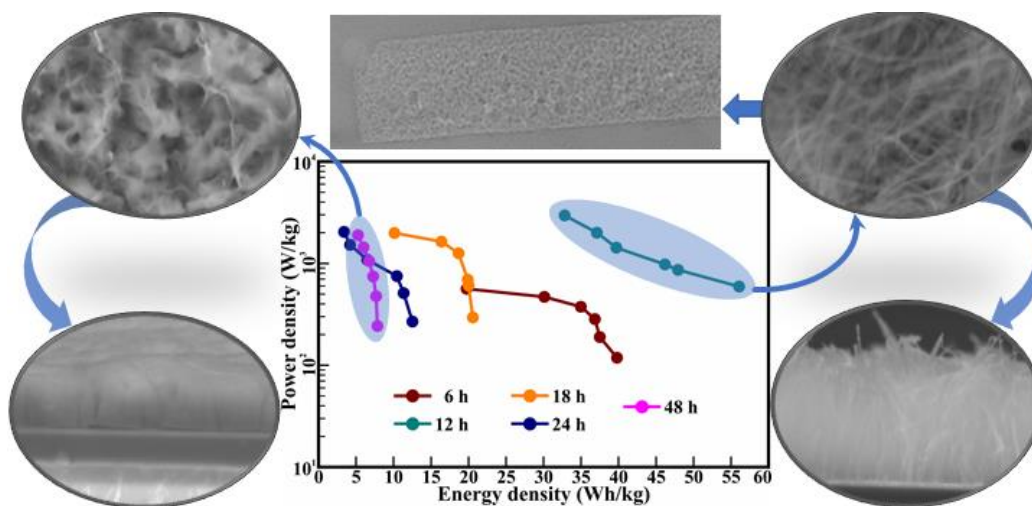


Figure 7.1. 1D nanobelts (right panel) and 2D nanosheets (left panel) morphology of NiO has significantly controlled the pseudocapacitive performance in the KOH electrolyte. The perforated and interlocked mesoporous structure of NiO nanobelts have delivered higher power density and energy density (middle panel) than that of nanosheets.

The mesoporous cobalt titanite (CoTiO_3) microrods incorporating interlocked nanoparticles with clearly visible textural boundaries are synthesized by the sol-gel technique (Figure 7.2). The CTO nanoparticles of average diameter ~ 59 nm hierarchically organized in the hexagonal form delivered mesoporous microrods of average diameter ~ 800 nm and the average pore size distribution of 3.919 nm throughout the microrod body. The CTO nanoparticles of mesoporous rods are of the hexagonal crystalline phase to the space group of R-3. The interconnection of CTO nanoparticles resulted in the formation of mesoporous rods with increased textural boundaries offered a larger surface area for considerably greater diffusion of OH^- ions, further leading to

larger specific capacitance (C_s) in an aq. 2 M KOH electrolyte. The diffusion-controlled access to the OH^- ions ($0.27 \mu\text{s}$) deep inside the rod structure offers an energy density of 9.77 Wh/kg and power density of 4835.7 W/kg. Furthermore, the outstanding cyclic stability up to 1950 continuous charging-discharging cycles with the capacitance retention of 82.3 % suggests the mesoporous CTO microrods as an efficient working electrode material for the supercapacitor.

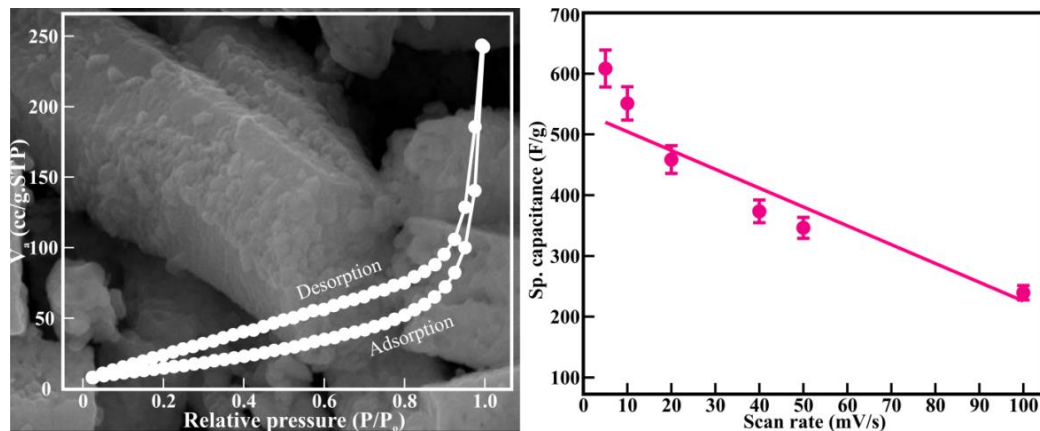


Figure 7.2. The interconnection of CTO nanoparticles resulted in the formation of mesoporous CTO rods with increased textural boundaries (left panel), offered significantly larger diffusion of OH^- ions deep inside the rod structure, and delivered a specific capacitance of 608.4 F/g (right panel), the specific power of 4835.7 W/kg, and specific energy of 9.77 Wh/kg.

The mesoporous nickel titanite (NiTiO_3) rods encompassing hierarchically interlocked nanoparticles were synthesized by the sol-gel synthesis route (Figure 7.3). The NTO nanoparticles of diameter ~ 30 nm hierarchically arranged in the hexagonal form delivered mesoporous rods of the average pore size distribution of 17.481 nm throughout the rod body. The hierarchical interlocking of NTO nanoparticles resulted in the formation of mesoporous microrods with increased textural boundaries offered a higher surface area for significantly larger diffusion of OH^- ions, further leading to improved specific capacitance (C_s) of 542.26 F/g in optimized 2 M aq. KOH electrolyte solution. The diffusion-controlled easy access to the OH^- ions ($20.4 \mu\text{s}$) deep inside the rod body through the mesoporous gained energy density of 8.06 Wh/kg and power density of 4320 W/kg. Moreover, the cyclic stability up to 2100 cycles with the capacitance

retention of 91 % projected the mesoporous NiTiO₃ rods as capable electrode material for the supercapacitor with stable performance.

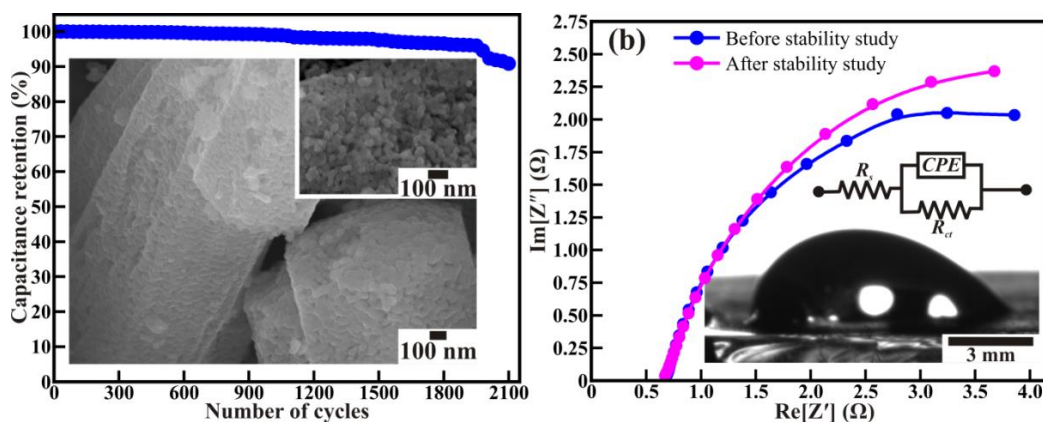


Figure 7.3. Mesoporous nickel titanate rods encompassing hierarchically interlocked nanoparticles (inset of left panel) provided diffusion-controlled easy/faster and enhanced access to the OH⁻ ions deep inside the rod body (inset of right panel) and delivered highly stable long-life cycle (left panel) up to 2100 cycles with partial reduction in the charge diffusion mechanism (right panel).

The best performing mesoporous NTO has been explored to form nano-hetero-architectures with promising MnO₂ nanosheets as electrode materials for supercapacitors to enhance the specific capacitance and cyclic stability further. The heteroarchitecture of MnO₂@NTO possesses an average pore size distribution of 3.92 nm throughout the porous structure. XPS analysis revealed the insignificant existence of Ni²⁺/Ni³⁺, Ti⁴⁺/Ti³⁺, and Mn⁴⁺/Mn⁶⁺. It confirmed the formation of sufficient penetration of electrolyte ions and helped to enhance the specific capacitance. The electrode made of NTO@MnO₂ core-shell heteroarchitecture works under a voltage window of 0.6 V and exhibits excellent capacitive performance in terms of power density, energy density, and cycle life. The NTO@MnO₂ achieves a higher density of 15.7 Wh/kg at a power density of 1822.8 W/kg, which is much larger than the NTO microrod (Figure 7.4). The large energy density at a high power delivery rate and excellent cycling stability enables the NTO@MnO₂ to be a suitable electrode material for pseudocapacitor applications.

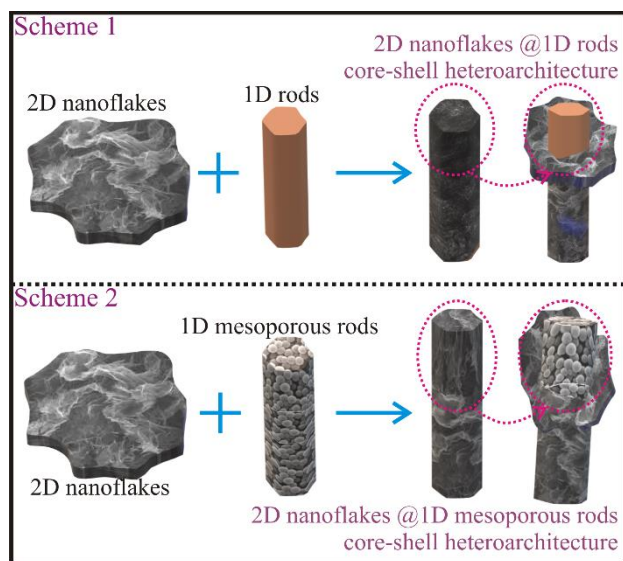


Figure 7.4. The synergistic heteroarchitecture of interlinked 2D nanoflakes and 1D mesoporous rods of interconnected nanoparticles provided relatively larger access for ions to diffuse deep inside and delivered excellent energy storage performance as the electrode.

Overall, this study reports the electrochemical energy storage performance of three different morphological forms of mesoporous metal oxides, i.e., nanobelts, rods composed of interconnected nanoparticles, and core-shell heteroarchitecture of nanoflakes and rods. The mesoporous morphologies have assisted in improving the electrochemical performance compared to their solid morphologies reported in the literature. However, a comparison of the observed results in this study (Table 7.1) indicates that the core-shell heteroarchitecture of 2D MnO_2 nanoflakes and 1D NiTiO_3 mesoporous rods have delivered higher specific capacitance, larger specific energy density, better specific power density, and excellent cyclic stability than the pristine NiO mesoporous nanobelts, NiTiO_3 mesoporous rods and CoTiO_3 mesoporous rods.

Table 7.1 Comparison of energy storage performance of the electrode materials explored in the present study.

Electrode material	C_s (F/g)	E (Wh/kg)	P (W/kg)	C_s retention (% @ 2000 cycles)
NiO nanobelts	794	57	2963	88.6
CoTiO_3 perovskite	608.4	9.77	4835.7	82.3
NiTiO_3 perovskite	542.3	8.06	4320	91
NTO@MnO_2	1054.7	15.7	3892.5	90.4

7.2 Future scope

Supercapacitors have several futuristic applications, which include (i) the transportation industry, (ii) consumer electronics as backup energy sources for mobile phones and computers, and (iii) temporary backup power in uninterrupted power supply systems (UPS). Further supercapacitors have shown promising application for critical-load operations, like the banking sector, hospitals, cell phone towers, airport control towers, etc., due to their ability to provide power within milliseconds to a few seconds, and effectively bridge the power outage and generator. Moreover, the hybridization of the supercapacitor is expected to challenge the battery. Therefore, one should look to improve the specific energy and power density of the supercapacitor in the near future. The present electrochemical energy storage studies signify that mesoporous NiO, CoTiO₃, NiTiO₃, and MnO₂@NiTiO₃ materials delivering excellent specific capacitance and long cyclic stability, shall be competent electrode materials for hybrid supercapacitors. Nevertheless, some of the key findings gave further links to explore replacement for A (i.e., divalent metal ions) in ATiO₃ perovskites and their nano-hetero-architectures with different combinations, such as:

1. Study the effect of MnO₂ and NiO shell layer over mesoporous CTO rods in the electrochemical energy storage performance.
2. Explore the mesoporous ATiO₃ (A= Zn, Fe) perovskites, where A can be Mn, Cu, Fe, Zn, etc., as a working electrode electrochemical supercapacitor.
3. Study the effect of doping at A sites in the overall electrochemical performance of ATiO₃ perovskites.
4. These ATiO₃ materials shall be competitive candidates for applications in water splitting, photocatalysis, and gas/ humidity sensors.